UNIVERSITY OF NOVA GORICA
GRADUATE SCHOOL

STRUCTURAL, MORPHOLOGICAL AND CHEMICAL PROPERTIES OF METAL/TOPOLOGICAL INSULATOR INTERFACES

DISSERTATION

Katja Ferfolja

Mentor: prof. dr. Mattia Fanetti

Nova Gorica, 2021

UNIVERZA V NOVI GORICI
FAKULTETA ZA PODIPLOMSKI ŠTUDIJ

STRUKTURNE, MORFOLOŠKE IN KEMIJSKE LASTNOSTI STIČNIH PLOSKEV MED KOVINO IN TOPOLOŠKIM IZOLATORJEM

DISERTACIJA

Katja Ferfolja

Mentor: prof. dr. Mattia Fanetti

Nova Gorica, 2021

UNIVERSITY OF NOVA GORICA
GRADUATE SCHOOL

Katja Ferfolja, *Structural, Morphological and Chemical Properties of Metal/Topological Insulator Interfaces,* Dissertation, (2021)

ACKNOWLEDGEMENTS

First of all, I would like to express my sincerest gratitude to my mentor prof. dr. Mattia Fanetti for his guidance, encouragement, patience and help with all scientific work encountered during my PhD studies. Thank you also for introducing me into the field of electron microscopy and for all your effort put into my training.

I would like to extend my gratitude to the head of our laboratory prof. dr. Matjaž Valant for his help regarding the chemistry related topics, for reviewing articles and valuable critique.

Thanks to prof. dr. Sandra Gardonio for always being available for explanations or advice and for teaching me about the XPS.

Many thanks also to dr. Mirco Panighel at CNR-IOM for his help with the STM measurements and to scientist at Bach beamline at Elettra Synchrotron for their help when performing the XPS measurements, especially to dr. Igor Píš for his kindness and help during the measurement and with further analysis.

Next thank goes to the Laboratory of Organic Matter Physics for allowing me to do some experiments in their lab and for their help while carrying them out.

Many thanks to all my colleagues of the Material Research Laboratory, especially to Mojca Vrčon Mihelj for being a perfect office mate. Thank you for all conversations, advices and great time spent together. Thanks to dr. Blaž Belec for his help with the TEM and fun lunchbreaks, and to dr. Andraž Mavrič for his help in the laboratory and for inviting me to go on a PhD journey. Thanks also to former member of our laboratory dr. Iuliia Mikulska for her help at the very beginning of my PhD studies. Thanks also to our secretary Saša Badalič for taking care of the paperwork, for always being so positive and for the best coffee breaks.

Finally, I would like to thank my family for supporting and encouraging me throughout my study, especially to my husband Erik to whom I also dedicate this work.

ABSTRACT

Topological insulators (TIs) represent a new state of matter that possess a different band structure than regular insulators or conductors. They are characterized with a band gap in the bulk and conductive topological states on the surface, which are spin polarized and robust toward contamination or deformation of the surface. Since the intriguing properties of the TIs are localized at the surface, it is important to obtain knowledge of the possible phenomena happening at the interface between TIs and other materials. This is especially true in the case of metals, due to the fact that such interfaces will be present in the majority of foreseen TI applications.

The presented study combines microscopy and spectroscopy techniques for characterization of morphology, stability and chemical interaction at the interface between TI and metals deposited by means of physical vapor deposition. Our research is based on the interface of Bi_2Se_3 topological insulator with Ag, Ti and Pt – metals that can be encountered in devices or applications predicted to utilize the special properties of topological insulators.

STM and SEM imaging of Ag/Bi_2Se_3 interface showed that Ag atoms arrange on the surface in the form of islands, whereas significantly bigger agglomerates are found at the surface steps. The interface was found to be unstable in time and resulted in the absorption of the metal into the crystal at room temperature. Evidences of a chemical reaction at the Ag/Bi_2Se_3 interface are presented, showing that new phases (Ag_2Se, $AgBiSe_2$ and metallic Bi) are formed.

Deposition of Ti on Bi_2Se_3 resulted in different morphologies depending on the film thickness. At a very low coverage (<1 Å) islands are formed. However, the islands growth is hindered before the completion of a full layer due to the occurrence of a chemical reaction. No surface features could be detected by SEM for Ti coverage up to 20 nm. In contrary, when Ti thickness reached 40 nm, compressive stress triggered buckling of the deposited film. XPS analysis revealed that a redox solid-state reaction occurs at the Ti/Bi_2Se_3 interface at room temperature forming titanium selenides and metallic Bi. The reaction has significant kinetics even at cryogenic temperature of 130 K.

Pt forms a homogenous film over the whole substrate surface, which is stable in time at room temperature. Although the interface of Pt with Bi_2Se_3 was found to be less reactive compared to Ag and Ti, an interfacial phase formed upon annealing to ~90 °C was detected by TEM cross section experiment.

A model for prediction of interfacial reactions between a metal and Bi_2Se_3 based on the standard reduction potential of the metals and Gibbs free energy for a model reaction is presented. Based on these two values the reaction can be expected to result in the formation of binary and/or ternary selenides and Bi.

Presented work shows on the importance of metal/topological insulator interfaces characterization taking into account the possibility of a chemical reaction with all of its consequences. Results should be considered for future theoretical and applicative studies involving such interfaces as well as for the possible engineering of 2D TI heterostructures.

Keywords: topological insulators, topological surface states, Bi_2Se_3, thin films, Ag, Ti, Pt, morphology, interfaces, solid-state reaction, metal selenides, reactivity, stability, electron microscopy

POVZETEK

V doktorski disertaciji je predstavljena študija stičnih ploskev med kovino in topološkim izolatorjem (TI). Topološki izolatorji predstavljajo novo vrsto materialov, ki se po svoji elektronsko pasovno strukturi razlikujejo od običajnih izolatorjev ali prevodnikov. Za notranjost materiala je značilen prepovedan pas, medtem ko so na površini prisotna prevodna topološka stanja. Stanja na površini so topološko zaščitena in posledično veliko bolj obstojna v primeru kontaminacije ali deformacije v primerjavi z običajnimi elektronskimi stanji na površini. Poleg tega so topološka stanja na površini spinsko polarizirana, kar preprečuje povratno sipanje elektronov pri transportu. Ker so posebne lastnosti TI lokalizirane na površini, so študije stičnih ploskev med TI in drugimi materiali izrednega pomena. To še posebej velja za primer stične ploskve s kovino, saj je takšen kontakt predviden za večino aplikacij, kjer bi se TI lahko uporabljali.

Raziskava zdužuje mikroskopske in spektroskopske metode za karakterizacijo morfologije, stabilnosti in kemijskih interakcij na stični površini med TI in kovinami, ki so nanešene s pomočjo metod fizikalnega nanosa iz parne faze. Raziskava opisuje stično ploskev med topološkim izolatorjem Bi_2Se_3 ter Ag, Ti in Pt – kovinami, ki jih srečamo v napravah ali drugih aplikacijah, predvidenih za izkoriščanje posebnih lastnosti topoloških izolatorjev.

STM in SEM meritve stične ploskve Ag/Bi_2Se_3 so pokazale, da atomi Ag na ravni površini Bi_2Se_3 tvorijo skupke, medtem ko se na prehodih med posameznimi plastmi tvorijo veliko večji aglomerati. Stik med Ag in Bi_2Se_3 se je izkazal kot nestabilen, saj sčasoma pride do absorpcije kovine v substrat. Posledično se morfologija površine spremeni. Zaznane spremembe so posledica kemijske reakcije na stični ploskvi. Uporaba različnih spektroskopskih metod je omogočila določitev produktov, ki nastanejo v reakciji, in sicer Ag_2Se, $AgBiSe_2$ in Bi.

Morfološka struktura Ti na Bi_2Se_3 je odvisna od debeline nanešenega filma. Pri nanosu zelo majhne količine Ti (<1 Å) na površino Bi_2Se_3 nastanejo skupki. V začetku se ti skupki z večanjem debeline nanosa Ti povečujejo, vendar se rast nato ustavi zaradi pojava kemijske reakcije, ki onemogoča nastanek homogenega sloja. SEM analiza nanometrskih filmov Ti (>5 nm) je pokazala enako morfologijo površine kot v primeru čistega Bi_2Se_3. Pri večjih debelinah nanešenega Ti (okrog 40 nm) pa se je v filmu ustvarila tlačna napetost, ki je sprožila nagubanje in mehanski razpad filma. XPS analiza je pokazala, da pride na stiku Ti/Bi_2Se_3 do kemijske redoks reakcije v trdnem, pri kateri se tvorijo titanovi selenidi in kovinski Bi. Reakcija poteče hitro tudi pri nizki temperaturi (130 K).

Pt tvori homogen film čez celotno površino Bi_2Se_3. Film ne kaže vidnih morfoloških sprememb v času po hranjenju pri sobnih pogojih. Čeprav se je stična ploskev med Pt in Bi_2Se_3 izkazala za veliko manj reaktivno v primerjavi z Ag in Ti, je segrevanje vzorca na temperaturo ~90 °C privedlo do nastanka nove faze, ki je bila detektirana s pomočjo TEM.

Na osnovi standardnega redukcijskega potenciala in Gibbsove proste energije za teoretično reakcijo smo izdelali model za napovedovanje reakcije na stični ploskvi med kovino in Bi_2Se_3. Glede na omenjeni vrednosti lahko predvidimo ali bo kemijska reakcija privedla do nastanka binarnih in/ali ternarnih selenidov in Bi.

Predstavljeno delo kaže na pomen karakterizacije stičnih ploskev kovina/topološki izolator z ozirom na nastanek kemijske reakcije in posledic, ki jih le-ta povzroči. Dobljene rezultate je smiselno upoštevati za nadaljne teoretične in eksperimentalne študije, ki vključujejo podobne stične površine, kot tudi za možnost načrtovanja in sintezo 2D heterostruktur s topološkimi izolatorji.

Ključne besede: topološki izolatorji, topološka površinska stanja, Bi_2Se_3, tanki filmi, Ag, Ti, Pt, morfologija, stične ploskve, reakcija v trdnem, kovinski selenidi, reaktivnost, stabilnost, elektronska mikroskopija

Table of Contents

Abbreviations

AES Auger electron spectroscopy
AFM atomic force microscopy
ARPES angle resolved X-ray photoelectron spectroscopy
BB band bending
BE binding electron
BL bilayer
BSE backscattered electrons
CCD charge coupled device
EDS or EDX energy dispersive spectroscopy
EELS electron energy loss spectroscopy
ESCA electron spectroscopy for chemical analysis
FT Fourier transform
FWHM full width half maximum
HER hydrogen evolution reaction
HSA hemispherical electron energy analyzer
HT high temperature
LDOS local density of states
LEED low energy electron diffraction
LEEM low energy electron microscopy
LT low temperature
ML monolayer
NP nanoparticles
PDF powder diffraction file
PE pass energy
PECS precision etching and coating system
PIPS precision ion polishing system
PVD physical vapor deposition
PVP polyvinylpyrrolidone
QL quintuple layer
QSH quantum spin Hall state
RT room temperature
SAED selected area electron diffraction
SE secondary electron
SEM scanning electron microscope
SOC spin-orbit coupling
STEM scanning transmission electron microscopy
STM scanning tunneling microscopy
STS scanning tunneling spectroscopy
TEM transmission electron microscope
TI topological insulator
TSS topological surface states
UHV ultra-high vacuum
VdW Van der Waals
XPS X-ray photoelectron spectroscopy
XRD X-ray diffraction

1 INTRODUCTION

Over the past few decades, new materials with intriguing electronic properties were discovered, which are called topological insulators (TIs). Their electronic structure is characterized with an energy gap in the bulk and topological surface states (TSS) which cross the band gap [1, 2]. The TSS have a spin-split, massless, linear dispersion which is protected from non-magnetic perturbations. Such novel properties make TI interesting materials for their use in electronic and spintronic devices, quantum computing and catalysis [3-5].

The study described in this work focuses on the interface between a TI and a metal. Characterization of such interfaces gives the fundamental knowledge about the processes that can appear at the contact. This is especially important since there is almost no application where such interface would not be present, and it can have an impact on the device performance.

As a model TI material for our research we decided for Bi_2Se_3. Bi_2Se_3 is the simplest 3D TI from the aspect of electronic structure and is therefore regarded as a prototypical material for studies connected with the properties of TI. Three metals were chosen to be interfaced with Bi_2Se_3: Ag, Pt and Ti. Ag and Pt belong to the group of noble metals and, together with Au, represent metals which can be used not only as contacts, but also for catalytical applications. In the last years, in the field of catalysis, TIs gained attention due to reported studies about enhanced catalytic activity of systems with topological materials. On the other hand, Ti is used in the field of electronics as an adhesive layer in the metal contact fabrication for transport measurements. By choosing those three metals (together with Au, which was already under investigation in our group), we were able to cover a variety of applications where TI are predicted to be used.

Characterization of metal/TI interfaces was focused i) on their chemical and structural properties, ii) on the growth mode and morphology of metal films and iii) on their stability, since these information are mostly missing in literature.

The investigation on the structure and chemistry at the interface gives fundamental knowledge about the possible chemical interaction between the metal and the TI, if new interfacial phases are formed and if the surface of TI, where TSS are located, is preserved. The characterization of the morphology and the chemistry in the thin film regime (0.1 – 20 nm) allows for deep understanding of the metal/TI interaction. Moreover, in some cases the thin film regime corresponds to the systems actually used in applications, e.g. the adhesive layers for electrical contacts (usually few nm), catalytic films [6-8] or in more complex architectures [9]. In these cases, the understanding of the behavior of the metallic thin film is crucial. Finally, stability of the interface can also be a crucial issue. Instability of the interface in a form of a chemical reaction or diffusion has to be taken into account since the produced phases can shift the TSS below the interface [10, 11] or increases its resistance. Due to diffusion cracks can also appear, which reduce the contact area and destroy the metal contact. Knowledge about stability of contacts is therefore crucial in the design of reliable devices [12].

1.1 From band theory to topological insulators

Ever since the birth of the band theory of solids, materials were described based on their energy distribution of electrons in a material [13]. In contrary to a single isolated atom, where the electrons have discrete energy levels, when more atoms are put in a close proximity to form a solid, an overlap of the valence electron wavefunctions occupying adjacent atoms occurs, leading to a splitting of the energy levels according to the Pauli exclusion principle. Consequently, the discrete atomic energy levels are replaced by discrete ranges of energies called energy bands. The energy separation between adjacent energy levels decreases as the number of interacting atoms increases. In a crystal the band distribution can be considered as continuous (see Figures 1ab).

When the electrons are in a periodic potential (as it happens in a crystal), their wavefunctions are modulated with the same periodicity of the lattice. The electronic states in the bands can be effectively described in terms of their energy and their electron crystal momentum **k**. The relationship between the energy and crystal momentum of the available (filled or empty) electronic states is commonly represented with band diagrams (in Figure 1c the one for Ge). For each value of **k**, Schrödinger equation has multiple solutions with different energy levels, which evolve smoothly with changes in **k**.

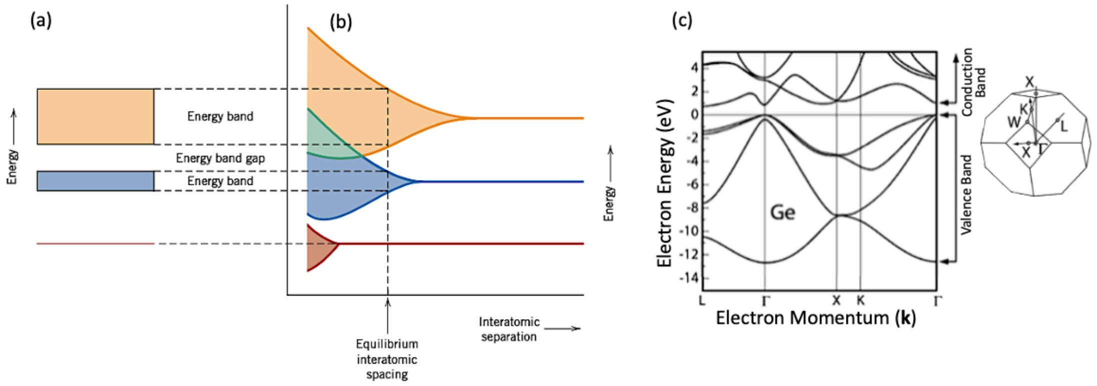

*Figure 1: (a) Scheme of the electron band structure for a solid material at the equilibrium interatomic separation. (b) Electron energy versus interatomic separation for an aggregate of atoms showing how atomic levels split into electron bands. [14] (c) Diagram of energy vs. electron crystal momentum **k** for electronic states in Ge, with a Brillouin zone indicating positions in the reciprocal space.[15]*

Based on the transport properties, materials can be classified into three main groups: insulators, semiconductors and metals (conductors). From the electronic band structure point of view, the difference between these categories lies in the presence of an energy gap (range of energies without a valid solution to the Schrödinger equation) between the valence and conduction band as shown in Figure 2.

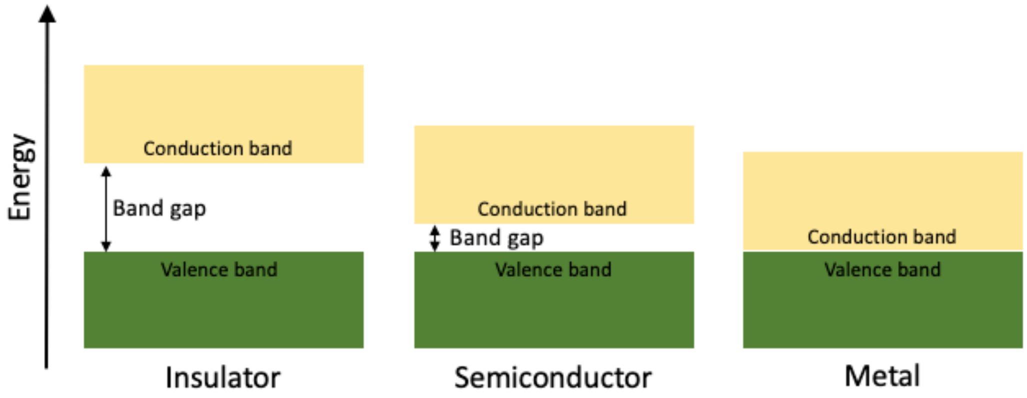

Figure 2: Scheme of the energy band structure of insulators, semiconductors and metals at 0 K.

In insulators the valence and conduction band are separated by a large energy gap (> 4 eV), therefore a substantial amount of energy is needed in order to excite an electron into the conduction band. Semiconductors also have an energy gap, but the size of it is smaller compared to insulators (1-1.5 eV for conventional and 2-4 eV for wide band gap semiconductors) therefore at temperatures above 0 K, a finite number of electrons can cross the gap (depending on the size of the band gap), enter the conduction band and enable electron conductivity. In doped semiconductors, extra energy states are created within the gap which further increase the conductivity [15]. In conductors there is no energy gap and very little energy is required to promote a substantial number of electrons into the low-lying empty states, therefore the magnitude of the electrical conductivity in conductors is the highest.

Over the past decades a new classification of materials, which distinguishes materials based on their topological order came into use. The concept emerged in the 1980s with the discovery of a quantum Hall state [16], which led to the classification of electronic structures according to so called topological invariants [17, 18]. Topological invariants are properties that are constant in different objects within the same topological phase and are distinct in objects belonging to different phases. This concept can be much easier understood from the aspect of geometry. A classic example of objects with topologically different invariants are a sphere and a torus, since the torus has a hole and a sphere has not (see Figure 3). It this case the considered topological invariant is the genus, i.e. the number of holes in the object [19]. Just by a simple deformation (homeomorphism), without gluing or tearing, the torus can be transformed into a coffee cup (which also has a hole, i.e. the handle), which makes them topologically equivalent, i.e. belonging to the same topological phase with genus = 1. On contrary, there is no way of transforming a torus into a sphere just by a simple deformation. Hence, the sphere is not topologically equivalent to torus, it has different invariant (genus = 0) and they do not belong to the same phase. Instead, the sphere belongs to the same phase of a simple glass.

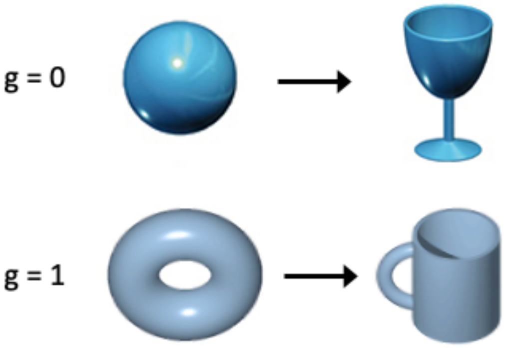

Figure 3: Topologically different objects (sphere and torus), which differ in their genus, and a possible result of homeomorphism.

Regarding the classification of materials, the first idea would be to classify them based on the presence or absence of an energy gap in the band structure. In this case insulators and semiconductors would belong to the same topological phase. If this was true, it would be possible to smoothly transform the band structure of any material within this topological phase into another by changing the material parameters without closing the energy gap. However, a change of paradigm occurred after the discovery of materials which at first appear to be ordinary insulators (i.e. they have a bandgap) but turn out to have topologically different character. For these materials some topological invariants are different from the ordinary electronic structure of an insulator or of the vacuum. Therefore, a continuous deformation of their band structure cannot result into that of a trivial insulator. These materials are called topological insulators.

The key theoretical breakthrough was made in 2005 by Kane and Mele who predicted the existence of topological insulators in systems beyond the specific case of the Quantum Hall effect [1]. An important role in these materials is played by the spin-orbit coupling (SOC), an effect in which the electron's angular momentum (spin) is coupled with its orbital motion. The Quantum Spin Hall (QSH) state represents the simplest 2D topological insulator which, in contrary to a quantum Hall state, does not require the presence of an external magnetic field [1]. As in an ordinary insulator, in the 2D TI there is an energy gap in the interior, but its electronic structure is topologically different (i.e. has a different topological invariant) with respect to an ordinary insulator. Accordingly, at the interface between the TI and a trivial insulator (or the vacuum) there are edge states, which host electrons with the opposite spin propagating in the opposite direction. The direction of the electron motion is determined by the spin direction, meaning that the electron cannot change its momentum without changing its spin. This property is called spin-locking and is responsible for backscattering suppression.

The next important theoretical development, in 2007, was the prediction of 3D topological insulators, in which the surface states resemble the edge states of 2D TI [2]. The electron crystal momentum is also here locked with the direction of the spin, which varies continuously as a function of propagation direction. In surface states the electrons are confined to movement only in direction parallel to the surface, therefore the electrons do not experience any k_z dispersion and can be labeled by the in-plane crystal momenta k_x and k_y. Consequently, the surface states are considered as a 2D metal.

The fact that the presence of edge/surface states crossing Fermi is necessary at the interface between topologically different materials is expressed by the so-called bulk boundary correspondence [20]. The number of times the edge/surface states cross E_F, N_{EF}, is actually connected with the change in topological invariant across the interface between topological insulator and its environment. According to it, the change in topological invariant, $\Delta\nu$, is connected to N_{EF} by the following relation:

$$N_{E_F} = \Delta\nu \bmod 2 \qquad [1]$$

When the topology phase at the interface changes (i.e. $\Delta\nu = 1$) the surface states will necessarily cross the Fermi edge an odd number of times, i.e. at least once.

Figure 4 shows a band structure of a trivial insulator, with surface states, and of a topological insulator. Electronic structure is represented between two Kramers points, k. These are the points in the Brillouin zone where the states are doubly degenerate due to the time reversal symmetry (τ) [21]. In a trivial insulator, by moving E_F up or down in energy (or by a continuous deformation of the band structure), the surface states can intersect E_F an even or zero number of times. On the other hand, in topological insulator the states will necessarily cross E_F an odd number of times.

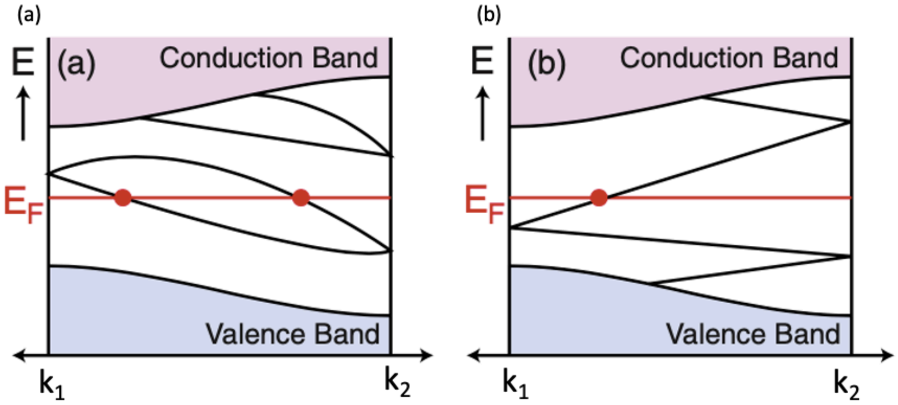

Figure 4: Electronic dispersion between two Kramers points of a trivial (a) and topological (b) insulator. In the case of trivial insulator, the number of surface states crossing the Fermi energy E_F is even, whereas in the case of TI it is odd. [20]

In summary, TIs are characterized by a band gap in the bulk, like trivial insulators, but their electronic structure is different in some topology invariant. For this reason, at the interface between TIs and trivial insulators (or with vacuum), special edge states appear which cross the band gap and enable conductivity on the boundaries of the material. These states are topologically protected, meaning that they emerge from the special bulk band structure. As long as the bulk band structure of TI is preserved (with its topology invariant and its bandgap), these surface states are necessarily present at the interface with a trivial insulator. Consequently, these states are extremely robust towards contamination and deformation of the surface.

1.2 From theory to experiments

TIs were first predicted theoretically and were soon after observed experimentally. The first 2D TI was realized in 2007 in a quantum well structure made by a thin layer of HgTe sandwiched between two layers of CdTe [22]. When the theory was extended to 3D TIs, it was predicted that such phase could be realized in a semiconducting alloy $Bi_{1-x}Sb_x$ [2]. Just one year later the unusual surface bands of $Bi_{1-x}Sb_x$ were mapped in an angle-resolved photoemission spectroscopy (ARPES) experiment and are shown in Figure 5 [23].

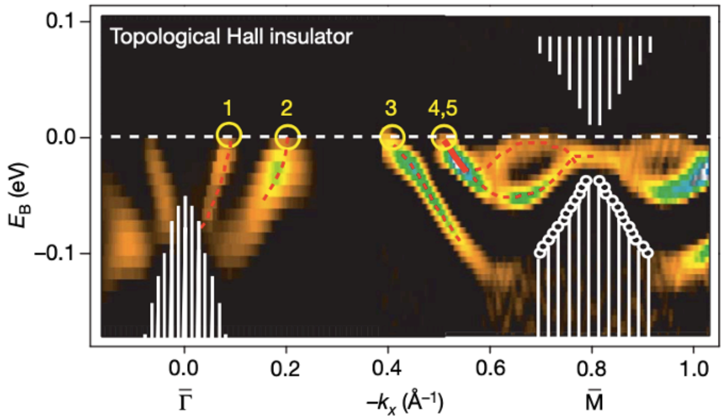

Figure 5: ARPES map of the first observed topological surface states on the (111) surface of topological surface states $Bi_{1-x}Sb_x$. The map probes the occupied surface states as a function of momentum on the line connecting the τ invariant points Γ and M in the surface Brillouin zone. The surface bands cross the Fermi energy five times. [23]

Although the surface structure of this alloy was found to be complex, this work motivated the scientific community to search for other TIs. The search resulted in prediction and experimental confirmation of the ‘second generation’ of 3D TIs: Bi_2Se_3, Bi_2Te_3 and Sb_2Te_3 [24-27]. These compounds have much simpler electronic band structure with only one nearly linearly dispersing state crossing the band gap, which is located in the Γ point in the surface Brillouin zone. Additionally, these compounds are stoichiometric, which in principle means that they can be prepared at higher purity, and they also have larger band gap than $Bi_{1-x}Sb_x$. Discovery of this group of compounds caused a huge increase of theoretical and experimental research in this newly established field (see Figure 6). Later on the field expanded to other topologically non-trivial materials, such as topological crystalline insulators [28] and afterwards Weyl and Dirac semimetals [29, 30].

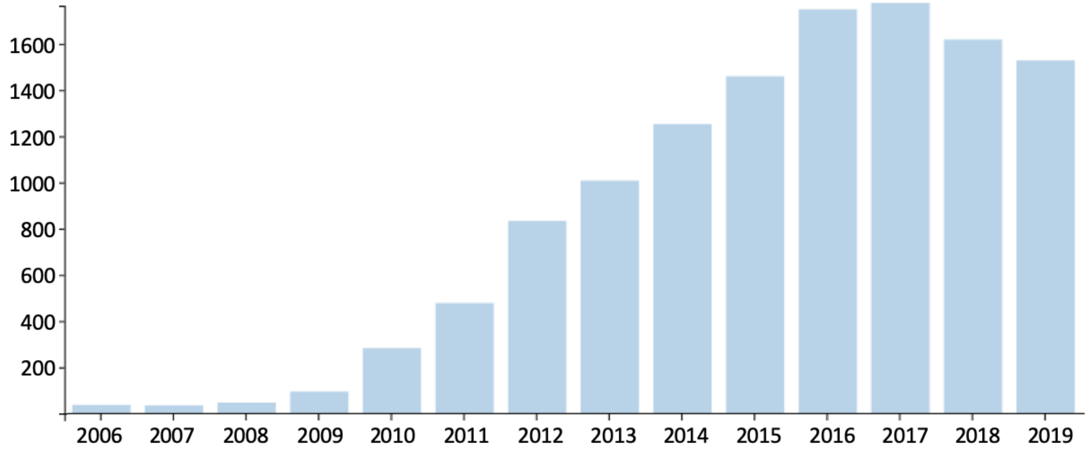

Figure 6: Number of articles on the topic of topological insulators over the years. [31]

1.3 Crystal and electronic structure of Bi_2Se_3

Bi_2Se_3 is a long-known material, which was studied due to its good thermoelectric properties. With the discovery that Bi_2Se_3 is a TI the research deviated into studies of its electronic properties and new applications where it could be used.

Bi_2Se_3 is a layered chalcogenide material. It has rhombohedral crystal structure, presented in Figure 7 ($a = b = 4.1430$ Å, $c = 28.6360$ Å, $\gamma = 120$ °). The unit cell of Bi_2Se_3 consists of five atomic layers arranged along the z-axis, known as quintuple layers (QL), which are approximately 1 nm thick. Each QL consists of three Se and two Bi atomic layers in arrangement Se_1-Bi_1-Se_2-Bi_1'-Se_1'. Within the QL, the atoms are connected with covalent-ionic chemical bond, whereas between individual QL van der Waals interactions are present. QL are separated by a Van der Waals (VdW) gap measuring 2.43 Å. Due to weak VdW interactions the material can be easily exfoliated, which is beneficial for a simple clean surface preparation.

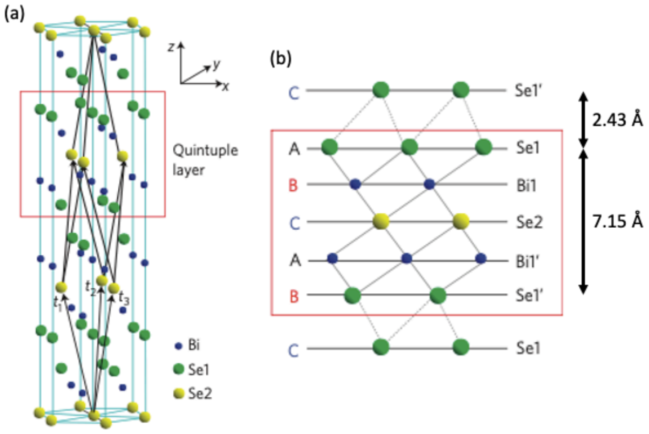

Figure 7: (a) Crystal structure of Bi_2Se_3 with indicated quintuple layer in the red square. (b) Side view of the quintuple layer showing the stacking order of atomic layers and denoted sizes of the QL and the VdW gap. [24]

Bi_2Se_3 belongs to a class of 3D TIs, meaning that it has a band gap in the bulk and conductive topological surface states on its surface [24], which are a consequence of the non-trivial bulk band structure [2]. Since the composition of this material includes heavy element Bi, the compound is subjected to strong SOC, which causes the highest valence states to be pushed above the lowest conduction band states as shown in Figure 8. Bi_2Se_3 is consequently topologically non-trivial due to the inversion between p_z orbitals at the Γ point, which results in a phase transition in which one topological invariant changes [24].

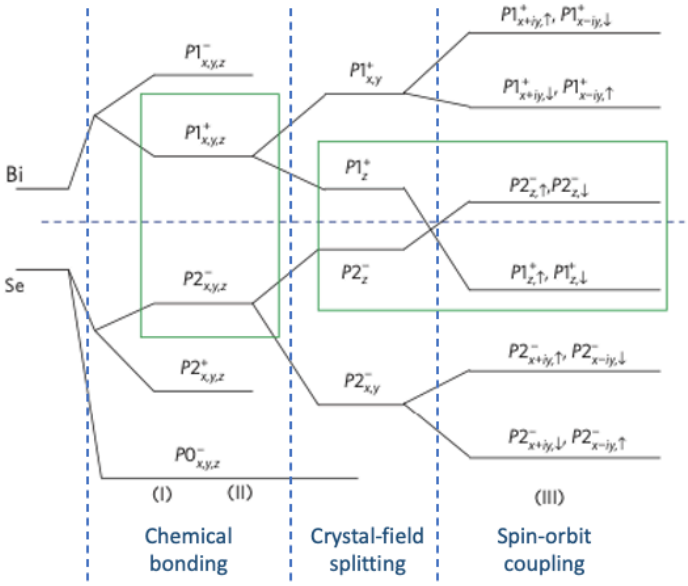

Figure 8: Evolution of atomic orbital energy levels in Bi_2Se_3 at the Γ point after introduction of chemical bonding, crystal-field splitting and SOC interactions. [24]

There are three major interests in the electronic structure of Bi_2Se_3 compared to the first known 3D TI $Bi_{1-x}Sb_x$. First, the surface state of Bi_2Se_3 has nearly ideal linear energy–momentum dispersion with only a slight curvature. The second benefit is that it is stoichiometric, and third, it has a relatively large band gap (compared to other TIs) of 0.3 eV which means that it can exhibit topological insulator behavior at room temperature (RT), which significantly increases its potential for applications [20, 23]. Among the second generation of TIs, Bi_2Se_3 also has the simplest Dirac cone spectrum and the largest band gap, making it the most appropriate for fundamental studies regarding TIs.

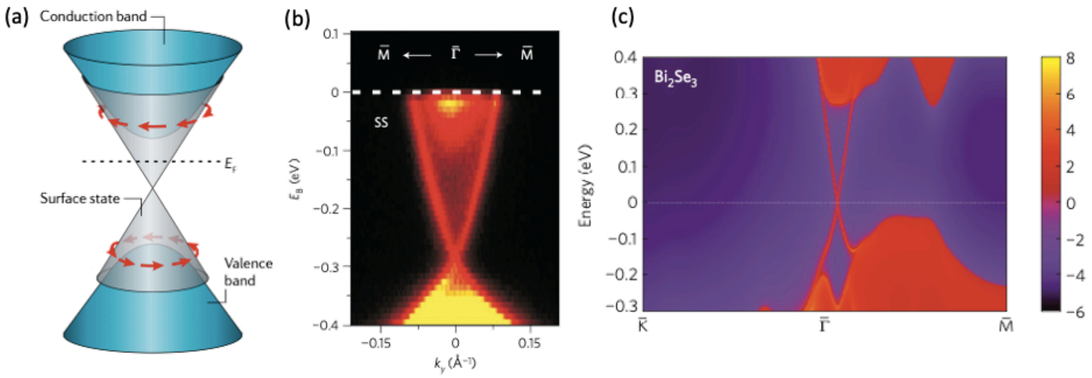

Figure 9: (a) Schematic representation of a Dirac cone showing the linear dispersion of the TSS. [32] (b) High-resolution ARPES measurements of surface electronic band dispersion on Bi_2Se_3 (111). [24] (c) Ab-initio calculation of the band structure of Bi_2Se_3 with the TSS clearly visible around the Γ point. [24]

There are multiple properties connected with the TSS structure in Bi_2Se_3. As described above, the TSS of Bi_2Se_3 are linearly dispersed. Generally, the TSS are said to be dispersed in a Dirac cone as it is presented in Figure 9. This means that the kinetic energies of the conductive electrons are directly proportional to their momenta and thus they have no effective mass. The TSS are also spin polarized, meaning that the direction of the electron's spin is locked to its momentum. As shown in Figure 9a, the spins are oriented in plane parallel to the surface and create a vortex like pattern around the Γ point, which changes chirality when crossing the Dirac point: the upper Dirac cone has a left-handed while the lower Dirac cone shows a right-handed spin texture [33]. While the constant-energy contour in Bi_2Se_3 exhibits a round shape, Bi_2Te_3 shows significant hexagonal warping (see Figure 10) [25, 26]. The difference in the

TSS between the two materials lies also in the dispersion of the TSS, which are less linear in the case of Bi_2Te_3.

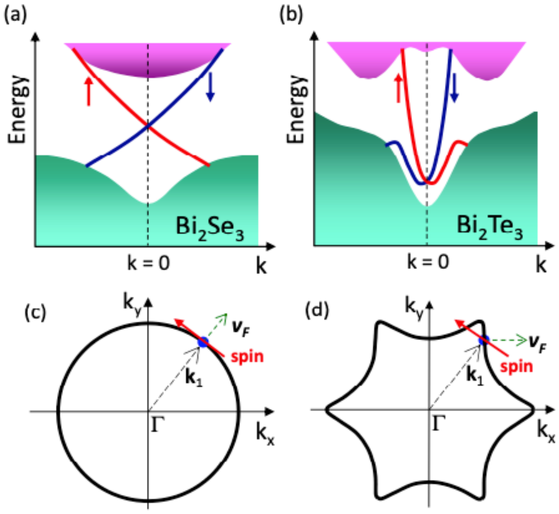

Figure 10: The surface state structure of Bi_2Se_3 *(a) and* Bi_2Te_3 *(b). Constant energy contour of* Bi_2Se_3 *with round shape (c) and of* Bi_2Te_3 *exhibiting hexagonal warping (d).[34]*

TSS are protected by τ symmetry, which consequently makes them robust in the presence of impurities. Theoretically, the presence of magnetic disorder should open a gap at the Dirac cone making it a regular insulator (semiconductor) [20].

Many theoretical applications utilizing the TSS require the Fermi level to lie near the Dirac point, in between the valence and conduction bands, where only the TSS are present. However, in a real Bi_2Se_3 crystal the bulk Fermi level is not positioned in the gap. This is due to the Se-vacancy defects present in the material, which makes the material n-doped and push the Fermi level into the conduction band [35]. Due to Se vacancies also the bulk conductivity is substantial, making it difficult to separate the contribution of the bulk and of the surface from the overall conductivity [36, 37]. Several approaches were used to overcome this problem. Doping with Ca or other impurities is frequently used to deplete the formation of Se vacancies [38]. In order to have some control over the conductivity, the position of the Dirac point can also be shifted by gating [37, 39]. Another option to reduce the bulk conductivity is to use nanosized materials (e.g. thin films) and increase surface to volume ratio. However, there is one limitation. When the thickness of Bi_2Se_3 thin film falls below 6 QL the wavefunction of the top and the bottom state start to overlap and a gap opens at the Dirac point, making the material a trivial insulator as depicted in Figure 11 [40].

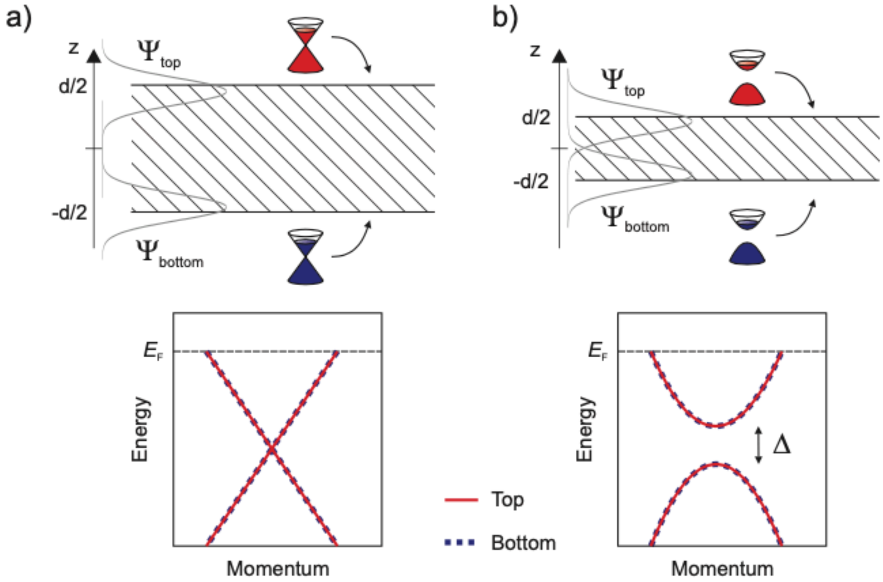

Figure 11: (a) Dirac cones on opposite sides of a Bi_2Se_3 film with dispersion of the two states in the lower panel. (b) Overlap of surface states of <6 QL thick Bi_2Se_3 film due to hybridization between the top and bottom states of the film and consequent gap opening. [41]

1.4 Applications of topological insulators

Due to the fascinating properties of the TSS, many applications where TI materials (mostly in the form of thin films or nanomaterials) could be used were predicted.

Compared to other materials where energy dissipation is common, in TIs the suppression of backscattering in the TSS allows for exceptional transport mobility and reduced energy consumption making TIs useful for low-power electronics [3].

Second major area where TI could be exploited is the field of spintronics – electronics based on the electron spin. Such devices have the potential to further reduce energy dissipation related to conventional joule heating charge transport. Several studies in literature claim the observation of spin polarized current in TIs [42, 43]. The unique spin structure of TIs makes these materials useful in memory or spin-torque devices [3, 44].

One of the exciting applications in the field of physics is the potential to use the TSS as a host for Majorana fermions [45, 46]. They can be created by combining topological insulators with superconductors through the proximity effect. Majorana fermions can be used as a basis for a qubit in quantum computing.

TIs are also promising candidates to be used in the field of catalysis, especially as a support for various metallic catalysts [4, 5]. TSS can serve as an electron bath and thus facilitate the donation or acceptance of electrons from the adsorbates. Consequently, the electron transfer can enhance the reactivity of the supported catalyst. TI and other topological materials are being studied also as catalysts on their own and show promising result for various reactions, e.g. hydrogen evolution reaction (HER) or photochemical water splitting [47-50]. Due to promising results, the use of TIs in the field of chemistry is gaining more and more attention over the last years.

There are many other possibilities where TIs could be used, e.g. as photodetectors [51, 52], in magnetic devices, field-effect transistors or optoelectronic devices [53]. In order to realize the majority of predicted applications more progress will have to be made to reduce the bulk conductivity and constrain the chemical potential to the bulk bandgap [53, 54].

1.5 Phenomena at the topological insulator/metal interfaces

The investigation of the interface between a metal and TI is interesting from fundamental physics and applicative point of view. Regarding the fundamental questions, it is interesting to verify if TSS survive upon deposition of metal, how they are modified, how metal atoms arrange on the surface and, more in general, how does a metal interact with a topological insulator. Moreover, a detailed knowledge about the growth mode and the film structure allows for more accurate modelling in the theoretical studies.

From applicative point of view, it is important to understand what happens at the metal/TI interface, because such interface is present in most of predicted applications. The most relevant example is the integration of TIs in electronic circuits, which necessitates a contact between a metal and a TI. The metal/TI interface is retrieved also in other applicative fields, e.g. catalysis. The electronic and transport properties, the performance and the capability to exploit the peculiar TI properties will depend on the interaction at the metal/TI interface as well as on the interface structure and stability. Therefore, a deep understanding of the metal/TI film and interface structure and their chemical and thermal stability is of fundamental importance for TI applications.

Further subsections will describe the common phenomena happening at the metal/TI interface and the arrangement of metal atoms on surfaces.

1.5.1 Growth modes of thin solid films

The most common way which is routed to create an interface between metals and TI, both in applicative and fundamental studies, is the deposition from vapor phase. For this reason, some basics of the thin film growth mode are described in the following.

The growth of thin films from vapor phase starts with adsorption and diffusion of individual atoms on the substrate surface. The film growth afterwards depends on the interplay between thermodynamics and kinetics. The general trend in the film growth is described within the thermodynamic approach with respect to the relative surface and interface free energies. However, the film growth mode is also a kinetic process, in which the rate-limiting steps can affect the net growth mode and the final film morphology [55-57].

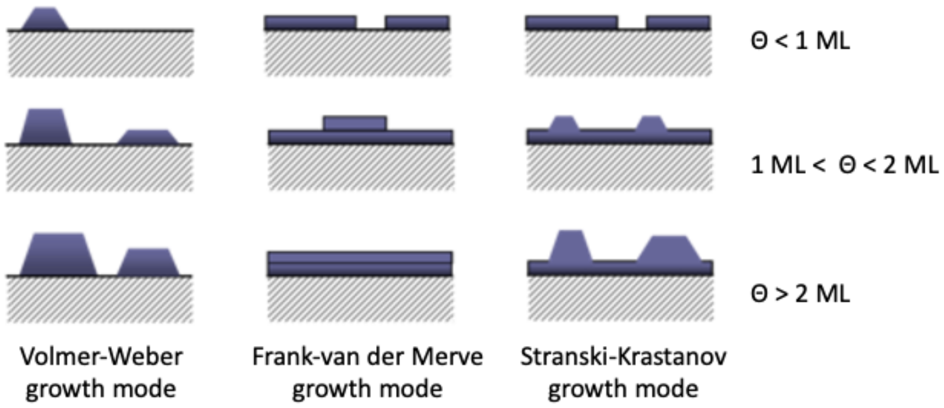

Figure 12: Schematic representation of the three general growth modes. Θ denotes the coverage.

Three general growth modes are distinguished and are presented in Figure 12:

- Layer-by-layer, or Frank-van der Merve, growth mode refers to the case when the adsorbate arranges on the surface in the form of layers. Each layer has to be (usually) first fully complete before the next one starts to grow, making the growth 2-dimensional. In a layer-by-layer growth mode the adsorbate usually grows epitaxially, meaning that the crystal lattice of the deposited film has a specific orientation with respect to the crystal structure of the substrate. This growth mode is associated to cases when the deposited atoms are more strongly bound to the substrate than to each other, and a suitable match between the film and the substrate crystal structures is possible. An example of this is Au on Pt [58].

- Island, or Vollmer-Weber, growth mode refers to the case when the adsorbate nucleates on the surface and creates 3-dimensional islands. Such growth mode occurs when the film atoms are more strongly bound to each other than to the substrate. An example of this is Fe on graphene [59].
- Layer-plus-island, or Stranski-Krastanov, growth mode consists of a complete 2-dimensional wetting layer, which "passivates" a reactive substrate, on which growth of 3D islands takes place. An example of this is growth of Si on SiC(0001) [60].

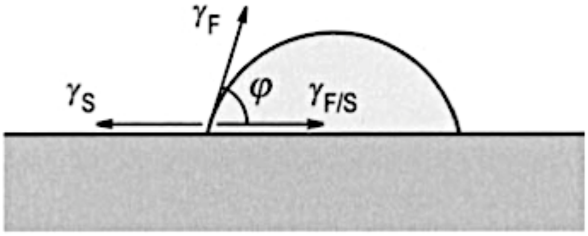

Figure 13: Scheme of a surface island with surface tensions γ and contact angle φ. [55]

The occurrence of different growth modes can be described in the context of surface and interface free energy, treated as vectors of surface tension (work that has to be performed to build a surface of unit area or a force per unit length of boundary). Figure 13 shows an island on the substrate and associated vectors. If the contact angle is φ, the force equilibrium is expressed as:

$$\gamma_S = \gamma_{F/S} + \gamma_F \cos\varphi, \tag{2}$$

where γ_S is the surface tension of the substrate surface (i.e. the interface free energy between the substrate and the environment or vacuum), γ_F the surface tension of the island surface (i.e. the interface free energy between the adsorbate and the environment or vacuum), and $\gamma_{S/F}$ the surface tension of the adsorbate/substrate interface (i.e. the interface free energy between the adsorbate and the substrate). Based on the size of the contact angle and the magnitude of tensions, the three main growth modes can be determined as follows:

- Layer-by-layer growth: $\varphi = 0$, therefore $\gamma_S \geq \gamma_{F/S} + \gamma_F$
- Island growth: $\varphi > 0$, therefore $\gamma_S < \gamma_{F/S} + \gamma_F$
- Layer-plus-island growth: first the condition for layer-by-layer growth is fulfilled, formation of the intermediate layer then alters the values of γ_S and $\gamma_{S/F}$ leading to conditions for island growth.

Growth mode can be experimentally determined by Scanning Tunneling Microscopy (STM), Atomic Force Microscopy (AFM), Low-Energy Electron Microscopy (LEEM) or other surface sensitive spectroscopic techniques such as Auger Electron Spectroscopy (AES) and X-ray Photoelectron Spectroscopy (XPS).

Most often thin films are formed by nucleation, growth and coalescence [61]. When atoms arrive at the substrate different processes occur (Figure 14). The atoms are initially adsorbed on the surface, which creates a population of single adatoms on the substrate. Adatoms afterwards diffuse over the surface until a further stage. Some of these adatoms may desorb, other may become captured by the existing islands or at defect sites, or the individual adatoms combine to form small islands. The small islands are unstable and may decay back to individual adatoms. When the nuclei grow and reach the critical size, any additional atom added to the nucleus will make it stable.

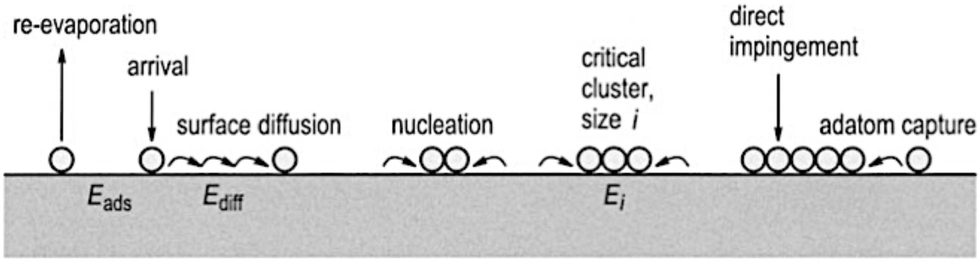

Figure 14: Scheme illustrating the atomic processes involved in nucleation and growth on surfaces. [55]

At the beginning the density of islands is high and after reaching a maximum it decreases with further deposition due to one or more of the following processes: growth coalescence, Ostwald ripening and island mobility coalescence. Growth coalescence occurs during deposition when the nuclei combine with their neighbors, coalescing into a single larger island. In the Ostwald ripening process atoms leave the small islands, diffuse over the surface and attach to the larger ones. The process is thermodynamically driven in order to reduce the free energy cost associated with island edges. Island mobility process can occur when adatom aggregates can move substantial distances on the substrate surface and coalesce together into bigger islands.

The growth mode and the film morphology of metals deposited onto TI surfaces is still a topic with a wide lack of knowledge. Even if in several theoretical studies the metal film is modelled as a layered film [62-66], the growth of ordered layers has been experimentally observed only in specific cases, namely for deposited Sb and Bi.

Sb was found to grow at RT in a form of a bilayer (BL; two atomic layers) islands on Bi_2Se_3 and Bi_2Te_2Se [67, 68], which do not completely cover the substrate surface before increasing in height. However, the growth evolution differs between the two substrates as shown in Figure 15.

At low coverage, Sb atoms on Bi_2Se_3 spread over the surface as adatoms or small clusters of less than 1 nm lateral size. With increasing coverage aggregation of Sb adatoms into compact 2D islands begins. At first the islands measure 1 BL in height and have a rough surface, with further deposition Sb arranges into wide islands, majority of which has a height of 2 BL with flat tops.

On Bi_2Te_2Se Sb islands of 1-5 BL heights are formed. Most of the islands exhibit height of 2 or 3 BL while 1 BL islands are very rare. Islands of 3, 4, and 5 BL heights have compact and atomically well-ordered structures, while the surface of 2 BL films is rather disordered with vacancies and clusters.

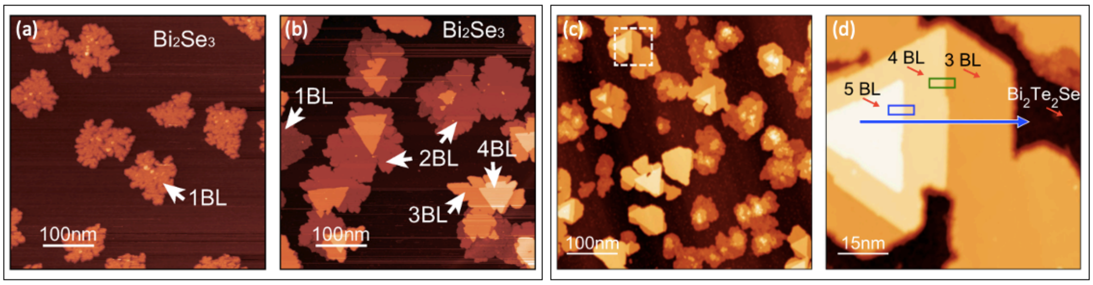

Figure 15: STM images of Sb islands on: Bi_2Se_3 at a coverage of ~0.2 BL (a) and ~1.5 BL (b) [68]; and on Bi_2Te_2Se at a coverage of >2 BL (c) with a close-up for an ordered Sb island (d), indicated by the dashed rectangle in (c). [67]

Deposition of Bi on $Bi_2Se_3(0001)$ [69], $Bi_2Te_3(0001)$ [70] and Bi_2Te_2Se [71] resulted in similar morphology (see Figure 16) although different deposition temperatures (250 K, 200 K or RT respectively) were used. The growth on Bi_2Te_3 and Bi_2Te_2Se starts by formation of individual triangular BL islands of Bi(111), whereas on Bi_2Se_3 the islands have irregular shape. With increasing coverage, the islands on all three substrates coalesce into a continuous BL film with small triangular holes and the second BL starts to nucleate after the first BL is almost complete (Figure 16d). Growth of Bi BL on Bi_2Se_3 and Bi_2Te_3 was reported to be pseudumorphic, meaning that Bi takes over the lateral lattice constant of the substrate.

Chen *et al.* [72] studied the growth of Bi on Bi_2Te_3(111) with temperature and showed that at RT triangular Bi(111) BL islands with one of the side parallel to the step edge are formed (Figure 16). Above 0.5 BL coverage coalescence of Bi islands occurs leading to the growth of a complete BL film. Growth of Bi at RT can be described by BL by BL growth mode, on the contrary, the growth at the substrate temperature of 450 K evolves via step-flow mode and results in the formation of atomically flat surface of Bi. No detailed information regarding the LT deposition (T_{sub} < 150 K) were reported, except that islands with a typical size of 3 nm are formed.

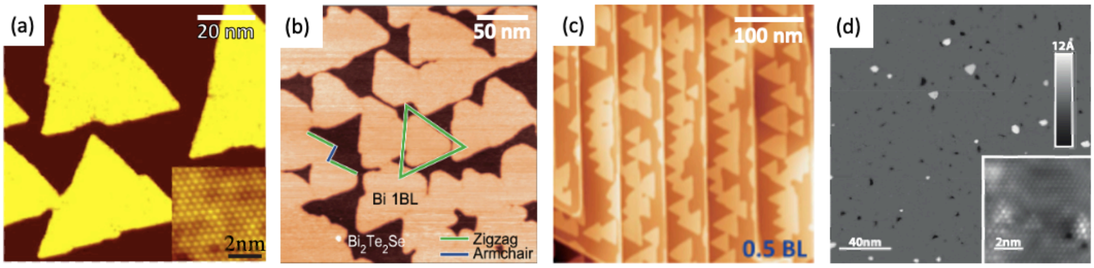

Figure 16: STM images of Bi(111) BL islands on: (a) Bi_2Te_3(0001) at a coverage of 0.5 BL [70]; (b) on Bi_2Te_2Se(0001) [71]; (c) Bi_2Te_3(111) at a coverage of 0.5 BL [72] and; (d) on Bi_2Se_3(0001) at a point of an almost continuous BL [69].

Apart from the abovementioned epitaxial growth (of either 2D islands or layers) reported for Bi and Sb, majority of transition metals deposited on TIs at RT resulted in the growth of 3D islands.

When Fe was deposited and observed at LT on Bi_2Se_3 (T < 150 K) the surface exhibited features belonging to single adatoms (Figure 17a) [73, 74]. With increasing temperature (either of deposition or post deposition annealing) triangular depressions, assigned to Bi substitutional defects, and islands were formed on the surface (Figure 17b). In the case of RT deposition formation of two types of islands, which differ in size, were observed and reported on $Bi_{1.91}Mn_{0.09}Te_3$, Bi_2Te_3 and Bi_2Se_3 (pristine and

Ca-doped) substrates [74-77]. Deposition of 0.2 ML of Co on Bi_2Se_3 at RT as well resulted in the formation of two size distinguished islands [78].

Among the transition metals that were reported to form islands on TI are also Nb, Cu and Au.

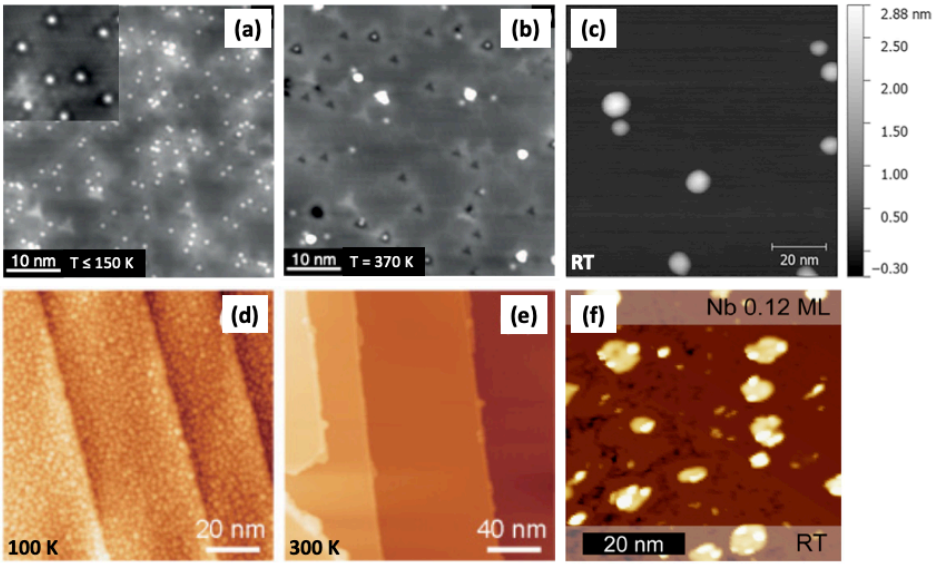

Figure 17: STM images of 0.01 ML Fe deposited on Bi_2Se_3 at 150 K (a) and post annealed to 370 K (b) [74], of < 2 Å of Au deposited on Bi_2Se_3 at RT (c) [79], of 0.5 ML Cu deposited on Bi_2Se_3 at 100 K (a) and 300 K (b) [80]and of 0.12 ML Nb deposited on $Bi_2Te_{1.95}Se_{1.05}$ at RT (f) [81].

Deposition of 0.12 ML of Nb at RT on $Bi_2Te_{1.95}Se_{1.05}$ (111) resulted in formation of islands of irregular shape with high aspect ratio (see Figure 17f). Additional clusters could also be observed on the already existing islands [81]. Completely different morphology was observed in the case of RT deposited Au on Bi_2Se_3 where Vollmer-Weber growth mode was confirmed by the observation of dome-shaped islands with a minimum lateral size of 2 nm forming on the surface of Bi_2Se_3 (Figure 17c) [79].

Interesting temperature dependence of surface morphology upon metal deposition was observed in the case of Cu on Bi_2Se_3 [80]. When 0.5 ML of Cu was deposited at 100 K the whole substrate surface became covered with small clusters with a lateral size of 1.5 nm, whereas if the same amount of Cu was deposited at 300 K the surface remained almost unchanged and only a few clusters were observed on the step edges as shown in Figures 17de. Such difference was ascribed to higher diffusion coefficient at a higher temperature enabling Cu to diffuse over the substrate terraces and intercalate into the VdW gaps before forming clusters.

In summary, layer-by-layer epitaxial growth (or at least BL by BL island growth) on TIs has been only observed by deposition of metals which are also present as cations in the crystal structure of TIs, namely Bi and Sb. In other cases, a 3D island growth has been observed for Fe, Co, Nb, Cu and Au. For deposited Fe [76] and Cu [80] a chemical reaction and intercalation were detected, respectively.

The growth modes described at the beginning of this section can be used when a stable interface between the metal and the TI is present, without interdiffusion, reaction and formation of new phases. However, in the last years it is becoming clear that this is not the ordinary case, as described in the next section.

1.5.2 Chemical reactions and intercalation

One of the processes which can happen at the metal/TI interface is the diffusion of the metal within the TI, resulting in the intercalation or chemical reaction, with subsequent formation of new phases. Therefore, it is of great importance to know whether the interfaces are chemically and thermally stable, especially for the purpose of applications. The formation of a new phase at the interface can influence the electronic properties of the system and modify its functionality. In this subsection some general chemical reactions and aspects will first be briefly presented followed by the literature review of the observed chemical interactions at the metal/TI interfaces.

Intercalation describes the process of insertion of a guest molecule into a host material that, in general, has a layered lattice (most known host materials are transition metal dichalcogenides, graphite, zeolites, clays ...) [82]. When such process occurs, the host structure is only slightly perturbed, unlike in the usual solid-state reactions involving extensive bond breaking and structural reorganization. However, the chemical, optical, electronic and magnetic properties of the host lattice can be significantly changed and also tuned by the control of the guest concentration. Intercalation is either chemically or thermally reversible process that can occur also at ambient temperature, but in general the reaction temperature should be high enough to enable mobility of the guest molecules and at the same time ensure that the bonds in the host lattice are not broken.

Solid-state reactions refer to chemical reactions that occur between solid reactants without the presence of a solvent [83]. A typical experimental procedure for this kind of reaction includes mixing and grinding of the reactants to maximize the surface contact area and subsequent heat treatment. Solids are not expected to react together at room temperature in the time scale of hours therefore, it is usually necessary to anneal the reaction mixture to high temperature (at least a few hundred °C but still below the melting temperature of the reactants) to promote the diffusion of the reactants and formation of a new phase. The reaction occurs only at the interface of the two solids and once the surface layer has reacted, reaction continues with the diffusion of reactants from the bulk to the interface. Once the new formed phase is too thick for the unreacted atoms to diffuse through, the reaction mixture has to be ground again to bring fresh (unreacted) surfaces into contact.

Redox (reduction-oxidation) reactions are a type of chemical reactions where the atoms change their oxidation state by gaining or losing electrons [84]. Such reactions are many times conducted in electrochemical cells in order to control and exploit the electron transfer. Chemical species have been organized into electrochemical series based on their standard reduction potential (E^0), their ability to donate or accept electrons. Values of E^0 have been obtained from potential difference measurements in aqueous solutions (or calculated from calorimetric methods if systems cannot be investigated in aqueous media) and are relative to the potential of the standard hydrogen electrode. By calculating the difference of E^0 between two chemical species it can be determined whether the redox reaction will evolve spontaneously ($\Delta E^0 > 0$) or not.

Chemical reactions can be described from the aspect of thermodynamics or kinetics. Chemical thermodynamics is associated with the study of chemical equilibrium, direction of the chemical reaction and changes of energies in chemical reactions, whereas the kinetics are connected with the rate and mechanisms of a reaction [85]. The direction of a spontaneous chemical reaction is always towards the decrease of the Gibbs free energy of the system ($\Delta G < 0$) until a minimum value is obtained. At that point, there is no further change in the Gibbs free energy and the reaction is at equilibrium. Although a spontaneous reaction is thermodynamically favored it is not necessarily a fast process, since the rate of the reaction does not depend on the energy change between the reactants and products but on the height of the activation barrier for a particular process within the reaction mechanism.

Due to the layered structure of Bi_2Se_3 or its analogues and the presence of a VdW gap, in the early studies regarding metal/TI interfaces, intercalation process was often the first and only option for the description of a strong interaction between a metal and a TI at RT [86-89]. This can also be due to the fact that solid-state reactions are usually encountered at high temperature (HT), e.g. for ceramic materials. However, it seems that the metal/TI interaction was many times wrongly interpreted and it often resulted in the formation of interfacial phases with different crystal structure at the contact between a metal and a TI through interdiffusion and chemical processes. This problem is especially encountered when Bi_2Se_3 is studied in the context of TIs, where the interface phenomena play a crucial role.

Bi_2Se_3 and similar ternary compounds are good thermoelectrics and were as such studied for over 50 years. Studies about interdiffusion at the interface, especially from the aspect of diffusion barriers for prevention of formation of an interfacial layer and protection of devices from degradation of their performance, have been reported, but always after thermal treatment. Majority of the studied thermoelectric materials were ternary compounds of $(Bi,Sb)_2Te_3$ and $Bi_2(Se,Te)_3$ interfaced with metals and annealed. Reactions or interdiffusion were found at contacts with Sn [90, 91], Ni [92-94], Pd and Ag [94] producing metal tellurides or selenides (Figure 18).

With the emergence of TI character of Bi_2Se_3 (and similar dichalcogenides), the studies on metal/Bi_2Se_3 were focused on the atomic scale phenomena.

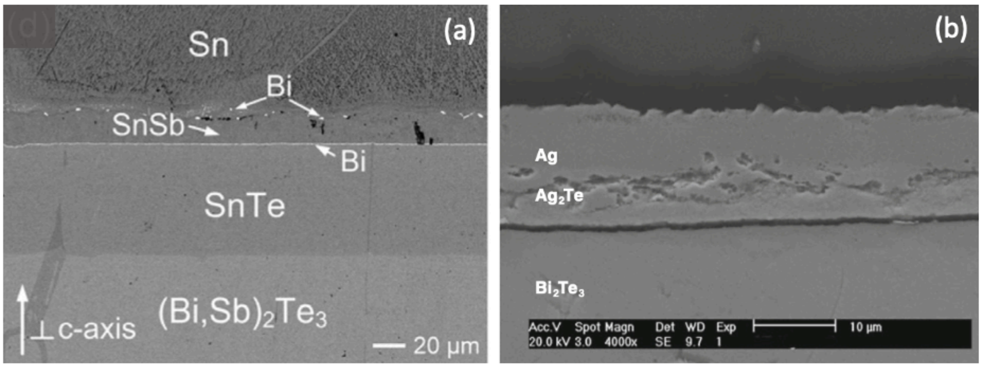

Figure 18: SEM images of cross-section of (a) the Sn/$(Bi,Sb)_2Te_3$ sample after annealing at 180 °C for 4 h [91], and (b) of Ag/Bi_2Te_3 interface after annealing at 250 °C for 10 h [94].

Computational study of Ryabishchenkova *et al.* [95] where the adsorption, diffusion, and intercalation of alkali metal atoms on the $Bi_2Se_3(0001)$ surface has been examined showed that Li and Na are able to intercalate into the VdW gaps due to their small size, whereas intercalation for K, Rb and Cs atoms is energetically unfavorable and requires overcoming high energy barriers. The scenario with Rb was calculated also in the paper of Gosalvez *et al.* [96], where two transition metals, Cu and Ag, were also studied at low coverage at RT. The results showed that Cu can easily intercalate into the VdW gaps. Intercalation was expected also for Ag atoms, which at first accumulate at the steps and then gradually intercalate into the VdW gap [89].

From experimental point of view, the studies redirected into the use of surface sensitive techniques, such as XPS, ARPES, STM. The interfaces were examined on the atomic level using Transmission Electron Microscope (TEM), metals were deposited at low coverages and measurements were performed at low temperatures or RT.

Among transition metals, Cu was substantially studied in the context of TI, since doping Bi_2Se_3 with Cu was found to induce superconductivity [86, 97, 98]. Besides doping, interfacing TI with Cu also appears very intriguing. There are multiple articles describing the intercalation of Cu into the VdW gaps of Bi_2Se_3 and Bi_2Te_3 [99-104]. Upon Cu deposition by electrochemical process, solution-based deposition, solid-state deposition or other methods, Cu is intercalated into the structure of the TI, most likely into the VdW gaps as shown in Figure 19a. The inserted Cu influences the electronic properties by acting as a donor enhancing the n-type character of Bi_2Se_3 while changing the native p-type character of Bi_2Te_3 to an n-type [105]. Interestingly the reverse process, deintercalation, can be achieved by heating or acid leach [99, 100]. Upon deposition of higher concentrations of Cu, cation exchange process occurs forming Cu_2Se or Cu_2Te phases and separate domains of Bi can be detected (Figures 19bc). However, the deintercalation efficiency strongly depends on any interaction between the intercalant and the host lattice and some Cu can be left in the Cu-TI system, probably as copper selenide/telluride. Intercalation of Cu can also significantly enhance light transmission through thin nanoplates of chalcogenides, making these systems interesting for potential use in optoelectronic applications [102].

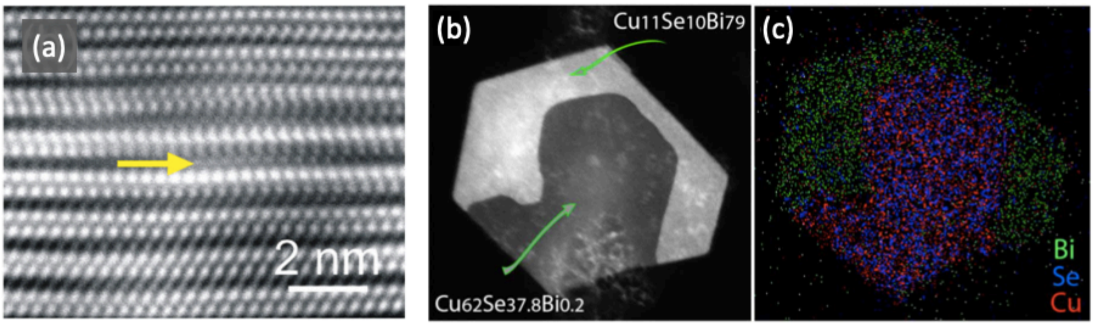

Figure 19: (a) High resolution STEM image of heavily Cu-doped Bi_2Se_3 with visible small Cu-rich precipitate with additional column atoms (yellow arrow) located between QLs [104]. (b) STEM image of Bi_2Se_3 platelet which underwent cation exchange upon annealing to 350 °C and developed separate $Cu_{2-x}Se$ and Bi-rich domains and corresponding EDX map (c) [99].

The second transition metal that attracted a lot of attention was magnetic element Fe, which was studied from the point of view of altering the electronic structure of TI by opening a gap at the Dirac cone [73, 74, 106]. The effect of Fe on the TSS is still questionable [76, 107-110], however it was observed that interfacial phases can be formed at the contact as was observed by EDX analysis and microscopy (STM, STEM) (Figure 20). Upon deposition of Fe on Bi_2Se_3 and subsequent annealing to 300-350 °C reaction occurs, forming a layer of FeSe [69, 110], which can also arrange epitaxially [111]. The reaction can result also in the formation of $FeSe_{0.92}$ phase already at RT [109]. Similar process was found on the interface with Bi_2Te_3, forming FeTe [76, 77, 109].

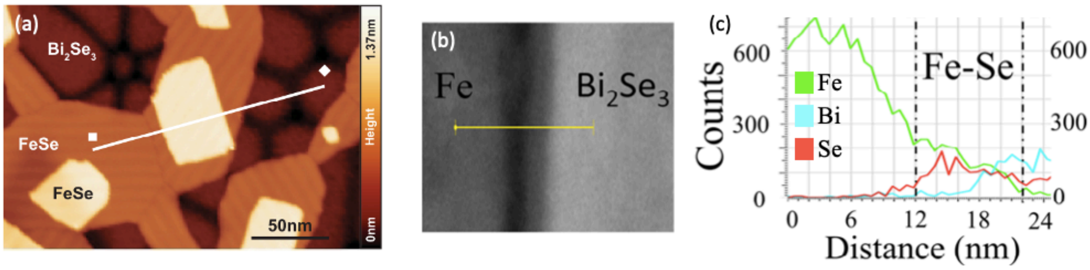

Figure 20: (a) STM image of ultrathin FeSe islands on Bi_2Se_3 prepared by RT deposition of Fe and subsequent annealing to 570 K for 45 min [69]. (b) STEM image of a Fe/Bi_2Se_3 interface cross-section with corresponding EDX line profile [109].

The observed phenomena for Cu and Fe, made the community aware that the characterization of the interface chemistry is crucial in understanding the transport at the metal/TI interface, and necessary for the design of majority of TI-based applications. The first systematic study regarding the chemical processes at the metal/TI interface was reported by Walsh *et al.* [112]. The study covers interfaces between Bi_2Se_3 and deposited metals and alloys (Au, Cr, Fe, Co, Ni, Ir, Pd, CoFe, NiFe), examined by XPS and, for some metals, by TEM. From the set of studied metals only Au showed no (or small) interaction with Bi_2Se_3 substrate, without formation of additional phases, the rest resulted in the formation of an interfacial layer as shown in Figure 21. Hypothesis based on the work function and the Gibbs free energy of formation of the metal selenide, $(\Delta_f G_{metal-Se})$, was proposed to explain interactions at the interface. Cr and Fe, having the lowest work function, exhibited the strongest interaction and produced M_xSe_y phase. Co and Ni resulted in the interfacial layer of M_xSe_y and $M_xBi_ySe_z$, whereas Ir and Pd, that have the highest work function from the set of studied metals, produced a layer of $M_xBi_ySe_z$. In all cases metallic Bi or intermetallic species of Bi were also formed within the interfacial reaction. Although this model can be used to explain the observed chemical reactions in that study, it does not correctly describe our systems and detected interfacial reactions. A new model is proposed in Chapter 6 of this work, which combines the findings from the literature and from our work that could be used for the future research regarding metal/Bi_2Se_3 interfaces.

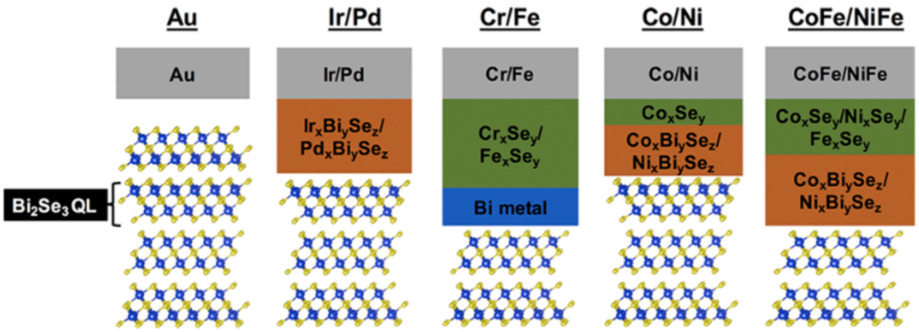

Figure 21: Scheme of the interfacial phases produced upon deposition of various metals and alloys on Bi_2Se_3.[112]

In summary, several theoretical and experimental studies confirmed a chemical interaction at the metal/TI interface either in a form of intercalation (for alkali metals and Cu) or chemical reaction (Fe, Ni, Co …) that modify the chemical composition of the interface and results in the formation of new phases. Such modifications of the interface could alter changes in the electronic structure, especially on the TSS, of the original system and should be as such taken into account.

1.5.3 Consequences of interfacial phenomena

The occurring of interfacial phenomena has potential consequences on the system properties, especially for TI, where the most interesting properties are localized at their surface. In the following we briefly describe two possible consequences of reaction at the metal/TI interface.

Relocation of the TSS

When the interfacial reaction reaches its equilibrium, the relocation of the TSS can occur as was observed upon deposition of different materials on top of TI. Due to the proximity effect the TSS can be relocated to different positions around the interface. As calculated by Wu *et al.* [11], deposition of a conventional insulator (CI) on top of Bi_2Se_3 can either position the TSS to the top of the CI film, it can leave them at the CI/TI interface or push them deeper into the TI substrate, depending on the work function of the CI, interfacial binding energy and spin-orbit splitting of the CI (see Figure 22). Among the investigated CI (ZnS, ZnSe, ZnTe), the interaction between Bi_2Se_3 and ZnSe resulted in the relocation of the TSS to the top surface of CI, causing a topological phase transition of ZnSe. Such relocation can affect the catalytic properties of the TI heterostructure and was reported also in other studies. Calculations reported by Li *et al.* [113] show that a heterostructure constructed from 1 ML of ZnSe on top of Bi_2Se_3 has optimum activity towards hydrogen adsorption and HER. Improved catalytic effect is due to interaction between the dangling bonds of ZnSe and electron bath provided by TSS that are relocated to the top of the ZnSe overlayer. Relocation of the TSS was also observed in the study by Shoman *et al.* [114]. In contrary to the previously mentioned studies, here the TSS migrated from the surface of 3D TI $TlBiSe_2$ to the attached bilayer of Bi, showing that the relocation is not reserved only for deposited CI but it also applies for metals. Also, in the work of Spataru *et al.* [115] a strong hybridization between the *d*-bands of some metals and TSS is described (for Pd, Pt and Ni, not for Au), which results in delocalization of the TI surface states over the metal region.

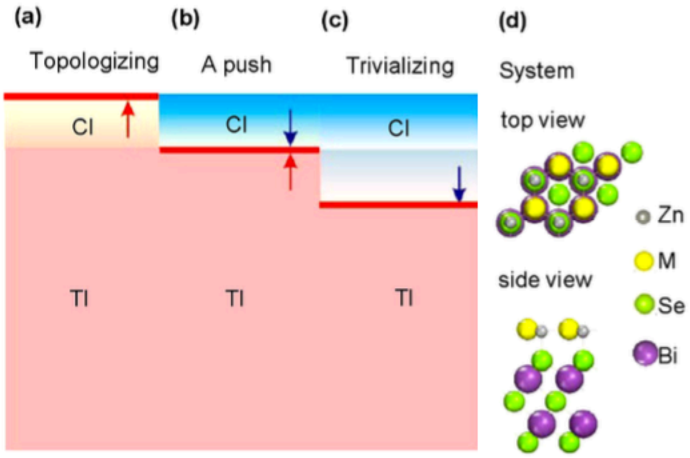

Figure 22: Scheme of the location of the TSS upon coverage of a TI with a layer of conventional insulator. (a) TSS floating to the top of CI; (b) staying put at the CI/TI interface; (c) diving into the TI. The red lines denote the TSS and the arrows indicate the resulting direction of the topological phase transition. (d) The atomic structure of ZnX/Bi_2Se_3 (X = S, Se, Te). [11]

Change of transport properties

Interface phenomena studied within this work can also affect the transport properties of metal/TI interfaces. For this reason, a summary of the electronic phenomena at the metal/semiconductor (SC) interface and possible consequences are described in the following.

When a metal and a SC are put in contact, the electrons will flow from the SC to the metal or vice versa, due to the difference in their work functions, until the Fermi levels of the metal and the SC are aligned, as presented in Figure 23 [116]. When the equilibrium is reached, an electric field is established at the interface forming a space charge region in which the energy bands shift towards or away from the vacuum level. This phenomenon is called band bending (BB). Depending on the magnitudes of the work functions of the metal and the SC, the obtained contacts can be either Ohmic or rectifying with formation of a Schottky barrier.

As the TI are generally also semiconductors, the described BB applies also to this class of materials. Due to high work function of Bi_2Se_3 (5.6 eV) ohmic contacts are expected to be formed when contacted with metals. However, other TI with a lower work function (e.g. $TlBiSe_2$, $\phi_S = 4.7$ eV) could result in a Schottky barrier, especially with Au ($\phi_S = 5.1$ eV) which is most frequently used in transport properties for production of contacts [117].

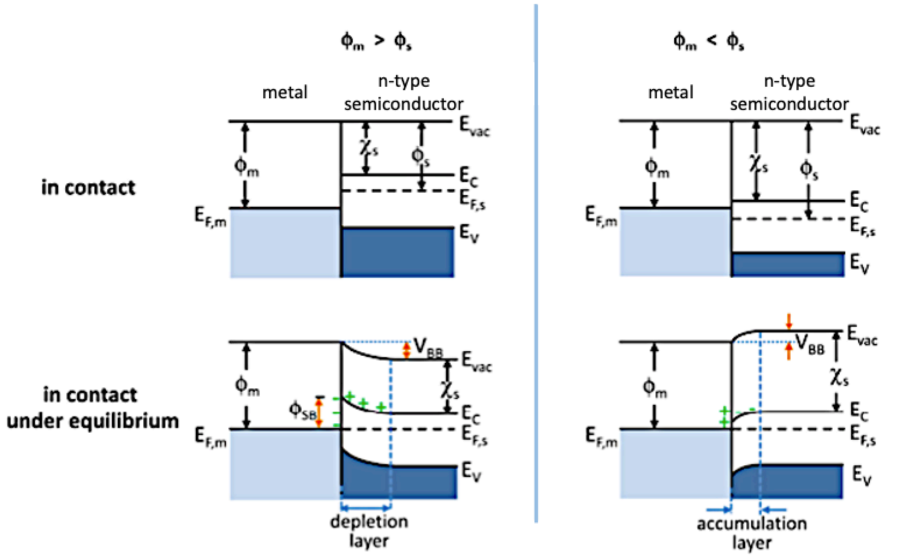

Figure 23: Energy band diagrams of metal/n-type semiconductor interface. E_{vac} – vacuum energy; $E_{F,m}$ – Fermi level of the metal; $E_{F,s}$ – Fermi level of the semiconductor; E_c – energy of conduction band minimum; E_v– energy of valence band maximum; Φ_m – metal work function; Φ_s – semiconductor work function; χ_s – electron affinity of the semiconductor; V_{BB} –band bending potential; Φ_{SB} – Schottky barrier. [116]

Deposition of alkali – K [118, 119] (Figure 24), Rb, Cs [120], and transition metals – Ni [121], Cu, Mn [122], Co [78], Fe [74, 107], Au [79], Cr [106, 108] on TI Bi_2Se_3 resulted in BB where the electron bands were shifted away from the vacuum level. The results are consistent with the transport measurements, where ohmic contacts were found for the applied metal contacts.

Spataru and Leonard [115] theoretically studied the contact of Bi_2Se_3 with Au, Ni, Pt and Pd. Regardless of the metal, the interface always resulted in n-type doping although p-type was expected for the interface with Pt. This result was attributed to the high electronegativity of the terminating Se layer, since the calculation with Bi-terminated surface in contact with a metal gave the opposite direction of the BB. However, in their study the metal layer was modeled as a layered film, without considering possible different arrangements (e.g. clusters) or chemical reactions forming new phases, which in most cases are still not reported in literature (e.g. for Pt).

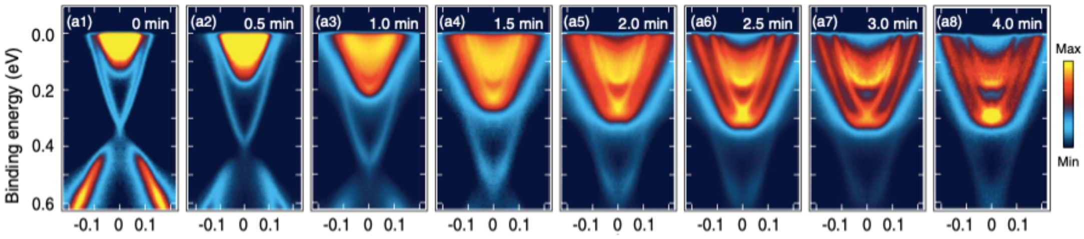

Figure 24: Evolution of the Bi_2Se_3 *electronic structure upon subsequent K depositions showing a downward shift of the Dirac cone. [118]*

Brillson [123] studied the connection between the chemical reactivity of metal/semiconductor interfaces and formation of the Schottky barrier. Chemical reactions and interdiffusion that alter the interface region introduce new phases, defects and localized electronic states, which can impact the Schottky barrier formation. This kind of study gives additional value to the characterization of chemical behavior at the metal/semiconductor interface, since the presence of interfacial phases can influence the electronic properties of such interface. Similar effect can as well be expected for metal/TI systems and for this reason chemical stability of the interface should be investigated.

1.6 State of the art regarding the interfaces between topological insulators and the studied metals

1.6.1 Ag/topological insulator interface

Many innovative technical solutions have been proposed based on the Bi_2Se_3 topological insulator interfaced with Ag as an electrode, a functional layer or a co-catalyst [5, 9, 63, 124, 125]. In these studies, the interface between Ag and Bi_2Se_3 is assumed to be stable. However, the morphology and the growth mode of Ag on $Bi_2Se_3(0001)$ surface are not known, as well as the structural and chemical properties of the interface. Moreover, articles regarding Ag/Bi_2Se_3 interface do not take into account aging of the systems due to the possible chemical changes at the interface.

One example is the theoretical work of Xiao *et al.*, [5] where the focus was on catalytic properties of different metal clusters on Bi_2Se_3, and it was found that the activity of Ag clusters depends on the type of reaction where such systems are employed. In the case of catalytic oxidation, the activity of Ag cluster does not significantly change, whereas for the HER the activity is improved. This result is due to the intrinsic reactivity of the metal towards the referred reaction and increased adsorption induced by the TSS. However, it should be noted that interfaced Ag atoms were modelled as 7-atom clusters, which do not strongly interact with the substrate. Obviously, consideration of a possible chemical interaction with formation of new phases would change the resulting scenario.

Another example is the article of Shi *et al.* [9], where charge-to-spin conversion in the Bi_2Se_3/Ag/CoFeB system was reported where the dominant role was assigned to Ag/Bi_2Se_3 interface and Ag was considered as a 5 nm layer. The interpretation of the results clearly depends on the possible reactivity and stability of the Ag/Bi_2Se_3 interface which was not taken into account.

To our knowledge, no experimental studies on Ag deposited on a Bi_2Se_3 single crystal have been reported before, and the growth mode, the stability and the interfacial chemistry is still not known. Still, some studies have been reported which tackle the problem of Ag/TI interface, which are summarized in the following.

The theoretical research of Otrokov *et al.* [89] predicted that upon deposition of Ag onto Bi_2Se_3 substrate the deposited atoms intercalate into the VdW gaps by a step-mediated intercalation. Factors responsible for this process are big diffusion length of

Ag atoms on the surface and within the VdW gap and a significant decrease in the total energy of the system upon relocation of a single Ag atom from the surface to the VdW gap.

Experimental studies regarding intercalation of Ag into TIs were also performed [88, 126]. Koski *et al.* [88] used Bi_2Se_3 nanoribbons in which various metals were intercalated by a disproportionation redox reaction. As prepared samples were examined by different analytical techniques within a TEM and by XRD that showed zero valent character of the metals. For the intercalation of Ag, $AgNO_3$ was used as a precursor. Although many characterization techniques have been used to describe the Ag/Bi_2Se_3 system, the reported data mostly rely on the comparison of results obtained from the analysis of other metals studied within the reported work. As the strongest evidence, a diffraction pattern obtained by Selected Area Electron Diffraction (SAED) has been used. The pattern shows superlattice spots connected with the ordering of the intercalant within the host lattice (see Figure 25b). However, for the Ag/Bi_2Se_3 system the interpretation of the SAED pattern leaves space for different interpretations due to diffuse, azimuthally spread nature of the superlattice spots suggesting mismatch in the natural periodicity of the Bi_2Se_3 host and the Ag intercalant layers. In contrary, Das *et al.* [124], who also reported deposition of Ag on Bi_2Se_3 nanoflakes from $AgNO_3$ precursor, claims that such deposition results in formation of nanocrystals attached on the surface of Bi_2Se_3 (Figure 25c). The presented data in this article are not conclusive about the reactivity at the interface, especially the XRD pattern, which is presented in such way, that small changes cannot be observed (Figure 25d). Interestingly, also this research used SAED to confirm the observation. However, the interpretations of the obtained patterns are different here since the authors claim that Ag remains on the surface of nanoflakes in its metallic form and that the crystal structure upon adsorption remains undistorted.

De Jong [127] found that evaporation of Ag on $Bi_{1.5}Sb_{0.5}Te_{1.7}Se_{1.3}$ results in efficient intercalation into the VdW gaps accompanied by low-level substitution for the Te/Se atoms of the termination layer of the crystal. Figure 25a shows selected XPS data from the mentioned studies of the Ag/TI interface, where an additional component in the Bi5d core level indicates a partial reaction of the deposited Ag.

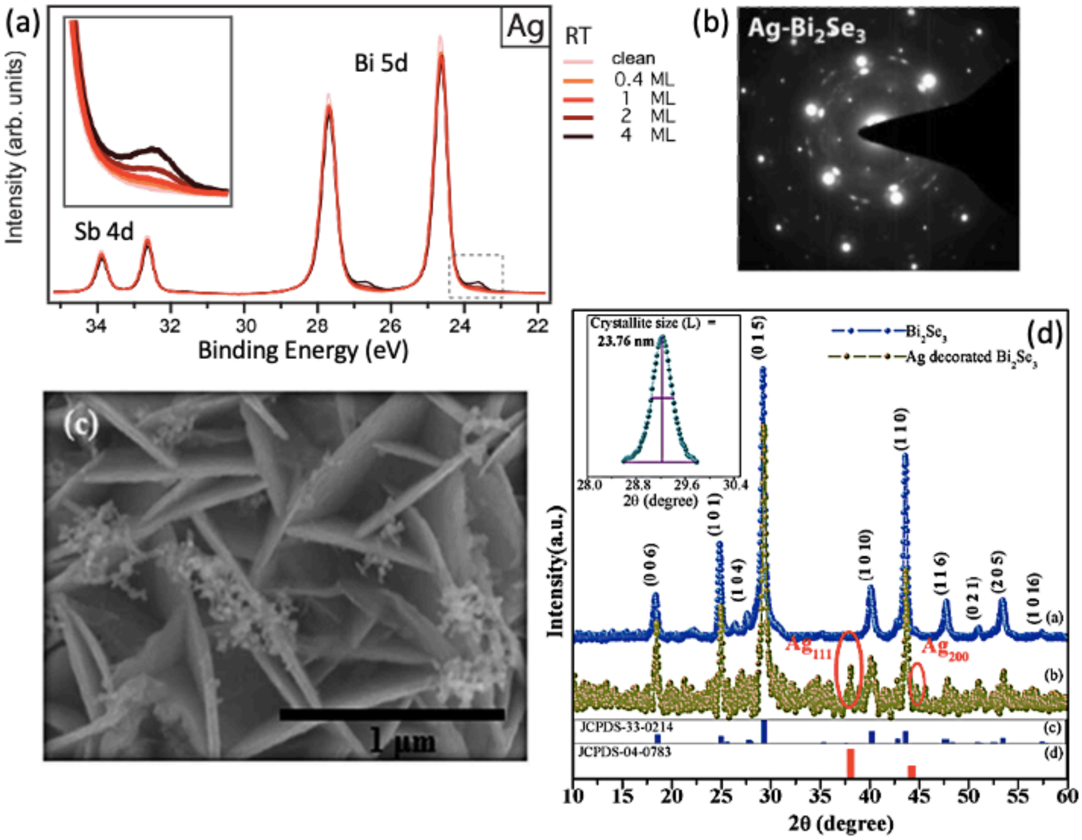

Figure 25: (a) High-resolution core-level spectra of Bi 5d and Sb 4d core levels for Bi$_{1.5}$Sb$_{0.5}$Te$_{1.7}$Se$_{1.3}$ *decorated with the indicated amounts of Ag evaporated and measured at RT.[127] (b) Superlattice patterns observed with intercalation of zerovalent Ag atoms, showing strong satellite spots associated with each* Bi$_2$Se$_3$ *Bragg spot.[88] (c) SEM image of Ag particles attached to* Bi$_2$Se$_3$ *nanoflakes and corresponding XRD pattern (d).[124]*

A solid-state reaction at the interface between 10 μm thick Ag film and analogous topological insulator Bi$_2$Te$_3$ was reported by Lin *et al*. [94]. Sample was annealed to 250 °C for 10 h and Ag$_2$Te phase was detected by EDX. That analysis was performed at the micrometer scale, without description of the interface structure and of the overall reaction.

In summary, according to previous literature, the interface between Ag and TI is present in several studied systems [5, 9, 88, 94, 124, 127]. Studies focused on the Ag/TI interface report either the intercalation of Ag atoms with possible accompanied substitution of constituent atoms of TI [88, 89, 94, 127] or in a simple adsorption of the deposited Ag without reaction [5, 9, 124]. For the specific Ag/Bi$_2$Se$_3$ interface different outcomes were reported, making it impossible to unambiguously know what happens at the interface. The growth mode, the interface chemistry and stability of the Ag film, fundamental for the appropriate modelling of the systems and prediction of applicative properties, are still not known.

1.6.2 Ti/topological insulator interface

Majority of the foreseen TI applications exploiting the peculiar nature of the TSS is in the field of electronics (spintronic devices, low power electronics), where an electric contact is necessary. When producing metal contacts for characterizing device performance or measuring transport properties, titanium is commonly used as an adhesive layer to enhance the adhesion between the TI and the metal contact (Au, Pt...) [128-130]. In several cases the presence of Ti adhesive layer did not prevent the observation of the TSS related phenomena but in some cases anomalous behavior was reported [131, 132]. However, despite the frequent use of Ti with contacts on TIs, the structure and chemistry of the Ti/Bi_2Se_3 interface has never been characterized so far, and no information about its stability is available.

In the article of Kong *et al.* [132] where the influence of Bi_2Te_3 orientation on resistivity of Cu metal contact was studied, absorption of Cu into the Bi_2Te_3 was detected. To suppress the diffusion of Cu, a Ti barrier layer was deposited, which successfully prevented absorption of Cu into the substrate. Despite the reduced Cu absorption, the contact resistivity did not improve, in fact, it even increased. It has been suggested that the effect could be due to the reduction of some compounds at the interface. However, the research was performed on a µm scale, therefore, it was not possible to detect possible reactions occurring between the interfacial layers of Bi_2Te_3 and Ti.

In the research of Cho *et al.* [131] it was published that the use of Ti or Cr adhesion layer for metal contacts on ultrathin Bi_2Se_3 made the contact resistance to increase rapidly with time. Oxidation of the adhesion layer was suggested, but no data or discussion were reported.

Since Ti is more easily oxidized (based on the standard reduction potential) than other metals that were found to exhibit an interfacial reaction with Bi_2Se_3 and other TIs (e.g. Fe, Cu or Ni) the occurrence of an interfacial reaction with formation of new phases can be expected also for the Ti/Bi_2Se_3 system. Additionally, such outcome could even explain the observations reported in ref. [131, 132].

1.6.3 Pt/topological insulator interface

Pt belongs to the class of noble metals and is present in many applications as a catalyst. The interface between Pt and TI could therefore be beneficial from the perspective of enhanced catalytic activity of Pt film or clusters due to the presence of the TSS. The influence of TSS on the catalytic activity was initially studied with *ab initio* calculations by Chen *et al.* [4] for Au, and more systematically by Xiao *et al.* [5] for Au, Pd, Ag, Pt and Cu. For Pt they found that the presence of the TSS significantly improves the adsorption of oxygen molecules on Pt cluster but has a negative overall effect on catalytic oxidation and HER activity due to the increased binding energy with reactant, which reduces the kinetics of the reaction. However, in their work Pt was modeled as clusters of seven atoms on top of the Bi_2Se_3 surface. The real morphology of Pt after deposition on the Bi_2Se_3(0001) surface is not known yet, and can be greatly different, as for example happens in the Au case where clusters with the size of < 2 nm are not observed [79]. Moreover, the presence of reaction and/or absorption of Pt into the TI, which could have crucial influence on the resulting properties of the Pt/Bi_2Se_3 system, is not known as well.

Pt/TI interface is present also in other applications. In the article of Zhang et at. [133] the applicative value of Pt/Bi_2Se_3 interface was analyzed from the perspective of wearable and flexible non-volatile memory devices. The research showed good rewritable resistive switching properties and low switching voltages of Pt wires coated with Bi_2Se_3 which is desirable in the low power memory devices. In the research of Kacsich *et al.* [134] the main aim was to find the optimal diffusion barrier between Bi_2Te_3 and Cu, which is used as a metallic electrode in thermochemical devices. Among the chosen materials, 90 nm thick Pt film was also used as a diffusion barrier but proved to be inefficient in preventing Cu diffusion.

Ab-initio calculations regarding the electronic properties of Pt/Bi_2Se_3 interface were performed by Spataru *et al.* [115]. Calculated cross-section of the electrostatic potential perpendicular to Pt/Bi_2Se_3 interface showed connecting paths below the Fermi level suggesting that there is no tunnel barrier for the electron transport between Bi_2Se_3 and deposited Pt. Strong charge transfer is responsible for the band bending potential of around 0.7 eV, locating the Fermi level well above the conduction-band edge. Strong hybridization between Pt and Bi_2Se_3 also has a strong influence on the TSS leading to resonances with relaxed spin-momentum locking. Described properties make Pt less promising candidate for metal contacts on TI due to stronger coupling at the interface. However, their model is based on a Pt film made of 6 atomic layers. This would be the case in a layer-by-layer growth, but the real growth mode and arrangement of atoms is not known.

Until now, experimental data about the structural and chemical properties of the Pt/Bi_2Se_3 interface are missing, but some hypothesis can be formulated from the behavior of similar systems.

Study about the Au/Bi_2Se_3 interface was carried out by members of our laboratory [79] and results showed very weak interaction between these two materials. Accordingly, Volmer-Weber growth of the vapor phase deposited Au thin film was observed. Since Au belongs to the group of noble metals, as Pt does, similar weak interaction can be at first expected at the interface. However, due to the smaller mobility of Pt, a different morphology can be expected.

Since Pd exhibits similar properties as Pt (they both belong to the so-called Pt group) some outcomes about Pt/Bi_2Se_3 interface can be predicted from the reported behavior of Pd on TIs. Walsh *et al.* [112] reported the formation of an interfacial phase $Pd_xBi_ySe_z$ upon deposition of Pd on Bi_2Se_3. Interdiffusion for such interface was reported also by Mlack *et al.* [135] where Pd/Bi_2Se_3 samples were prepared by annealing above 200 °C. However, nearly complete desorption of Pd and reshape of the Bi 5d and Se 3d core level spectra to resemble spectra of the clean Bi_2Se_3 upon annealing to 300 °C suggest low interaction at the interface. Qu *et al.* [136], who studied the superconductivity at Pt/$Bi_{1-x}Sb_x$ junction reported that there is a slight lattice disorder at the interface resulting in a 2 nm thick Pt-intercalated $Bi_{0.91}Sb_{0.09}$ layer.

In summary, studies regarding the Pt/TI interface are very sparse and usually do not focus on this interface but rather have it present within the studied system. Considering the behavior of similar metals, one can hypothesize either a weak interaction (as in the case of Au) or the formation of an interfacial layer (as in the case of Pd). Surely, characterization of Pt/Bi_2Se_3 interface is important for future theoretical and experimental studies, especially in the field of catalysis, as well as for interpretation of the reported results.

1.7 Motivation and aim of the research

As described above, an interface between a metal and TI is an important issue both for fundamental and applicative field. Despite its presence in majority of the studied systems (theoretical or experimental) the knowledge about these interfaces is still lacking deep characterization. The aim of this work is to explore the interface between Bi_2Se_3 and three metals: Ag, Ti and Pt.

Ag and Pt are noble metals and their interface with TIs is potentially interesting both for electronics and catalysis research field. On the other hand, the interface between Ti and TI is frequently found in the literature since the use of Ti adhesion layer in the fabrication of metal contacts is commonly used.

In order to provide the missing knowledge about the selected metal/Bi_2Se_3 interfaces and find general trends in metal/TI interfacial phenomena, the aims of this work are the following:

- characterization of the metal growth mode and of the film morphology on single-crystal Bi_2Se_3 surface;
- determination of metal/TI interface stability in time, both at room temperature and at elevated temperatures;
- determination of the interface structure and chemical reactions happening at the interfaces between a metal and Bi_2Se_3;
- considering the observed results together with what is already reported in the literature, discuss the relevant parameters to predict the interface phenomena between a metal and Bi_2Se_3 and search for the possible phenomena explaining the interactions observed at the metal/TI interface.

2 METHODS AND EXPERIMENTAL SECTION

This chapter is meant to provide the information regarding the experimental techniques used within the presented research work. For a more thorough review of the theory and instrumentation the reader is referred to references [137-142]. The second part of the chapter describes the synthesis and procedures used for sample preparation.

2.1 Scanning Electron Microscopy

A Scanning Electron Microscope (SEM) is an instrument that allows for observation and characterization of organic and inorganic materials on a nanometer and micrometer scale (Figure 26a). A focused beam of electrons (energy range for JEOL JSM 7100F is 0.1 - 30 kV) is generated and a raster is scanned over the surface of the sample to form images. The beam can as well be stopped at a selected location if a point analysis is required. A wide variety of surfaces can be inspected, with the limitation that samples are conductive (or covered with a thin conductive coating), and stable under the electron beam and in vacuum conditions.

SEM operates in vacuum ($p_{\text{specimen chamber}} = 10^{-4}$ Pa, $p_{\text{gun}} = 10^{-8}$ Pa) in order for electrons to reach the specimen and the detector with minimized interactions with gas molecules. The vacuum is also necessary to prevent the burning of the filament producing electrons and contamination of the surface during the analysis. Figure 26b shows the structure of the apparatus. Electrons are generated in the electron gun on the top of the microscope column. Afterwards they are accelerated and focused by electromagnetic lenses to a spot size of around 1 nm (if a Schottky field emission source is used, as in this case) enabling the image resolution in the nm range. For the microscope used in this work (JEOL JSM 7100F) the specifications state the lateral resolution is 1.2 nm at 30 kV and 3 nm at 15 kV.

Scan coils deflect the electron probe in the x and y direction so that it scans in a raster fashion over a rectangular area of the sample surface. Point by point, signals emitted from the surface are afterwards collected with different detectors and are displayed as images or spectra.

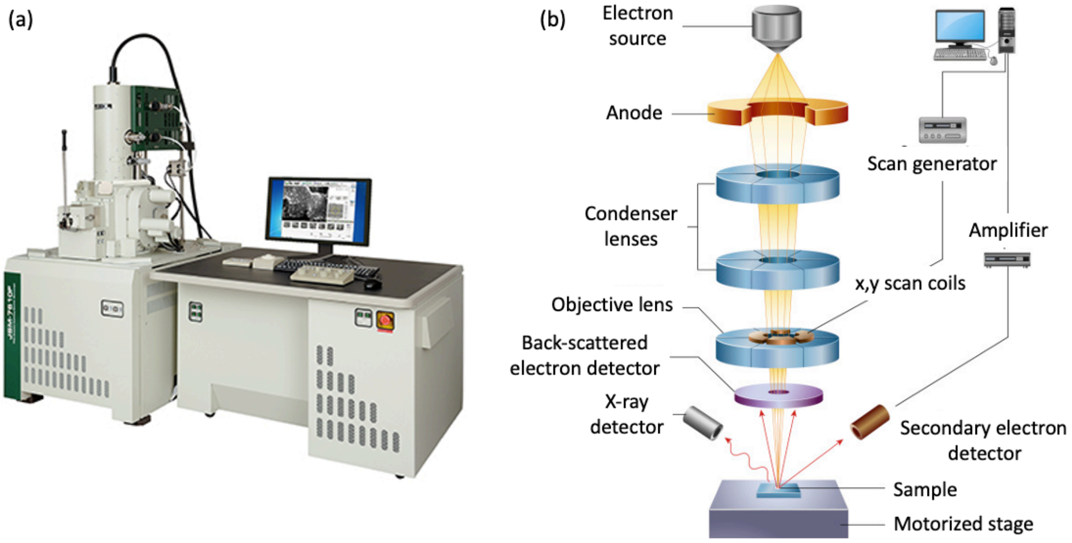

Figure 26: Photo of the JEOL JSM 7100F microscope (a) [143] and a scheme showing the structure of an SEM (b). [144]

Upon electron-sample interaction different signals are generated at different depths within the interaction volume, each carrying different information about the sample. Figure 27 represents a scheme of the interaction volume showing where the specific signals are generated. The size of the interaction volume depends on the specimen and the energy of the electron beam. If the sample composition consists of lighter elements, the interaction volume will be larger, the same is true if higher accelerating voltage is used. Consequently, the size of the interaction volume determines the resolution of the SEM. Using the following Kanaya-Okayama equation it is possible to calculate the electron range within the interaction volume

$$R_{KO} = \frac{0.0276A}{Z^{0.89}\rho} E_0^{1.67}, \qquad [3]$$

where A is the atomic weight (g/mol), Z is the atomic number, ρ is the density (g/cm^3), E_0 is the beam energy (keV), and R_{KO} is the electron range in µm.

Principal signals used during an SEM measurement are the secondary electrons, carrying information about the morphology of the surface, as well as the backscattered electrons and characteristic X-rays providing the information about the elemental composition.

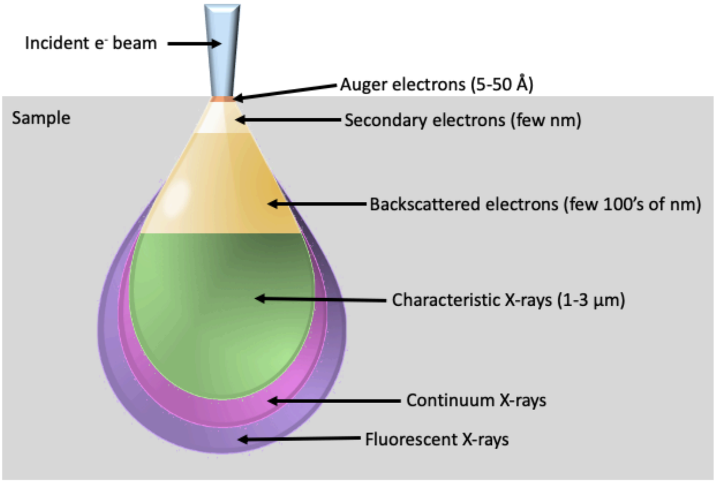

Figure 27: Scheme of the interaction volume showing where the different detected signals are generated.

Backscattered electrons (BSE) are beam electrons which have undergone numerous elastic scattering events and accumulated enough deviation from the incident beam path to return back to the surface and scatter back out of the sample. The maximal number of BSE is emitted in the direction of the incident beam; therefore, the BSE detectors are positioned above the sample in a ring type arrangement, concentric with the electron beam. Number of BSE reaching a BSE detector is proportional to the mean atomic number of the sample since heavier atoms (with a higher atomic number, Z) have greater cross-section for backscattering. The contrast in BSE images is therefore based on the average Z in the sample where brighter areas correspond to greater Z and darker to lower Z. Imaging with BSE is helpful for obtaining high-resolution compositional maps of a sample and for quickly distinguishing different phases.

Secondary electrons (SE) are the electrons of the specimen atoms that are produced by inelastic scattering interaction with the beam electrons and have enough kinetic energy to be ejected from the atom and the specimen surface. Since the energy of SE is very small (<50 eV), those generated at higher depths are quickly absorbed by the specimen and only those at the top surface of the specimen can intersect the surface and escape. This means that SE-signal intensity is very surface sensitive, their escape depth is within a few nanometers. In contrast to BSE, SE are relatively insensitive to atomic number. SE yield depends on the angle between the incident beam and the sample surface. When the incident electron beam enters the specimen perpendicularly to the local surface orientation, the amount of the SE emission is smaller than when it enters obliquely. Thus, since the local surface orientation is a source of contrast, SE imaging is an appropriate signal to observe the morphology of the specimen surface.

Upon electron bombardment of the sample two types of X-rays are produced: continuum and characteristic X-rays. Characteristic X-rays occur when a an inner shell ionization is produced and the hole is filled with an outer shell electron (Figure 28a). When this process happens, an X-ray with characteristic energy of the electron transition for that atom is emitted. These X-rays therefore carry the information about the elemental composition of the sample. They are collected by an energy dispersive X-ray spectrometer (EDS or EDX) and are presented as a spectrum where number of X-rays detected is plotted versus their energies (Figure 28b) or as maps showing how the intensity of a characteristic X-ray peak varies over the inspected area of a sample. Since the escape depth of X-rays is several μms, the detected X-rays originate from the full interaction volume. EDX technique is much less surface sensitive compared to imaging with SE or BSE. The achievable lateral resolution is of the same order of magnitude of the maximum width of the electron interaction volume.

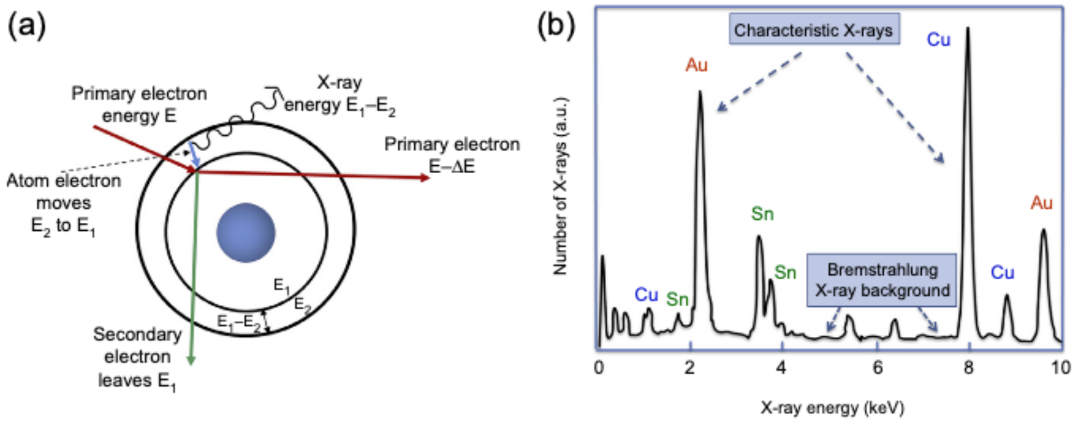

Figure 28: (a) Characteristic X-ray generation. (b) Example of an EDX spectrum exhibiting characteristic X-rays at specific energies.

A quantitative composition of the sample can be extracted from the EDX spectrum with a relative error in the range from 2-5 % when the measurements are performed in optimal conditions, i.e. for a flat sample with homogeneous composition. Many factors can reduce the accuracy of the quantitative analysis, such as corrugated or irregular morphology, high concentration of light elements (e.g. C or O, for which the X-ray emission is strongly suppressed) or non-homogeneous sample (e.g. layered structures or deposited films).In these cases, some accuracy can partially be recovered by advanced spectrum analysis software.

SEM also allows to image samples at different temperature if a special heating stage is used (Figure 29). In this case the sample is mounted on the heating stage that has a motorized lid allowing to transfer the sample into the SEM without air exposure (in vacuum or inert atmosphere). Sample is heated by a ceramic resistance heater placed below it and the temperature is controlled by the PID controller and water-cooling system. With increasing temperature the pressure inside the microscope can increase due to degassing, therefore pressure should be carefully monitored during the experiment. In order to lower the pressure liquid nitrogen trap can also be used.

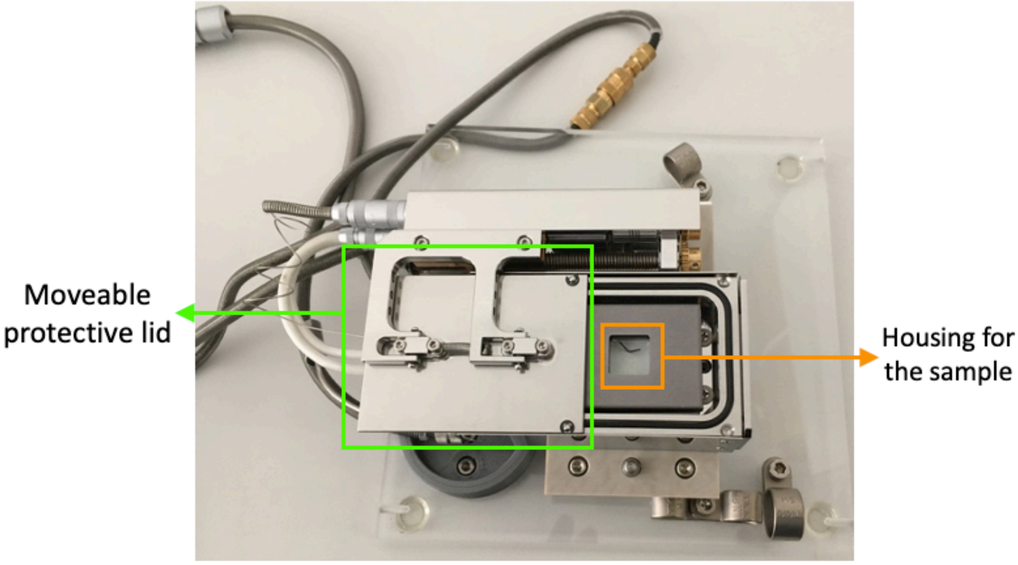

Figure 29: Image of the SEM heating stage used for annealing experiments.

A field emission SEM (FESEM, JEOL JSM 7100F TTLS) equipped with an energy dispersive X-ray spectrometer (EDX, Oxford X- Max80) operating at a base pressure $<1\cdot10^{-4}$ Pa was used for the measurements described in this work. For a standard imaging the electron energy was set to 15 kV, current to 0.1 nA and working distance to approximately 6 mm. For EDX analysis 10 kV energy and current of 0.15 nA was typically used. Working distance was kept at 10 mm, corresponding to the distance at which the EDX apparatus is calibrated. For the experiments with the heating stage (Kammrath&Weiss) the sample had to be kept at higher working distance (13.7 mm). To improve the SE signal the sample was tilted for 15 °. Beam energy of 20 kV and current 0.2 nA was used. Base pressure in the instrument during these experiments was $< 3.6\cdot10^{-4}$ Pa.

2.2 Transmission Electron Microscopy

In a Transmission Electron Microscope an electron beam (with energy typically in the range 100-300 keV) is transmitted through a thin section of the sample. In contrary to SEM, in TEM the beam is not focused and scanned over the sample but is parallel and illuminates the area of interest. Consequently, in TEM a spatially resolved detector (fluorescent screen and/or charge couple device (CCD) camera) placed below the sample is used. Due to much higher energy of the electrons, the resolving power of TEM is significantly better than in the SEM. In modern TEMs a resolution in the range of 0.1 nm and the capability to distinguish atomic planes in a crystal are ordinarily achieved (in the TEM used for this work the resolution at 200 keV is 0.1 nm). Samples have to be very thin (<100 nm) in order the electrons pass through them. Usually a special preparation procedure is used to produce such thin samples.

In order to increase the mean free path of the electrons the TEM column operates under high vacuum ($\sim 10^{-5}$ Pa). A series of pumps are used to achieve the appropriate conditions for the measurement as well as the cold trap to adsorb gases in the vicinity of the specimen.

A TEM (see Figure 30) is composed of the electron gun generating electrons which are focused into a coherent beam by the condenser lens. A condenser aperture with diameter ranging from ~10 μm to 200 μm, inserted into the second condenser lens, determines the divergence angle and the dose of the incident beam and reduces spherical aberration. The beam afterwards passes through the specimen. Transmitted electrons are focused by the objective lens. Intermediate and projector lenses finally magnify the image which is visualized on a phosphorous screen or by a CCD camera.

As the electron beam is transmitted through the sample, a variety of beam-specimen interactions occur, forming transmitted electrons, elastically and inelastically scattered electrons, X-rays and Auger electrons. Most of the transmitted and elastically scattered electrons are used to form an image. In general, the darker parts of the image represent those areas of the sample where fewer electrons are transmitted through the specimen and the lighter areas where more electrons pass through the specimen. However, the image contrast can be due to the difference in the thickness of the sample (mass thickness contrast), the atomic number of the constituent elements (Z contrast), crystal structure or orientation (diffraction contrast) and interference between the transmitted and diffracted waves with different phase, which is used in high-resolution imaging (phase contrast).

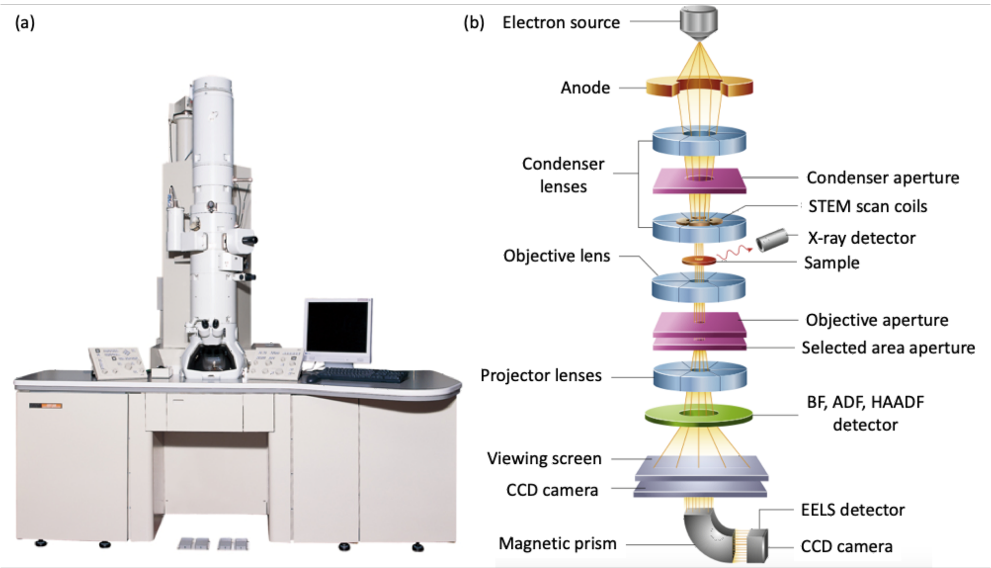

Figure 30: Photo (a) [143]and scheme (b) of the TEM instrument. [144]

Apart from imaging, TEM allows also to use the elastically scattered electrons to perform electron diffraction on a part of the sample (Selected Area Electron Diffraction, SAED). An aperture located in the first image plane below the sample is inserted in the column to define the area from which the diffraction pattern is to be recorded. The advantage of such electron diffraction, compared to X-ray diffraction, is that much smaller part of the sample determined with a nanometric precision can be analyzed. The typical size of an area studied by SAED is a few hundreds of nanometers. SAED can be used to measure lattice parameters, to identify the crystal structure or phase, to determine the growth direction or the orientation of the sample and for other phenomena connected with the crystal structure.

In Scanning Transmission Electron Microscope (STEM) the beam is focused to a nanometer spot on the sample and scanned over the area of interest (as in the SEM). Imaging can be performed in the bright field, collecting the transmitted electrons, or in the dark field detecting the electrons scattered away from the path of the transmitted electrons. In this case an annular electron detector is used, which detect only the electrons deviating from the beam. In the latter the image intensity correlates to the density of the sample and the atomic number of the elements present. Operating in STEM mode allows for high resolution elemental analysis and mapping by EDX or EELS.

As described for SEM, EDX analysis can be performed also in the TEM, due to generation of X-rays upon interaction of the electron beam with the specimen. EDX is performed in STEM mode, to achieve the control over the area of the specimen on which the analysis is done. Compared to EDX in the SEM, in TEM much higher spatial resolution can be achieved due to a smaller spot size (down to 0.2 nm in our apparatus) and because the interaction volume is limited to the thickness of the sample.

The work presented in this thesis was performed using field emission TEM (TEM JEOL JEM 2100F-UHR) operating in TEM and STEM mode using energy dispersive X-ray spectroscopy (EDX, Oxford X-Max80T attached to JEOL JEM 2100F-UHR). During the measurement the vacuum was kept below $1.5 \cdot 10^{-5}$ Pa and the acceleration voltage was set to 200 kV. For STEM imaging and EDX analysis the spot size was set to 0.7 nm.

2.3 Scanning Tunneling Microscopy

Scanning Tunneling Microscopy was invented in 1981 by Gerd Binnig and Heinrich Rohrer, for which they were awarded the Nobel Prize in physics. STM was the first instrument that allowed imaging of the sample surface at the atomic level. A scheme of the technique is presented in Figure 31.

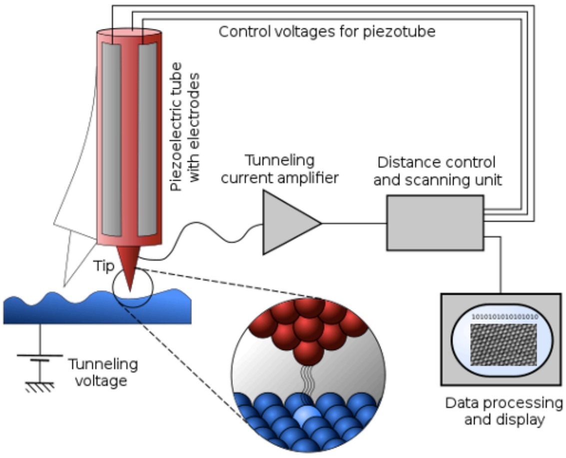

Figure 31: Scheme of an STM instrument. [145]

The main component of the STM instrument is a sharp conducting tip that is scanned over the sample surface forming an image of surface topography. The technique requires the sample to be conductive and it is, in general, performed in the Ultra High Vacuum (UHV) to prevent any contamination of the surface.

The basis of STM is the quantum mechanics phenomenon called tunneling, for which particles, in this case electrons, can tunnel through a potential barrier. When the tip approaches the sample to a very small distance and a bias voltage is applied between them a tunneling current is established along the direction of the bias. The principle of tunneling is described in Figure 32. In a metal, the energy levels of the electrons are filled up to the Fermi energy. In order for an electron to leave the metal (field emission), it has to overcome an energy barrier that is equal to its work function, Φ. However, when the specimen and the tip are brought close to each other so there is only a narrow region of empty space left between them and a voltage, lower than Φ, is applied between them, the electrons can ‘tunnel’ through the vacuum barrier, in this example from the specimen to tip, resulting in a net electron current, called the tunneling current. Typical applied bias is between 0.05 and 1 V (either positive or negative). With such a bias voltage, and distance between the tip and the surface in the order of 1 Å, the tunnel current should be in the range of nA to pA.

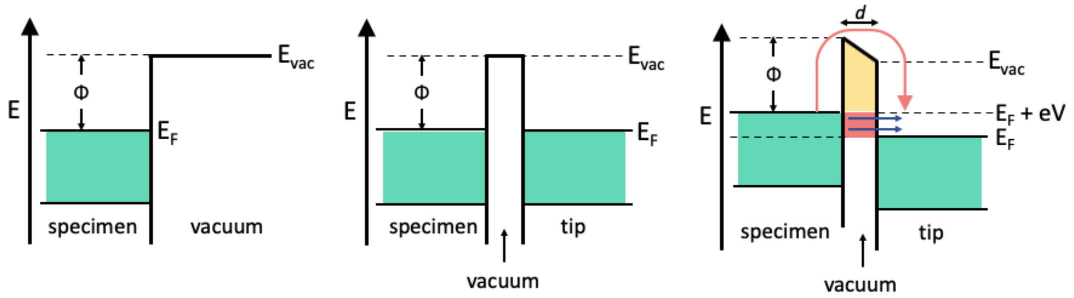

Figure 32: Energy structure of a conductive specimen (a); of the specimen and the tip when placed in the close vicinity; Fermi energies are aligned (b) and the situation when a bias voltage is applied between the specimen and the tip causing tunneling current.

Tunneling current depends on the tip-surface distance *d*, on the voltage *V*, and on the height of the barrier Φ as described in the following approximate relation [146]

$$I \approx V e^{-2\frac{\sqrt{2m\Phi}}{\hbar}d} \qquad [4]$$

The formula shows that the current depends exponentially on the distance *d*, therefore very small changes in the tip-sample separation induce large changes in the tunneling current. For a typical value of the work function Φ of 4 eV for a metal, the tunneling current is reduced by a factor of 10 for every 1 Å increase in *d*, making STM extremely sensitive technique to the local electronic spatial distribution at the surface.

The tunneling current is directly proportional to local density of states (LDOS) within the applied bias since tunneling requires an empty level of the same energy as the electron in order the electron to tunnel to the other side of the barrier. If a positive bias is applied between the tip and the sample, electrons will tunnel into the empty states in the sample. In the case of a negative bias, the electrons will tunnel out of the occupied states in the sample into the tip. Therefore, an STM image actually represents a contour map of the LDOS near the Fermi level.

In the STM measuring process the tip is raster scanned (x-y direction) across the surface of the sample. There are two imaging modes used, the constant-height and constant-current mode. In the first, the tip is maintained at a constant height and is scanned over the surface. In this imaging mode, the mapped physical quantity is the tunneling current. If the surface is composed of different atoms the measurement in the constant-height mode will give information regarding the surface composition (due to different work functions of atoms) and defects. Such measurement mode however requires an atomically flat and horizontal surface, and it is only occasionally used. In the much more common constant-current mode, STM uses a feedback circuit to keep the tunneling current constant by adjusting the height of the tip at each measurement point by changing the voltage applied to the piezoelectric height control mechanism. In the constant current mode the mapped quantity is the tip position in z axis, adjusted by the feedback circuit, which provides information on the topography of the sample surface if it is composed of the same atoms. In the case of non-homogeneous composition, the tunneling current depends not only on the distance, but also on the work function of the specific atom and LDOS. For this reason, the mapped quantity is called “apparent height”.

The resolution of an STM image in the z direction can be as low as 0.01 Å, whereas the lateral resolution is about 1 Å. In order to achieve such resolution piezoelectric materials are used to control the motion. Resolution of the image also depends on the shape of the scanning tip. Blunt tip reduces the lateral resolution, whereas in the case of tip having two tips instead of one at the end causes double-tip imaging, since both tips contribute to the tunneling.

An STM also allows to perform spectroscopy measurement (STS) by sweeping voltage and measuring the current at a specific location. Such measurement gives information about the LDOS at a specific feature on the surface. The energy-band gap of semiconductors or superconductors can also be directly obtained.

STM measurements described in this work were done at CNR-IOM Trieste, Italy. Measurements were performed in UHV at RT using an Omicron VT-STM apparatus with acquisition software SCALA. Sample preparation (cleaving, metal deposition), LEED analysis as well as the measurement were carried out *in situ*. The STM measurements were performed at a base pressure of $2 \cdot 10^{-10}$ mbar in a constant current mode, with the applied bias referred to the sample. Image analysis was done using the Gwyddion analysis software [147].

2.4 X-ray Powder Diffraction

Due to the correlation between the distances between neighboring atoms and the electromagnetic wavelength of X-rays, the X-Ray Diffraction (XRD) is the most used method for a detailed three-dimensional structural investigation of compounds.

XRD is based on the constructive interference of monochromatic X-rays and a crystalline sample. When X-rays reach the sample, they can either be reflected or they enter the crystal lattice and are diffracted by the lattice that is acting as a diffraction grating. The interaction of the incident rays with the sample produces constructive interference if the scattered waves remain in phase and the difference in the path lengths of the two waves is equal to an integer multiple of the wavelength. Such conditions satisfy the Bragg's Law

$$n\lambda = 2d\sin\theta, \qquad [5]$$

where n is a positive integer, λ the wavelength of the incident beam, d the interplanar distance and θ the diffraction angle (Figure 33). Constructive interference gives a peak in the powder diffraction pattern where the intensity of the reflected beam is plotted against the Bragg angle.

When polycrystalline or powdered samples consisting of many randomly oriented particles are scanned through a range of 2θ angles, all possible crystallographic planes should be attainable for diffraction. In contrary, when working with single crystals the sample has to be precisely rotated in all three dimensions to expose all crystallographic planes to X-rays and obtain a diffraction pattern for further analysis.

Maxima in the powder diffractogram correspond to a set of crystallographic planes with the same interplanar distance (d-spacing) that satisfy the Bragg condition. Intensity and positions of diffraction peaks give information about the type of material from which the sample is made, crystallinity, phase purity and changes in the element composition of isomorphous structures, whereas the shape of diffraction peaks gives information on the particle sizes, deformations and disorder.

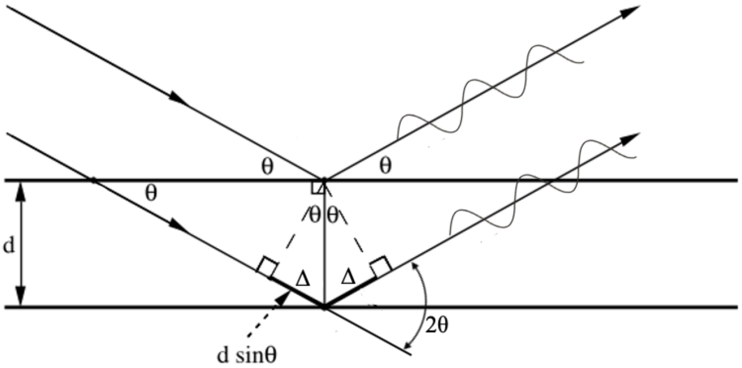

Figure 33: Geometry for interference of a wave scattered from two planes separated by a spacing, d.

d-spacing values allow identification of the phases from which the unknown sample is made since every compound has a unique set of *d*-spacings. These values are obtained by solving the Bragg equation for each peak using the appropriate value of λ. Once all *d*-spacings are determined, an automated search is carried out where the calculated values are compared to hundreds of thousands known reference compounds found in various databases as the Powder Diffraction File (PDF). A systematic procedure is used by ordering the *d*-spacings in terms of their intensity beginning with the most intense peak. Matching of *d*-spacings with a reference from the database enables the identification of the unknown sample. Phases found in the sample produce its diffraction independently from the other phases present allowing quantitative analysis to be performed by comparing the intensities of individual phase with some standards or by Rietveld analysis.

Powdered samples used in the research were analyzed by an X-ray powder diffractometer Rigaku MiniFlex with Cu Kα radiation source ($\lambda = 1.541$ Å) from 10-90° (2θ), with a speed of 2°/min.

2.5 X-ray Photoelectron Spectroscopy

X-ray Photoelectron Spectroscopy, also known as Electron Spectroscopy for Chemical Analysis (ESCA) is a technique for analyzing the composition and chemistry of solid surfaces based on Einstein's photoelectric effect.

XPS measurement requires high or ultra-high vacuum conditions ($<10^{-9}$ mbar) to ensure the longest possible mean free path of the photoelectrons and to avoid the contamination of the sample surface. However, XPS apparatuses operating at near-ambient pressure (in the proximity of the surface) also exist. Scheme of the instrument is shown in Figure 34. When not on a synchrotron, XPS apparatus rely on standard X-ray source, where the X-rays are generated by electron bombardment of a metal target (usually Al or Mg) and only one wavelength is used for the measurement. On the other hand, synchrotrons allow to choose a desired wavelength that can optimize the information about the elements present in the material. They also provide better overall energy resolution, higher photon flux, smaller beam (better spatial resolution) and allow to use a polarized beam.

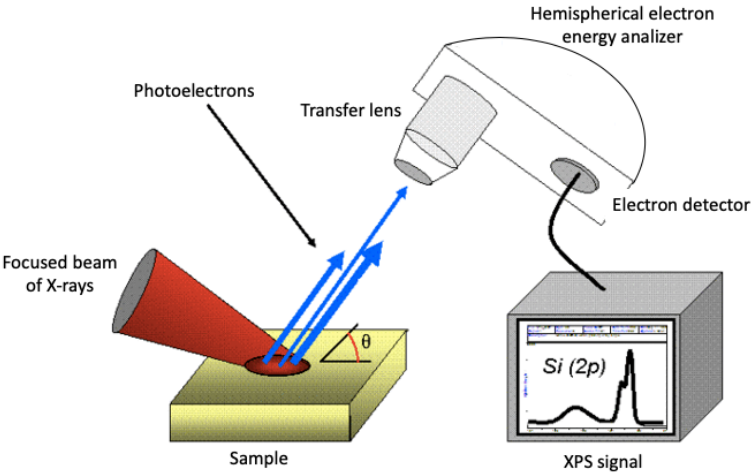

Figure 34: Scheme of the XPS instrument.

When X-ray beam hits the surface, electrons from the inner shells (core level electrons) are emitted from the surface of the sample. Although the X-ray beam can penetrate micrometers below the surface, only the photoelectrons generated in the surface region (depth <10 nm) can leave the surface before absorption and reach the detector (see Figure 35). By measuring the kinetic energy of these photoelectrons and knowing the energy of the incoming photons, binding energies of the electrons can be determined by:

$$E_B = E_p - E_{kin} - \Phi, \qquad [6]$$

where E_B is the binding energy (BE) of the electron, E_p the energy of the X-ray photons used, E_{kin} the kinetic energy of the photoelectron and Φ the work function of the instrument.

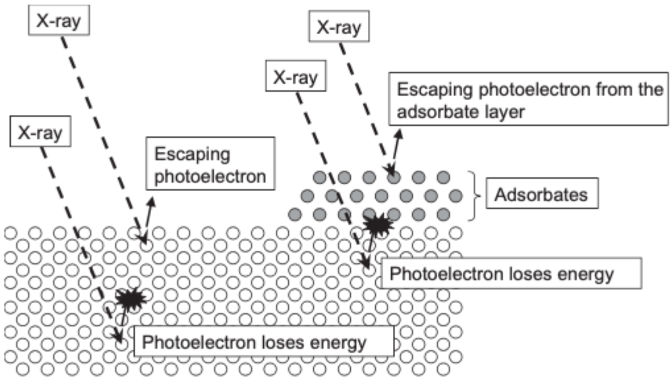

Figure 35: Illustration of photoelectron emission from a solid material (the hollow circles) and the surface adsorbate layer (the gray circles). [139]

The mean free path of a photoelectron through the specimen is described by the so called “universal curve” (Figure 36). It defines the electron escape depth for a given kinetic energy of the electron. In the XPS typical range for photoelectron kinetic energy (10-1000 eV) the inelastic mean free path is typically less than 2 nm, and it may be of a few Å.

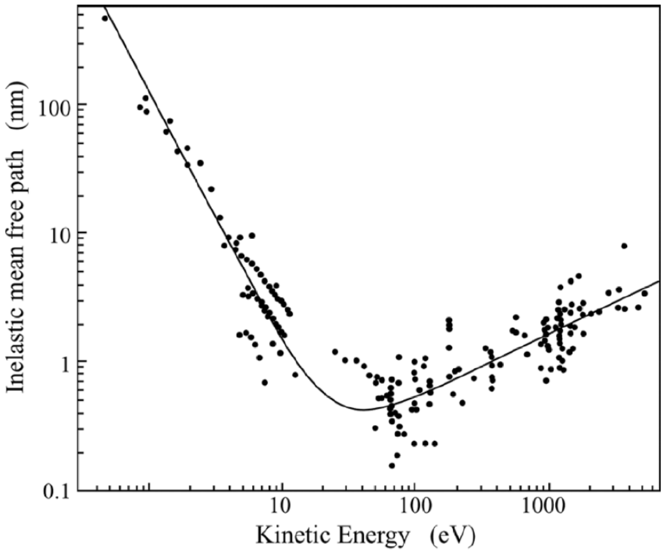

Figure 36: Graph of the inelastic mean free path of the electron versus its kinetic energy – Universal curve. The dots are experimental data, while the solid line is the fit according to the model in ref. [148]

Sensitivity of XPS is primarily a function of the photoemission cross section, i.e. the yield of photoelectrons from a given core-level produced as a function of the incident photon energy, and the spectral background level. XPS is in general a very sensitive technique and can detect elements if their concentration is >0.1 atomic %.

By calculating the BE of photoelectrons from their kinetic energy it is possible to determine the element and orbital from which the electron is emitted since the elements emit electrons of characteristic energy. However, the exact BE of an electron does not only depend on the level from which photoemission is occurring, but also on the oxidation state of the atom and its local chemical and physical environment. Small shifts (a fraction of an eV to a few eV) in the position of photoelectron signal, called chemical shifts, can be used to identify the oxidation state of the element as shown in Figure 37. Atoms with a positive oxidation state exhibit peaks at higher BE due to the extra coulombic interaction between the photoemitted electron and the ion core, whereas the BE of electrons from atoms with negative oxidation state is lower compared to the BE of the element. This chemical sensitivity greatly expands the usefulness of the technique.

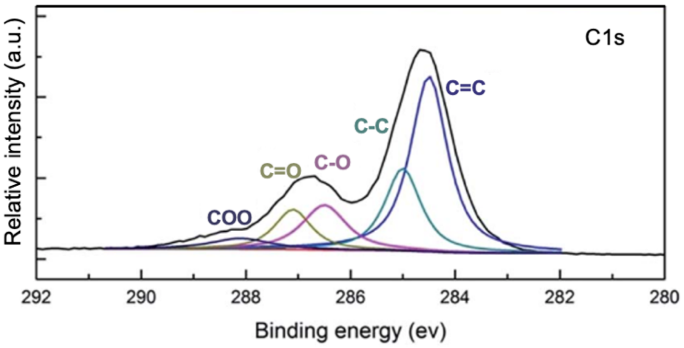

Figure 37: Fitted XPS C 1s core level spectra showing the variation on the BE position due to different oxidation state and environment of the element. [149]

Kinetic energy of photoelectrons is commonly measured by hemispherical electron energy analyzer (HSA) that also provides the possibility to measure angular distribution of photoelectrons (ARPES). Before the photoelectrons enter HSA they are collected by a transfer lens, transferred through an aperture and then focused onto the analyzer entrance slit. HSA consists of two concentric hemispheres, one inside the other. Applying specific potentials to these hemispheres allow only electrons of a given energy (the so-called Pass Energy, PE) to arrive at the detector slits and onto the detectors where they are counted. Electrons of a specific initial kinetic energy are measured by setting voltages of the lens system that focuses the electrons of the required initial energy onto the entrance slit and retards their velocity so that their kinetic energy after passing through the transfer lenses matches the PE of the HSA. HSA usually operates in fixed analyzer transmission (FAT) mode where the PE is kept constant and a spectrum is recorded by scanning over voltages applied to transfer lenses.

Energy resolution in XPS (*ΔE*) depends on the full width half maximum (FWHM) of the photon source, on the line width of the photoelectron emission and the energy resolution of the energy analyzer. XPS instruments using synchrotron light source can easily achieve energy resolution of <0.05 eV.

XPS measurement is usually carried out by first collecting energy spectra over all accessible energies (survey spectra) and then concentrating on particular photoelectron core-level peaks. This ensures that all elements are accounted for during the quantification and that the data are collected in a time-effective manner. XPS spectra are presented as graphs of photoelectron count vs. binding energy. Obtained spectra are analyzed by peak fitting. This process allows to identify the elements present on the surface from their peak positions. A semi-quantitative analysis of the elements present on the sample surface can be performed by measuring the peak areas of specific elemental peaks. Chemical environment and the oxidation state of the elements in the measured compound are responsible for energy shifts from the BE of a pure element. Such shifts therefore allow to identify the chemical state of the elements in the sample by comparison with databases or with the literature.

The XPS measurements were carried out at the BACH beamline of Elettra Synchrotron (Trieste, Italy) using the VG-Scienta R3000 hemispherical electron analyzer. The spectra were collected at a normal emission at a base pressure lower than $3.3 \cdot 10^{-10}$ mbar. Measurements were taken at beam energy 650 eV with a total energy resolution (electron spectrometer and monochromator) of 0.2 eV. Pass energy of the analyzer was set to 50 meV and the acquisition step of 25 meV was used, enabling to detect peak shifts of 50 meV. The binding energy scale was calibrated using Au $4f_{7/2}$ peak (84.0 eV) of a clean gold reference. Fitting of the spectra was performed with KolXPD software [150]. All spectra were fitted with the spin-orbit doublets using Doniach-Sunjic line shape convoluted with a Gaussian function and a Shirley-type background. Lorentzian width, branching ratio and spin-orbit splitting were determined from the clean surface and were kept constant throughout the fitting analysis, while the Gaussian width, intensity and energy position were allowed to vary. Fitting parameters are presented in Table 1. The asymmetry parameters for metallic components were fixed to a non-zero value.

Table 1: Fitting parameters for the analysis of XPS data of Ti/Bi_2Se_3 interface.

	Core level		
	Bi 5d	Se 3d	Ti 2p
Lorentzian width	0.294	0.094	0.095
Spin-orbit splitting	3.067	0.850	5.989
Peak ratio	1.832	1.536	2.326
Asymmetry parameter	0.180	/	0.183

2.6 Low Energy Electron Diffraction

Low Energy Electron Diffraction (LEED) is a standard technique to determine the long-range order, crystal structure and quality of single crystalline sample surfaces. It is based on the diffraction of a monochromatic beam of low energy electrons (20-200 eV) elastically scattered by the materials surface.

Wavelength of low energy electrons corresponds to interatomic distances in materials or less, satisfying the atomic diffraction condition, similar as in the XRD. The mean free path of the low-energy electron is of the order of a few atomic layers. Therefore, only the electrons scattered from the near surface can leave the surface without the loss of energy (i.e. elastically), making LEED a surface sensitive technique.

LEED apparatus is schematically presented in Figure 38. The instrument is typically attached to a UHV apparatus together with other techniques (STM or XPS in our case). Monochromatic electrons are generated from heated W filament and collimated by the electrostatic lens. The beam impinges on the sample surface with normal incidence. The back scattered electrons produced in the interaction between the beam and the sample afterwards propagate towards the detector, which usually consists of three or four hemispherical retarding grids and a phosphorous screen. The grids are used to filter the inelastically scattered electrons, whereas the elastically electrons pass through the grids and cause fluorescence on the screen creating the LEED pattern. LEED pattern can only be detected if sufficient order exists on the surface.

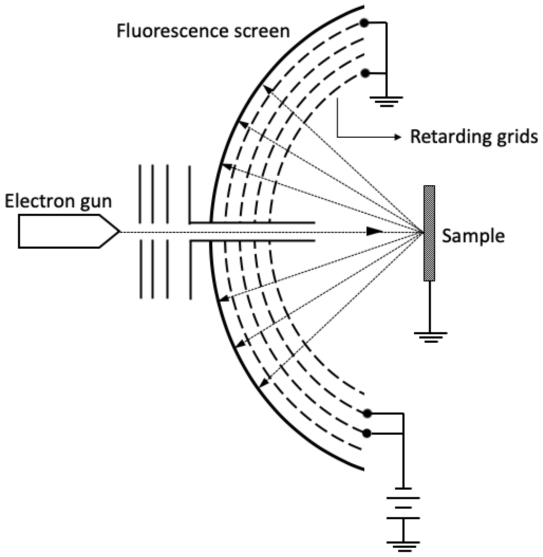

Figure 38: Scheme of the LEED apparatus.

Analysis of the spot positions in the LEED pattern gives information about the symmetry and the 2D periodicity of the surface structure, of the possible reconstructions as well as of the surface quality. Additionally, information about the size, symmetry and rotational alignment of the adsorbate unit cell with respect to the substrate unit cell can be obtained. LEED also allows for a quantitative analysis if the intensities of diffracted beams are recorded as a function of the incident electron beam energy. In this way, I-V curves are generated which by comparison with theoretical curves, may provide accurate information on atomic positions.

2.7 Synthesis and sample preparation techniques

All chemicals were used as received without further purification.

2.7.1 Synthesis of Bi_2Se_3 single crystal

For the synthesis of the Bi_2Se_3 single crystals, the Bridgman method was used. 600 mg of selenium (≥99.999%) and 220 mg of bismuth (99.999%) were put in a quartz ampule and sealed in vacuum. The ampule was placed vertically in an oven at 860 °C for 24 h. Afterward, the temperature was slowly (2 °C/h) reduced to 650 °C. The ampule was kept at this temperature for 7 days and then cooled down to room temperature.

Samples for measurement were obtained by cutting the big single crystal into small flakes that were less than 1 mm thick and had approximate size of 4 × 4 mm (Figure 39).

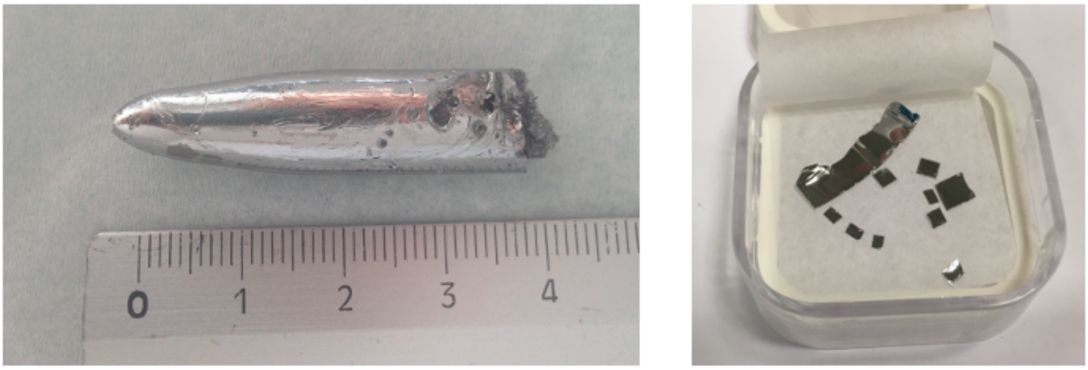

Figure 39: Photo of Bi_2Se_3 single crystal and flakes.

2.7.2 Synthesis of Bi_2Se_3 nanoparticles

The synthesis of Bi_2Se_3 nanoparticles was performed by addition of 160 mg of NaOH (98%) into 20 mL of ethylene glycol (99%). The solution was kept at room temperature and stirred for 2 hours until NaOH was completely dissolved. Afterwards, 400 mg of polyvinylpyrrolidone (PVP, molecular weight (MW) 8.000) was added. Solution was stirred until all PVP dissolved. Then, 233 mg of Bi_2O_3 (99.98%) and 119 mg of Se powder (≥99.5%) was added to the reaction mixture. After 2 hours, the reaction mixture was sealed in a Teflon autoclave and put into an oven at 200 °C for 9 h. When the reaction was completed, the formed solid particles were separated by centrifugation and washed several times with deionized water. The obtained particles have hexagonal shape. Majority of them exhibit a distinct spiral shape in (0001) direction. Such morphology suggests that a screw dislocation occurs during the nucleation process. Particles are 15 – 25 nm thick and measure up to 1 μm in diameter. They are shown in Section 3.4 (Figure 57).

2.7.3 Synthesis of Ag nanoparticles

For the synthesis of Ag nanoparticles, 600 mg of PVP was dissolved in 30 mL of ethylene glycol and heated to 150 °C. In another beaker, a solution of $AgNO_3$ (400 mg; >99.9%) in 23 mL of ethylene glycol was prepared. The solution of $AgNO_3$ was added dropwise in the hot solution of PVP. The prepared mixture was stirred for half an hour and left to slowly cool down. The Ag particles were separated from the liquid by centrifugation and washed with water and acetone. The obtained powder in general consists of 50-160 nm large faceted crystallites. They are shown in Section 3.4 (Figure 58).

2.7.4 Cleaving

Layered structure of Bi_2Se_3 enables to obtain clean (0001) surface of a single crystal by a simple mechanical cleaving technique.

Samples used for SEM and TEM imaging were prepared by cleaving in air using an adhesive tape. Single crystals were first fixed to a sample holder by a carbon tape or silver paste. An adhesive tape was afterwards placed on top of the sample and pulled. The top layers stuck to the adhesive tape leaving behind a clean surface. The process could be repeated several times if the cleave was unsuccessful (i.e. if sample did not cleave or it only partially cleaved). SEM image of cleaved Bi_2Se_3 single crystal is presented in Figure 40.

Mechanical cleaving was used for STM and XPS measurements as well. In these cases, conductive epoxy was used to first fix the sample on a sample holder. A metal or ceramic post was then mounted on top of the sample using the same epoxy. As prepared samples were cleaved *in situ* in the UHV preparation chamber by pushing the post with a wobble stick, consequently removing the first few layers of Bi_2Se_3.

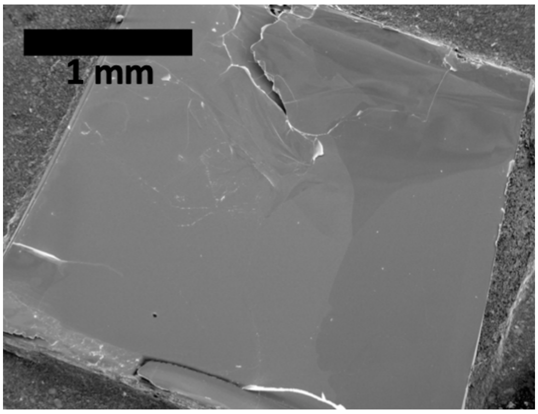

Figure 40: SEM image of cleaved Bi_2Se_3 single crystal.

2.7.5 PECS deposition

Deposition of metals for SEM and TEM measurements were performed using Precision Etching Coating System (PECS, Gatan 682). PECS apparatus allows the deposition of thin films of a variety of materials, usually metals (but also C, Si or others), from vapor phase. The thickness of the deposited film is typically in the range from a few nanometers to 100 nm. The apparatus is used for a variety of application, e.g. to produce a conductive coating over non-conductive samples to be analyzed with electron microscopy.

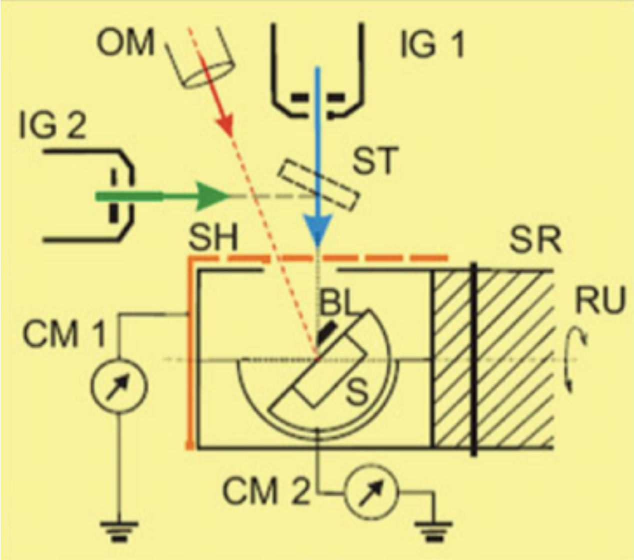

Figure 41: Arrangement of the elements in the Gatan PECS apparatus: IG2 - ion gun for coating, ST – sputter target, S - sample, SR - sample holder, RU - rocking/rotation unit, SH – shutter, CM1 – absorbed shutter ion beam current, CM2 – absorbed sample ion beam current. [151]

Deposition in PECS is performed in vacuum (10^{-4} Pa) and is based on physical vapor deposition technique called sputter coating. Scheme of the interior of the apparatus is presented in Figure 41. Ar^+ ion beam produced in the ion guns (acceleration voltage in the range 3-9 keV) bombard a cathode metal target causing erosion of it. The produced metal atoms and clusters are sputtered from the target in all directions and deposited on the sample surface (anode) lying below the target. To produce a homogenous film, the sample is rotating and rocking during the deposition. The thickness of the film is controlled by a quartz microbalance, enabling stopping of the deposition when the desired nominal thickness is reached (estimated accuracy of the nominal coverage is 10 %).

The deposition rate can be controlled by varying the beam energy. Table 2 gives rates of metal deposition used for sample preparation in this work, as measured by the quartz microbalance. Although the same beam energy and current was used for all Ag deposition, different deposition rates have been recorded, most likely due to the modifications of the ion guns and/or the target in time. We assumed that such change did not drastically affect the resulting morphology of the film.

Table 2: Rates of metal deposition performed in PECS.

Target material	Thickness [nm]	Beam energy [keV]	Rate [Å/s]
Ag (99.98%)	3, 4 and 5	4.8	0.8
	10	4.8	1.5
	>100	4.8	1.3
Ti (>99.6%)	5 to 50	7.0	0.5
Pt (99.95%)	5 to 20	4.8	0.3

Prior to deposition the samples were cleaved in air and then immediately inserted into the PECS apparatus. During the deposition the pressure in the chamber was $2 \cdot 10^{-4}$ Pa. The temperature of the sample cannot be monitored, but effects of heating on the specimens during the deposition have never been reported so far in this system.

2.7.6 TEM cross-section sample preparation

In order to observe the metal/Bi_2Se_3 interface the samples had to be prepared following the standard specimen preparation procedure for a thin film cross-section analysis. The process is presented in Figure 42.

First, two pieces of glass (5×5 mm) were glued together using bicomponent epoxy resin. A stripe of Bi_2Se_3 single crystal was then mounted on top using the same epoxy resin. Curing of the epoxy was performed at 90 °C for 1 h. Bi_2Se_3 surface was afterwards cleaved in air. At this point the sample was placed in the PECS apparatus for the metal deposition. Afterwards, additional two pieces of glass were glued on top of the specimen to obtain a “sandwich” assembly and the sample was again heated to 90 °C for 1h for the epoxy to harden. Sandwich was cut using a diamond wire saw into approximately 750 µm thick slices, which were afterwards shaped into a 3-mm disk, the standard diameter for TEM’s sample holder, with ultrasonic disc cutter (Gatan 601). In order to make the sample suitable for transmission of electrons, the disks were first thinned to 80 µm thickness by polishing with polishing paper on both faces.

In general, the next step in the sample preparation is dimple grinding (sphere-shaped deepening of the area of interest). However, since our samples were very fragile, we decided to skip this step and insert the polished plan-parallel disk into the Precision Ion Polishing System (PIPS, Gatan 691) to perform ion milling process. In this apparatus, two focused Ar ion beams with grazing incidence mill the sample in such a way that a hole results at the disk center. The edges around the hole are sufficiently thin to be used for the TEM measurement. For the ion milling process the ion guns were operating at 5 keV energy producing a current in the range from 65-85 μA. The beams were incident on the disk surfaces at an angle of 2.5° (from bottom) and 4° (from top). When obtaining a hole through the sample, ion milling proceeded at a lower beam energy (3 and 1 keV) until the hole expanded over the interface region. As prepared samples were then used for TEM measurements.

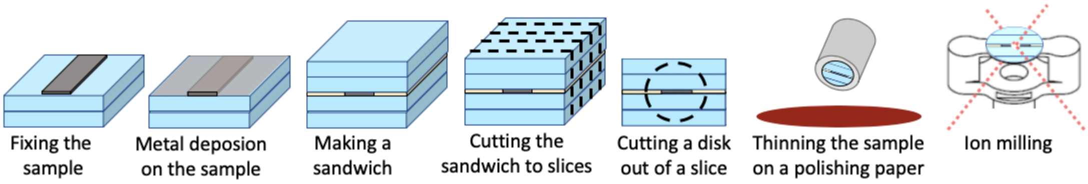

Figure 42: Illustration of the procedure steps for preparation of a cross-section sample for TEM imaging.

3 Ag/Bi_2Se_3 INTERFACE

In this chapter, the study of the interface between Ag and Bi_2Se_3 is presented. The interface was studied in three different systems: single crystal with deposited Ag by physical vapor deposition (PVD), reaction of Bi_2Se_3 nanoparticles (NP) with Ag^+ precursor and a direct contact between Bi_2Se_3 and Ag nanoparticles. Growth mode, morphology and chemical and thermal stability of the interface are described. Combining the experimental data obtained from all studied systems allowed us to identify a chemical reaction happening at the interface.

3.1 Growth mode and morphology of Ag on Bi_2Se_3(0001)

Morphology and growth mode of Ag on Bi_2Se_3 below 1 nm coverage was studied by means of STM. STM measurements were carried out in a UHV chamber at RT using a constant current mode imaging technique. Cleaving of Bi_2Se_3 crystal along the (0001) plane and Ag deposition by resistive evaporation ($I = 0.8$ A, $U = 0.63$ V) was performed *in-situ*. The evaporator was constructed from a basket made of W wire in which a piece of Ag with purity 99.9 % was melted. Coverage of Ag was estimated from the volume of the surface features using Gwyddion software [147].

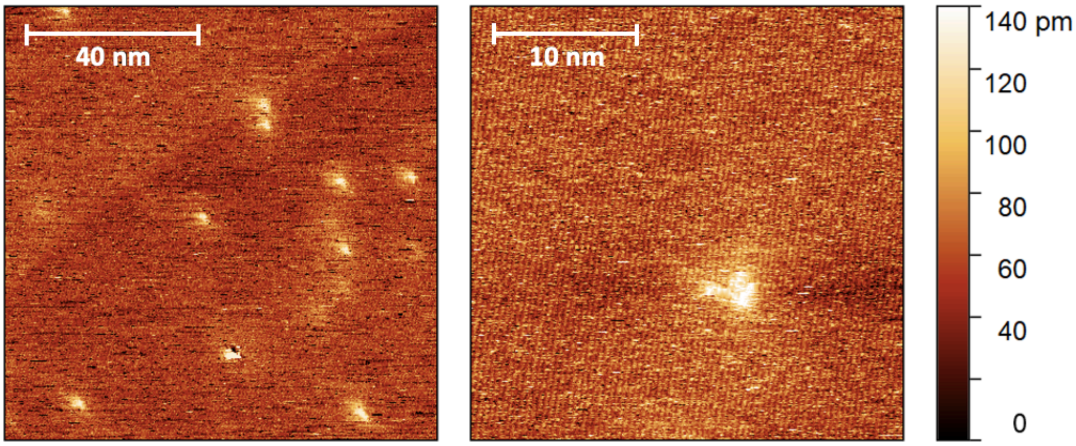

Figure 43: STM images of Bi_2Se_3 surface after cleaving at different magnification.

Figure 43 shows an STM image of the pristine Bi_2Se_3 surface after cleaving. The surface has defects in a form of 130 pm (σ = 30 pm) high protrusions. Density of defects is $(10.3 \pm 1.0) \cdot 10^{10}$ cm^{-2}.

After depositing 0.3 Å (± 0.1 Å) of Ag (equivalent to 0.15 ML) two different features were observed on the surface depending on the bias used. Images of the same area taken consecutively at different biases are presented in Figure 44. Big islands (marked with blue circles in Figure 44) have irregular shape and are located on fixed positions. They are 3.6 nm (σ = 0.6 nm) wide and their apparent height is 3.6 Å (σ = 0.5 Å). These features are well observed at a positive bias but are also visible at a negative bias, with smaller width (2.3 nm with σ = 0.5 nm) and height (2.4 Å with σ = 0.6 Å) and are ascribed to islands made of Ag. Beside these islands, smaller round islands are also observed. They are visible only at a negative bias. Their size and shape are uniform with apparent height of 2.1 Å (σ = 0.3 Å) and 2.5 nm (σ = 0.3 nm) width. In contrary to the big islands, the small ones are not always recognized in subsequent images acquired on the same area (see the green circles in Figure 44), which means that they can move over the surface.

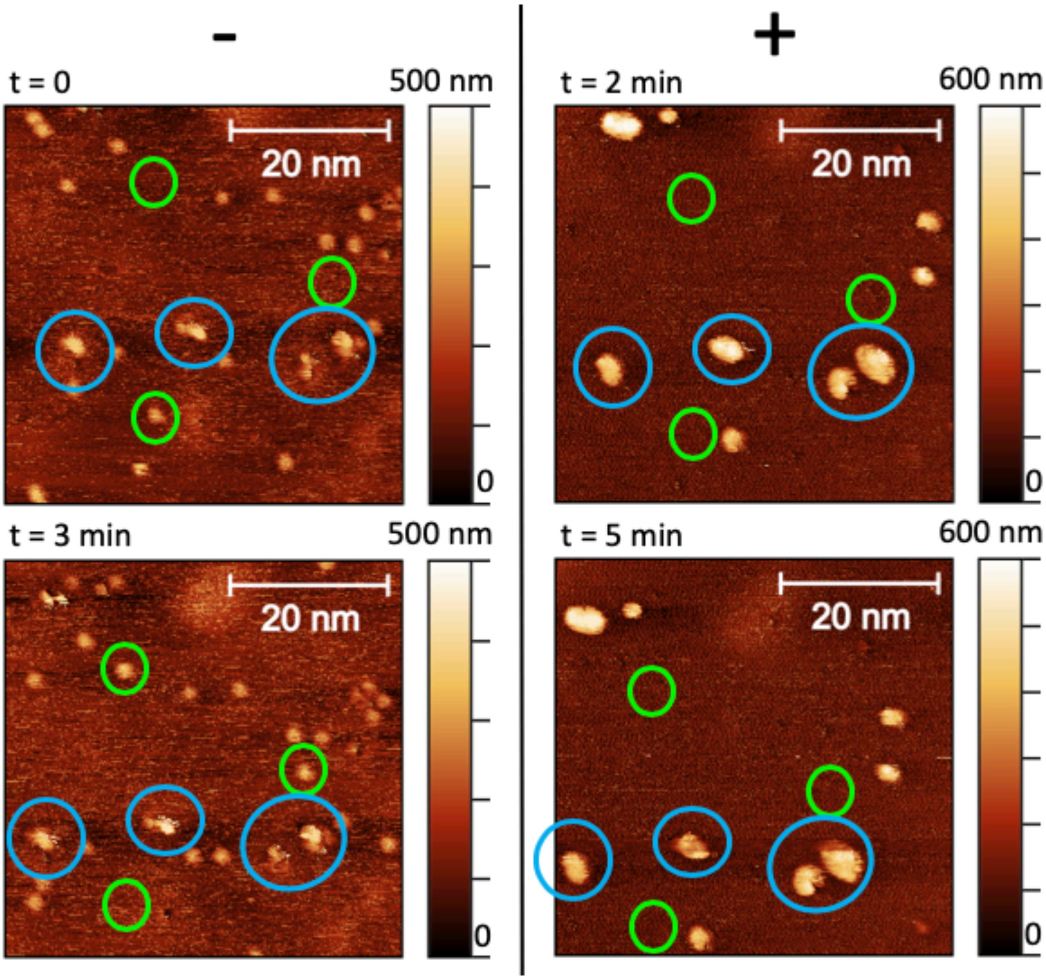

Figure 44: Subsequent STM images of the same region of $Bi_2Se_3(0001)$*, with 0.3 Å of deposited Ag, with applied bias referred to the sample (+/- 0.5 V, I = 0.1 nA). Big islands are marked with the blue circles. Green circles mark the areas of the surface where the small islands are either present or absent due to their diffusion over the surface.*

Growth mode of Ag observed in our experiment appears, at least in the early stages, bimodal. Similar formation of two types of islands with no preferential adsorption site was found for deposited Fe on $Bi_{1.91}Mn_{0.09}Te_3$ [75, 76] and on Bi_2Te_3 [77]. In both cases strong chemical interaction at the interface was concluded. The similarities between these reported data and our observation suggest some chemical interaction is possibly taking place. In this hypothesis, the small islands may either be assigned to Ag islands composed of a few atoms or to the products formed within the interaction between Ag and Bi_2Se_3.

Morphology analysis of Ag/Bi_2Se_3 film at higher Ag coverage has been performed by SEM. Sample preparation included cleaving of Bi_2Se_3 single crystal in air and subsequent immediate insertion into the PECS apparatus where Ag deposition was performed (see Sections 2.7.4 and 2.7.5). Figure 45a presents the flat part of the surface of Bi_2Se_3 (i.e. away from surface steps) with deposited Ag at different nominal coverage. On the flat regions, no features were visible at a nominal coverage < 4 nm. After reaching 4 nm coverage two surface features were observed: very small islands with a size of 7 nm ($\sigma = 2$ nm) and bigger agglomerates with size in the range from 0.3 to 1.0 μm (Figure 46a). The first appeared on the flat regions and were homogenously distributed whereas the latter were found at the surface steps (see Figure 46b). At 5 nm nominal coverage, the density of the big agglomerates increased (see Figures 46bc), while the islands on the flat parts grew to an average size of 15 nm ($\sigma = 4$ nm). After increasing the coverage to nominal 10 nm, about a half of the surface was covered with the Ag islands. At this coverage some agglomerates were observed also on the flat parts (Figure 45a, last on the right), but they were much smaller (average size is 150 nm ($\sigma = 80$ nm)) compared to the big agglomerates still present at the surface steps. The formation of islands, observed also at lower coverage with STM, confirms that at RT Ag atoms have enough energy to diffuse over the crystal surface and form both islands and agglomerates. The surface steps represent nucleation sites where the Ag atoms agglomerate. Au islands on Bi_2Se_3 were also found to preferentially nucleate on the surface steps although their size was the same both on the terraces and steps [79]. Difference in the size of Ag agglomerates and islands suggests on high diffusion of Ag atoms along the steps. This can explain the slightly elongated shape of the agglomerates in the direction of the step (yellow circle in Figure 45b).

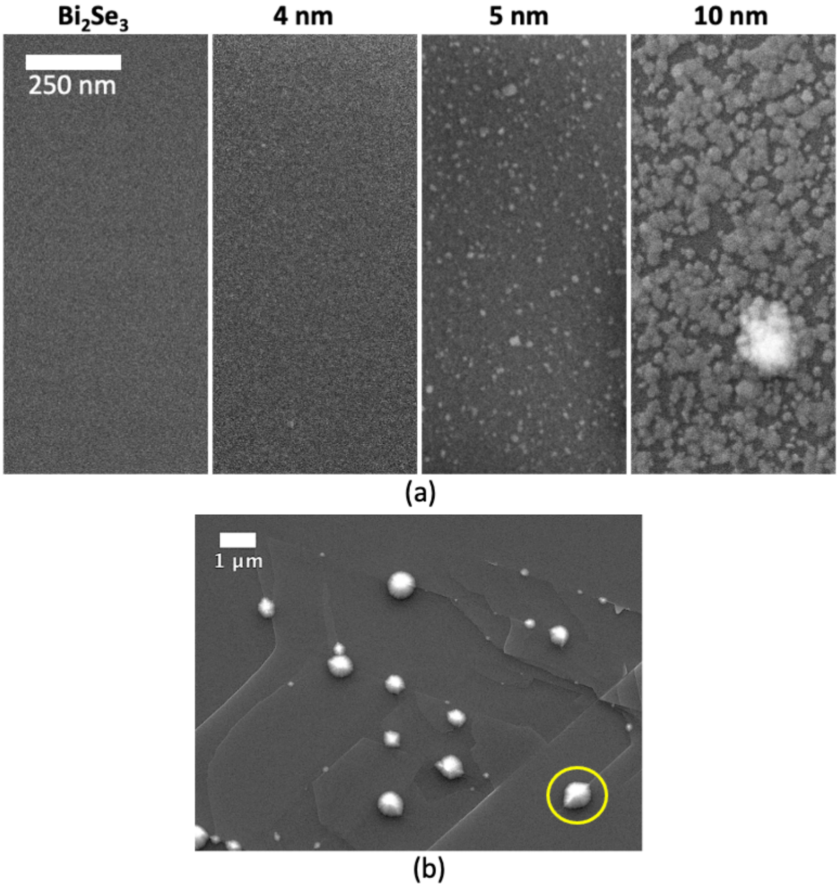

Figure 45: (a) SEM images of the flat surface of Bi_2Se_3 *single crystal without any Ag and with nominal coverage of 4, 5, and 10 nm Ag and (b) Ag agglomerates on the surface steps at 5 nm coverage.*

Based on STM and SEM measurement, the morphology of Ag on Bi_2Se_3 can be described to the Volmer-Weber growth mode, with additional formation of agglomerates at the surface steps.

An experiment where a much thicker film of Ag was deposited was also carried out. Figure 47 shows the surface of Bi_2Se_3 at Ag coverage of >100 nm. The surface is completely covered with Ag film, which is composed of grains with a size in the range 20-70 nm. Features in the shape of conical agglomerates, as observed at lower coverages, are also present. In the flat regions between the agglomerates the measured thickness of the film is 80 nm (σ = 3 nm) (Figure 47c), whereas the height of the agglomerates is between 160 and 440 nm. Conical agglomerates evolved from the big agglomerates that were previously observed on the surface steps and are therefore significantly higher than the film thickness in the flat regions. In Figure 47d - showing a partially detached flake of Bi_2Se_3 – the difference in height between conical agglomerates and the film is evidenced.

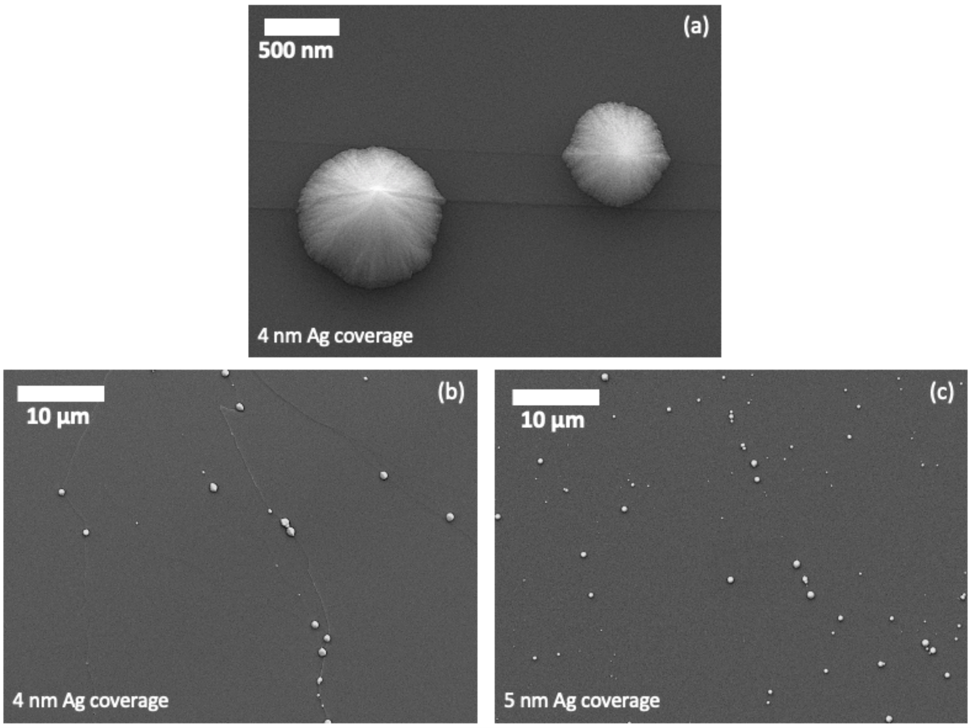

Figure 46: SEM images of big agglomerates (a) and of the Ag/Bi_2Se_3 interface at 4 nm (b) and 5 nm (c) coverage showing the difference in the density of the agglomerates.

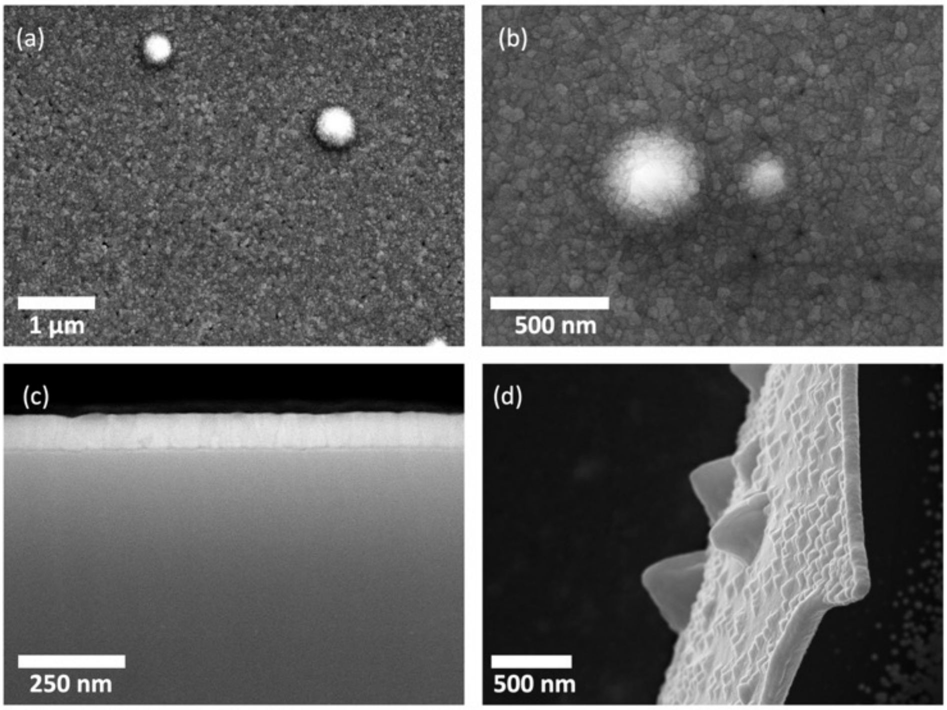

Figure 47: SEM images of nominal >100 nm thick film of Ag on Bi_2Se_3 substrate from top view (a, b) and from cross-section view (c). Image of partially detached flake with visible surface profile (d).

3.2 Stability and evolution of the Ag/ Bi_2Se_3 interface at RT

By imaging the samples after long periods in time – in which the samples were kept at RT in air – the morphology of the deposited Ag islands and agglomerates showed significant variations.

Figure 48a shows a Bi_2Se_3 single crystal with the 10 nm nominal Ag coverage immediately after the deposition and then 3, 8, and 70 days after the deposition. Immediately after the deposition, the surface is densely covered with the islands. Changes in the morphology are clearly visible already after 3 days. The islands shrink in size and more Bi_2Se_3 surface is exposed. After 8 days the islands are significantly reduced in size and after 70 days they are completely absent, even if the surface is not featureless as for clean Bi_2Se_3.Traces of the big agglomerates can still be observed at the steps. The morphology of the big agglomerates changes in time as shown in Figure 48b. Agglomerates shrink in size and their surface is no longer smooth. The center part of the agglomerate, which is the thickest, is still visible, whereas the edge parts are transformed into grainy structure. These results suggest the absorption of Ag into the Bi_2Se_3 crystal.

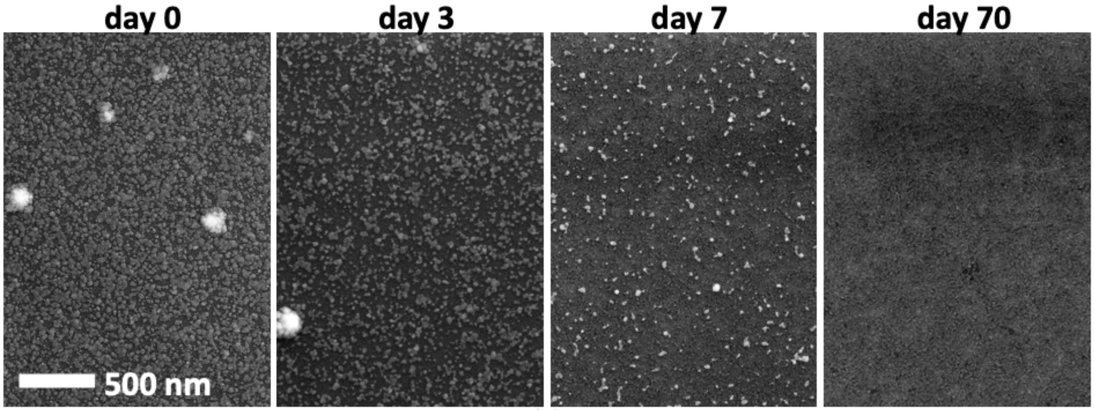

(a)

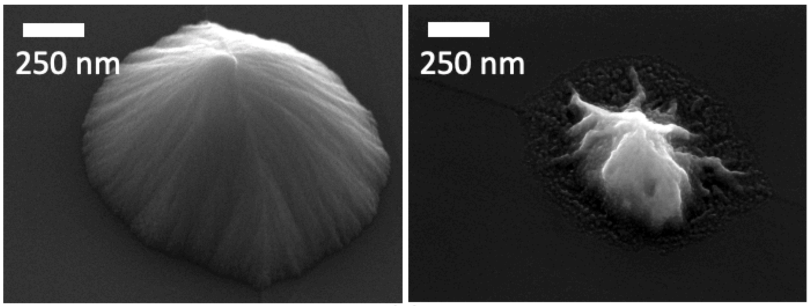

(b)

Figure 48: (a) Evolution of island morphology of Bi_2Se_3 single crystal at 10 nm nominal Ag coverage and (b) morphology of big agglomerates (at 5 nm Ag coverage) immediately after deposition (left) and 3 days after deposition (right).

Evolution of the Ag film in the sub-monolayer regime was observed by STM measurement as presented in Figure 49. Few hours after deposition of 0.3 Å of Ag on Bi_2Se_3 the substrate started to exhibit holes which were not present on the clean substrate nor immediately after the deposition. Holes, of 1.5 Å (σ = 0.4 Å) apparent depth and a lateral size of 3.7 nm (σ = 0.4 nm), are observed both at positive and negative bias, confirming that they are very likely of morphological character. Absorption of Ag into the crystal, observed also in the SEM experiment, probably affects the crystal structure, which as a consequence results in the formation of shallow holes. Due to the significantly smaller amount of deposited Ag, evolution of the surface morphology for 0.3 Å coverage (Figure 49) is observed in a shorter period of time compared to the sample with 10 nm coverage.

In the article of Schlenk *et al.* [74] the deposition of ~0.01 ML of Fe on Bi_2Se_3 was performed and morphology was monitored at different temperatures. At 260 K, triangular depressions were observed on the surface together with a decrease in the density of Fe adatoms and formation of clusters. Increasing the temperature to 370 K significantly promoted the formation of these depressions. Since a chemical reaction was found for the Fe/Bi_2Se_3 interface [76, 112], the described morphological change can be a consequence of the interfacial reaction. Due to the resemblance with the morphology evolution of Ag/Bi_2Se_3 interface, a reaction could explain the formation of holes.

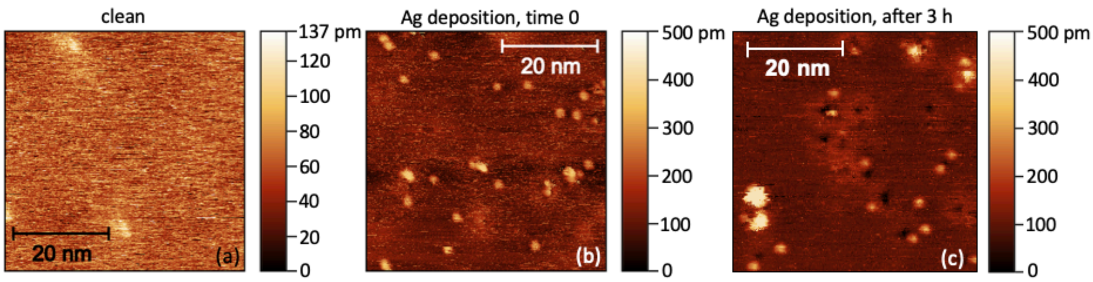

Figure 49: STM images of clean substrate (a) and of Ag/Bi_2Se_3 interface at a coverage of 0.3 Å immediately after the deposition (b) and 3 h after deposition.

Surface evolution on a sample with 0.3 Å Ag coverage was monitored *in-situ* also by LEED within the STM apparatus after the cleaving of pristine sample and after Ag deposition (base pressure was $2 \cdot 10^{-10}$ mbar and the electron energy used was 96.8 eV). Figure 50 shows that upon deposition the LEED pattern is preserved. With time the diffraction spots become less sharp and the background increases. Even if the

Bi_2Se_3 surface is quite inert toward water, oxygen and carbon dioxide in UHV [152, 153], a possible contribution from contamination of the sample surface cannot be excluded to explain the LEED pattern degradation. However, it is likely that the increase in crystallographic disorder of the surface observed by LEED is due to the modifications observed by STM and SEM experiment.

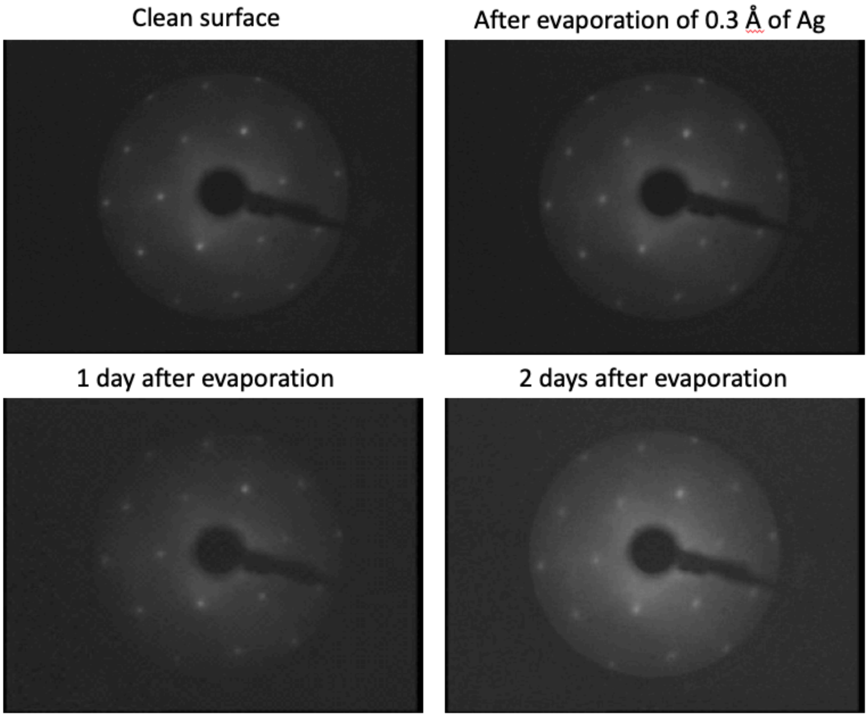

Figure 50: LEED pattern of clean and Ag deposited (0001) surface of Bi_2Se_3 at a coverage of 0.3 Å taken at electron energy of 96.8 eV.

EDX mapping confirms the homogeneous distribution of Ag over the whole surface, with higher signal coming from the large agglomerates at the steps. Elemental analysis of Bi_2Se_3 at Ag coverage of 10 nm was monitored over a longer period of time (same as in the SEM imaging) over an area of 1000 μm^2. Figure 51 shows that the signal intensity for Ag Lα line was decreasing with time and that Ag was detected even when the islands could not be observed any more on the flat surface of Bi_2Se_3. Intensity values were compared by calculating the integral of counts (with subtracted background) for the energy range corresponding to Ag Lα line. This result indicates that the shrinkage of islands and agglomerates observed by SEM is certainly due to the absorption of Ag atoms into the substrate. After 70 days, the decrease in the intensity seems to have stopped at about 70% of the initial signal indicating that the absorption has stopped and Ag atoms are no longer penetrating deeper into the Bi_2Se_3 crystal but are confined near the top surface of the Bi_2Se_3 substrate.

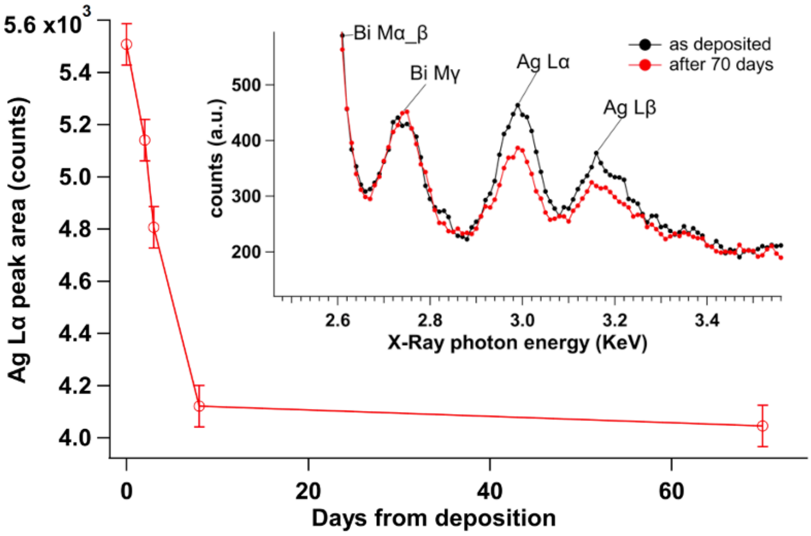

Figure 51: Reduction of the Ag signal intensity in the EDX with time. The error bars are the statistical uncertainty. The inset shows the EDX spectra taken from the Bi_2Se_3 crystal surface with the 10 nm nominal coverage immediately after the deposition and 70 days later.

3.3 Thermal stability

10 nm of Ag was deposited on Bi_2Se_3 substrate by PECS (see Sections 2.7.4 and 2.7.5). The sample was mounted on a heating stage and inserted into the SEM apparatus (base pressure $2.8 \cdot 10^{-4}$ Pa), where the surface has been investigated at different temperatures in a period of a few hours. Measurement started at 25 °C (RT) and continued till 200 °C. Figure 52 shows the thermal evolution of the interface. Below 100 °C a slight decrease in the Ag coverage (within the error) was observed. In general, the flat surface was covered with islands and big agglomerates were located on the surface steps. At 100 °C the clusters started to diffuse into the crystal and with increasing temperature the process was accelerated. The modification of the surface was observed as shrinking of islands and formation of cavities, which appear as darker spots. Figure 53 shows the change in the total surface area covered with Ag islands with increasing temperature. In each point the value is the average of the covered area measured on 5 images (error bars are the standard deviation). Increase in absorption was also promoted by the beam; therefore, it was necessary to make images on surfaces that were not imaged before to get reliable results. At 150 °C most of the islands were absorbed within the substrate. Increasing the temperature to 200 °C further modified

the surface morphology. The islands completely vanished and the surface exhibited 10-50 nm wide holes as shown in Figure 52.

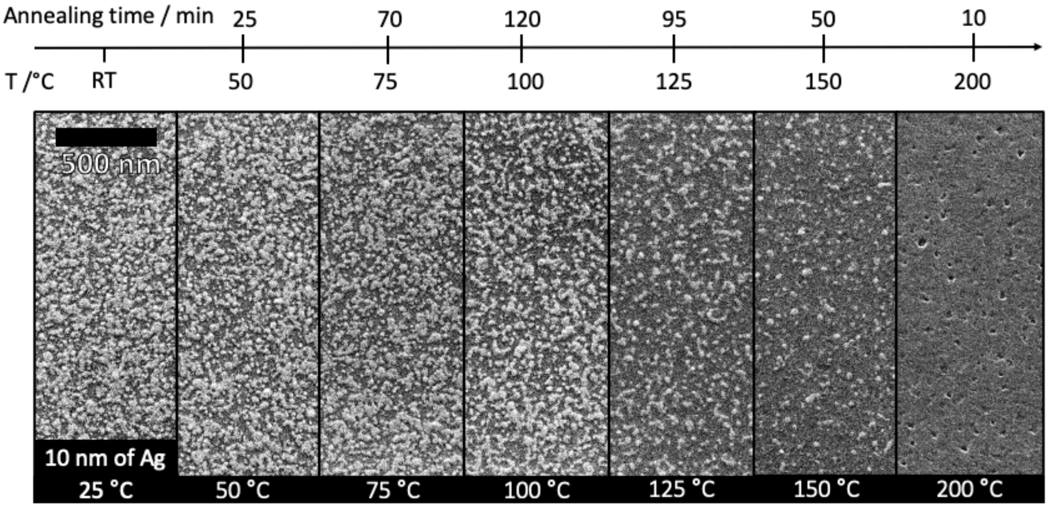

Figure 52: Thermal evolution of the flat regions of Ag/Bi_2Se_3 interface at the coverage of 10 nm in vacuum.

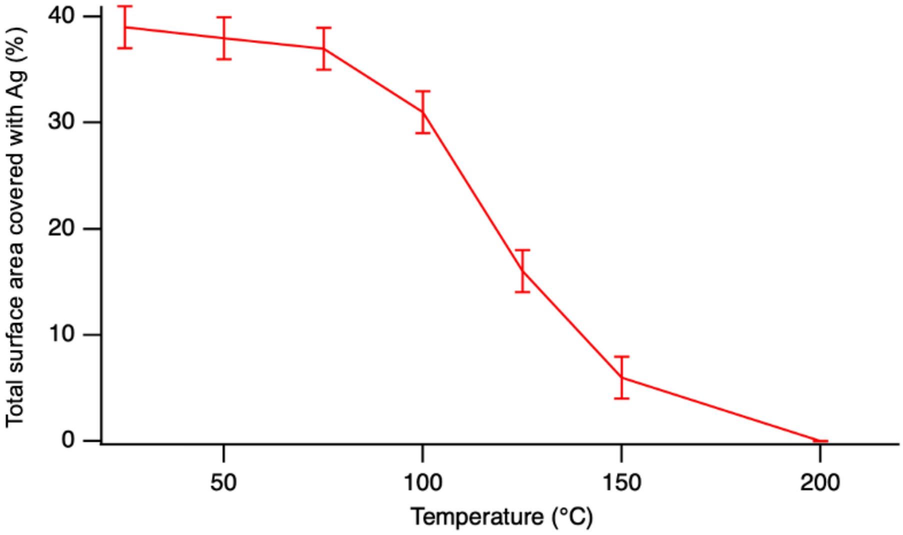

Figure 53: Graph of total surface area covered with Ag islands with increasing temperature during the annealing experiment. Each point corresponds to a temperature step in Figure 51.

The big agglomerates were more stable and exhibited almost no morphology change up to 150 °C. At this temperature only slight morphology change could be seen on the edges of the agglomerates, where the thickness of the agglomerates is the smallest (see Figure 54).

However, when the temperature reached a value between 150 and 200 °C (the exact temperature was not determined due to a 50 °C step increase) a drastic change happened. Big agglomerates completely decomposed leaving behind “rose” shaped features.

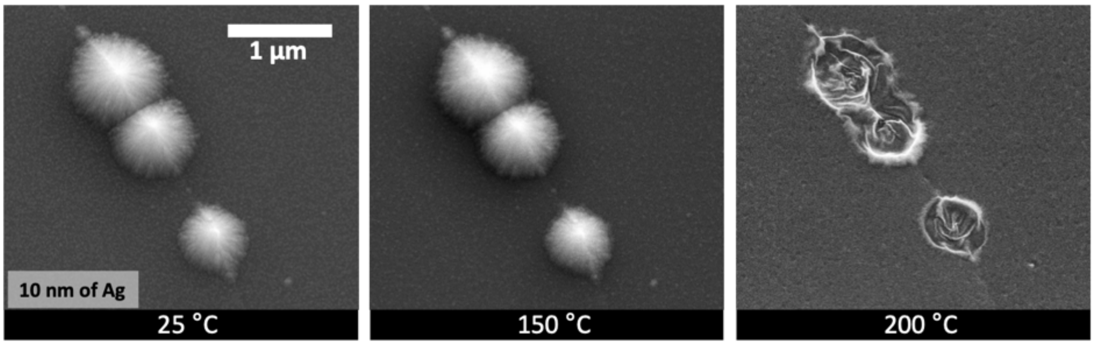

Figure 54: Thermal evolution of the big agglomerates of Ag/Bi_2Se_3 interface at the coverage of 10 nm in vacuum.

Evolution of surface morphology by heating in vacuum was similar to the evolution of the interface at RT in air with time, but with some differences. At ambient conditions the flat surface also exhibited shrinkage of islands and formation of holes (see Figure 55), however, the big agglomerates (after 70 days) did not reach the point where they would be completely decomposed. The differences between the two resulting morphologies are due to the kinetics of the process at different temperatures. Pressure and the presence/absence of ambient gasses can also be affecting the resulting morphology, but the absence of atmosphere (as for the experiment with heating stage) does not prevent Ag absorption into the crystal to occur.

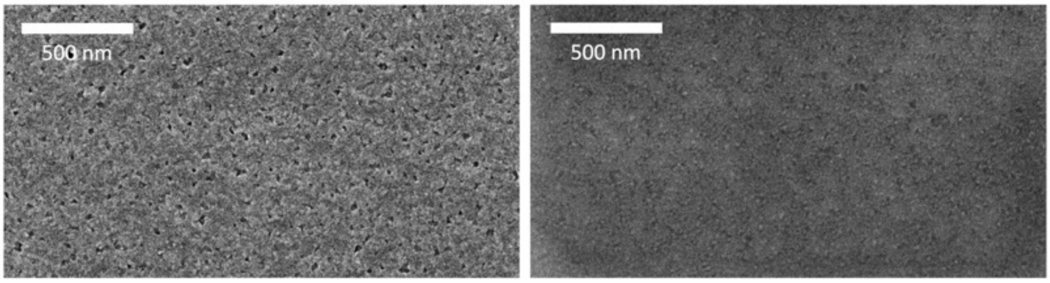

Figure 55: SEM image of the Bi_2Se_3 surface at a coverage of 10 nm of Ag after annealing to 200 °C (left) and after the sample being kept at ambient conditions for 70 days (right).

3.4 Solid-state reaction

The evolution of the Ag/Bi_2Se_3 interface, as studied by STM and SEM, suggests on a chemical reaction taking place. Since the occurrence of chemical reactions in the bulk is determined by thermodynamic phase equilibrium and does not depend on the size or morphology of the initial phases (contrary to their kinetics), we can study the reactions better in systems where higher contact surface area between reactants can be provided. For this reason, we carried out an experiment using Bi_2Se_3 and Ag in a form of nanopowders.

Nanopowders were obtained by drying suspensions of Ag and Bi_2Se_3 NPs at 90°C (synthesis is described in Sections 2.7.2 and 2.7.3). Both nanopowders were characterized by XRD and SEM. Figure 56 presents diffraction patterns of both compounds. The measurements show that the synthesized products are pure Bi_2Se_3 or Ag with no traces of secondary phases.

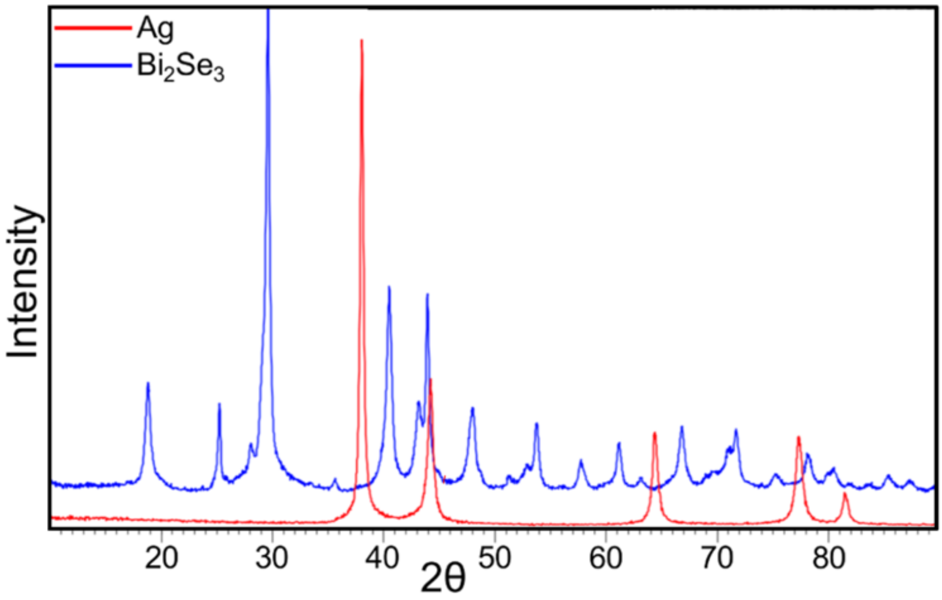

Figure 56: XRD pattern of Bi_2Se_3 nanoparticles and Ag nanoparticles. The diffraction lines fully correspond to 9011965 and 9008459 PDF reference patterns, respectively. The XRD patterns show no traces of secondary phases.

SEM imaging of synthesized Bi_2Se_3, presented in Figure 57, shows hexagonally structured nanoparticles. During the nucleation of nanoparticles screw dislocation in (0001) direction, responsible for the resulting morphology of nanoparticles, occurs. NPs are approximately 20 nm thick and measure up to 1 μm in diameter. Particles are found individually or as agglomerates (Figure 57b).

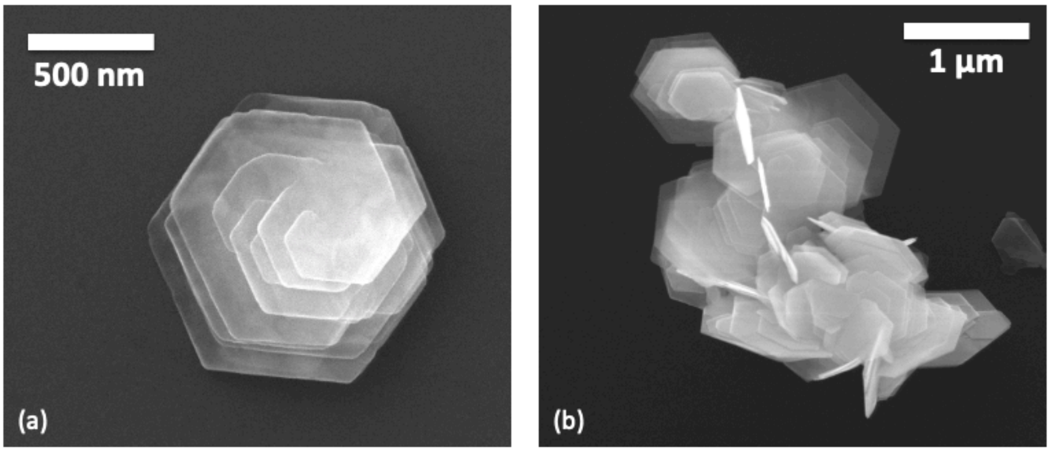

Figure 57: SEM images of Bi_2Se_3 NPs showing individual spiral grown NP (a) and an agglomerate where perpendicular ingrowth of NPs is visible (b).

SEM images of Ag nanopowder are shown in Figure 58. The powder in general consists of 100 nm (σ = 20 nm; size range 50-160 nm) large faceted crystallites.

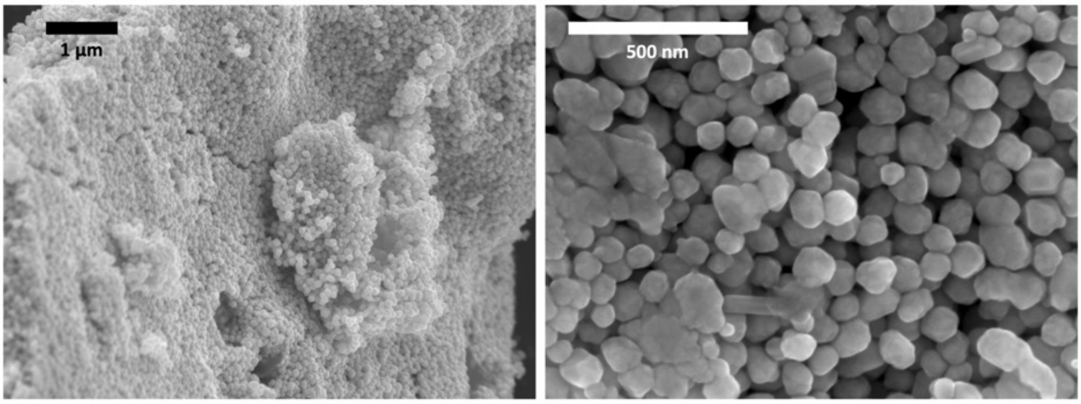

Figure 58: SEM images of Ag nanoparticles at lower (right) and higher (left) magnification.

In the experiment, powders of Ag and Bi_2Se_3 with a molar ratio Ag:Bi_2Se_3 = 2:1 were mixed together in a mortar to form a homogeneous system and to maximize the surface area. The first XRD analysis was taken right after the mixing. Afterward, the system was kept fixed on a sample holder at ambient conditions and was analyzed daily to monitor any phase changes. By keeping the sample fixed and without any manipulation we excluded possible factors influencing the measurement coming from handling the sample. In this way, we were also not accelerating the reaction by putting the fresh surface into contact. Such method is also beneficial from analytical point of view since the comparison of the measurement results is more reliable. Figure 59 shows the evolution of the phase composition with time. XRD patterns taken right after the mixing and then 7, 14 and 21 days later were normalized to the highest peak and are shown as overlapping. By following the changes in diffraction patterns, it was possible to determine which phases are evolving inside the Ag-Bi_2Se_3 mixture. The XRD pattern at zero time shows diffraction lines at $2\theta = 30.6°$, 33.4°, and 34.7° which do not belong neither to Bi_2Se_3 nor to Ag phase. This means that the phase change had already occurred during the homogenization process when the powders were ground together. With time, intensities of these new peaks increased, which allowed us to identify the new phases as $AgBiSe_2$ and Ag_2Se. Results prove a solid-state reaction taking place at the interface between Ag and Bi_2Se_3.

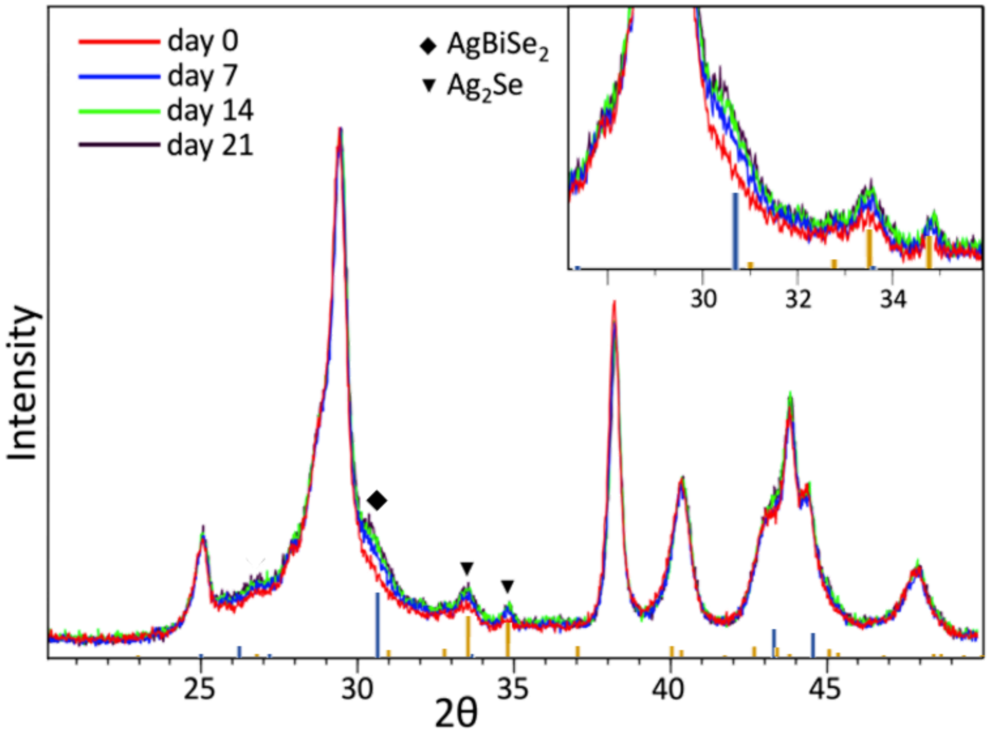

Figure 59: XRD patterns of the mixture of Bi_2Se_3 and Ag powders at room temperature indicating a phase evolution with the inset showing a close-up of the area of interest. The blue reference pattern refers to $AgBiSe_2$ (PDF Reference No.: 9011023) and the yellow one to Ag_2Se (PDF Reference No.: 2230972).

3.5 Reaction from Ag^+ precursor

Chemical deposition of a metal in suspension is a very common method for the preparation of nanoclusters on particles (e.g., in catalysis). Two experimental studies where Ag^+ precursor was used for the deposition of Ag on nanoribbons [88] and nanoflakes [124] of Bi_2Se_3 were reported. Therefore, we decided to carry out such experiment and additionally support the findings from our previous experiments, where single crystal and dry nanopowder of Bi_2Se_3 were used and compare them with the reported data.

30 mg of $AgNO_3$ were added into the suspension of Bi_2Se_3 NP (for the synthesis see Section 2.7.2) in ethylene glycol. In this case ethylene glycol has a role of the solvent as well as of a reducing agent, transforming Ag^+ ions into metallic Ag. The mixture was stirred at room temperature for 20 hours. Afterwards it was washed several times with deionized water and dried to obtain a dry powder.

The obtained product was first characterized by XRD. Comparison of XRD patterns from pristine Bi_2Se_3 NPs (red curve) and from the product obtained within the reaction of Bi_2Se_3 NPs with Ag^+ precursor (blue curve) is presented in Figure 60. The XRD pattern of the dry powder from the reaction of Bi_2Se_3 NPs and Ag^+ precursor shows no diffraction lines of the metallic Ag. Instead, it clearly shows the occurrence of diffraction patterns, which were observed also in the mixture of dry powders of Ag and Bi_2Se_3 and were ascribed to Ag_2Se and $AgBiSe_2$ phases. Compared to the solid-state reaction experiment, here the changes in the XRD pattern are much more pronounced, therefore, we can ascribe the new formed phases with more accuracy. The biggest difference in the XRD pattern before and after the deposition is in the peak positioned at 30.6°, which belongs to $AgBiSe_2$ phase. In experiments where the deposition time was shorter (e.g. 2 h) the reaction did not evolve enough to produce significant amounts of the products. In such cases, only the highest peak belonging to $AgBiSe_2$ phase was detected in the XRD pattern due to the low intensity of Ag_2Se phase.

No change in the position or of the Bi_2Se_3 diffraction lines was observed which is inconsistent with the claim of Koski *et al.* [88], who reported on the intercalation process taking place. If this was true, it would result in the expansion of the Bi_2Se_3 unit cell and consequently shifted diffraction peaks. Due to the intercalated species new diffraction lines would also appear changing the overall profile of the pattern. In our study, these changes were not observed.

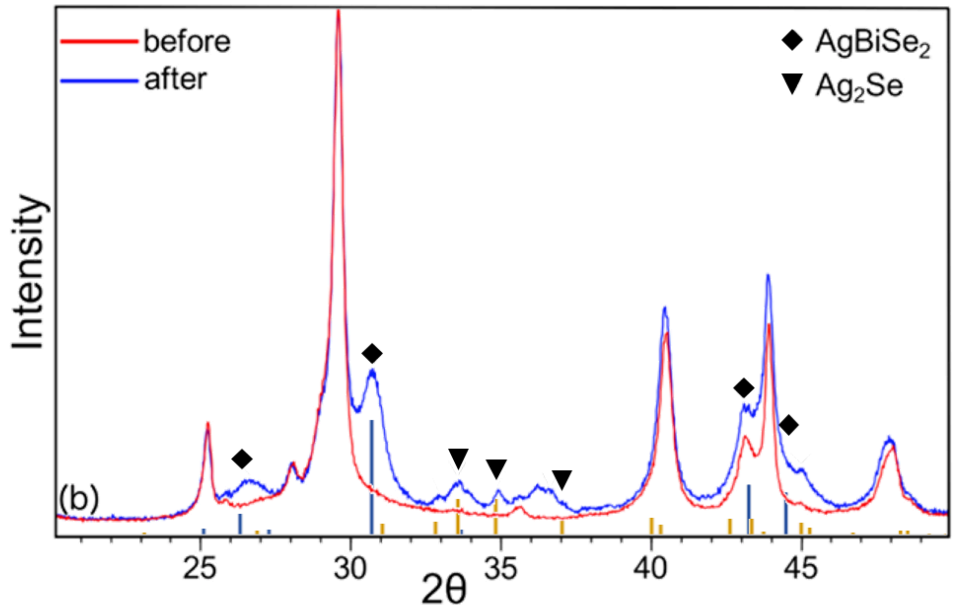

Figure 60: Pure Bi_2Se_3 (red line) and product after chemical deposition of Ag in suspension (blue line). Not assigned peaks belong to Bi_2Se_3. The blue reference pattern refers to $AgBiSe_2$ (PDF Reference No.: 9011023) and the yellow one to Ag_2Se (PDF Reference No.: 2230972).

The obtained product from the reaction of Bi_2Se_3 NPs with Ag^+ precursor was characterized also by electron microscopy and EDX spectroscopy. SEM imaging showed the presence of Bi_2Se_3 NPs with distinct bubbly features on the surface (Figure 61a) and separated particles which differ in morphology from pristine Bi_2Se_3 NPs (Figure 61b). EDX mapping together with XRD analysis results enabled us to recognize the first as the $AgBiSe_2$ phase and the latter as Ag_2Se. EDX mapping showing the areas with these phases is show in Figure 62. The solid circle marks the part of the sample where significant signal for Bi, Se and Ag is detected. This phase was therefore assigned to $AgBiSe_2$. The dashed circle marks the area where the signal of Bi is negligible compared to the signals of Ag and Se, identifying it as Ag_2Se.

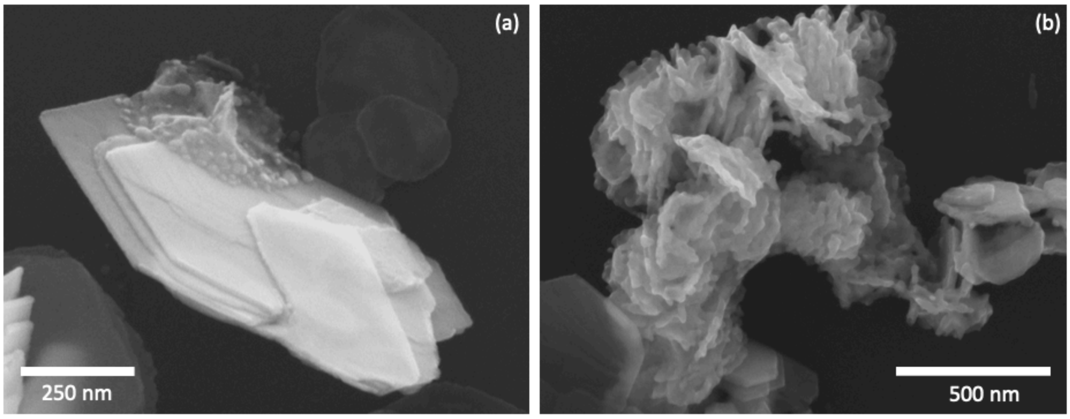

Figure 61: SEM image of (a) Bi_2Se_3 nanoparticle with $AgBiSe_2$ phase on top and (b) of Ag_2Se NPs.

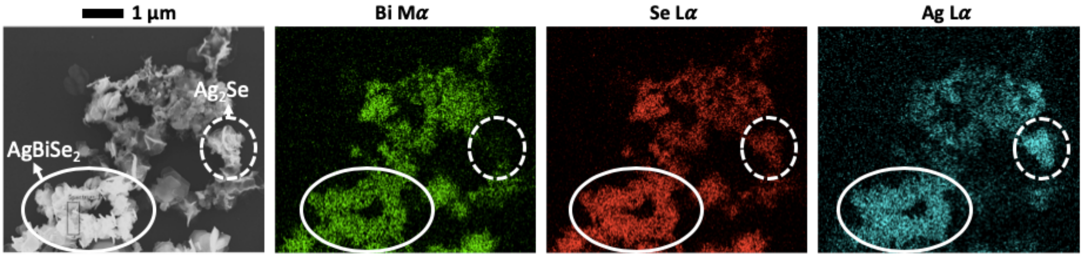

Figure 62: EDX mapping of the product after reaction of Bi_2Se_3 nanoparticles with Ag^+ precursor onto showing maps of Bi, Se and Ag made by SEM.

The data collected from all experiments indicates that a chemical reaction is taking place, which was not considered in any previously reported study on Ag/Bi_2Se_3 interface [88, 89, 124]. We proposed the following reaction occurring at the interface:

$$3Ag + Bi_2Se_3 \rightarrow AgBiSe_2 + Ag_2Se + Bi$$

Since $AgBiSe_2$ phase was always found on top of Bi_2Se_3 and Ag_2Se phase was found separately, it is possible that the reaction happens in two steps.

1st step: $$3Ag + 2Bi_2Se_3 \rightarrow 3AgBiSe_2 + Bi$$

2nd step: $$AgBiSe_2 + 3Ag \rightarrow 2Ag_2Se + Bi$$

More research of the reaction equilibrium and mechanism should be carried out in order to clearly determine how the reaction evolves. Additionally, we did not observe the disappearance of $AgBiSe_2$ phase to prove the two-step reaction in any of our experiments and since $AgBiSe_2$ and Ag_2Se phase were always detected together the one step reaction allows for more general description of the reaction.

However, regardless of the reaction evolution, Bi phase necessarily has to be produced in order to form any of the two phases and to equalize the reaction, but it was not detected by XRD or SEM EDX.

By performing EDX mapping analysis using TEM operating in STEM mode, which allows for better lateral resolution compared to SEM, we detected particles with the size of about 100 nm that were rich in Bi with absent Ag and Se signals, which were assigned to Bi phase (see the white circles in Figure 63). This result supports the hypothesized reaction.

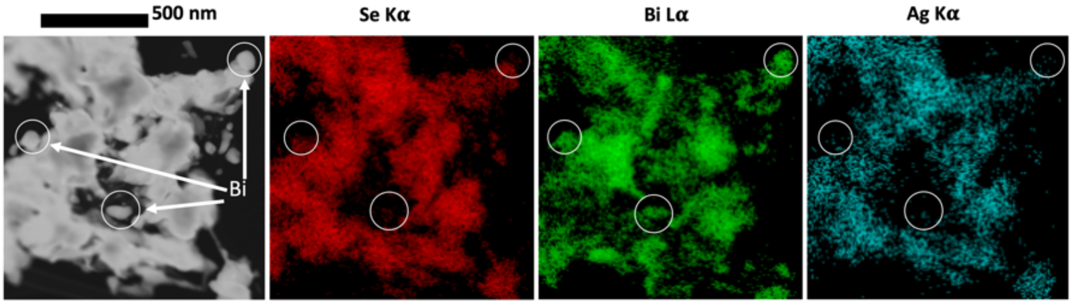

Figure 63: EDX mapping of the product after reaction of Bi_2Se_3 nanoparticles with Ag^+ precursor showing maps of Se, Bi, and Ag made by STEM.

3.6 Summary and conclusion

The interface between Ag and Bi_2Se_3 topological insulator was studied within three different systems.

1) Ag was deposited on a single crystal of Bi_2Se_3 by means of PVD, in order to characterize the metal growth and morphology of the interface. At sub nanometer coverage the morphology resulted in the formation of two types of islands, which were distinguished by their size, mobility and appearance at +/− bias. Deposition with Ag coverage in the nanometer range and subsequent SEM imaging showed formation of islands on the flat part of the crystal and big agglomerates (0.3-1 µm) at the surface steps. Morphology was observed to evolve in the timescale of hours or days (depending of the film thickness) with the formation of holes (observed by STM) and defects (observed by SEM), due to the absorption of Ag within the crystal. The process was confirmed by EDX analysis. Results indicate thermodynamic instability of the interface already at room temperature.

2) Ag and Bi_2Se_3 nanopowders were mixed and the evolution of the structure has been followed by XRD. Immediately after the mixing two additional phases were present: Ag_2Se and $AgBiSe_2$. Their intensity in the XRD diffraction pattern increased with time in the timescale of days.
3) The product of the reaction in the suspension of Bi_2Se_3 NPs with Ag^+ precursor was characterized by XRD, SEM and EDX. In the reaction product Ag is not present in the metallic form, whereas Ag_2Se and $AgBiSe_2$ peaks in the diffractogram are clearly observed. Microscopy combined with microanalysis allowed the recognition of these resulting phases, together with the metallic Bi, which is the expected product of the reaction.

Results indicate that the interface between Bi_2Se_3 and Ag in not stable at RT. From experiments using NPs of Bi_2Se_3 and Ag it was possible to determine that in such system the following solid-state redox reaction takes place:

$$3Ag + Bi_2Se_3 \rightarrow AgBiSe_2 + Ag_2Se + Bi$$

Morphology evolution compatible with the occurring of a reaction has been observed for a thin film of Ag deposited on a Bi_2Se_3 single crystal. For nanometer Ag coverage the SEM and EDX analysis showed that the Ag atoms diffuse into the Bi_2Se_3 crystal during the reaction and stop when the interface layer becomes too thick for the non-reacted species to diffuse through it and further react. In contrary to the reported studies [88, 89, 124] we had no evidences of Ag intercalation within Bi_2Se_3 crystal.

At RT and at ambient pressure the kinetics of the reaction are on the timescale of days. The reaction is accelerated with temperature, becoming very fast (timescale of < 1 min) at a temperature between 150 and 200 °C. Absence of ambient atmosphere does not prevent the reaction to occur.

4 Ti/Bi_2Se_3 INTERFACE

In this chapter, the morphological and chemical characterization of the interface between Ti and Bi_2Se_3 is presented. Measurements performed by STM, LEED, SEM, TEM, EDX and XPS enabled the detection of a chemical interaction at the interface resulting in the formation of interfacial layer. By using the elemental and chemically sensitive techniques we were able to locate and describe the newly formed interface phases.

4.1 Growth-mode and surface morphology of Ti film deposited onto Bi_2Se_3(0001)

The study of the growth mode and morphology of Ti on Bi_2Se_3 at ultra-low coverage has been performed by STM. Ti was deposited using e-beam evaporator and the evaporation was performed in a UHV chamber at RT and at a base pressure of $2\cdot10^{-10}$ mbar. Voltage and current parameters of the filament were controlled to obtain the constant value of the flux for each evaporation. Ti nominal coverage was evaluated *ex post* by comparison of the intensity of the EDX Ti peak between samples used within the STM and XPS experiments (for calibration in the XPS, see Section 4.2). 1 Å coverage corresponds to 0.43 ML of Ti. The best imaging conditions were found at small tunneling currents and negative bias referred to the sample. If positive bias was applied the resolution was immediately lost. At a very low Ti nominal coverage (0.03 Å) the Bi_2Se_3 surface exhibits some defects that are not present on the clean surface (see Figure 64). Majority of them are in the form of triangular depressions, while other appear as bright features. Two types of bright features are distinguished based on their size. The small ones have apparent height of 2.2 Å (σ = 0.5 Å) and are assigned to single atoms on the surface. The bigger ones are much more sparsely distributed over the surface. They have larger average apparent height of 4.1 Å (σ = 0.8 Å) and are assigned to clusters comprised of a few atoms. Both bright features were not diffusing over the surface indicating strong interaction with the substrate. Line-scans over the features are presented in Figure 65. Average width of the small bright features is 0.4 nm (σ = 0.1 nm) and of the big ones 0.8 nm (σ = 0.2 nm))

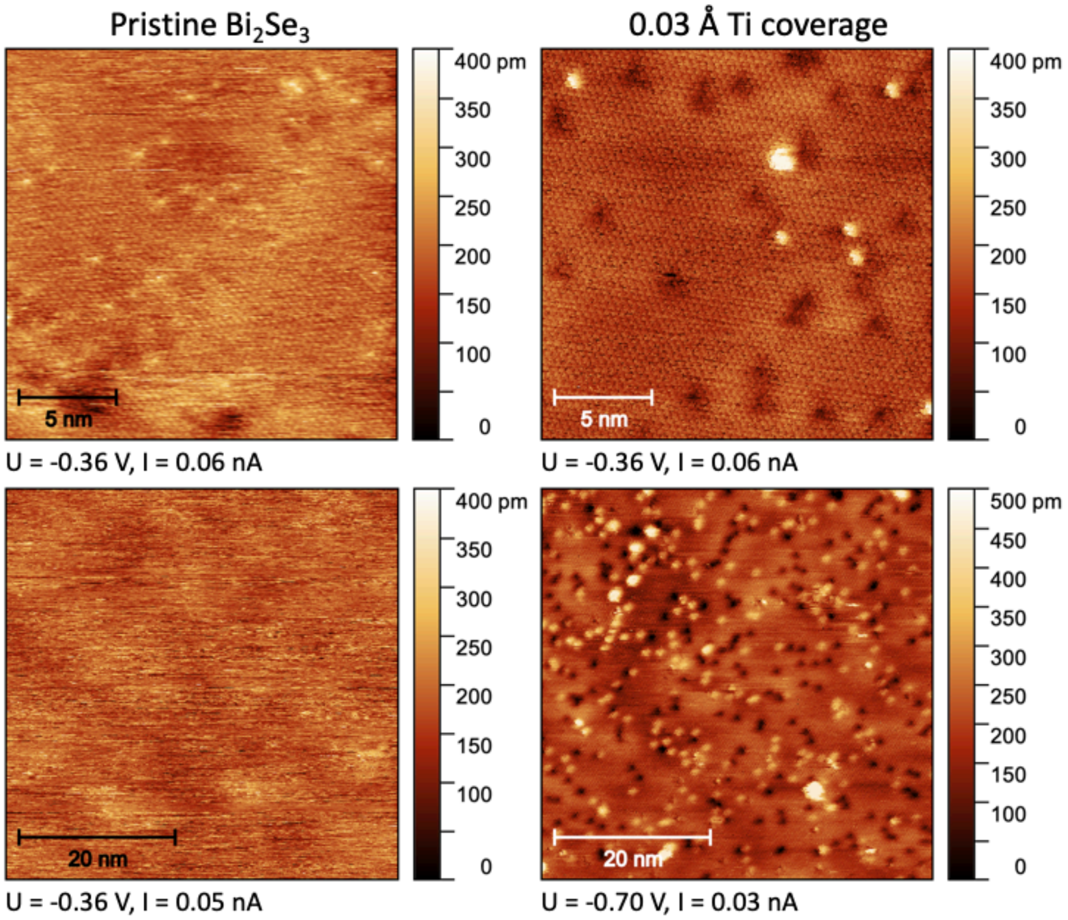

Figure 64: STM images of the pristine substrate (left) and Ti/Bi_2Se_3 interface at the coverage of 0.03 Å (right) at different magnification.

Triangular depressions have apparent depth of 1.5 Å (σ = 0.3 Å). Atomic resolution images show that the depression area can either appear as a hole (not all atoms are visible) or as a feature where all surface atoms can be seen, i.e. this feature is not due to a missing atom at the surface. In any case the depressions are very likely a consequence of a subsurface defect and can be ascribed to substitutional Bi_{Ti} defect [74, 154-156].

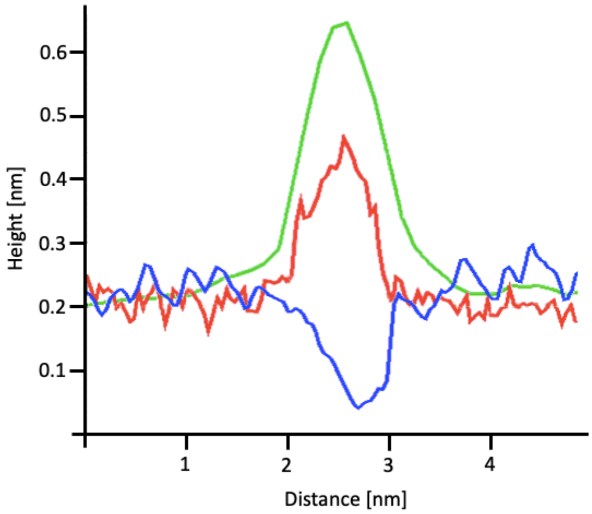

Figure 65: Linescan over the small bright features (red), big bright features (green) and triangular depression (blue).

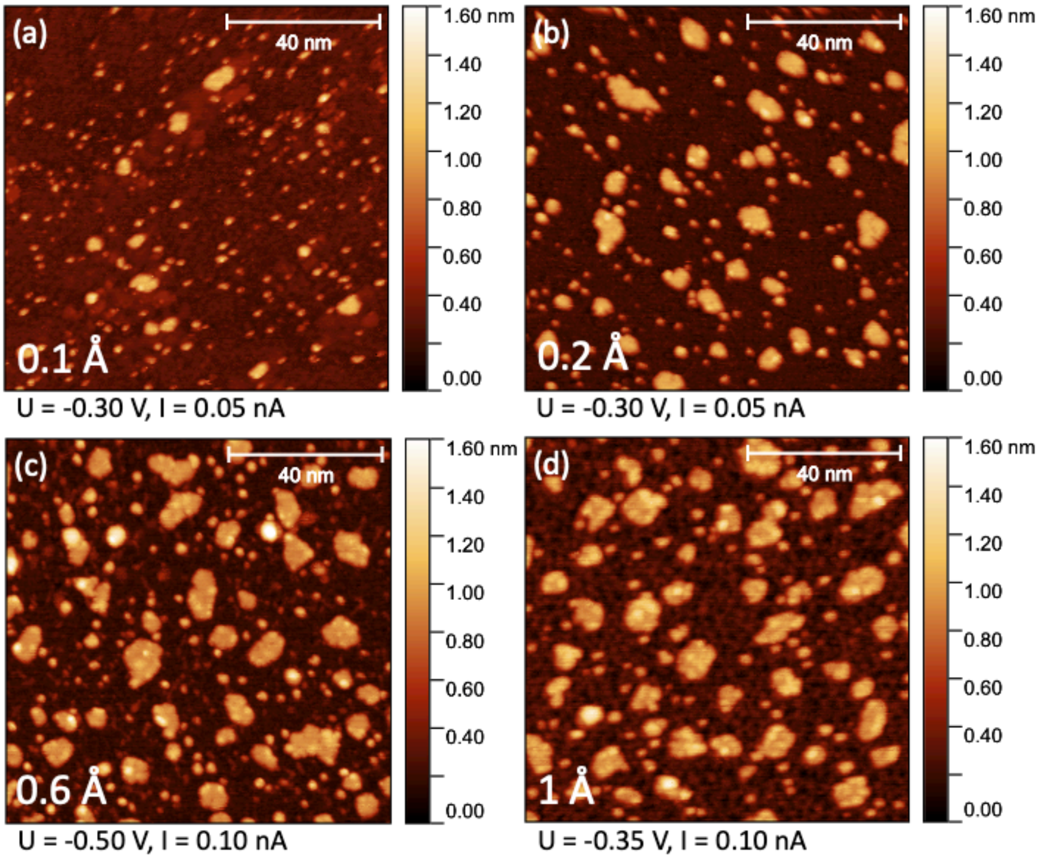

Figure 66: STM images of Bi_2Se_3 substrate at different Ti coverages showing the evolution of surface morphology with increasing coverage.

Further Ti deposition (0.1 Å), presented in Figure 66a, results in an island growth mode, where two types of the islands with different sizes are distinguished. At 0.2 Å coverage (Figure 66b), the size of both types of islands increases, more pronouncedly for the bigger ones, which measure on average 5 nm (σ = 2 nm) in lateral size whereas the lateral size of the small ones is 1.6 nm (σ = 0.5 nm). Figure 67 shows the size distribution of the islands. Areas of islands were determined, and the equivalent disk diameter was calculated for comparison since the big islands have irregular shape. Additionally, at this coverage the formation of new clusters on the top of the already existing big islands begins to be observable, with apparent height of 3.1 Å (σ = 0.8 Å) with respect to the island top surface. The increase in lateral dimension of islands (see Figure 67) and formation of clusters continues with increasing coverage. Line-profiles over the islands at a coverage of 0.5 Å are presented in Figure 68. The big islands, that show a flat top surface, have an apparent height of 8.2 Å and a narrow height distribution (σ = 0.4 Å). The apparent height of the small islands is 7 Å (σ = 1 Å).

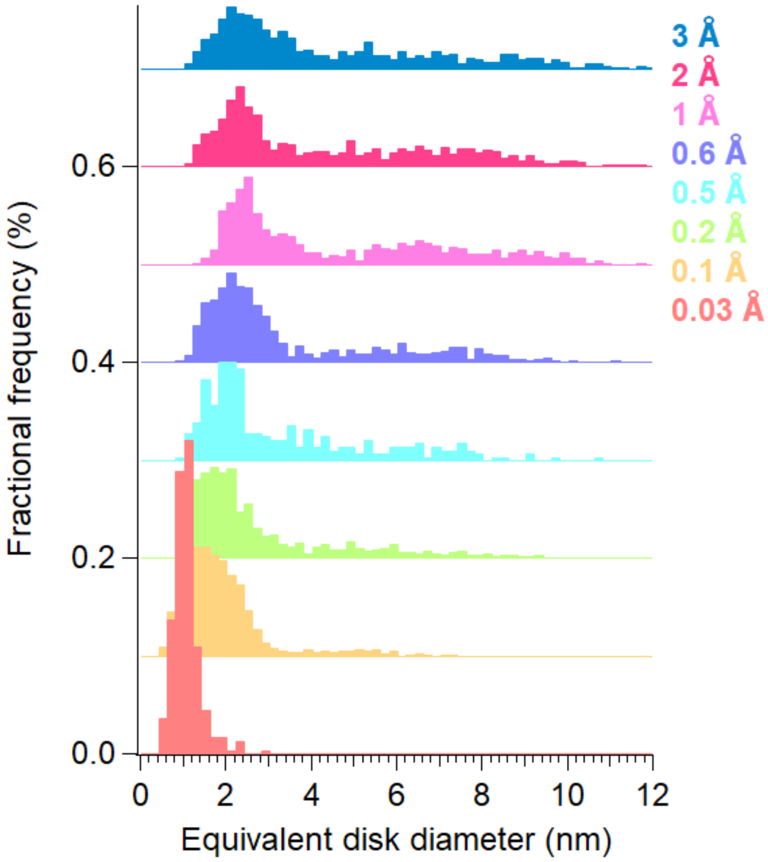

Figure 67: Lateral size distribution of islands at different coverages (vertically shifted for clarity). Number of islands used for the analysis for each coverage: 0.03 Å – 815, 0.1 Å − 1818, 0.2 Å − 1308, 0.5 Å − 277, 0.6 Å – 1258, 1 Å −1086, 2 Å – 850, 3 Å – 483.

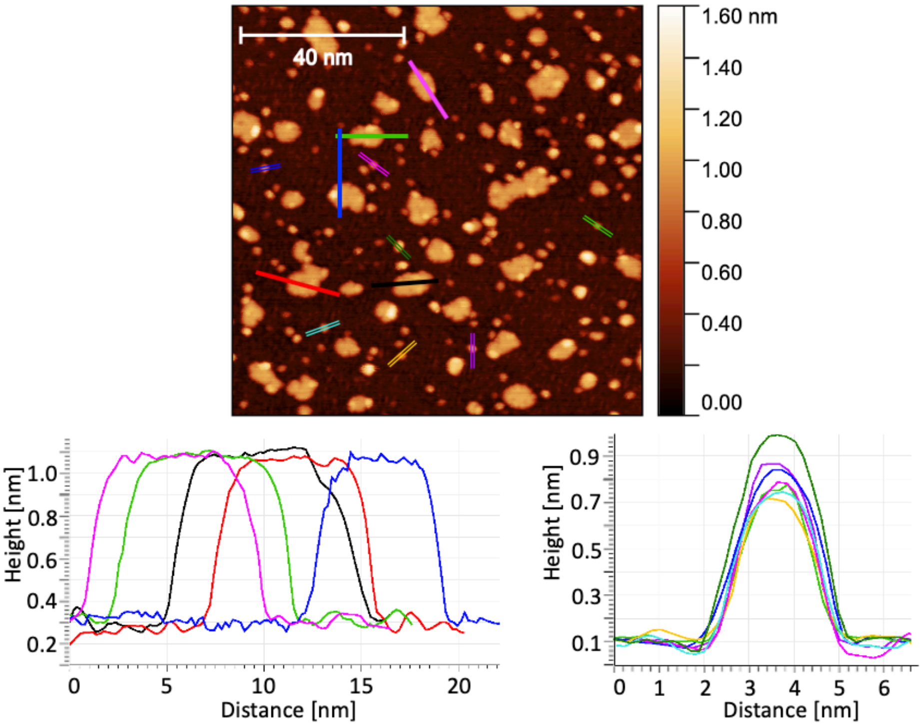

Figure 68: STM image of Ti/ Bi_2Se_3 sample at the coverage of 0.5 Å (I=0.030 nA, V=-250mV) (a) with corresponding line profiles over the big (b) and small islands (c).

At 0.5 Å also the clusters become more visible due to their increase in size (height 3.8 Å, σ = 0.8 Å). Figure 69 shows Bi_2Se_3 substrate at the coverage of 0.5 Å where clusters are easily observed as red spots on top of the islands.

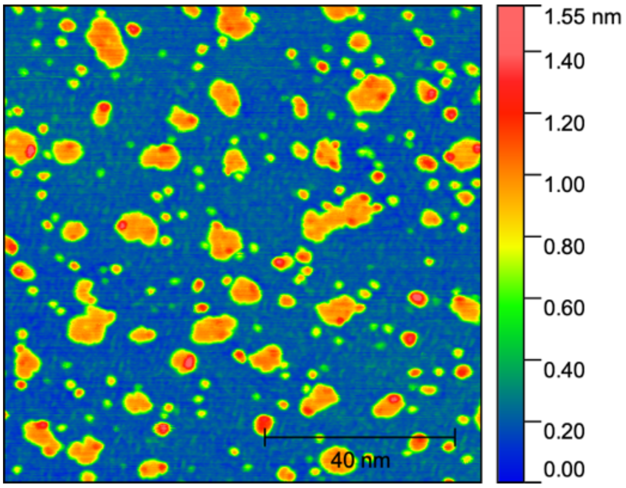

Figure 69: STM image of Ti/Bi_2Se_3 interface at the coverage of 0.5 Å presented with multicolor scale where the substrate and surface features are distinguished by different color (blue-substrate, green and orange-islands, red-clusters).

At 0.6 Å Ti coverage (Figure 66c) the islands further increase in size as presented in Figure 67, the average lateral size of the small islands is 2.1 nm ($\sigma = 0.5$ nm) and of the big ones 6 nm ($\sigma = 2$ nm). At this point 20 % of the surface is already covered with islands. At the Ti coverage of 1 Å a morphology change of the Bi$_2$Se$_3$ substrate from smooth to coarse is observed (Figure 66d). The substrate exhibits pits that are 1.6 Å ($\sigma = 0.5$ Å) deep and 3 nm wide ($\sigma = 0.4$ Å) (see Figure 70).

Together with the coarsening of the Bi$_2$Se$_3$ substrate, the LEED pattern of Bi$_2$Se$_3$ (Figure 71) is almost completely lost despite a significant part of the surface is still not covered by the islands. This indicates the loss of the crystallographic order in the Bi$_2$Se$_3$ substrate. Progressive loss of structural long-range order (as well as bimodal island formation) was observed also with the deposition of Fe on Bi$_{1.91}$Mn$_{0.09}$Te$_3$ [75]. Similarity in the film morphology and loss of the LEED pattern in that and in our system suggest similar processes happening at the metal/Ti interface.

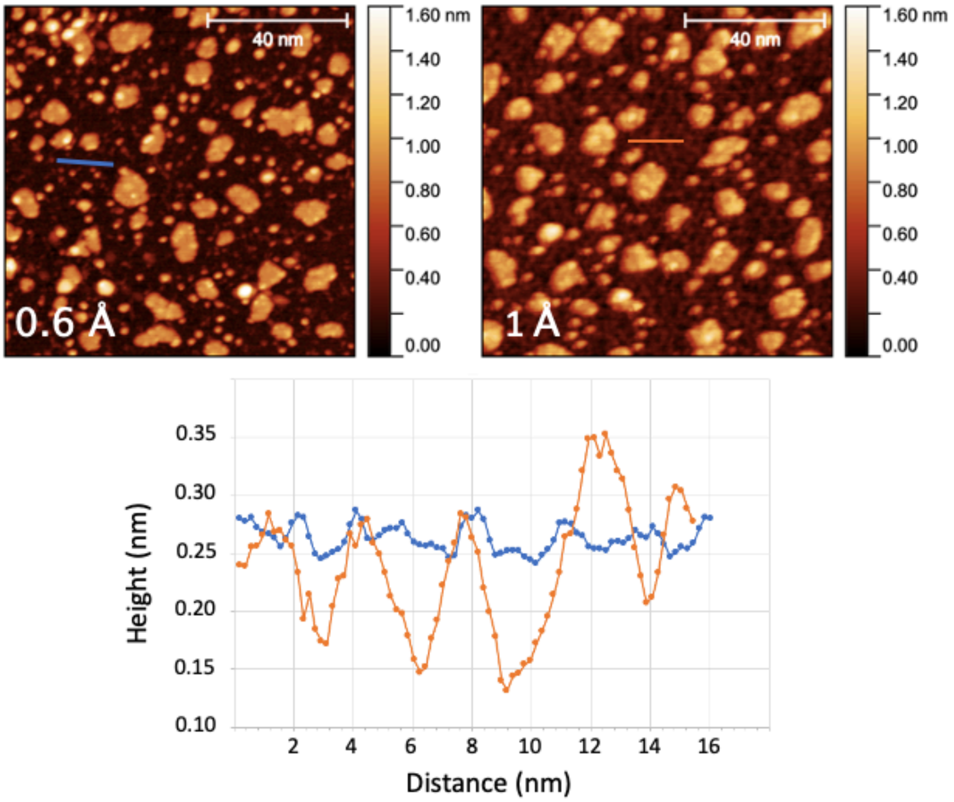

Figure 70: Line profiles over the Bi$_2$Se$_3$ surface at Ti coverage of 0.6 and 1 Å, showing the formation of pits at higher Ti coverage.

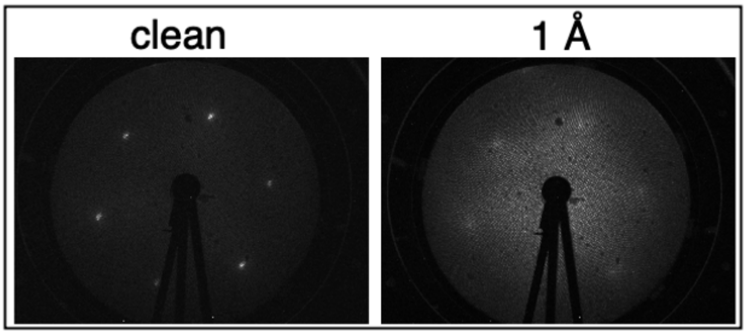

Figure 71: LEED pattern of the clean and Ti-covered Bi_2Se_3 surface (e^- energy = 65 eV).

Above the 1 Å coverage the lateral growth of the islands is strongly suppressed (average size of the small islands is 2.6 nm (σ = 0.8 nm) and of the big islands 7 nm (σ = 2 nm)) and with further Ti deposition the islands stop increasing in their lateral size (Figure 72). Instead, the growth continues with increase of island height and adsorption of material onto the areas between the islands as shown in Figure 73.

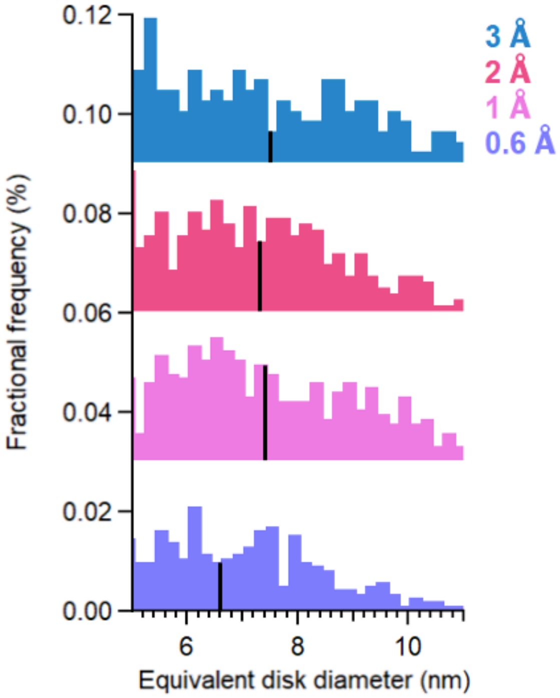

Figure 72: Lateral size distribution of the big islands at coverage of 0.6, 1, 2 and 3 Å (vertically shifted for clarity). Black lines indicate the average size of the big islands.

The XPS data described in Section 4.3 highlights the fact that a chemical interaction is present at the Ti/Bi_2Se_3 interface which results in the formation of new phases. From the XPS data it results that, at the coverage explored by STM, all deposited Ti was consumed in a reaction, and no metallic Ti is detected (see Section

3.4). The islands observed by STM are therefore not composed of metallic Ti. Hence, the observed surface features should be composed of the reaction products, such as titanium selenide or Bi. Difference in the morphology of the two types of islands could be due to different composition. It can be hypothized that the larger ones present titanium selenide phases, whereas the small ones could be made of Bi. However, further investigations are necessary to identify the nature of different islands.

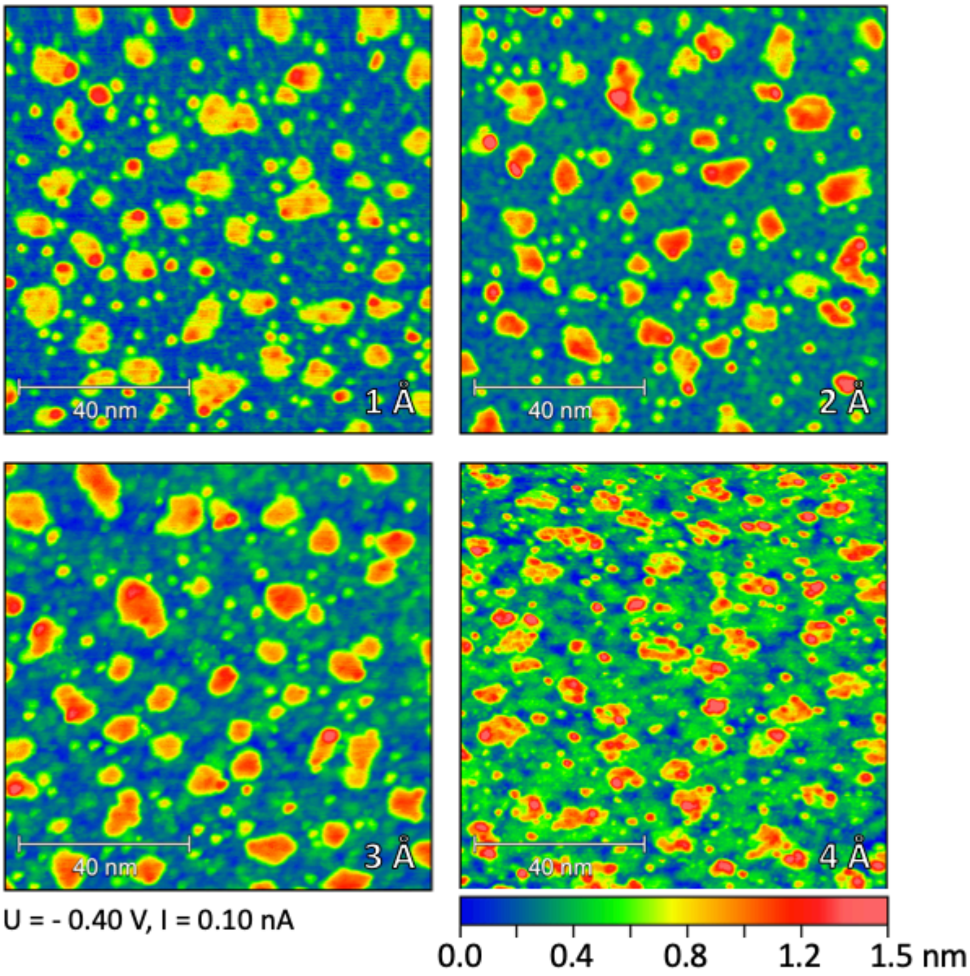

Figure 73: STM images of Ti on Bi_2Se_3 with increasing coverage from 1 to 4 Å.

Morphology at low coverage was investigated also for low temperature (LT) Ti deposition (Figure 74). Ti was deposited on Bi_2Se_3 substrate at a temperature of 88 K. Sample was afterwards allowed to heat up to RT. STM measurement shows different morphology compared to the RT deposition. The surface is densely covered with islands smaller than for RT deposition. Also here two types of islands are distinguished: the bigger ones measure 2.6 nm (σ = 0.6 nm) in diameter and have apparent height of 5.5 Å (σ = 0.6 Å), whereas the small ones are 0.5 nm (σ = 0.2 nm) wide with apparent height of 2.6 Å (σ = 0.4 Å). Size distribution of islands for RT and LT deposition is presented in Figure 75.

Differences observed in Figure 74a and b could be explained by the temperature dependence of Ti diffusion. Hindered diffusion at LT disables the formation of larger islands, therefore the surface morphology results in high density of smaller islands. Based on this difference it is hypothesized that a stable chemical equilibrium at the Ti/Bi_2Se_3 interface of the LT sample is established before reaching RT. For this reason, heating this system does not result in the formation of large islands as for RT deposition, because the deposited Ti has already transformed into a new phase.

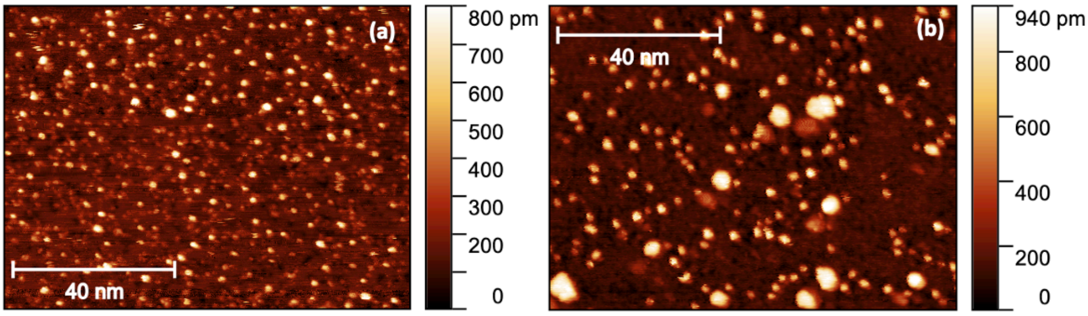

Figure 74: STM images of Bi_2Se_3 substrate with 0.1 Å of Ti deposited at LT (a) and RT (b).

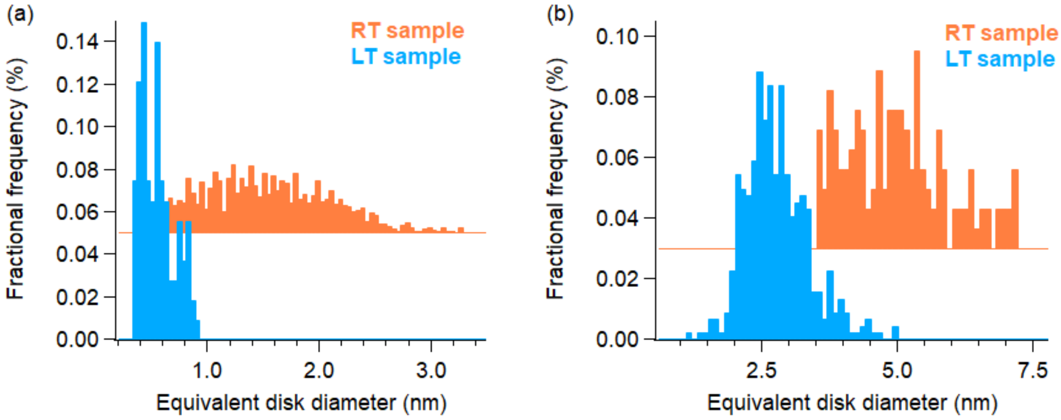

Figure 75: Lateral size distribution of small (a) and big (b) islands on Bi_2Se_3 substrate after 0.1 Å deposition of Ti at LT and at RT. Number of islands used for the analysis was 1818 (for RT) and 740 (for LT).

Morphology at higher coverage was investigated by SEM measurement (sample preparation is described in Sections 2.7.4 and 2.7.5). Up to 20 nm Ti coverage it was not possible to see any features of the Bi_2Se_3 surface by SEM. EDX mapping revealed that Ti is homogenously distributed over the whole surface without variations at the surface steps (see Figure 76). No change in the surface morphology could be observed even after the sample being kept at the ambient conditions for a month, conversely to what observed with Ag.

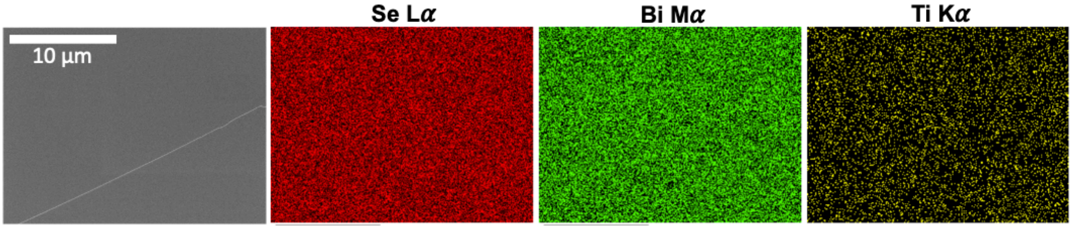

Figure 76: EDX mapping of Bi_2Se_3 *sample with 20 nm of deposited Ti.*

After trespassing a certain film thickness threshold (between 20 and 40 nm) an important morphology change occurs. The surface develops networks of buckles as presented in Figure 77a. The networks with bigger mesh sizes have 1.5 µm wide buckles whereas the buckles of more dense networks with smaller mesh sizes are 0.35 µm wide. Images acquired on broken buckles (Figures 77bc) indicate that they are empty, developed due to the detachment of the Ti film, and that the Ti film is composed of two layers. Such distinction between the two layers indicates that they are composed of different phases.

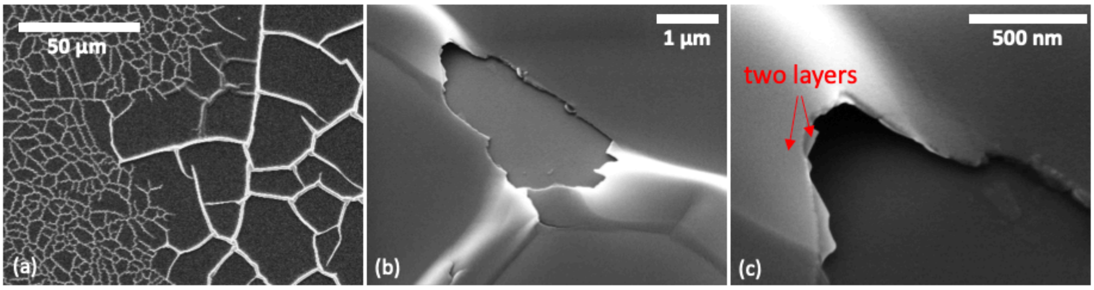

Figure 77: SEM images of 40 nm thick film on Bi_2Se_3 *showing different morphology of the buckles (a), hollow inner part of the buckles (b) and a close-up image of the delaminated film where layered composition of the film is visible.*

This kind of surface structure, where hollow buckles of the deposited thin film are formed, is ascribed to the buckle delamination phenomenon. Typically, such morphology is observed after release of compressive stress in the hard layer on a soft substrate. With increasing coverage, the compressive stress is building up in the Ti polycrystalline film. When the stress overcomes the adhesive strength, buckling occurs. The flat surface becomes unstable and stress is released by formation of a spinodal-like pattern of wrinkles or buckles [157].

The smaller buckles show typical morphological features such as network-like telephone cords, denoted with the yellow line in Figure 78a [158]. Some buckles are found as single cords while the majority of them branch into two daughter cords after a certain distance of propagation. Consequently the surface exhibits formation of a web of buckles with lots of nodes as presented in Figure 78b. Usually there are some major buckle fronts propagating far in one direction and the daughter buckles are formed alternatively to the left and to the right of the propagation direction (see Figure 78b) [159]. The daughter fronts are usually shorter because they stop propagating when they approach an adjacent buckle.

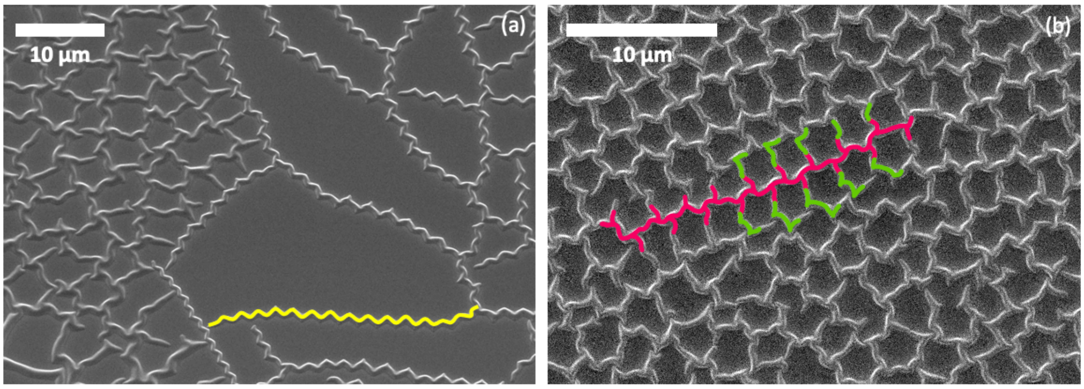

Figure 78: SEM images of Ti/Bi_2Se_3 at a coverage of 40 nm showing different morphologies of smaller buckles: (a) web of buckles and a single telephone cord denoted in yellow; (b) web of buckles where the major telephone cord and its splitting is denoted with the pink and daughter branches with the green color.

The bigger buckles follow the same propagation, as observed with the smaller ones, with the splitting into two daughter branches as shown in Figure 79a. Close inspection reveals also some sort of cracks at the buckle edges (Figure 79b). Cracks often accompany the formation of buckles, they occur either on the top or on the sides of the buckle, depending on the properties of materials. Accordingly to the article of Flores-Johnson *et al.* [160] the cracks in our system suggest high stiffness and low toughness of the interface since the cracks are present on the sides of the buckles. On the top of the nodes darker lines, probably shallow cracks, forming hexagonal shape are seen. Specific geometry of these features is very likely connected with the crystal structure or symmetry of the underlying substrate.

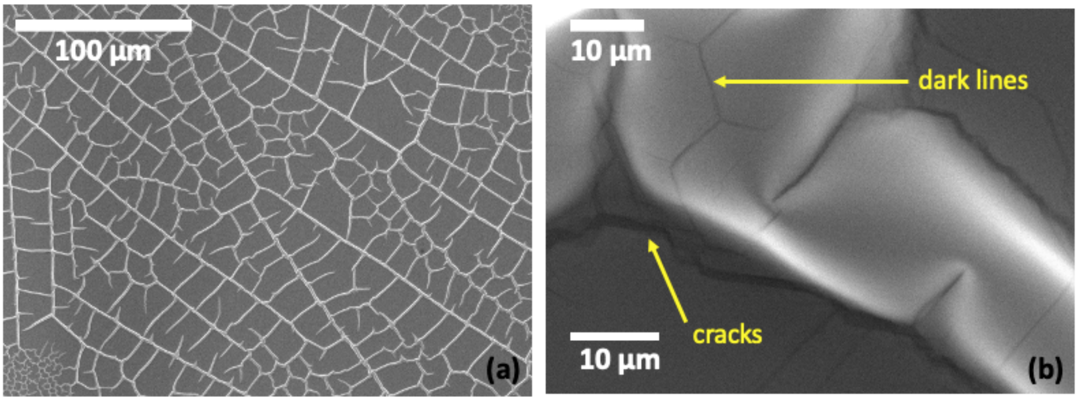

Figure 79: SEM images of bigger buckles formed by 40 nm thick film of Ti on Bi_2Se_3 substrate showing: (a) morphology; (b) dark features on top of the buckles and side cracks.

To prove that buckle delamination is not generated by oxidation of Ti after exposure to air, in a second experiment, immediately after the deposition of a 40 nm thick Ti film, a protective layer of Pt (10 nm) was deposited atop within the same apparatus. The sample exhibited the same morphology as without the Pt layer, ruling out the possibility that the oxidation process is responsible for the buckling.

Buckle delamination phenomenon has been widely studied in the past few decades, since it has a great effect on the mechanical properties and can lead to the loss of functionality of the film/substrate systems. In the here reported case of Ti/Bi_2Se_3, the observed buckling has to be taken into account when designing devices. In some areas, such as in Figure 78b, the buckled area, where the metal is detached from the substrate, can cover one third of the total surface.

In general buckling is considered as a nuisance to be avoided. However, recent interests in micro/nano-scale thin film materials have exploited wrinkling and buckle delamination processes for applications in the field of flexible electronics [161], surface micro patterning [162] and tunable diffraction gratings [163]. Another interesting way to harness buckling delamination is to use the microchannel networks for the transfer of fluids [164, 165]. Mentioned applications give an added value on the observed morphology of Ti/Bi_2Se_3 systems, making it interesting for further research.

4.2 The chemistry at the Ti/Bi_2Se_3 interface: an XPS investigation

The morphology evolution observed by STM, the LEED pattern degradation and the observed double layer in the buckles reported in the previous Section 4.1 gave some indications that a chemical reaction is taking place at the interface between Ti and Bi_2Se_3. Such chemical interaction at the Ti/Bi_2Se_3 interface was studied by XPS. The Bi 5d, Se 3d and Ti 2p core levels were measured at photon energy of 650 eV for the nominal Ti coverage ranging from 0.5 to 28 Å. Ti deposition was performed by e-beam evaporator at a pressure of $3 \cdot 10^{-10}$ mbar. Voltage and current parameters of the filament were controlled to obtain the constant value of the flux for each evaporation. All depositions were performed at RT, unless stated differently. Deposition rate of 0.23 ± 0.02 Å/min was determined from the attenuation of the substrate photoemission signals on Bi_2Se_3 and Au substrates during a dedicated calibration session before the experiments. O 1s core level was monitored during the whole measurement to detect any possible contamination or oxidation. With the increase in the Ti coverage, the spectral shape changed significantly (Figure 80), which shows on a strong chemical interaction at the interface. The observed changes indicate a change in the valence states and formation of new interfacial phases.

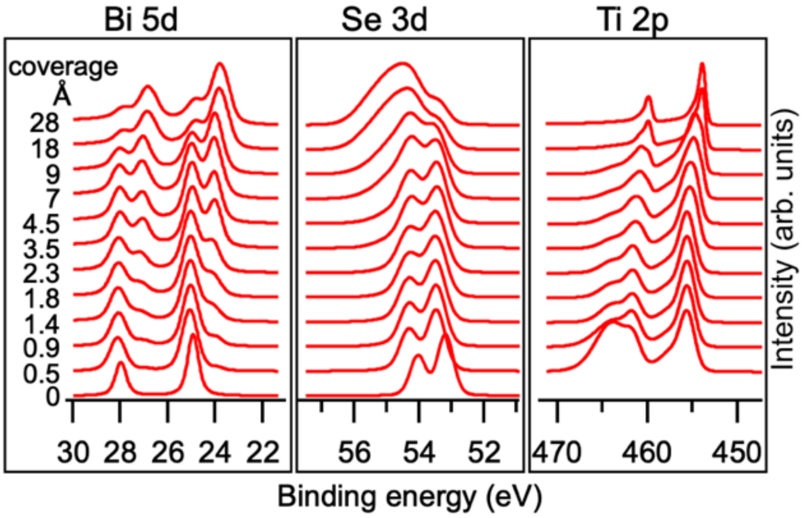

Figure 80: Evolution of Bi 5d, Se 3d and Ti 2p core level spectra with increasing Ti deposition on Bi_2Se_3. The spectra were normalized to the highest peak.

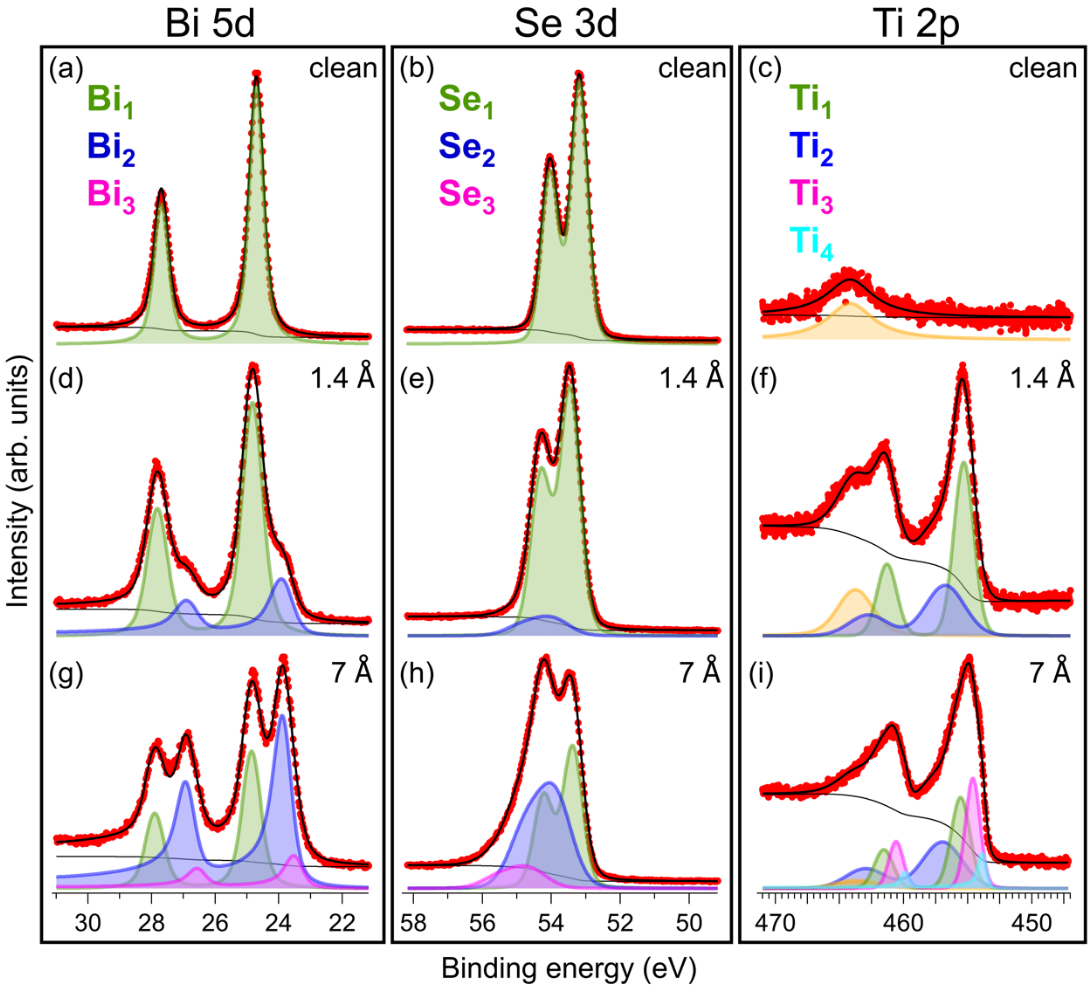

Figure 81: Bi 5d Se 3d and Ti 2p core level spectra of the Ti/Bi_2Se_3 samples at different coverage: pristine Bi_2Se_3 (a,b,c); 1.4 Å of Ti (d,e,f); and 7 Å of Ti (g,h,i). Red dots are the experimental data. Black line is the resulting fit. The yellow component corresponds to the Bi $4d_{3/2}$ core level peak.

A more detailed analysis of the XPS spectra was performed to reveal the chemistry of the interaction in detail. The Bi 5d and Se 3d core levels of the clean Bi_2Se_3 surface were deconvoluted with one spin-orbit doublet. The corresponding peaks are positioned at BE of 24.7 and 53.2 eV, respectively (see Figures 81ab) and are hereafter named Bi_1 and Se_1.

Starting from the lowest Ti coverage (0.5 Å), a shift of 0.25 eV towards higher BE is observed for the Se_1 and Bi_1 components, which is ascribed to the band bending. Upon Ti deposition new components emerge in Se 3d and Bi 5d core levels (Se_2 and Bi_2, represented as blue components in Figures 81de), indicating a chemical reaction at the interface. The Se_2 component has 0.5 eV higher BE than Se_1, whereas the Bi_2 component is at 1.1 eV lower BE than Bi_1 and fits well with the peak position of metallic Bi [166]. As visible, the metallic Bi phase (as well as all the other components ascribed to metallic phases) exhibit characteristic asymmetry at high binding energy tail. Positions and assignments of Se, Bi as well as Ti components are listed in Table 3.

Table 3: Position and assignment of Bi 5d, Se 3d and Ti 2p core levels components.

Core level	Component	Binding energy	Assigned to
Bi 5d	Bi_1	24.9 eV	Bi^{+3} in Bi_2Se_3
	Bi_2	23.8 eV	Metallic Bi
	Bi_3	26.5 eV	Metallic Bi alloyed with Ti
Se 3d	Se_1	53.5 eV	Se^{-2} in Bi_2Se_3 **and** in $TiSe_2$
	Se_2	54.0 eV	Se in under-stoichiometric $TiSe_2$
	Se_3	54.7 eV	Se^{-2} in TiSe
Ti 2p	Ti_1	455.5 eV	Ti^{+4} in $TiSe_2$
	Ti_2	457.0 eV	Ti in under-stoichiometric $TiSe_2$
	Ti_3	454.6 eV	Ti^{+2} in TiSe
	Ti_4	453.8 eV	Metallic Ti

With the increase in the Ti coverage, the Bi_1 component, corresponding to Bi^{3+} in Bi_2Se_3, decreases because of higher Ti coverage and formation of new surface phases. The Se_1 component decreases much slower in its spectral weight than Bi_1 (Figure 82). This is in line with the fact that BE of Se_1 corresponds, not only to Se^{2-} from Bi_2Se_3, but also to the newly formed $TiSe_2$ [167-170]. The position of the Se_2 component corresponds to non-stoichiometric intermediate metal selenides [171] formed during the ongoing reaction.

The same interfacial chemical process also reflects in the evolution of Ti 2p core level spectra. Upon a low Ti-deposition coverage of 1.4 Å, the Ti 2p core level spectra display two components, Ti_1 and Ti_2, at 455.5 and 457 eV BE, respectively (Figure 81f). The peak position of Ti_1 components is in a good agreement with the reported data for $TiSe_2$ [167, 168, 170, 172], which is considered as a product of the reaction between Bi_2Se_3 and Ti. The Ti_2 component (together with Se_2) is ascribed to the $TiSe_2$-based intermediate phase with an under-stoichiometric Se content [173].

After deposition of more than 4.5 Å of Ti, a new reaction regime is reached where new components emerge in all measured core levels. In the Ti 2p core level spectra, a Ti_3 component at BE of 454.6 eV appears (pink colored in Figure 81i). Its BE is between that of Ti^0 and Ti^{4+} and can be attributed to Ti^{2+} due to the formation of TiSe. The corresponding Se component of TiSe is Se_3 at BE 54.7 eV (pink colored in Figure 81h) [171].

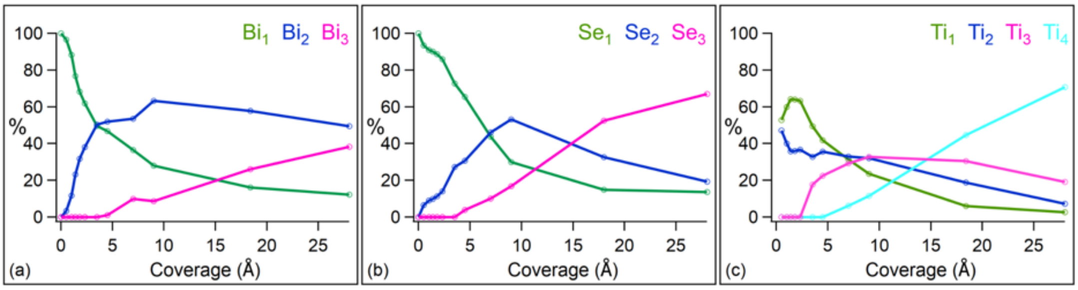

Figure 82: Change of the spectral weight of individual components in Bi 5d (a), Se 3d (b) and Ti 2p (c) core levels with increasing Ti coverage.

Due to the presence of the interfacial phases acting as the diffusion barrier, the deposited Ti is not completely consumed in the reaction and some of it remains in the metallic form. Ti^0 corresponds to the Ti_4 component at BE 453.8 eV (light blue in Figure 81i), which becomes dominant above the 18 Å coverage (Figure 80 and Figure 82). In the Bi 5d core level, the new Bi_3 component (pink colored in Figure 81g) appears at 0.3 eV lower BE than Bi_2. It is ascribed to metallic Bi [174, 175] with a different chemical environment, possibly due to alloying with Ti.

Figure 82 shows how the spectral weight of each component (fraction of the area of a component to the overall area of the core level) changes with increasing coverage. Due to hindered diffusion the components describing phases where the ratio between Ti and Se is less than 1:2 (i.e. under-stoichiometric $TiSe_2$, TiSe) are increasing in their fraction and majority of Ti remains in its metallic form.

By performing the XPS measurement at different beam energy the inelastic mean free path of the photoemitted electrons can be varied. Inelastic mean free path is closely related with the escape depth of the electron [139]. Therefore, by increasing the beam energy photoelectrons from deeper regions of the sample can reach the detector and it is possible to get some information about the location of components in the spectrum. Figure 83 shows spectra taken at beam energies 900 and 500 eV (550 eV for Ti 2p). From the Bi 5d core level measured at 500 eV it can be seen that the metallic Bi components have significantly higher spectral weight than the component Bi_1, belonging to Bi_2Se_3 ($Bi_{1,500}$ = 22 %, $Bi_{1,900}$ = 38 %). The spectral shape of Se 3d core level is also clearly different depending on the photon energy at which the spectrum was acquired. The difference comes from the increase of Se_2 (14 %) and decrease of Se_1 intensity (14 %). The decrease of Bi_2Se_3 component in Se 3d core level does not appear as pronounced as in the Bi 5d core level, because Se from $TiSe_2$ is additionally contributing to the overall intensity of Se_1. In summary, the analysis on Bi 5d and Se 3d confirm that metallic Bi and titanium selenide compounds are lying above the Bi_2Se_3 substrate.

When analyzing the 2p core level spectra of Ti taken at variable photon energy the change in the Ti_4 component is pronounced. Metallic Ti is expected to be located at the very top of the sample surface, since it was additionally deposited on the sample and it is unreacted. The spectrum in Figure 83f confirms this, since the spectral weight of Ti_4 component is significantly larger than in the spectrum taken at 900 eV ($Ti_{4,550}$ = 16 %, $Ti_{4,900}$ = 10 %). Interpretation of changes in other Ti components is less obvious. As observed by STM, Ti deposition results in the formation of islands and clusters atop of them. Surface morphology has an influence on the area from which the electrons are emitted into the analyzer acceptance cone; therefore, it can hinder the signal coming from the regions below the islands or below the clusters, which makes the interpretation of changes in other Ti components not straightforward. The pronounced decrease in the Ti_2 component ($Ti_{2,550}$ = 25 %, $Ti_{2,900}$ = 38 %), stronger than for Ti_1, suggests that under-stoichiometric $TiSe_2$ is found either deep below the top surface or in the regions below the islands. Further investigation is needed to get a clearer picture of partially reacted phases' location.

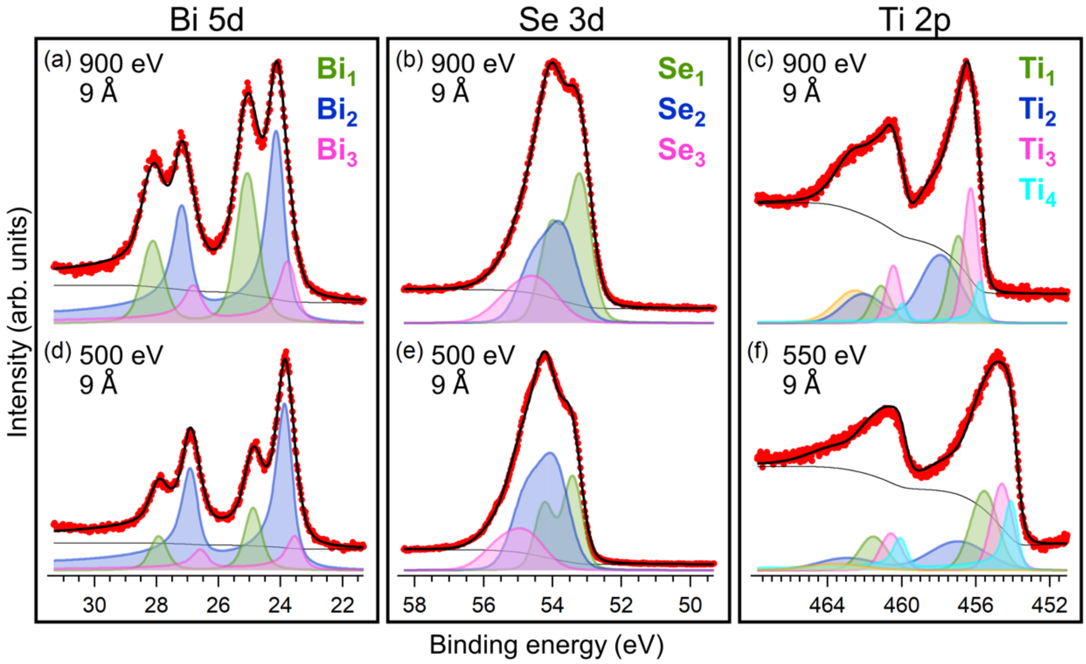

Figure 83: XPS spectra of Bi 5d (a, d), Se 3d (b, e) and Ti 2p (c, f) core levels measured at different beam energies. The yellow component in Ti 2p core level spectra corresponds to the Bi 4d$_{3/2}$ core level peak.

In order to observe if thermal treatment makes the reaction to further evolve, an experiment was conducted measuring a sample with Ti coverage of 3.5 Å before and after annealing at 100 °C (rate = 4°/min, $t_{annealing}$ = 10 min). Comparison of the spectra is presented in Figure 84. It shows that the processes happening at the interface evolve with increasing temperature and that the fractions of the newly formed components are increasing. After annealing, metallic Bi (Bi$_2$) slightly increases (4 %) with respect to Bi$_1$. In Se 3d spectra the intensity of intermediate phase (Se$_2$) is slightly lower after annealing (4 %), indicating that HT causes the progress of the chemical reaction at the interface. In Ti 2p core level spectra the annealing results in the decrease of spectral weight of Ti$_3$ (11 %). HT increases the energy of the atoms and promotes their diffusion. Consequently, interdiffusion is enhanced enabling the non-reacted species to come in contact and react. The process is observed as an increase of components presenting the new phases formed within the chemical reaction and preferential formation of stoichiometric TiSe$_2$.

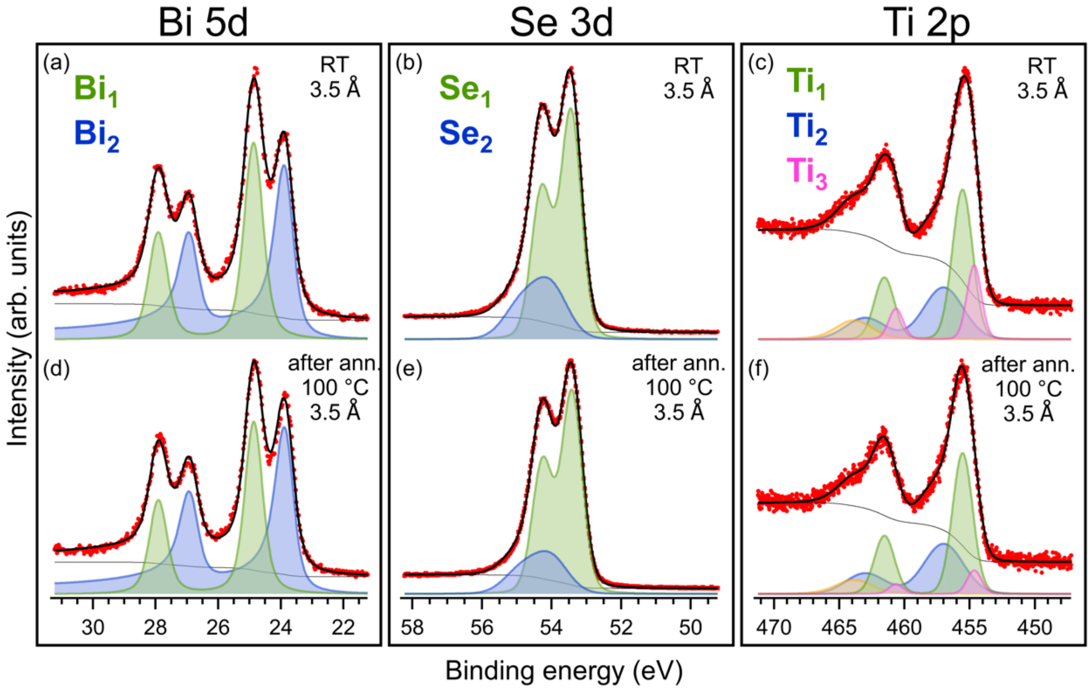

Figure 84: XPS spectra of Bi 5d (a, d), Se 3d (b, e) and Ti 2p core levels (c, f) of Ti/Bi_2Se_3 interface measured before and after annealing to 100 °C. The yellow component in Ti 2p core level spectra corresponds to the Bi $4d_{3/2}$ core level peak.

Deposition and subsequent measurement was performed also at LT, at 130 K. Figures 85abc present the spectra acquired at LT from a sample on which 7 Å of Ti was deposited at LT (LT sample). For both Bi and Se core level spectra, the components corresponding to reacted species (Bi_2, Bi_3, Se_2, and Se_3) are still clearly observed, indicating that the reaction takes place also at 130 K. In Bi 5d core level spectrum (Figure 85a) the Bi_3 component of the LT sample has 15 % higher spectral weight than of the RT sample (Figure 81g). Bi_3 appeared as the last component in the RT experiment and was formed due to the hindered diffusion preventing the reaction to fully proceed. At LT the diffusion is even lower, therefore the ratio between Bi_2 and Bi_3 component at RT is much larger (LT = 1.2:1, RT = 5.3:1). Differences in Se 3d core levels spectra acquired on LT (Figure 85b) and RT (Figure 81h) sample were also observed, however, they were much less pronounced compared to Bi 5d core level spectra (spectral weight ratio of Se_1:Se_2:Se_3 at LT is 4.1:4:1 and at RT 4.4:4.6:1).

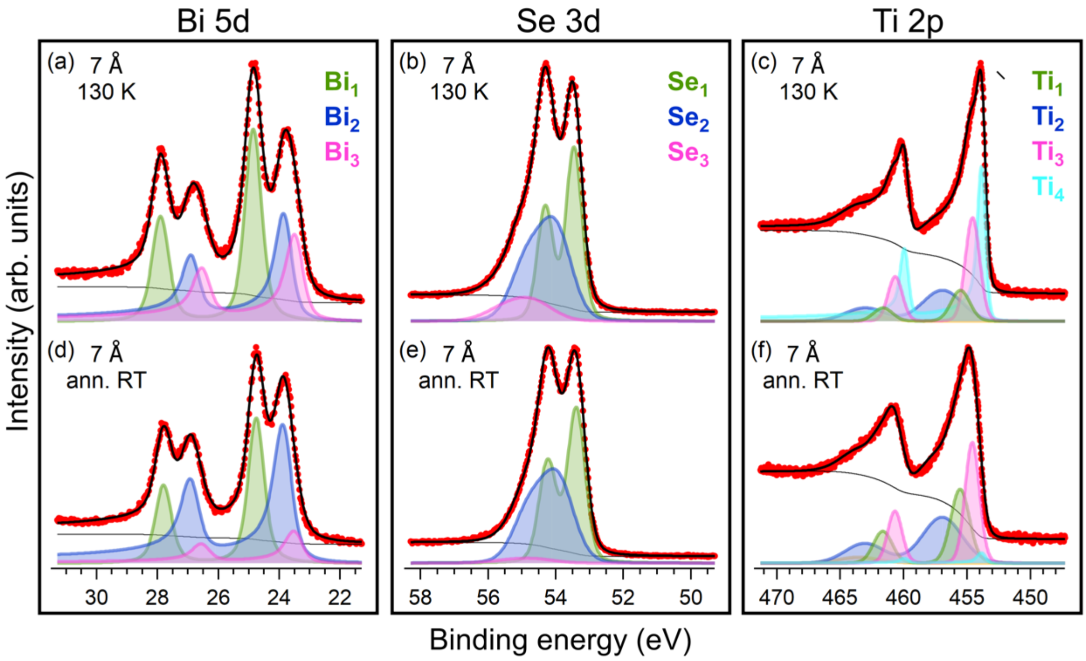

Figure 85: XPS spectra of Bi 5d (a, d), Se 3d (b, e) and Ti 2p core levels (c, f) of Bi_2Se_3 sample on which Ti was deposited at LT. Upper row represent spectra of LT sample measured at LT and the bottom row spectra of the same sample annealed to RT.

In the case of Ti 2p core level, the component Ti_4 of metallic Ti is significantly higher (for 26 %) when deposited at LT (Figure 85c) than at RT (Figure 81c). The result shows that 32 % of deposited Ti cannot participate in the reaction due to the reduced kinetics at LT. Still, reacted Ti (Ti_1, Ti_2 and Ti_3) is clearly present also on LT sample.

By heating up the LT sample to RT it was possible to follow the change in the component ratios and thus the evolution of the interfacial reaction. Figures 85def show spectra of Bi 5d, Se 3d and Ti 2p core levels from annealed LT sample. It is clearly seen that Bi_3 component largely transforms into Bi_2, which is the major reaction product (Bi_3 decreases for 14%). In the Se 3d core level the ratio between Se_1 and Se_2 components remains practically the same (1:1 before annealing; 1.1:1 after annealing) but the intensity of Se_3 drops (for 8 %). Se_3 is associated with TiSe, a compound which appears when the amount of Ti at disposal for reaction decreases due to hindered diffusion. The biggest change in the Ti 2p core levels is in the Ti_4 component, which decreases for 30 % in its spectral weight upon annealing. This is because annealing promotes diffusion of metallic Ti and subsequent participation in the reaction. Upon annealing Ti_1 component increases for 16 %, Ti_2 for 10 % and Ti_3 for 4 % indicating the proceeding of reaction. The observed changes are exactly the opposite to the evolution of spectra with increasing Ti coverage at RT.

Finally, variation of Ti_3 component upon annealing provides another information. Position of Ti_3 component matches the peak of Ti in TiO [176], therefore it could also be the result of oxidation. Increase in Ti_3 component upon annealing to RT without any change in O 1s core level proves that the Ti_3 component is due to the reaction with Bi_2Se_3 and not to oxidation.

In summary, all results obtained within the XPS experiment show that the Ti/Bi_2Se_3 interface is chemically unstable. The observed chemical interaction at the interface is a redox solid-state reaction that is kinetically active already at cryogenic temperature (130 K). Ion diffusion is the main parameter that influences the kinetics of such type of reactions. The kinetics slows down with an increase in the diffusion path through the product layer. Therefore, the appearance of the intermediate phases (such as TiSe and under-stoichiometric $TiSe_2$) is expected. With annealing the amounts of intermediate phases are reduced. The interfacial reaction yields $TiSe_2$ and metallic Bi as the final products of the solid-state redox reaction according to the proposed equation:

$$3Ti + 2Bi_2Se_3 \rightarrow 4Bi + 3TiSe_2$$

During the reaction, Se remains in the -2 oxidation state, whereas the redox reaction happens between Bi^{+3} and Ti^0 producing metallic Bi and Ti^{+4} compounds. The observed solid-state reaction is thermodynamically favored at RT ($\Delta G_{298} = -256$ kJ/mol Ti [173, 177]).

4.3 TEM cross-section experiment

TEM studies on the interface cross-section were performed on samples with 20 and 50 nm thick Ti film deposited by PECS on Bi_2Se_3 at a rate of 0.6 Å/s (sample preparation is described in Section 2.7.6). This rate is much higher compared to the one used in STM and XPS experiments and better resemble the situation when fabricating metal contacts for electric measurements. Figure 86 shows a TEM image of a cross-section taken at a lower magnification where three different areas can be distinguished: Bi_2Se_3 substrate, Ti film and a darker region in between.

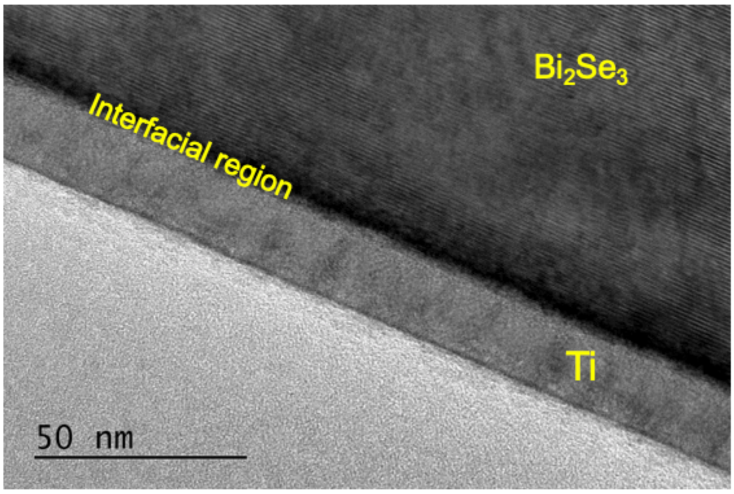

Figure 86: TEM image of Ti/Bi_2Se_3 *interface with denoted regions.*

In Figure 87 higher magnification images of individual regions are presented. The deposited Ti forms a polycrystalline film (Figure 87c). In the Bi_2Se_3 region the observed interplanar distance of 0.95 nm corresponds to the expected periodicity of Bi_2Se_3 quintuple layers. At the interface an interfacial layer with a crystal structure different from Bi_2Se_3 is observed. Within this layer, the darker area denotes a presence of heavier elements. Beside the darker region there is another interface phase which is often observed as small domains with a layered structure (see Figure 87b). The distance between these layers is about 0.60 nm, which fits well with the $TiSe_2$ (001) interplanar distance [172]. The thickness of the overall interface region is approximately 10 nm. Such thickness of the interface region is larger than in the RT XPS experiment. This is very likely due to the sample preparation process during which the sample has been kept at ~90 °C for 1h. Therefore, the situation corresponds more to XPS spectra shown in Figure 84, after annealing at 100 °C, where the amount of partially reacted products is low. However, in this case, the amount of deposited Ti at disposal for the reaction is much higher.

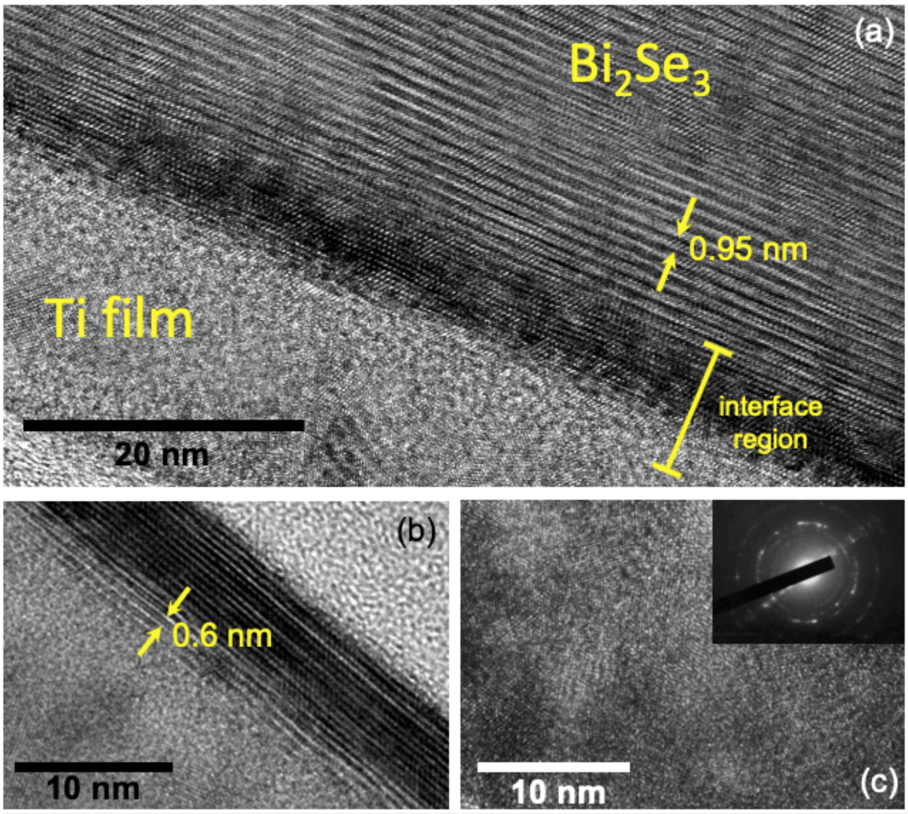

Figure 87: TEM images of (a) Ti/Bi$_2$Se$_3$ interface at the coverage of 20 nm;(b) TiSe$_2$ layers beside the darker Bi region and (c) Ti film with the inset of its diffraction pattern.

An EDX line-scan over the interface is shown in Figure 88 together with a dark field STEM image of the area of interest. On the left side, there is the unreacted Ti film (Ti EDX intensity profile is light blue). Deeper in the Ti film (from left to right), the first interfacial region with a thickness of 5 nm is Ti- and Se-rich with no Bi. This region is recognized as the titanium selenide phase. Further on, the second interfacial region contains almost only Bi, with the signals for Ti and Se reduced to extremely low intensity. Therefore, this region is ascribed to the metallic Bi, possibly with residual of Se and alloyed Ti. Deeper in the sample, the Bi and Se signals correspond to the bulk Bi$_2$Se$_3$. The observed structure of the interface with the presence of Ti selenide and metallic Bi is in agreement with the XPS observations. EDX results also point to the basic mechanism of the interface reaction. It appears that Ti deposition induces diffusion of Se atoms out of the crystal forming titanium selenide phases and leaving behind Bi.

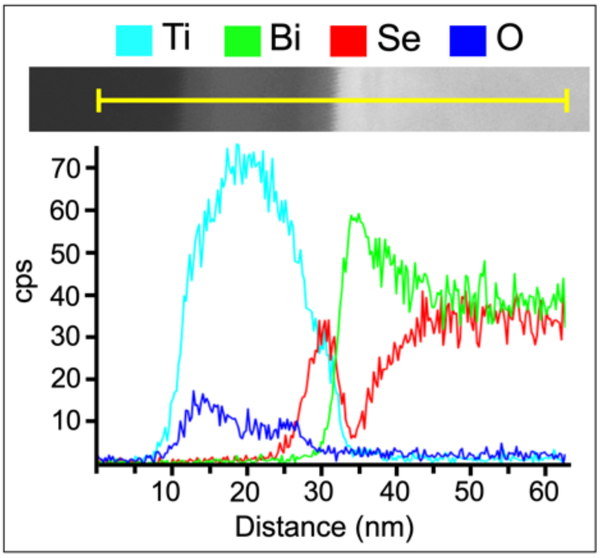

Figure 88: EDX line-scan over the interface region of the Ti/Bi_2Se_3 sample at the coverage of 20 nm.

Diffusion of Se atoms into the Ti film contributes to the compressive stress, which causes buckle delamination at higher Ti coverage. Examining the cross- section of the samples with 50 nm of deposited Ti, therefore, enabled further understanding of this process. Figures 89abc show TEM and STEM image of a buckle and the structure of the detached layer, whereas the EDX line-scan over the detached layer is presented in Figure 89d. The region on the inner part of the buckle has the highest Bi signal, suggesting that the delamination occurs at the interface between Bi_2Se_3 and Bi-rich area or within the Bi phase (this is in agreement with TEM imaging at high resolution, where QL were generally not observed on the detached layer). A suitable explanation for this lies in the properties of the metallic Bi phase, which is prone to plastic deformation and allows for sliding of the film.

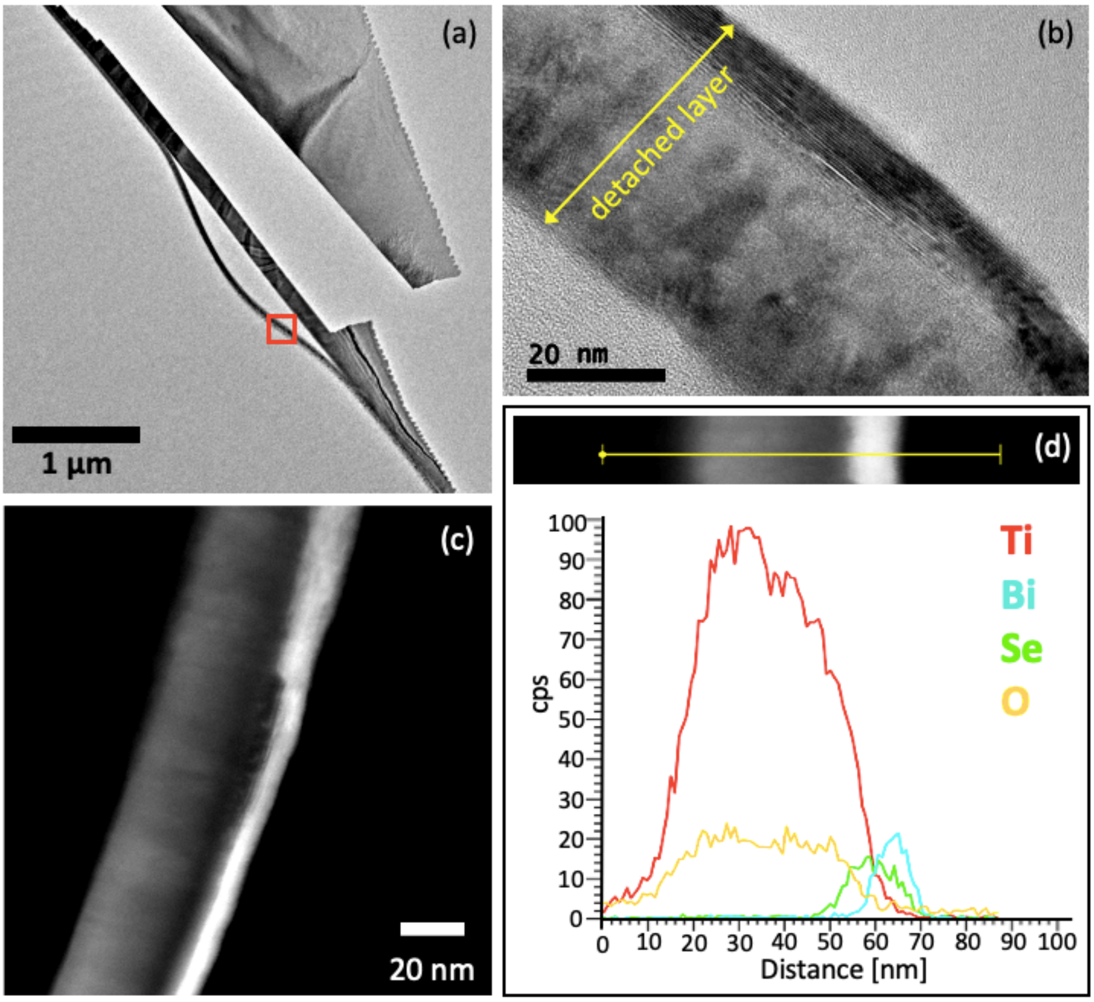

Figure 89: TEM image of a Bi_2Se_3 cross-section sample with the Ti coverage of 50 nm with a visible buckle at different magnification. The red mark in (a) indicates the area imaged in (b). (c) STEM image of the delaminated layer and, (d) an EDX line-scan measured over it.

4.4 Thermal stability

Thermal stability of the Ti/Bi_2Se_3 was examined using a heating stage inside the SEM apparatus. For this purpose, a sample with 40 nm thick Ti film was produced (for sample preparation see Sections 2.7.4 and 2.7.5). By covering half of the sample with a mask during the Ti deposition a narrow area with increasing Ti thickness going from 0 to 40 nm was obtained. Therefore, during the experiment we were able to observe at the same time the clean Bi_2Se_3 surface, the flat Ti film (thickness up to 20 nm) and the buckled film (up to 40 nm).

After analysis at RT, the sample was heated up in 50 °C steps until 250 °C. In the flat region (without buckles) no visible morphological change was observed in this temperature range. In the buckled region no major morphological changes were observed as well, and the buckles geometry was stable. The only observed phenomenon, when reaching the temperature of 250 °C, was the appearance of bright spots of irregular shape that evolved on some of the small buckles (see Figure 90).

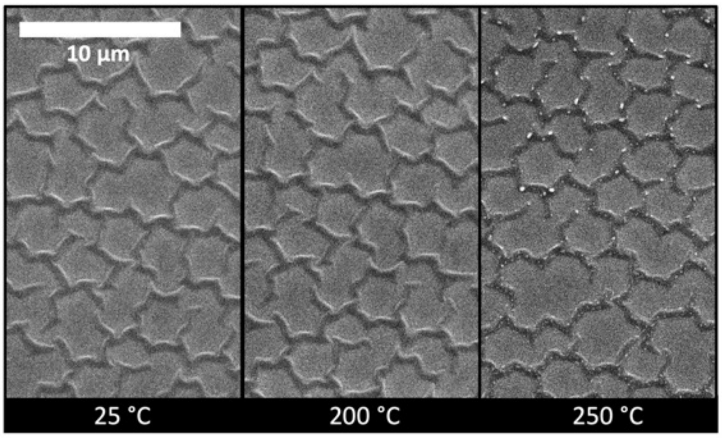

Figure 90: SEM images of Ti/Bi_2Se_3 interface at a coverage of 40 nm at different temperatures during thermal annealing experiment.

Sample was afterwards cooled down to RT in order to perform imaging with higher resolution and EDX analysis. SEM measurement showed that with the appearance of bright spots another feature was formed. On the small buckles dark triangles were found and they are shown in Figure 91c. While the bright spots appear quite random, the dark triangles are all oriented in the same direction (some of them marked in yellow in Figure 91c), indicating a crystallographic connection with the substrate. The two mentioned features were observed either individually or together and only on top of the smaller buckles, while the flat part of the Ti film as well as the bigger buckles did not exhibit any visible modifications (Figure 91).

Since the sample was in contact with air, while transferring it from the PECS apparatus into SEM, the surface of Ti film is oxidized and should not be modified at 250 °C. The observed changes upon annealing therefore evolved within the detached layer or on the ceiling of the buckles.

Figure 92 shows comparison of BSE and SE images. The buckles in the BSE images appear darker than the flat parts due to their empty structure. However, also the buckles themselves are imaged with different contrast. The bigger buckles always appear bright, whereas the smaller ones can exhibit different contrast. These variations cannot be visualized in the SE images and suggest on differences in composition.

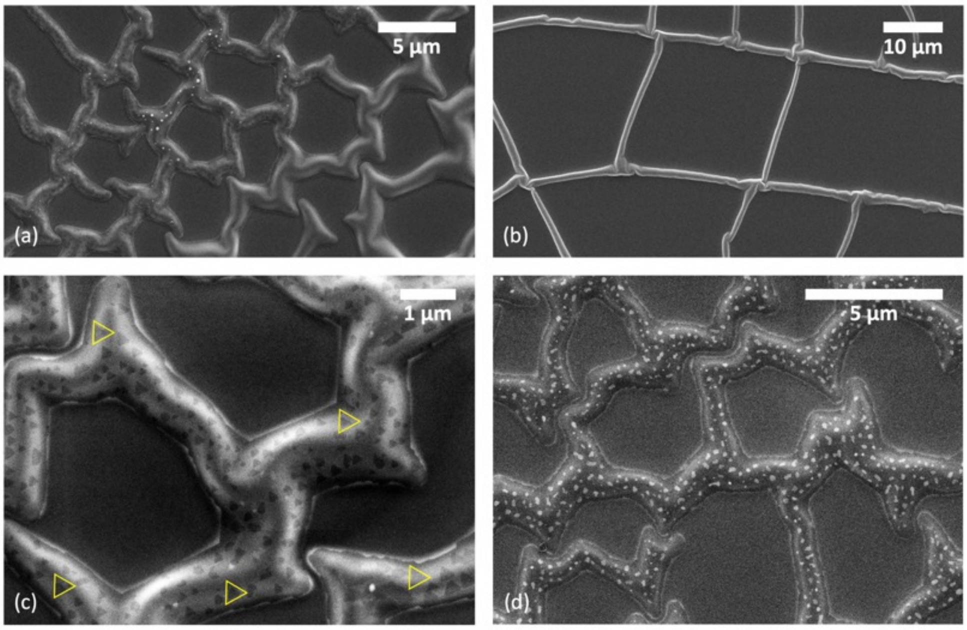

Figure 91: SEM images of 40 nm thick Ti film on Bi_2Se_3 after annealing to 250 °C showing smaller (a) and bigger (b) buckles, dark triangles (c) and bright spots (d).

The bright spots appear bright on both BSE and SE images (Figures 92cd) and suggest that they are composed of a heavier element, probably Bi. The triangles also appear dark on both kinds of images. Features on the buckles are very likely the result of thermal degradation or reaction evolution. Se and Bi also both have low melting temperature, 221 and 280 °C respectively, therefore annealing to 250 °C could affectively promote diffusion or even cause melting considering the phases to be nanosized. Based on this assumption together with the BSE images it can be reasonably assumed that the dark triangles represent holes in the detached layer (in other words, the inner ceiling of the buckles). This layer clearly has a memory of the orientation of the substrate which consequently influences the orientation of the holes. On the other hand, the bright spots could be agglomerates of metallic Bi, which was identified in the XPS and TEM measurements. EDX analysis was carried out to verify this. However, it could not confirm the composition of bright spots, and further investigations are necessary for this.

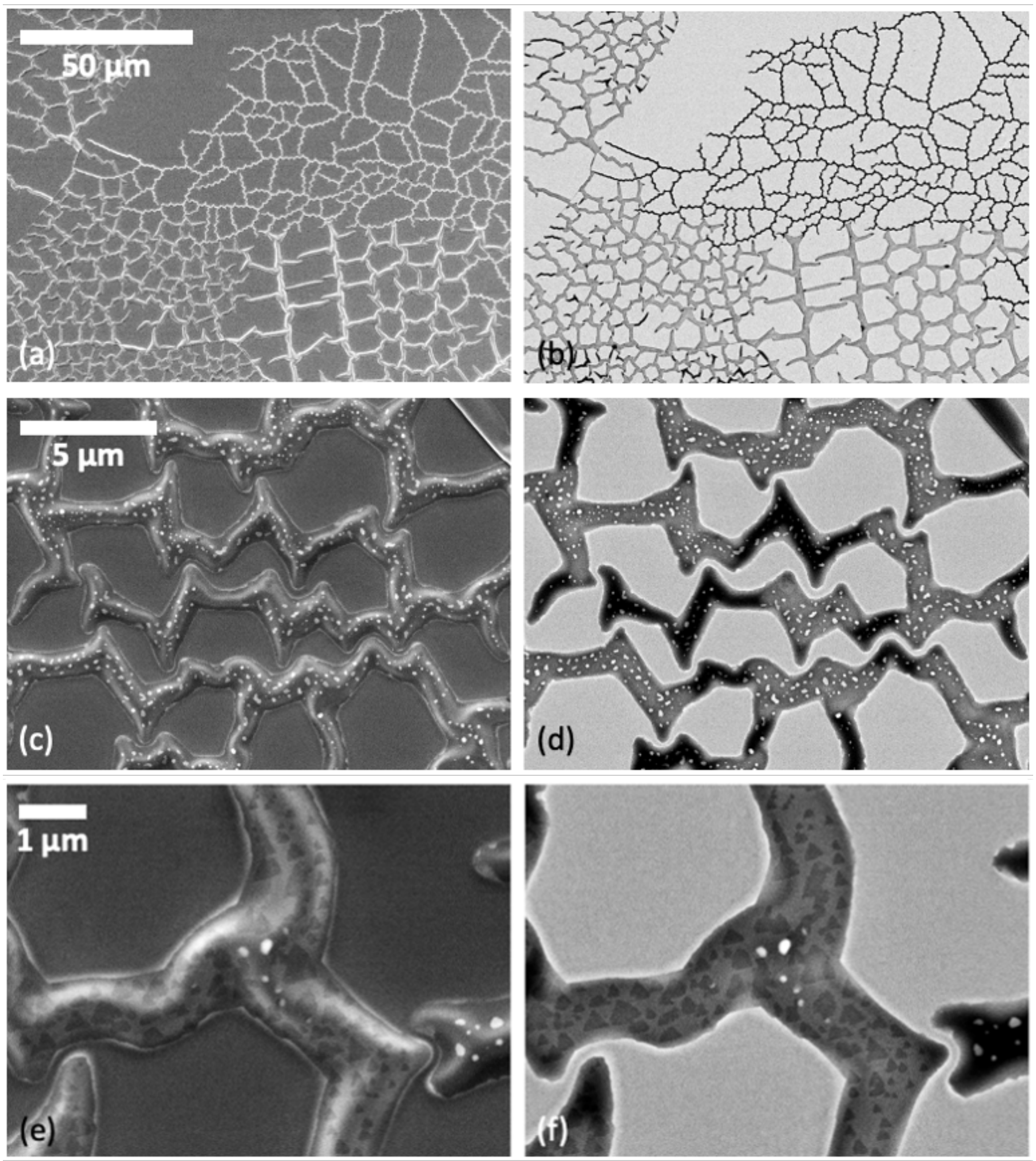

Figure 92: Comparison of the secondary and backscattered electron images of the 40 nm thick Ti film on Bi_2Se_3 at small magnification (a,b) and of bright features (c,d) and dark triangles (e,f) on the buckles.

4.5 Summary and conclusions

The interface between Ti and Bi_2Se_3 was studied by means of microscopy and spectroscopy techniques. Characterization of growth mode using STM and SEM showed that deposition of Ti initially results in bimodal formation of islands with subsequent growth of clusters on top of the preexisting islands. The island growth gets hindered well before the completion of a full layer. Correspondingly, a substrate modification (coarsening) occurs, which likely prevents the diffusion of Ti atoms. The substrate change is most probably a result of the chemical reaction between Ti and substrate species.

XPS measurement revealed that the Ti/Bi_2Se_3 interface is highly chemically unstable at RT and results in a chemical interaction, producing metallic Bi and titanium selenides. Reaction has been detected also at 130 K, which indicates significant reaction kinetics and reactivity at the interface already at this cryogenic temperature. TEM cross-section analysis showed an approximately 10 nm wide interface region containing interface phases of Bi and $TiSe_2$, further supporting the observations obtained with the XPS. Based on the location of produced interfacial phases it can be assumed that the reaction evolves by diffusion of selenium atoms out of Bi_2Se_3 and into Ti film. Since this is a solid-state reaction, it is limited by the diffusion of reacting species.

Based on the results, the following reaction at the interface is proposed:

$$2Bi_2Se_3 + 3Ti \rightarrow 3TiSe_2 + 4Bi$$

Scheme of the interface, which is formed within the reaction is presented in Figure 93.

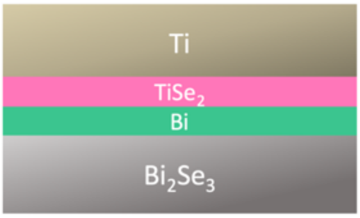

Figure 93: Scheme of the Ti/Bi_2Se_3 interface.

SEM analysis of higher Ti coverages (> 5 nm) resulted in the formation of a film without any visible surface features that homogenously covers the whole substrate surface. After a certain "buckling threshold" thickness is reached (between 20 and 40 nm) the Ti film exhibits webs of buckles of different sizes. This drastic change in the morphology is due to the buckle delamination process, which is caused by relaxation of compressive stress in the film. The interface reaction contributes to buckle delamination both by increasing the compressive stress, since the Se atoms are absorbed into the Ti film, and by the formation of the metallic Bi phase which enables the sliding of the film.

For thickness below the "buckling threshold", the morphology of the Ti film is stable in time at RT (and up to 250 °C). The same is true for the flat part between buckles observed at higher thickness. The only observed effect of annealing at 250 °C is the partial degradation of the buckles inner ceiling, where formation of bright spots and dark triangular features is observed.

5 Pt/Bi_2Se_3 INTERFACE

In this chapter, electron microscopy imaging of Pt/Bi_2Se_3 interface is presented. Measurement was performed on Bi_2Se_3 single crystal with different coverages of Pt film using SEM, TEM and EDX.

5.1 Growth mode and morphology of Pt on $Bi_2Se_3(0001)$

Metal film morphology was studied by means of SEM at coverages of 5, 10, 15 and 20 nm. The deposition was performed from vapor phase by means of PECS apparatus. The cleaving and deposition procedure, where a Pt target of 99.95% purity was used, are similar to the one for Ag and Ti described in the previous chapters (see Sections 2.7.4 and 2.7.5). In Figure 94 a comparison between pristine and Pt covered Bi_2Se_3 is presented, where the differences in the surface morphology are visible. At the Pt coverage of 5 nm bright features are observed that become more pronounced with increased coverage (their size is 12 nm with $\sigma = 2$ nm). Morphology of the Pt film on the surface steps exhibits the same morphology as on the terraces, indicating that the deposited metal does not preferentially nucleate on the surface steps. No clear edge between the metal and the substrate, that would enable us to unambiguously identify islands (as for Ag), could be distinguished with the resolution of the SEM. Surface morphology at 15 nm and 20 nm coverage is similar to the one at 10 nm coverage.

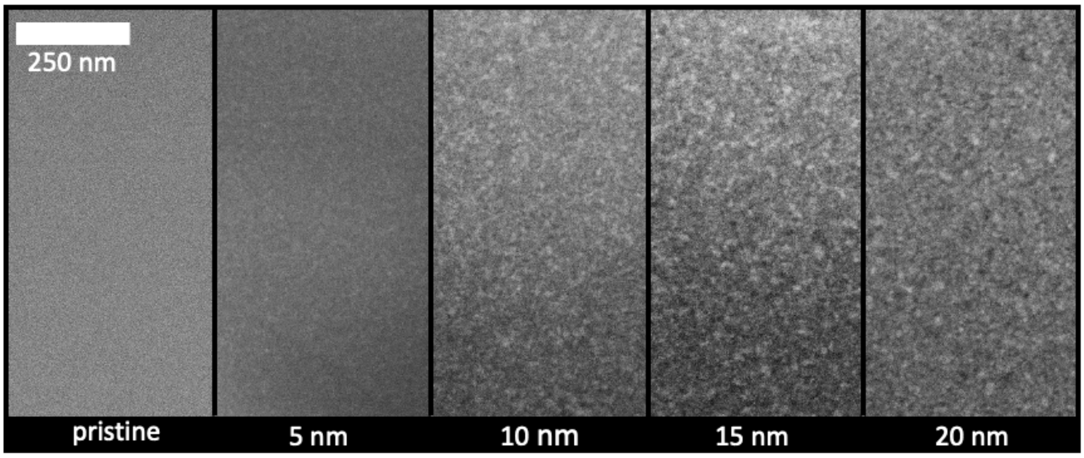

Figure 94: SEM images of pristine Bi_2Se_3 and Pt/Bi_2Se_3 interface at different film thickness.

Stability of the Pt film was checked by repeating the measurement after samples being kept at ambient conditions for a period of weeks. In Figure 95 SEM images of

10 nm thick Pt film are presented showing no morphological change upon aging. The result show that the interaction at the interface at ambient conditions reached an equilibrium shortly after deposition, unlike in the case of Ag where evolution of the surface was observed in the timescale of days.

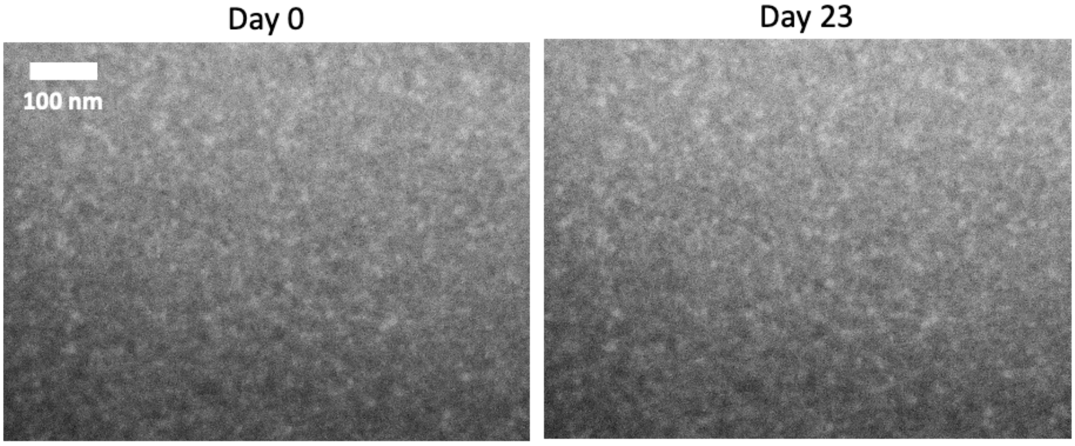

Figure 95: SEM image of Pt covered Bi_2Se_3 after the deposition and after the sample was kept at ambient conditions for 23 days.

Morphology of Pt film significantly differs from the morphology of Au film on Bi_2Se_3 [79], although both are noble metals and lie close together in the periodic table. Deposition of Au at RT results in the formation of well-defined 3D clusters [79], whereas Pt film exhibits small bright features without a clearly visible edge. From the aspect of the strength of the chemical bond between the Pt atoms in a metal and the metal free energy we would expect Pt to result in the island growth mode similar to what was observed at the Au/Bi_2Se_3 interface, since the bond energy between Pt atoms is higher than for Au (Pt-Pt: 306.7 kJ/mol, Au-Au: 226.2 kJ/mol [178])

Surface diffusion coefficient of a metal gives additional explanation for the morphology of metal thin films. Although these coefficients have not been calculated for metal/Bi_2Se_3 interfaces, an empirical relationship (proposed by Gjostein) for *fcc* metal surface self-diffusion D_s can give an estimation of the coefficient [179]:

$$D_s = 0.014 \exp\left(-\frac{\varepsilon T_M}{RT}\right), \qquad [7]$$

where ε is 54.4 $Jmol^{-1}K^{-1}$, T_M is the melting temperature of the metal, R is the gas constant 8.314 $Jmol^{-1}K^{-1}$ and T temperature. Figure 96 shows the dependence of the surface self-diffusion coefficient on temperature for Pt and Au calculated using equation [7] where melting temperature used for Pt was 2041 K and for Au 1337 K [84]. Several orders lower self-diffusion coefficient of Pt is due to the higher melting point of Pt. Consequently, the morphology of deposited Pt can be expected to result in the formation of smaller islands.

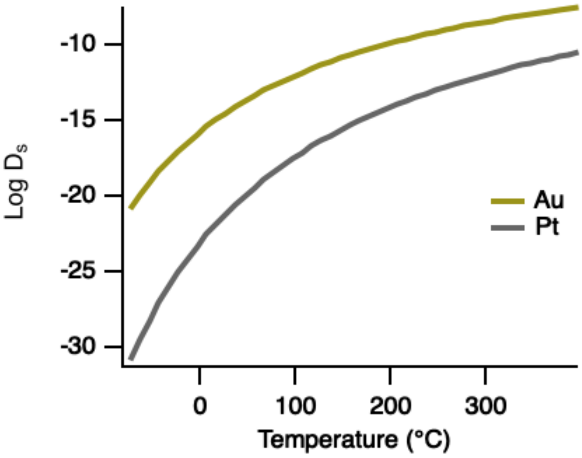

Figure 96: Dependence of the estimated surface self-diffusion coefficients on temperature for Pt and Au based on equation [7].

Such observation was reported by Francis *et al.* [180], who studied the morphology of *fcc* metals on ceramic substrates. In the case of Pt, the film deposited at 200 °C was almost completely flat (rms = 1 Å), whereas the Au atoms at the same temperature arranged themselves to form grains (rms = 34 Å).

Due to slow diffusion of Pt atoms the morphology of the Pt film is expected to wet the surface already at a low coverage. Continuity of the film the morphology was studied by resistance measurement, since a continuous film has lower resistivity. The reported values for the minimum thickness of the continuous Pt film are below 4 nm [181, 182].

Very important parameter when studying the growth morphology is also the interfacial energy between the deposited atom and the substrate. Stronger interaction at the interface compared to the interatomic interaction results in flatter morphology of the film. As is the interfacial energy affected by the oxygen affinity of the deposited metal on ceramic oxide substrates [180], the analogy can be made with the affinity of metal towards Se, which terminates the Bi_2Se_3 surface. The comparison of the Gibbs free energy of formation for the metal selenide ($\Delta_f G^{\circ}_{PtSe2} = -74$ kJ/mol [183], $\Delta_f G^{\circ}_{AuSe} = -36$ kJ/mol [177]) suggests higher selenium affinity for Pt than for Au. The observed morphology of Pt film on Bi_2Se_3 can therefore be the result of low diffusion coefficient (at RT) and/or it is due to a strong interaction at the Pt/Bi_2Se_3 interface.

In summary, SEM imaging showed that the morphology of the Pt film is different compared to other studied metals within this work and forms a homogenous film made of small features. Even though the resolution of SEM images cannot prove it, the hypothesis is that the film is made of clusters. This hypothesis is realistic considering the available literature of Pt films on different substrates and comparing the self-diffusivity, the Gibbs free energy of formation for the metal selenide and the morphology between Au and Pt on Bi_2Se_3. The system appears stable and does not undergo any morphology evolution at ambient conditions in the timescale of weeks.

5.2 Thermal stability

Thermal stability experiment was performed on a heating stage in the SEM apparatus. The studied sample of Bi_2Se_3 had deposited Pt film with the nominal thickness of 10 nm. Morphological changes were monitored within the temperature range from 25 to 375 °C with temperature increase steps of 25 °C.

Pt film proved to be stable below 350 °C since no visible change of the surface was observed (see Figure 97). After reaching the temperature of 350 °C morphological changes start to appear as shown in Figure 98.

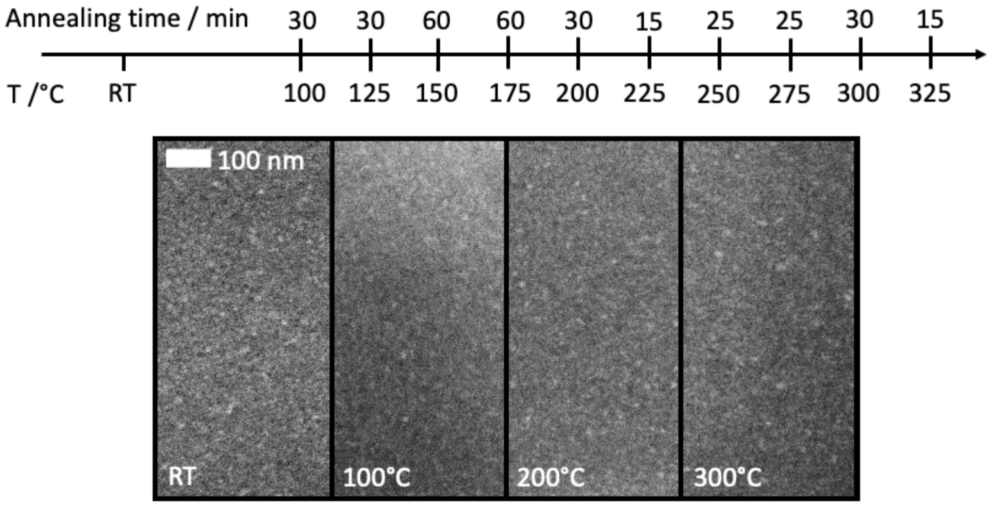

Figure 97: SEM images of Pt/Bi_2Se_3 interface at temperatures from RT to 300 °C. Annealing time represents the total amount of time the sample was kept at specific temperature.

At 350 °C the surface features become sharper and result as small clusters with an average diameter of 9 nm (σ = 2 nm) (Figure 98, annealing for 38 min). By keeping the sample at this temperature, the surface further evolved with previously visible clusters disappearing (see Figure 98, annealing for 48 min). Increasing the temperature to 375 °C led to the appearance of a speckled surface and formation of round dark spots that have a diameter smaller than 20 nm. The final morphology, where the dark spots are marked, is presented with higher magnification in Figure 99.

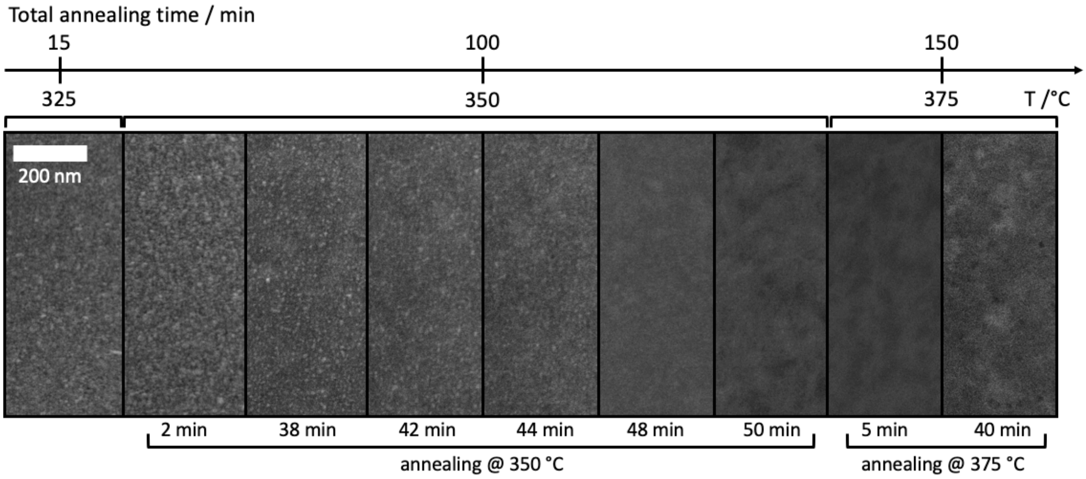

Figure 98: SEM images showing the evolution of the Pt/Bi₂Se₃ surface morphology at different annealing temperatures and times at Pt coverage of 10 nm.

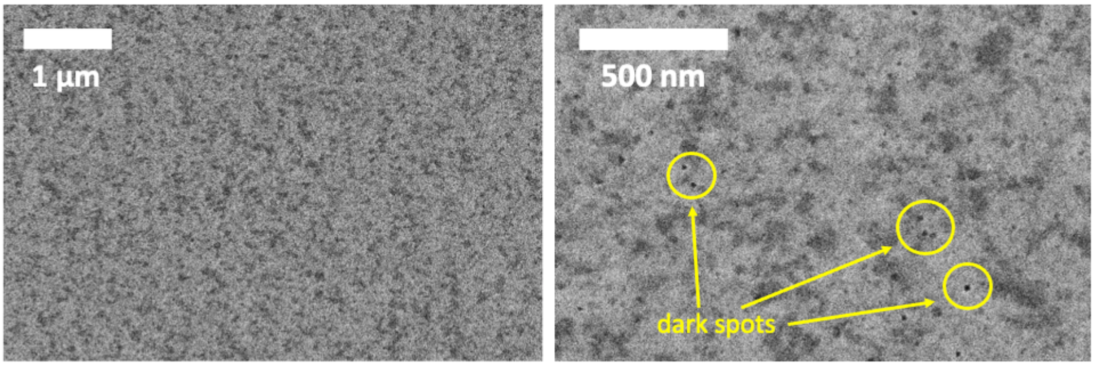

Figure 99: SEM images of Pt/Bi₂Se₃ interface at Pt coverage of 10 nm after annealing at 375 °C at lower (left) and higher (right) magnification.

Second annealing experiment was performed with 20 nm thick Pt film on Bi_2Se_3 single crystal. Sample was heated in a tube furnace under N_2 atmosphere at a rate of 8°C/min until reaching the temperature of 375 °C. Then it was annealed at this temperature for 1 hour and cooled down with a rate of 8 °C/min.

Figure 100 shows the surface of a 20 nm thick Pt film before and after annealing in N_2. The microstructure after heat treatment is different from the one observed in the first experiment. The surface appears more defective and the dark spots can exceed the diameter limit of 20 nm. The difference in the morphology between the two experiments is due to different Pt thickness and different annealing conditions.

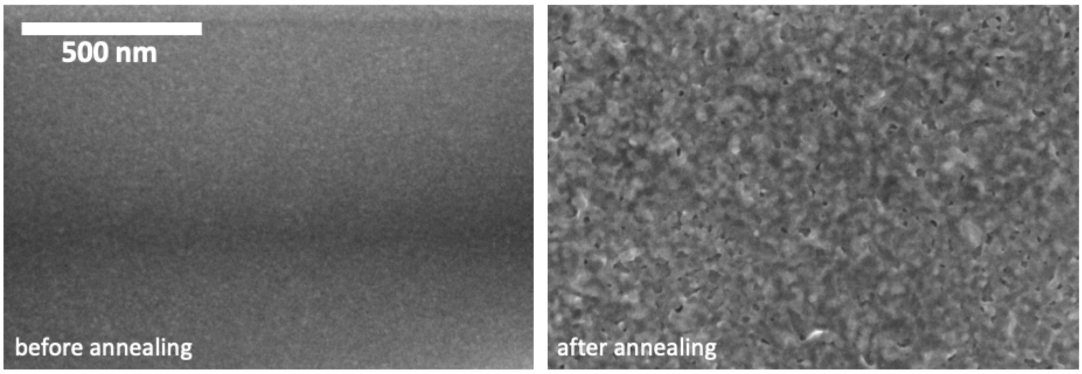

Figure 100: SEM images of Bi_2Se_3 surface covered with 20 nm of Pt before and after annealing under N_2 atmosphere at a temperature of 375 °C. The image scale is the same.

Figure 101 shows the comparison of the normalized EDX spectra before and after annealing. As visible, the signal of Pt is reduced.

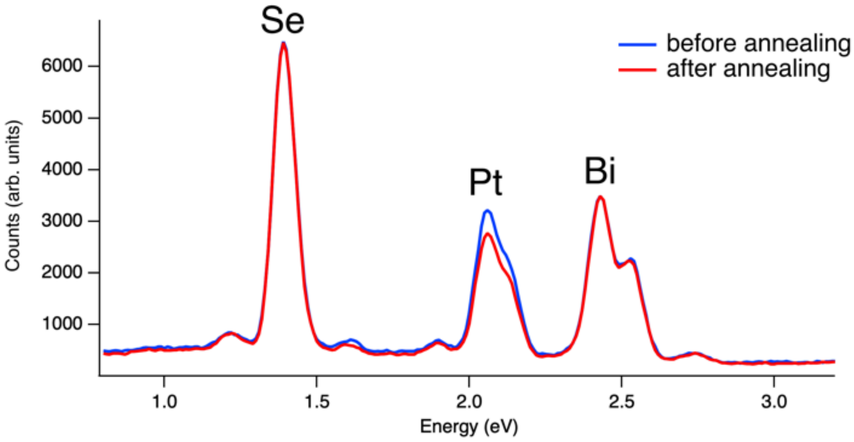

Figure 101: EDX spectra of 20 nm thick film on Bi_2Se_3 substrate before and after annealing at 375 °C under N_2 atmosphere.

Morphology evolution observed at 350 °C cannot be explained as the result of coalescence. The change can be described with the increased absorption of Pt atoms in the Bi_2Se_3 crystal - confirmed with the decrease of intensity of the Pt peak in the EDX spectra (similar effect was observed at the Ag/Bi_2Se_3 interface) - and the formation of a new phase, which results in the reshaping of surface features.

Studies regarding the morphology of annealed Pt films that are found in the literature are usually performed at temperatures above 400 °C either to control the film morphology and orientation or for protection of systems operating at HT in oxidizing environment [180, 184-187]. Different scenarios upon annealing of Pt films have been observed depending on the chosen substrate.

When non-reactive oxide substrates were used (sapphire, glass) annealing resulted in dewetting of the surface [184, 188]. The microstructure of the surface underwent reconstruction from a continuous layer to formation of bigger grains and voids, which increased in size with increasing temperature, becoming significant at 700 °C. The described morphological change is due to the increased diffusion of Pt atoms. Increase of the grain size improves crystallinity of the film and decreases the micro-strain that is accumulated in the film. Similar process upon annealing was observed for deposited Au on Bi_2Se_3 but already at lower temperatures (275 °C). Resulting surface morphology is presented in Figure 108.

Annealing of Pt film on other (more reactive) substrates can result in other processes, as is the occurrence of a chemical reaction. In the article of Strobel *et al.* [186] the dewetting behavior upon annealing of Pt thin films on silicon was studied and morphology evolution was monitored. Annealing resulted in a droplet formation and in formation of silicides above the temperature of 700 °C. In the studies of Conforto *et al.* [189, 190] where Pt was deposited by sputtering on Si substrate at 165 °C a solid-state reaction occurred already during the deposition process, producing Pt_2Si and other platinum silicide phases. The mechanism and evolution of this reaction is highly dependent on the thickness of the native silicon oxide layer, since the interdiffusion and reaction depend on the size and on the density of the oxide pinholes. Similar observation as on Si was detected with SiC substrates where the reaction was observed upon annealing at 500 °C [191, 192], but it occurred already during the deposition on a heated substrate (at 200 °C) [192]. The difference is due to increased reactivity of nano-sized materials, in this case of the incoming Pt atoms in the deposition process. Annealing of Ti/Pt interface results in diffusion of Ti into Pt layer and formation of $TiPt_8$ and $TiPt_3$ compounds [193, 194]. This reaction is observed at 500 °C. Interface reactions upon annealing Pt films were reported also for other substrates, e.g. with GaN at 550 °C [195] or with Al above 200 °C [196].

Based on the reported literature, the morphological changes observed in our experiments better fit into scenario where a chemical reaction occurs at the interface, since the annealing did not result in dewetting of the Pt film, but in reorganization of Pt atoms in the film and their absorption into Bi_2Se_3 crystal (confirmed by EDX).

5.3 TEM cross-section analysis

A 20 nm thick layer of Pt was deposited on Bi_2Se_3 single crystal. Sample for cross-section analysis was afterwards prepared for TEM observation following the standard procedure (see Section 2.7.6). During the preparation, in order to cure the epoxy resin, the sample was heated at about 90 °C for 1h.

Figure 102 and Figure 103 show the TEM and STEM images of the Pt/Bi_2Se_3 interface. Three phases are clearly distinguished: the Pt film, the Bi_2Se_3 crystal (with visible QLs) and the interfacial region in between. The diffraction pattern obtained from the Pt film is presented in Figure 102b, showing that the film is polycrystalline. The interface region is approximately 8 nm thick and exhibits layered structure which differs from the QL of Bi_2Se_3 as can be seen from the comparison of Fourier transform (FT) images in Figures 102cd giving different distances between the layers (5.4 and 9.6 Å for the interface region and the Bi_2Se_3, respectively). The observed periodicity proves that the interface region is certainly a different phase and not just artefacts of Bi_2Se_3 structure given by the local bending. The interface phase is homogenous and the distance between the atomic planes measures 5.4 Å. An atomically sharp boundary is visible on the contact between Bi_2Se_3 and interfacial layer, whereas its interface with Pt is less sharp. The contrast observed with STEM (Figure 103) around the interface region suggests that the density of the interface phase is between the density of Pt and the one of Bi_2Se_3.

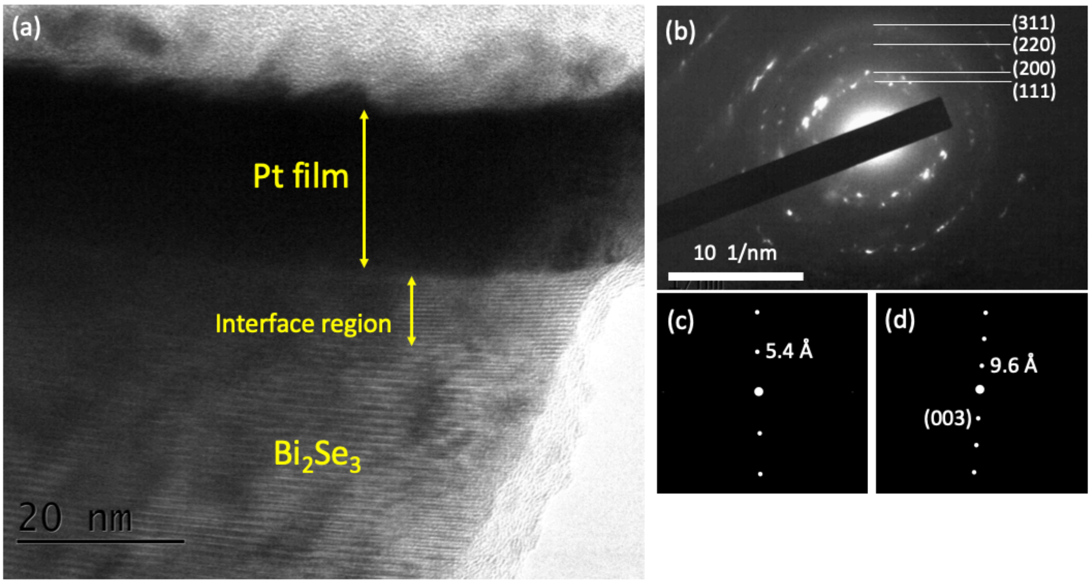

Figure 102:(a) TEM image of the Pt/Bi_2Se_3 interface region with marked areas of different phases. (b) SAED diffraction pattern taken from the region of the Pt film. Enhanced FT images of the interface region (c) and Bi_2Se_3 phase (d).

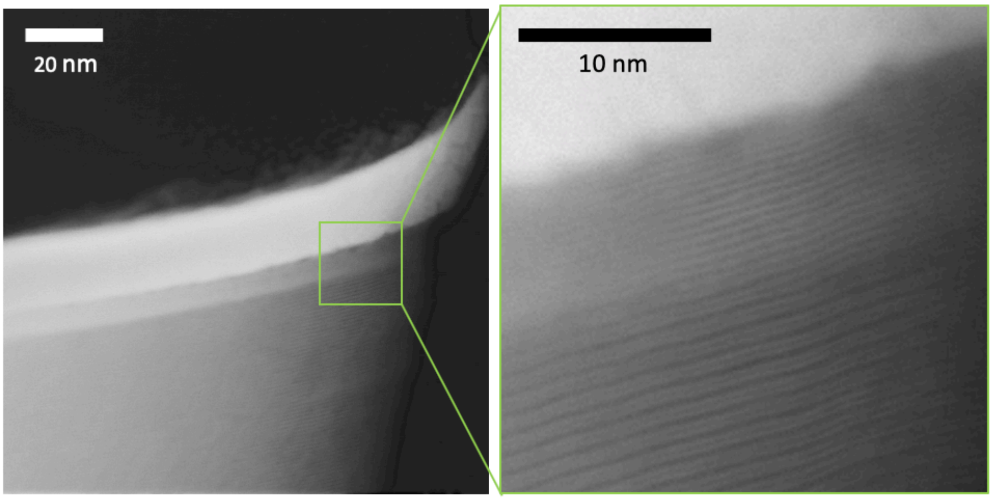

Figure 103: STEM cross-section image of Pt/Bi_2Se_3 interface at different magnification.

EDX line-scan over the cross- section area is shown in Figure 104. Curve representing the Pt signal is not symmetric and has a higher slope on the left side (top surface) than on the right side (interface). Intensities of Bi and Se signals within the interfacial region are similar to the intensities of the substrate. These results suggest that Pt is present in the metal film as well as in the interfacial layer together with Bi and Se.

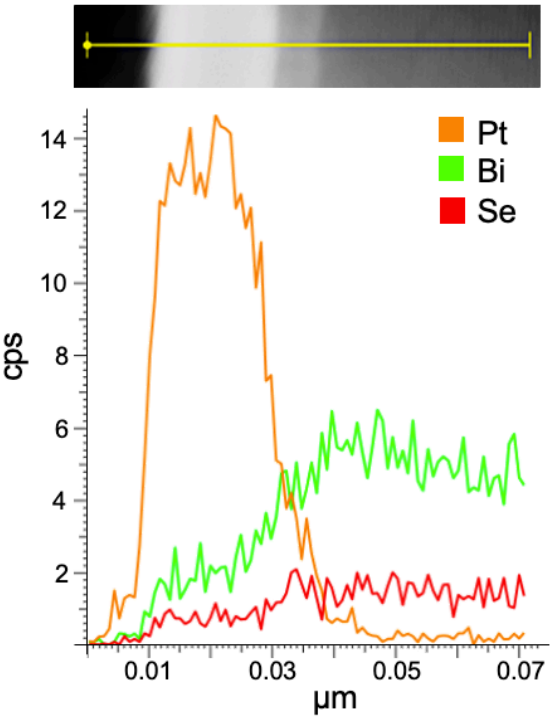

Figure 104: EDX linescan over the cross-section area of Pt/Bi_2Se_3 interface.

The possible composition of the interface phase observed with TEM tried to be determined based on the known compounds and the literature data. One hypothesis is that the interface region is composed of PtBi, ordered intermetallic compound, since the diffraction spots observed in Figure 102c fit well with the diffraction from (001) and (002) atomic planes (5.490 and 2.745 Å, respectively). The second possibility is that the interface layer is $PtSe_2$. This compound is layered and the reported interplanar distance of the (001) plane is 5.4 Å [197] or 5.3 Å [198]. Both compounds, PtBi and $PtSe_2$, also have a density between the one of Pt and of Bi_2Se_3, in agreement with the observed contrast shown in Figure 103. However, in both of these hypotheses, there is a question of the location of the remaining element, Se or Bi. Also, the EDX data does not favor any of those possibilities, since signals from both Bi and Se are present simultaneously in the interface region. The third option is therefore a ternary compound composed from all three elements. In the literature it is possible to find PtBiSe compound, a mineral of selenium not specified by name which has been incompletely investigated [199]. A handful of articles mentioning this compound can be found, where the compound is described as having metallic character and crystallizing in pyrite structure [200-203]. However, ternary compounds of other elements of the Pt group have been better characterized, especially $Bi_2Pd_3Se_2$, which was found to have superconducting properties [204, 205]. This suggests that ternary compounds of Bi, Se and Pt do exist, but are still to be investigated. Since Pt in compounds is present in +2 and +4 oxidation state, two hypothetical compounds could be formed at the interface, Bi_2PtSe_4 or Bi_2PtSe_5 respectively. Regardless of which of these two compounds is formed, Bi has to be formed within the reaction as well and can exist in its metallic form or as an intermetallic compound BiPt.

Figure 105a shows another TEM image of the interface cross-section where atomic plane periodicity is distinguished in a part of the interfacial region. Figure 105b shows FT image made from that part. The pattern was compared with the elements and known compounds of Bi, Se and Pt with available crystal structures, namely: $PtSe_2$, Pt_5Se_4, PtBi, Pt_2Bi, Bi_2Se_3, BiSe, Bi_4Se_3, but none of them fit. Therefore, the theory of a newly formed ternary phase, based on the results, seems most plausible.

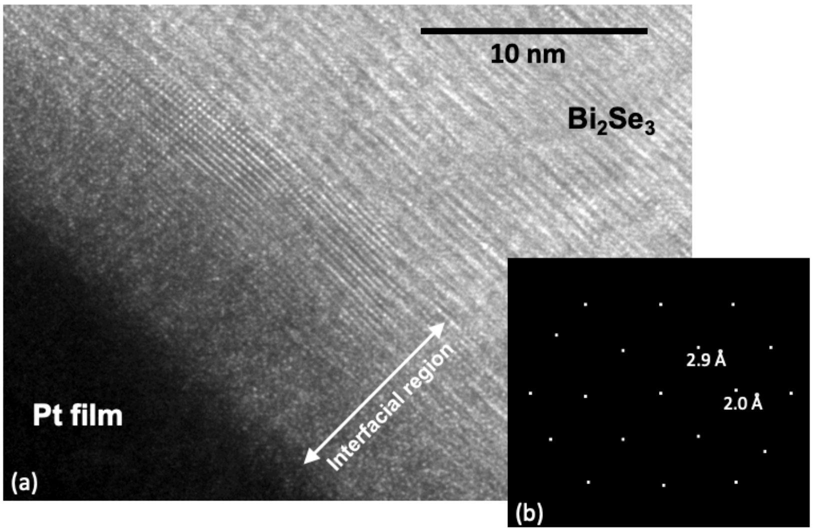

Figure 105: High-resolution TEM image of the Pt/Bi_2Se_3 interface (a) and an FT image of the area where individual rows of atoms are distinguished (b).

5.4 Summary and conclusion

Morphological analysis of Pt film on Bi_2Se_3 by means of SEM showed that Pt homogenously distributes over the whole surface, forming a compact layer with small features. No difference in morphology was observed at the steps. The morphology is stable at ambient conditions showing no observable change in the timescale of weeks.

Upon annealing, the Pt/Bi_2Se_3 film did not exhibit visible change below 350 °C. Afterwards the surface underwent morphological changes, together with absorption of Pt atoms below the surface, as confirmed by EDX analysis. Such transformation suggests an interaction between the Pt film and Bi_2Se_3 substrate, very likely in the form of a chemical reaction.

TEM cross-section imaging showed that the deposited Pt is a polycrystalline film. The interface region between Pt and Bi_2Se_3 exhibits a layered crystalline homogenous phase with an interlayer distance of 5.4 Å. No solid proofs of the interface being composed of any of the known compounds from Bi, Se and Pt was found and the EDX analysis suggests that the interface phase is a ternary compound, formed due to the absorption of Pt atoms into the Bi_2Se_3 crystal.

6 TRENDS IN METAL/Bi_2Se_3 INTERFACES

Previous chapters described the morphological and chemical properties of interfaces between chosen metals and Bi_2Se_3 topological insulator. The aim of this chapter is to compare the obtained results and extract the origin influencing the different behavior of individual metals as well as to predict the possible products of chemical reactions that were observed. For better comparison, especially between the noble metals, the interface between Au and Bi_2Se_3 will also be discussed in this chapter. Study of the Au/Bi_2Se_3 interface was performed by other members of our laboratory who found that deposition of Au by PVD at RT results in Volmer-Weber growth mode [79]. Core level analysis of the interface highlighted the diffusion of Bi toward the surface of Au islands, while the interaction between Au and atomic Se is limited to the interfacial region.

6.1 Comparison of morphology between different metal/Bi_2Se_3 interfaces at RT and upon annealing

Au, Ag, and Ti, which were studied from the early stages of deposition by STM, all resulted in the formation of islands of different geometries (see Figure 106): Au atoms arranged into minimum 2 nm big dome-shaped islands, whereas Ag and Ti formed islands that were bigger in the lateral dimension than in height. The lowest aspect ratio was found in the case of Ti, where the top surface of islands was found to be flat.

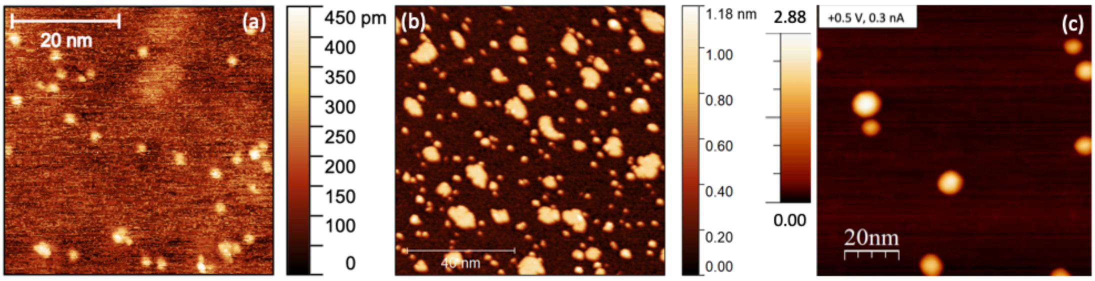

Figure 106: STM images of Bi_2Se_3 with deposited: (a) Ag at a coverage of 0.3 Å ($U=-0.7$ V, $I=0.1$ nA), (b) Ti at a coverage of 0.2 Å ($U=-0.3$ V, $I=0.05$ nA) and (c) Au at a coverage <2 Å ($U=0.5$ V, $I=0.3$ nA).

Morphological difference between Au, Ag, Ti and Pt on Bi_2Se_3 was observed also at higher film thicknesses studied by means of SEM as shown in Figure 107. Au is present in the form of islands, which were formed by connection of round islands upon increase of metal deposition. Deposited Ag forms islands as well. Compared to Au, more Bi_2Se_3 surface is left exposed due to formation of big agglomerates near the surface steps accumulating larger amounts of Ag atoms. SEM imaging of the third noble metal, Pt, shows the formation of smaller bright features without a sharp edge. The observed images are compatible with the assembly of very small islands into a continuous layer. Apart from the noble metals, the Ti film at this coverage does not show any surface features visible by SEM.

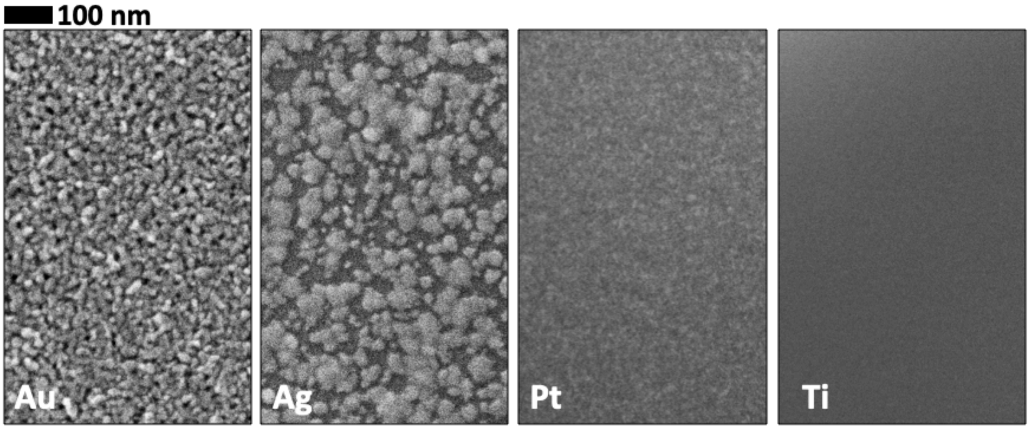

Figure 107: SEM images of metal films with 10 nm nominal thickness on $Bi_2Se_3(0001)$ surface deposited at RT.

While for Au, Pt and Ti the observed morphology at RT is stable in time (i.e. no detectable changes are observed in the timescale of days), for Ag this is not the case. By leaving the sample in air, the islands are observed to decrease their size and disappear, leaving behind a defected surface. EDX data confirmed that Ag is diffusing within the crystal at RT.

Significantly different behavior among the investigated metals is observed also upon annealing as presented in Figure 108. Heating of Au/Bi_2Se_3 interface results in the coalescence of Au islands that starts at 100 °C. With increasing temperature, the diffusion of Au atoms is increased and the metal forms big Au crystals with visible facets.

At the Ag/Bi_2Se_3 interface a morphology evolution in time with absorption of Ag into the crystal due to a chemical reaction was observed already at RT. In the annealing experiment the reaction is accelerated. Kinetics were found to greatly increase above 200 °C, resulting in complete decomposition of Ag islands and agglomerates in the timescale of minutes.

On the other hand, Pt does not show morphology change until much higher temperature (350 °C). At 90 °C a reaction occurs, generating a ternary phase with a thickness of a few nm at the interface. It is possible that the reaction happens already at RT, maybe at a lower extent. After reaching 350 °C modifications of the surface were detected, resulting in changed morphology of the surface features and absorption of the metal atom into the Bi_2Se_3 crystal, compatible with a chemical reaction with formation of a new phase.

A chemical reaction was detected (by XPS) already at RT (and also at 130 K) also for Ti/Bi_2Se_3 interface. However, Ti film of 10 nm thickness does not exhibit any morphology change upon heating. The stability of the Ti film morphology is likely due to the fast kinetics of the reaction, which rapidly results in the formation of stable interfacial phases already at RT. At 90-100 °C, this interface has a thickness of about 10 nm. After the formation of the interface, the reaction slows down to a point where the evolution is not detected any more (as observed by XPS).

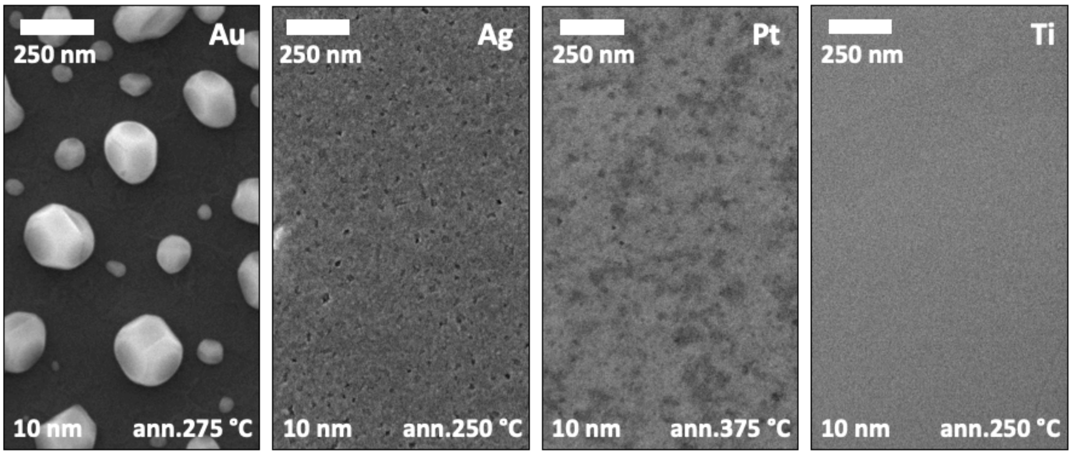

Figure 108: SEM images of metal/Bi_2Se_3 interfaces upon annealing.

Table 4 summarizes the results regarding the morphology and observed chemical reactions of the studied interfaces obtained within microscopy and other analytical techniques.

Table 4: Summary of the results.

Metal	Early stage morphology	Morphology at 10 nm coverage	Morphology change in time at RT	Evolution at HT	Reaction products at RT
Au	Dome-shaped islands	Islands	No change	Coalescence	Only weak interaction (diffusion of Bi into Au)
Ag	Islands	Islands + agglomerates at the surface steps	Absorption and reaction of Ag	Reaction acceleration	**Ternary and binary** ($AgBiSe_2$, Ag_2Se) + Bi
Pt	?	Homogenous film with small features	No change	Microstructure change + absorption of Pt	(possibly) **Ternary** (Pt-Bi-Se)
Ti	Islands with low aspect ratio	Homogenous film without visible features	No change	No change	**Binary** (Titanium selenides) + Bi

Morphology of Au, Ag and Ti indicates that, immediately after the deposition, metal atoms are able to diffuse over the surface to form islands. Such result can be expected: the surface of Bi_2Se_3 does not have any dangling bonds or reactive sites which would hinder the diffusion of adsorbed atoms. In this work, the highest diffusivity was noticed in the case of Ag, which also fits with the behavior expressed in equation [7], since Ag has the lowest melting point of the three.

Considerations on the free energy and the mobility of metal atoms can partially explain some aspects of the observed growth modes, morphology and high temperature evolution of the metal films. For example, they can explain the morphology of Au film, which can be assessed as Volmer-Weber growth mode [79], and also its evolution upon annealing. Coalescence and formation of Au crystals shows on preferential bonding between Au atoms than between Au and the substrate. Moreover, they can explain the difference in the Au and Pt morphology at RT, which is due to lower diffusion of Pt compared to Au, whereas the mobility of Ag is even higher than for Au and give rise to also to large agglomerates.

However, a growth model which does not consider the absorption of the metal into the substrate and the occurring of a chemical reaction with formation of new phases soon shows its limitation, and cannot be appropriately used for Ti, Ag and Pt (and most of the metals reported in literature) on Bi_2Se_3. The detected solid-state interfacial reactions, in fact, play a major role in defining the interface structure, and, for this reason, it is important to focus on the interface chemistry to find trends to predict if and which reactions will take place at the interface.

6.2 Predicting interfacial reaction between a transition metal and topological insulator

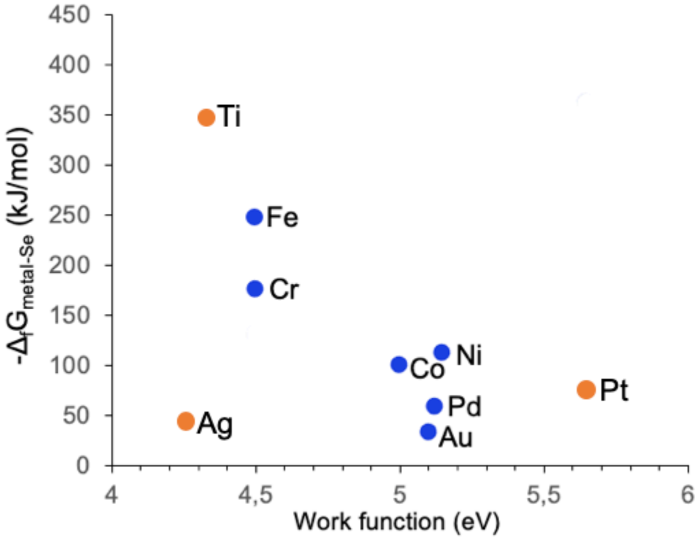

Figure 109: A scatter plot adapted from [112] showing the $\Delta_f G°$ for the metal-Se alloy as a function of metal vacuum work function. Considered metal selenides are: Fe_3Se_4, Cr_2Se_3, $CoSe_2$, $PdSe_2$, $NiSe_2$, AuSe, Ag_2Se, $TiSe_2$ and $PtSe_2$. (Blue dots are taken from [112], orange ones are added based on our research.)

A reactivity model was proposed in a work by Walsh *et al.* [112], where some transition metals/Bi_2Se_3 interfaces are investigated. Detectable reactions were observed for all studied metals except Au. Reactivity was described based on the produced interfacial phases, where reactions with the highest reactivity resulted in the formation of metal selenide and metallic Bi. With decreasing reactivity, a ternary phase is additionally formed, whereas the least reactive metals produce only a ternary phase. Metals with lower work function were predicted to demonstrate higher reactivity and this model fits well also with the metals used in our study. Walsh model states that the reactivity is not only influenced by the work function of metals but also by the Gibbs free energy of formation for the metal selenide ($\Delta_f G_{metal-Se}$) at RT, where lower $\Delta_f G$ value means lower reactivity (see Figure 109). Although the connection between the work function and $\Delta_f G$ fits well for Ti, the model is only partially true for the case of Pt: based on $\Delta_f G$ it fits among metals with lower reactivity, but the high work function value should make Pt even less reactive than Au. Also, the model does not correctly predict the situation observed with Ag. According to it, the low $\Delta_f G$ for Ag_2Se places reaction between Ag and Bi_2Se_3 among the least favored, and only ternary compound would be expected (as for Pd and Ir). This is in contrast to what was observed in our research.

Since all reported interactions are in fact redox reaction where the deposited metal gets oxidized, we believe it is more appropriate to use standard reduction potentials, E^0, in order to describe them. In general, metals with lower $E^0$are more easily oxidized than the ones with higher potential. Table 5 gives E^0 values for the metals that were reportedly interfaced with Bi_2Se_3 [79, 112, 206]. In has to be noted that E^0 values are relative to the standard hydrogen electrode and were obtained from potential difference measurements in a galvanic cell where solutions of particular metal species were used.

Table 5: Selected standard reduction potentials (at 298 K and 1 atm). [207, 208]

Reaction	E_0 [V]
$TiF_6^{2-} + 4e^- \rightarrow Ti(s) + 6F^-$ *	-1.19
$Cr^{3+} + 3e^- \rightarrow Cr(s)$	-0,74
$Fe^{2+} + 2e^- \rightarrow Fe(s)$	-0.44
$Co^{2+} + 2e^- \rightarrow Co(s)$	-0.28
$Ni^{2+} + 2e^- \rightarrow Ni(s)$	-0.24
$Bi^{3+} + 3e^- \rightarrow Bi(s)$	0.31
$Cu^+ + e^- \rightarrow Cu(s)$	0.52
$Ag^+ + e^- \rightarrow Ag(s)$	0.80
$PtO_2(s) + 4H^+ + 4e^- \rightarrow Pt(s) + 2H_2O$ *	0.92
$Pd^{2+} + 2e^- \rightarrow Pd(s)$	0.95
$Ir^{3+} + 3e^- \rightarrow Ir(s)$	1.16
$Au^+ + e^- \rightarrow Au(s)$	1.69

* Direct transformation from M^{4+} to M (s) could not be found, therefore such species are used in the table.

In order to evaluate if a reaction happens spontaneously, the Gibbs free energy of reaction, $\Delta G_r{}^0$, has to be calculated. The relation is given as

$$\Delta G_r{}^0 = -zFE_{cell}^0 \quad [8]$$

where z is the number of electrons transferred in the reaction, F the Faraday constant and ΔE^0 the potential difference between the species involved in the redox reaction. It is calculated as

$$E_{cell}^0 = E_{reduction\,process}^0 - E_{oxidation\,process}^0 \qquad [9]$$

using E^0 values from the tables. In order for the reaction to happen spontaneously, $\Delta G_r{}^0$ must be negative. Therefore, for the metals with E^0 lower than E_{Bi}^0 (i.e. 0.31 V) a reaction at the metal/Bi_2Se_3 interface can be expected. This shows that Ti can easily interact with Bi^{3+} in a redox reaction, whereas high value of E^0 makes Au very unlikely to participate in such process.

Based on E^0 values inertness could also be expected for Cu, Ag, Pt and Pd but the experimental data show the opposite. One of the reasons behind this discrepancy is in the fact that the tabulated values are based on electrochemical measurements in solutions at standard conditions, whereas in our case the redox reaction occurs in a solid state. For this reason, in order to describe the trends of the chemical interaction at metal/Bi_2Se_3 interfaces, it is appropriate to use a different approach to calculate $\Delta G_r{}^0$, as described in the next section.

6.3 Thermodynamics of reaction at metal/Bi_2Se_3 interface

The basic concept of the occurrence of chemical reactions is based on the thermodynamic properties of the reactants and products. At a constant temperature and pressure, the direction of any spontaneous change is toward a lower Gibbs free energy. From the literature it can be seen that the reaction of Bi_2Se_3 with a metal often results in the formation of metal selenides, bismuth metal selenides and metallic Bi [69, 76, 77, 109, 110, 112]. Although the data for such metal selenides can be easily obtained, on contrary the thermodynamic properties of ternary compounds $M_xBi_ySe_z$ are not available.

Using the available thermodynamic data for binary selenides, $\Delta G_r{}^0$ can be calculated and probability of a reaction between transition metals and Bi_2Se_3 can be estimated. A model reaction is proposed

$$Y\, Bi_2Se_3 + 3X\, M \rightarrow 3\, M_XSe_Y + 2Y\, Bi$$

Table 6 gives $\Delta G_r{}^0$ for the model reaction with different transition metals calculated using the following equations

$$\Delta H_r{}^0 = \sum \Delta_f H_{products}{}^0 - \sum \Delta_f H_{reactants}{}^0 \qquad [10]$$

$$\Delta S_r{}^0 = \sum \Delta S_{products}{}^0 - \Delta S_{reactants}{}^0 \qquad [11]$$

$$\Delta G_r{}^0 = \Delta H_r{}^0 - T\Delta S_r{}^0 \qquad [12]$$

where $\Delta_f H^0$ is standard enthalpy of formation, ΔS^0 standard molar entropy, $\Delta H_r{}^0$ standard enthalpy of reaction, $\Delta S_r{}^0$ standard entropy of reaction and T temperature. In the last column of Table 6 reported experimental observations regarding the number and type of phases detected within the interfacial reaction are given.

Table 6: Calculated Gibbs free energy of reaction per mole of a metal, based on the model chemical reaction. All data refer to the reference temperature of 298.15 K and to the standard state. Thermodynamic data for Bi_2Se_3 were taken from reference [177].

M_XSe_Y	ΔG_r° (kJ/mol M)	Reference for thermodynamic data	Reported experimental observations (RT)
Ag_2Se	−0.04	[199]	Binary + ternary phase
AuSe	41.4	[209]	Weak interaction [79, 112]
$Co_{0.84}Se$	−11.4	[199]	Binary + ternary phase [112]
Cr_2Se_3	−53.9	[199]	Binary phase [112]
Cu_2Se	−12.4	[177]	Binary + ternary phase [99]
$Fe_{1.04}Se$	−22.4	[199]	Binary phase [112]
$Ni_{0.88}Se$	−22.9	[199]	Binary + ternary phase [112]
PdSe	−4.1	[183]	Ternary phase [112]
$PtSe_2$	19.4	[183]	Ternary phase (possibly)
$TiSe_2$	−256.3	[173]	Binary phase
TiSe	−175.2	[177]	

The lowest value of the $\Delta G_r{}^0$ is found for Ti compounds, making reaction between Bi_2Se_3 and Ti highly thermodynamically favorable and can be expected to occur at RT. It has to be taken into account that a negative value of $\Delta G_r{}^0$ is a necessary but not a sufficient condition for a reaction to take place spontaneously, since an activation barrier must be first surpassed. Interestingly, in majority cases $\Delta G_r{}^0$ has a negative value, showing on the possibility of the model reaction to occur. From the table it is also clearly seen that such reaction (i.e. the formation of binary metal selenide) with Au and Pt should not evolve.

Based on the $\Delta G_r{}^0$ value, the reaction of Ag is an edge case. However, redox reaction between Ag and Bi_2Se_3 than has been detected did not undergo the route of the model reaction. This implies that a ternary compound has to be formed which additionally decreases the free energy change of the reaction process and allows for the reaction to occur. In some cases, even the formation of a ternary compound is not enough for the reaction to evolve at RT, as was detected for Au.

Figure 110 shows how $\Delta G_r{}^0$ for the model reaction varies with standard reduction potential of the metal. Chosen selenides represent the basic selenide compound for each metal. Although, only a fraction of transition metals is used in the diagram and the $\Delta G_r{}^0$ is based on a model reaction, a trend can be extracted. As described in Section 6.2, metals with low E^0 can easily oxidize and, as calculated, they also have the lowest $\Delta G_r{}^0$. Only one binary phase (metal selenide) is produced within the reaction with the corresponding metals. With increasing E^0, a region where binary and ternary compounds are formed is reached. Although metals with positive E^0 are less prone to oxidation, two such metals are found in this region (Cu, Ag). E^0 interval coinciding with the region where ternary phase was detected is limited by E^0 for Pt^{4+} and Ir^{3+}. Since there is no thermodynamic data available for Ir_2Se_3, $\Delta G_r{}^0$ could not be calculated. $\Delta G_r{}^0$ for $PtSe_2$ indicate that Pt should not form an interfacial phase with Bi_2Se_3 (although the value is much lower than of Au, which does not react). However, E^0 places Pt close to Pd, suggesting that a reaction where a ternary phase is formed, which would lower $\Delta G_r{}^0$, could be expected.

Comparison of E^0 and $\Delta G_r{}^0$ for the not yet studied transition metals with the diagram in Figure 110 presents a useful approach to evaluate the possibility of an interfacial redox reaction and for prediction of the products which are formed within such interaction.

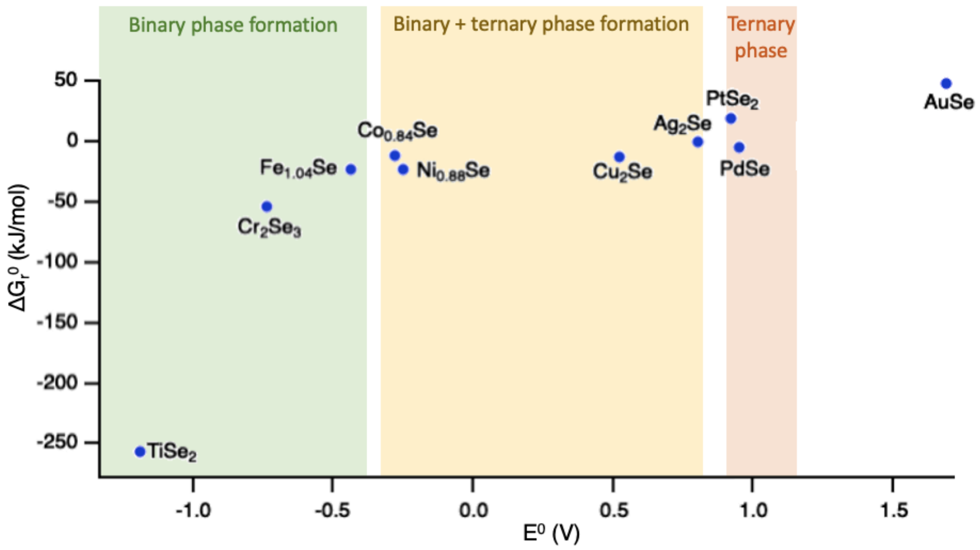

Figure 110: Diagram of $\Delta G_r{}^0$ for the model reaction versus standard reduction potential E^0 for selected transition metals.

6.4 Catalytic effect of topological surface states

The occurrence of a solid-state reaction between a metal and a covalent crystal at RT is uncommon. Also, the surface of Bi_2Se_3 does not display any dangling bonds or unsaturated orbitals and it has been observed to be almost inert toward water, oxygen, CO and CO_2 [152, 210]. Consequently, interfacial reactions with Bi_2Se_3 at first appear unlikely to occur. However, chemical reaction at the metal/ Bi_2Se_3 interface at RT have been detected. In our study, the reaction with Ag spontaneously proceeds at ambient conditions, and the one with Ti was observed even at cryogenic temperature of 130 K. What is most surprising about such reactions are not their thermodynamics but their kinetics, suggesting unusually low activation barrier for these chemical processes. The observed reactions at the metal/Bi_2Se_3 interface described in Chapters 3-5, raise the question on the origin of the Bi_2Se_3 surface reactivity at such rate.

Observed chemical reactions suggest the presence of a catalytic effect within the studied system. Our hypothesis is that the TSS electrons participate in the reaction by catalyzing it and lowering the activation barrier for the reaction to occur. Although the TSS are a part of the reactant, they can still be regarded as a catalyst as long as they only participate in the reaction but are not destroyed within the reaction process when Bi_2Se_3 is consumed. Catalytic role of TI was first predicted in the paper of Chen *et al.*

[4] where enhancement of adsorption energy of CO and O_2 molecules on Au covered Bi_2Se_3 was demonstrated. Afterwards, the role of the TSS in catalyzing surface reactions has been investigated either theoretically or experimentally and primarily for the use of TI as substrates for metal catalysts [5]. However, enhanced catalytic activity of the TI itself was already observed in the case of hydrogen evolution reaction [48, 113] and reduction of O_2 [50].

Catalytic activity of the TSS is attributed to electrons that can freely move over the surface, participate in hybridization and act as an effective electron bath [4, 211]. Due to the delocalization of the TSS, migration of electrons from TI to the adsorbates or vice versa is possible, enabling participation in both oxidation and reduction processes. Static electron transfer is also achievable because the TSS are not completely filled and the total energy of the system upon adsorption of a molecule can be lowered by the electron transfer.

An important role in the reaction kinetics observed in our research can be reasonably attributed to the TSS electrons, which can easily transfer between the substrate and deposited metal and promote redox reaction. However, such reaction may relocate the TSS and affect the catalytic or electronic properties of the heterostructure surface and consequently have an effect on the TI-based applications.

6.5 Conclusion

When metals are deposited on Bi_2Se_3 an interfacial redox reaction likely occurs (with exception of Au) with formation of new phases. A first prediction of number and type of phases produced within the reaction can be evaluated based on the standard reduction potential of the metal (E^0) and on the Gibbs free energy for a reaction where metal selenide and Bi are formed ($\Delta G_r{}^0$). Metals that can easily oxidize and have a substantially low $\Delta G_r{}^0$ will presumably form a binary phase with selenium. With decreasing E^0 and $\Delta G_r{}^0$ value both binary and ternary phase ($M_xBi_ySe_z$) can be expected to form. After reaching E^0 values of the Pt group metals (Ir, Pd, Pt) a reaction producing only the ternary phase is predicted.

The surprising fact about these interface reactions is the kinetics, since the processes are quite fast considering the fact that these are redox solid-state reactions happening at RT (even at 130 K for Ti). The reported results suggest that the TSS can enhance the surface reactivity between a metal and TI due to the electron bath effect, causing fast kinetics of a redox solid-state reaction. The occurrence of interface reactions and formation of new phases should be considered in devices and theoretical studies that incorporate metal/Ti interfaces.

7 CONCLUSIONS

The research was focused on the characterization of the interface between Bi_2Se_3 topological insulator and various metals from the aspect of metal growth mode, morphology and stability. In order to cover both electronic and catalytic fields of applications where TI are predicted to be used, Ag, Ti and Pt metal were chosen for the investigation. Majority of measurements were performed on Bi_2Se_3 single crystal, synthesized by Bridgman method, on which the metals were deposited using PVD techniques.

Morphology of Ag/Bi_2Se_3 interface was studied from the early stages of metal deposition by means of STM. Upon deposition two types of islands were observed, which could be assigned to either Ag islands or products of the chemical interaction occurring at the interface. Deposition of Ag on a nm scale showed the formation of islands of irregular shape on the flat parts of the surface, whereas large agglomerates were found on the surface steps. Ag/Bi_2Se_3 interface was found to be unstable at ambient conditions since absorption of Ag into the substrate was observed. Interaction at the interface was studied with experiments using a powder mixture of Ag and Bi_2Se_3 NPs and with a reaction in the suspension of Bi_2Se_3 NPs with Ag^+ precursor. XRD and STEM-EDX analyses of as prepared samples showed the formation of $AgBiSe_2$, Ag_2Se and metallic Bi phase. Results obtained from the set of experiments indicated an interfacial redox solid-state reaction between Ag and Bi_2Se_3 described by the following equation:

$$3Ag + Bi_2Se_3 \rightarrow AgBiSe_2 + Ag_2Se + Bi$$

Deposition of Ti on Bi_2Se_3 single crystal was studied from a very low deposition as with Ag. Two types of islands, which differ in their size, were found upon metal deposition. Increase in Ti coverage at first resulted in the increase of the island size, but later stopped with modification in the morphology of the substrate surface. Such unusual change suggested on a chemical interaction between the two compounds. No morphological features were found by SEM on Ti films below 20 nm nominal coverage, however the occurrence of buckle delamination was observed above 40 nm thickness.

XPS measurement proved the hypothesis of the chemical reaction at the Ti/Bi_2Se_3 interface and enabled to characterize formed interfacial phases – titanium selenides and metallic bismuth. The result was further supported by TEM and EDX measurement and allowed to visualize the two main reaction products – $TiSe_2$ and metallic Bi. TEM imaging suggest that the following reaction evolves by diffusion of Se atoms from Bi into Ti.

$$3Ti + 2Bi_2Se_3 \rightarrow 3TiSe_2 + 4Bi$$

The reaction surprisingly occurred also at a temperature of 130 K, which shows on the significant kinetics of the observed reaction.

Pt was found to arrange on the Bi_2Se_3 surface as a homogenous film consisting of small features that cover the surface already at a small coverage (5 nm). The resulting morphology is ascribed to the low surface diffusion of Pt atoms. The interface does not undergo any visible change upon being kept at ambient conditions in the timescale of weeks. Annealing of Pt/Bi_2Se_3 sample to 350 °C resulted in the rearrangement of the deposited metal and morphological change of the bright features. Comparison of the EDX spectrum before and after annealing showed that Pt atoms were absorbed into the substrate, similar to what was observed with Ag. TEM cross-section analysis confirmed the occurrence of a chemical reaction and showed that the interaction between Pt and Bi_2Se_3 results in the formation of a ternary interfacial phase.

The obtained results, combined with the findings reported in the literature, led us to the formulation of a model that would be useful for prediction of the interfacial reactions. The model is based on the comparison of standard reduction potentials of transition metals that were found to react with Bi_2Se_3 and Gibbs free energy for a proposed reaction $Y\,Bi_2Se_3 + 3X\,M \rightarrow 3\,M_XSe_Y + 2Y\,Bi$. As such, it allows for predictions regarding the type of phases produced at the metal/Bi_2Se_3 interface that are in agreement with the reported observations.

The unexpected kinetics of the studied interface reactions led us to hypothesis that the TSS electrons can participate in the reactions as a catalyst. As was described in the references [4, 211], the delocalization of TSS allows the electrons to act as an electron bath and facilitate their migration from the TI to the adsorbate or vice versa and participation in a redox process. Hence, the results of our research emphasize on a different aspect of the use of TIs. Although they were originally investigated for the peculiar properties of TSS, such as spin-momentum locking and symmetry protected character, it is becoming clearer that their special characteristics could also be exploited in other fields, especially in chemistry.

It is becoming more and more obvious that the reactivity of metal/TI interfaces and the formation of interfacial phases are phenomena that can easily occur and should be as such taken into account for the future development of the TI field. Formation of interfacial phases changes the structure of the interface due to the presence of a new compound and may also cause the relocation of the TSS. Therefore, it has to be considered when designing a TI device, since the new phase may affect the transport and mechanical properties of the system (e.g. by affecting the capability to maintain the spin-momentum locking, increasing the contact resistance, consuming the TI material) or give rise to mechanical instability. Knowledge about the morphology of the interface is important also when designing devices incorporating thin films or layers, for example to know whether homogenous thin layer covering the whole surface can actually be obtained.

On the other hand, the interfacial reactions could be beneficial in chemical processes either in catalysis or for preparation of new 2D heterostructures. Metal selenides that were observed to be formed at the interface also have interesting properties of their own (e.g. $AgBiSe_2$ is a thermoelectric material [212, 213], Ag_2Se is a potential 3D TI [214-216], $TiSe_2$ is a charge density wave material [217, 218]) and therefore provide new opportunities for the study of such heterostructures.

Finally, since the results of theoretical studies on TIs are highly dependent on the models used, a deeper knowledge about the growth mode and the actual structure of the metal/TI interface is fundamental to obtain reliable theoretical results and promote further experimental studies.

8 SCIENTIFIC CONTRIBUTIONS

Original research papers

- K. Ferfolja, M. Valant, I. Mikulska, S. Gardonio, M. Fanetti, Chemical Instability of an Interface between Silver and Bi_2Se_3 Topological Insulator at Room Temperature, *Journal of Physical Chemistry C* 122(18) (2018) 9980-9984.
- M. Fanetti, I. Mikulska, K. Ferfolja, P. Moras, P.M. Sheverdyaeva, M. Panighel, A. Lodi-Rizzini, I. Pis, S. Nappini, M. Valant, S. Gardonio, Growth, morphology and stability of Au in contact with the Bi_2Se_3(0001) surface, *Applied Surface Science* 471 (2019) 753-758.
- B. Belec, K. Ferfolja, T. Gorsak, N. Kostevsek, S. Gardonio, M. Fanetti, M. Valant, Inherent Surface Properties of Adsorbent-Free Ultrathin Bi2Se3 Topological Insulator Platelets, *Scientific Reports* 9 (2019) 19057.
- K. Ferfolja, M. Fanetti, S. Gardonio, M. Panighel, I. Píš, S. Nappini, M. Valant, Cryogenic solid-state reaction at the interface between Ti and Bi_2Se_3 topological insulator, *Journal of Materials Chemistry C* 8 (2020) 11492-11498.

Conference presentations

- K. Ferfolja, M. Fanetti, I. Mikulska, S. Gardonio, M. Valant, Room-Temperature Solid-State Reaction at the Ag/Bi_2Se_3 Interface. 23rd Slovenian Chemical Days Portorož, September 20-22, 2017.
- K. Ferfolja, M. Fanetti, S. Gardonio, M. Valant, Chemical (in)stability of interfaces between different metals and Bi_2Se_3 topological insulator. 24th Slovenian Chemical Days Portorož, September 19-21, 2018.
- K. Ferfolja, M. Fanetti, S. Gardonio, M. Valant, Chemical (in)stability of an interface between metals and Bi_2Se_3 topological insulator. 3rd International Conference on applied surface science (ICASS) Pisa, June 17-19, Italy.

9 REFERENCES

[1] C.L. Kane, E.J. Mele, Z_2 topological order and the quantum spin Hall effect, *Physical Review Letters* 95(14) (2005) 146802.

[2] L. Fu, C.L. Kane, Topological insulators with inversion symmetry, *Physical Review B* 76(4) (2007) 045302.

[3] D.S. Kong, Y. Cui, Opportunities in chemistry and materials science for topological insulators and their nanostructures, *Nature Chemistry* 3(11) (2011) 845-849.

[4] H. Chen, W.G. Zhu, D. Xiao, Z.Y. Zhang, CO Oxidation Facilitated by Robust Surface States on Au-Covered Topological Insulators, *Physical Review Letters* 107(5) (2011) 056804.

[5] J.P. Xiao, L.Z. Kou, C.Y. Yam, T. Frauenheim, B.H. Yan, Toward Rational Design of Catalysts Supported on a Topological Insulator Substrate, *ACS Catalysis* 5(12) (2015) 7063-7067.

[6] Q.L. He, Y.H. Lai, Y. Lu, K.T. Law, I.K. Sou, Surface Reactivity Enhancement on a Pd/Bi_2Te_3 Heterostructure through Robust Topological Surface States, *Scientific Reports* 3 (2013) 2497.

[7] L.P. Xiao, A.M. Zhu, Q.C. Xu, Y. Chen, J. Xu, J. Weng, Colorimetric Biosensor for Detection of Cancer Biomarker by Au Nanoparticle-Decorated Bi_2Se_3 Nanosheets, *ACS Applied Materials & Interfaces* 9(8) (2017) 6931-6940.

[8] K. Yin, Z.D. Cui, X.R. Zheng, X.J. Yang, S.L. Zhu, Z.Y. Li, Y.Q. Liang, A Bi_2Te_3@CoNiMo composite as a high performance bifunctional catalyst for hydrogen and oxygen evolution reactions, *Journal of Materials Chemistry A* 3(45) (2015) 22770-22780.

[9] S.Y. Shi, A.Z. Wang, Y. Wang, R. Ramaswamy, L. Shen, J. Moon, D.P. Zhu, J.W. Yu, S. Oh, Y.P. Feng, H. Yang, Efficient charge-spin conversion and magnetization switching through the Rashba effect at topological-insulator/Ag interfaces, *Physical Review B* 97(4) (2018) 041115.

[10] G. Schubert, H. Fehske, L. Fritz, M. Vojta, Fate of topological-insulator surface states under strong disorder, *Physical Review B* 85(20) (2012) 201105.

[11] G.F. Wu, H. Chen, Y. Sun, X.G. Li, P. Cui, C. Franchini, J.L. Wang, X.Q. Chen, Z.Y. Zhang, Tuning the vertical location of helical surface states in topological insulator heterostructures via dual-proximity effects, *Scientific Reports* 3 (2013) 1233.

[12] M.C. Shaughnessy, N.C. Bartelt, J.A. Zimmerman, J.D. Sugar, Energetics and diffusion of gold in bismuth telluride-based thermoelectric compounds, *Journal of Applied Physics* 115(6) (2014) 063705.

[13] F. Bloch, Über die Quantenmechanik der Elektronen in Kristallgittern, *Zeitschrift für Physik* 52 (1929) 555–600.

[14] W.D. Callister, D.G. Rethwisch, Fundamentals of Materials Science and Engineering: An Integrated Approach, 3rd ed., John Wiley & Sons, New Jersey, 2008.

[15] A. Rockett, The materials science of semiconductors, Springer, New York, 2007.

[16] K. v. Klitzing, G. Dorda, M. Pepper, New method for high-accuracy determination of the fine-structure constant based on quantized Hall resistance, *Physical Review Letters* 45(6) (1980) 494-497.

[17] M. Kohmoto, Topological invariant and the quantization of the Hall conductance, *Annals of Physics* 160(2) (1985) 343-354.

[18] X.G. Wen, Topological orders and edge excitations in fractional quantum Hall states, *Advances in Physics* 44(5) (1995) 405-473.

[19] T.W. Gamelin, R.E. Greene, Introduction to topology, Dover Publications, New York, 1999.

[20] M.Z. Hasan, C.L. Kane, Colloquium: Topological insulators, *Reviews of Modern Physics* 82(4) (2010) 3045-3067.

[21] C.L. Kane, E.J. Mele, Quantum spin Hall effect in graphene, *Physical Review Letters* 95(22) (2005) 226801.

[22] M. Konig, S. Wiedmann, C. Brune, A. Roth, H. Buhmann, L.W. Molenkamp, X.L. Qi, S.C. Zhang, Quantum spin hall insulator state in HgTe quantum wells, *Science* 318(5851) (2007) 766-770.

[23] D. Hsieh, D. Qian, L. Wray, Y. Xia, Y.S. Hor, R.J. Cava, M.Z. Hasan, A topological Dirac insulator in a quantum spin Hall phase, *Nature* 452(7190) (2008) 970-U5.

[24] H.J. Zhang, C.X. Liu, X.L. Qi, X. Dai, Z. Fang, S.C. Zhang, Topological insulators in Bi_2Se_3, Bi_2Te_3 and Sb_2Te_3 with a single Dirac cone on the surface, *Nature Physics* 5(6) (2009) 438-442.

[25] Y. Xia, D. Qian, D. Hsieh, L. Wray, A. Pal, H. Lin, A. Bansil, D. Grauer, Y.S. Hor, R.J. Cava, M.Z. Hasan, Observation of a large-gap topological-insulator class with a single Dirac cone on the surface, *Nature Physics* 5(6) (2009) 398-402.

[26] Y.L. Chen, J.G. Analytis, J.H. Chu, Z.K. Liu, S.K. Mo, X.L. Qi, H.J. Zhang, D.H. Lu, X. Dai, Z. Fang, S.C. Zhang, I.R. Fisher, Z. Hussain, Z.X. Shen, Experimental Realization of a Three-Dimensional Topological Insulator, Bi_2Te_3, *Science* 325(5937) (2009) 178-181.

[27] D. Hsieh, Y. Xia, D. Qian, L. Wray, J.H. Dil, F. Meier, J. Osterwalder, L. Patthey, J.G. Checkelsky, N.P. Ong, A.V. Fedorov, H. Lin, A. Bansil, D. Grauer, Y.S. Hor, R.J. Cava, M.Z. Hasan, A tunable topological insulator in the spin helical Dirac transport regime, *Nature* 460(7259) (2009) 1101-U59.

[28] L.A. Fu, Topological Crystalline Insulators, *Physical Review Letters* 106(10) (2011) 106802.

[29] X.G. Wan, A.M. Turner, A. Vishwanath, S.Y. Savrasov, Topological semimetal and Fermi-arc surface states in the electronic structure of pyrochlore iridates, *Physical Review B* 83(20) (2011) 205101.

[30] Z.J. Wang, Y. Sun, X.Q. Chen, C. Franchini, G. Xu, H.M. Weng, X. Dai, Z. Fang, Dirac semimetal and topological phase transitions in A_3Bi (A = Na, K, Rb), *Physical Review B* 85(19) (2012) 195320.

[31] www.webofknowledge.com

[32] Y. Tokura, K. Yasuda, A. Tsukazaki, Magnetic topological insulators, *Nature Reviews Physics* 1(2) (2019) 126-143.

[33] H.J. Zhang, C.X. Liu, S.C. Zhang, Spin-Orbital Texture in Topological Insulators, *Physical Review Letters* 111(6) (2013) 066801.

[34] Y. Ando, Topological Insulator Materials, *Journal of the Physical Society of Japan* 82(10) (2013) 102001.

[35] B.H. Yan, D.L. Zhang, C. Felser, Topological surface states of Bi_2Se_3 coexisting with Se vacancies, *Physica Status Solidi-Rapid Research Letters* 7(1-2) (2013) 148-150.

[36] H. Steinberg, D.R. Gardner, Y.S. Lee, P. Jarillo-Herrero, Surface State Transport and Ambipolar Electric Field Effect in Bi_2Se_3 Nanodevices, *Nano Letters* 10(12) (2010) 5032-5036.

[37] F.X. Xiu, L.A. He, Y. Wang, L.N. Cheng, L.T. Chang, M.R. Lang, G.A. Huang, X.F. Kou, Y. Zhou, X.W. Jiang, Z.G. Chen, J. Zou, A. Shailos, K.L. Wang,

Manipulating surface states in topological insulator nanoribbons, *Nature Nanotechnology* 6(4) (2011) 216-221.

[38] Y.S. Hor, A. Richardella, P. Roushan, Y. Xia, J.G. Checkelsky, A. Yazdani, M.Z. Hasan, N.P. Ong, R.J. Cava, p-type Bi_2Se_3 for topological insulator and low-temperature thermoelectric applications, *Physical Review B* 79(19) (2009) 195208.

[39] D. Kim, S. Cho, N.P. Butch, P. Syers, K. Kirshenbaum, S. Adam, J. Paglione, M.S. Fuhrer, Surface conduction of topological Dirac electrons in bulk insulating Bi_2Se_3, *Nature Physics* 8(6) (2012) 459-463.

[40] Y. Zhang, K. He, C.Z. Chang, C.L. Song, L.L. Wang, X. Chen, J.F. Jia, Z. Fang, X. Dai, W.Y. Shan, S.Q. Shen, Q. Niu, X.L. Qi, S.C. Zhang, X.C. Ma, Q.K. Xue, Crossover of the three-dimensional topological insulator Bi_2Se_3 to the two-dimensional limit, *Nature Physics* 6(8) (2010) 584-588.

[41] M.H. Berntsen, 2013, Consequences of a non-trivial band-structure topology in solids: Investigations of topological surface and interface states, PhD thesis, KTH Royal Institute of Technology, Stockholm.

[42] J.F. Tian, S. Hong, S. Sayed, J.S. Lee, S. Datta, N. Samarth, Y.P. Chen, On the understanding of current-induced spin polarization of three-dimensional topological insulators, *Nature Communications* 10 (2019) 1461.

[43] T.H. Hwang, H.S. Kim, H. Kim, J.S. Kim, Y.J. Doh, Electrical detection of spin-polarized current in topological insulator $Bi_{1.5}Sb_{0.5}Te_{1.7}Se_{1.3}$, *Current Applied Physics* 19(8) (2019) 917-923.

[44] I. Garate, M. Franz, Inverse Spin-Galvanic Effect in the Interface between a Topological Insulator and a Ferromagnet, *Physical Review Letters* 104(14) (2010) 146802.

[45] J. Linder, Y. Tanaka, T. Yokoyama, A. Sudbo, N. Nagaosa, Unconventional Superconductivity on a Topological Insulator, P*hysical Review Letters* 104(6) (2010) 067001.

[46] C.K. Chiu, G. Bian, H. Zheng, J.X. Yin, S.T.S. Zhang, D.S. Sanchez, I. Belopolski, S.Y. Xu, M.Z. Hasan, Chiral Majorana fermion modes on the surface of superconducting topological insulators, *EPL* 123(4) (2018) 47005.

[47] G.W. Li, C. Felser, Heterogeneous catalysis at the surface of topological materials, *Applied Physics Letters* 116(7) (2020) 070501.

[48] C.R. Rajamathi, U. Gupta, K. Pal, N. Kumar, H. Yang, Y. Sun, C. Shekhar, B.H. Yan, S. Parkin, U.V. Waghmare, C. Felser, C.N.R. Rao, Photochemical Water Splitting by Bismuth Chalcogenide Topological Insulators, *Chemphyschem* 18(17) (2017) 2322-2327.

[49] C.R. Rajamathi, U. Gupta, N. Kumar, H. Yang, Y. Sun, V. Suss, C. Shekhar, M. Schmidt, H. Blumtritt, P. Werner, B.H. Yan, S. Parkin, C. Felser, C.N.R. Rao, Weyl Semimetals as Hydrogen Evolution Catalysts, *Advanced Materials* 29(19) (2017) 1606202.

[50] S. Chen, Y.M. Fang, J. Li, J.J. Sun, G.N. Chen, H.H. Yang, Study on the electrochemical catalytic properties of the topological insulator Bi_2Se_3, *Biosensors & Bioelectronics* 46 (2013) 171-174.

[51] H.B. Zhang, X.J. Zhang, C. Liu, S.T. Lee, J.S. Jie, High-Responsivity, High-Detectivity, Ultrafast Topological Insulator Bi_2Se_3/Silicon Heterostructure Broadband Photodetectors, *ACS Nano* 10(5) (2016) 5113-5122.

[52] M. Yang, Q. Han, X.C. Liu, J.Y. Han, Y.F. Zhao, L. He, J. Gou, Z.M. Wu, X.R. Wang, J. Wang, Ultrahigh Stability 3D TI Bi_2Se_3/MoO_3 Thin Film Heterojunction Infrared Photodetector at Optical Communication Waveband, *Advanced Functional Materials* 30(12) (2020) 1909659.

[53] W.C. Tian, W.B. Yu, J. Shi, Y.K. Wang, The Property, Preparation and Application of Topological Insulators: A Review, *Materials* 10(7) (2017) 814.

[54] C.X. Yue, S.Y. Jiang, H. Zhu, L. Chen, Q.Q. Sun, D.W. Zhang, Device Applications of Synthetic Topological Insulator Nanostructures, *Electronics* 7(10) (2018) 225.

[55] K. Oura, V.G. Lifshits, A.A. Saranin, A.V. Zotov, M. Katayama, Surface Science: An Introduction, Springer Berlin Heidelberg, Weinheim, 2013.

[56] P.M. Martin, Handbook of Deposition Technologies for Films and Coatings: Science, Applications and Technology, Elsevier Science, Oxford, 2009.

[57] H. Lüth, Surfaces and Interfaces of Solid Materials, 3rd ed., Springer, Berlin, 1995.

[58] C. Berg, H.J. Venvik, F. Strisland, A. Ramstad, A. Borg, Nucleation and growth of Au overlayers on Pt(100)-hex-R0.7° studied by STM and photoelectron spectroscopy, *Surface Science* 409(1) (1998) 1-15.

[59] X.J. Liu, C.Z. Wang, M. Hupalo, W.C. Lu, M.C. Tringides, Y.X. Yao, K.M. Ho, Metals on graphene: correlation between adatom adsorption behavior and growth morphology, *Physical Chemistry Chemical Physics* 14(25) (2012) 9157-9166.

[60] A. Fissel, R. Akhtariev, W. Richter, Stranski-Krastanov growth of Si on SiC(0001), *Thin Solid Films* 380(1-2) (2000) 42-45.

[61] R.W. Vook, Nucleation and growth of thin films, *Optical engineering* 23(3) (1984) 343-349.

[62] K. Govaerts, K. Park, C. De Beule, B. Partoens, D. Lamoen, Effect of Bi bilayers on the topological states of Bi_2Se_3: A first-principles study, *Physical Review B* 90(15) (2014) 155124.

[63] C.H. Chang, T.R. Chang, H.T. Jeng, Newtype large Rashba splitting in quantum well states induced by spin chirality in metal/topological insulator heterostructures, *NPG Asia Materials* 8 (2016) e332.

[64] H. Aramberri, M.C. Munoz, Gap and spin texture engineering of Dirac topological states at the Cr-Bi_2Se_3 interface, *Physical Review B* 93(24) (2016) 245401.

[65] J. Zhang, J.P. Velev, X.Q. Dang, E.Y. Tsymbal, Band structure and spin texture of Bi_2Se_3 3d ferromagnetic metal interface, *Physical Review B* 94(1) (2016) 014435.

[66] H. Yang, X.Y. Peng, X.L. Wei, W.L. Liu, W.G. Zhu, D. Xiao, G.M. Stocks, J.X. Zhong, Quantum oscillation of Rashba spin splitting in topological insulator Bi_2Se_3 induced by the quantum size effects of Pb adlayers, *Physical Review B* 86(15) (2012) 155317.

[67] S.H. Kim, K.H. Jin, J. Park, J.S. Kim, S.H. Jhi, H.W. Yeom, Topological phase transition and quantum spin Hall edge states of antimony few layers, *Scientific Reports* 6 (2016) 33193.

[68] S.H. Kim, K.H. Jin, B.W. Kho, B.G. Park, F. Liu, J.S. Kim, H.W. Yeom, Atomically Abrupt Topological p-n Junction, *ACS Nano* 11(10) (2017) 9671-9677.

[69] A. Eich, M. Michiardi, G. Bihlmayer, X.G. Zhu, J.L. Mi, B.B. Iversen, R. Wiesendanger, P. Hofmann, A.A. Khajetoorians, J. Wiebe, Intra- and interband electron scattering in a hybrid topological insulator: Bismuth bilayer on Bi_2Se_3, *Physical Review B* 90(15) (2014) 155414.

[70] F. Yang, L. Miao, Z.F. Wang, M.Y. Yao, F.F. Zhu, Y.R. Song, M.X. Wang, J.P. Xu, A.V. Fedorov, Z. Sun, G.B. Zhang, C.H. Liu, F. Liu, D. Qian, C.L. Gao, J.F. Jia, Spatial and Energy Distribution of Topological Edge States in Single Bi(111) Bilayer, *Physical Review Letters* 109(1) (2012) 016801.

[71] S.H. Kim, K.H. Jin, J. Park, J.S. Kim, S.H. Jhi, T.H. Kim, H.W. Yeom, Edge and interfacial states in a two-dimensional topological insulator: Bi(111) bilayer on Bi_2Te_2Se, *Physical Review B* 89(15) (2014) 155436.

[72] M. Chen, J.P. Peng, H.M. Zhang, L.L. Wang, K. He, X.C. Ma, Q.K. Xue, Molecular beam epitaxy of bilayer Bi(111) films on topological insulator Bi_2Te_3: A scanning tunneling microscopy study, *Applied Physics Letters* 101(8) (2012) 081603.

[73] J. Honolka, A.A. Khajetoorians, V. Sessi, T.O. Wehling, S. Stepanow, J.L. Mi, B.B. Iversen, T. Schlenk, J. Wiebe, N.B. Brookes, A.I. Lichtenstein, P. Hofmann, K. Kern, R. Wiesendanger, In-Plane Magnetic Anisotropy of Fe Atoms on Bi_2Se_3(111), *Physical Review Letters* 108(25) (2012) 256811.

[74] T. Schlenk, M. Bianchi, M. Koleini, A. Eich, O. Pietzsch, T.O. Wehling, T. Frauenheim, A. Balatsky, J.L. Mi, B.B. Iversen, J. Wiebe, A.A. Khajetoorians, P. Hofmann, R. Wiesendanger, Controllable Magnetic Doping of the Surface State of a Topological Insulator, *Physical Review Letters* 110(12) (2013) 126804.

[75] I. Vobornik, U. Manju, J. Fujii, F. Borgatti, P. Torelli, D. Krizmancic, Y.S. Hor, R.J. Cava, G. Panaccione, Magnetic Proximity Effect as a Pathway to Spintronic Applications of Topological Insulators, *Nano Letters* 11(10) (2011) 4079-4082.

[76] I. Vobornik, G. Panaccione, J. Fujii, Z.H. Zhu, F. Offi, B.R. Salles, F. Borgatti, P. Torelli, J.P. Rueff, D. Ceolin, A. Artioli, M. Unnikrishnan, G. Levy, M. Marangolo, M. Eddrief, D. Krizmancic, H.W. Ji, A. Damascelli, G. van der Laan, R.G. Egdell, R.J. Cava, Observation of Distinct Bulk and Surface Chemical Environments in a Topological Insulator under Magnetic Doping, *Journal of Physical Chemistry C* 118(23) (2014) 12333-12339.

[77] J. Sanchez-Barriga, Ogorodnikov, II, M.V. Kuznetsov, A.A. Volykhov, F. Matsui, C. Callaert, J. Hadermann, N.I. Verbitskiy, R.J. Koch, A. Varykhalov, O. Rader, L.V. Yashina, Observation of hidden atomic order at the interface between Fe and topological insulator Bi_2Te_3, *Physical Chemistry Chemical Physics* 19(45) (2017) 30520-30532.

[78] M. Ye, S.V. Eremeev, K. Kuroda, E.E. Krasovskii, E.V. Chulkov, Y. Takeda, Y. Saitoh, K. Okamoto, S.Y. Zhu, K. Miyamoto, M. Arita, M. Nakatake, T. Okuda, Y. Ueda, K. Shimada, H. Namatame, M. Taniguchi, A. Kimura, Quasiparticle interference on the surface of Bi_2Se_3 induced by cobalt adatom in the absence of ferromagnetic ordering, *Physical Review B* 85(20) (2012) 205317.

[79] M. Fanetti, I. Mikulska, K. Ferfolja, P. Moras, P.M. Sheverdyaeva, M. Panighel, A. Lodi-Rizzini, I. Pis, S. Nappini, M. Valant, S. Gardonio, Growth, morphology and stability of Au in contact with the Bi_2Se_3(0001) surface, *Applied Surface Science* 471 (2019) 753-758.

[80] Y.L. Wang, Y. Xu, Y.P. Jiang, J.W. Liu, C.Z. Chang, M. Chen, Z. Li, C.L. Song, L.L. Wang, K. He, X. Chen, W.H. Duan, Q.K. Xue, X.C. Ma, Structural defects and electronic properties of the Cu-doped topological insulator Bi_2Se_3, *Physical Review B* 84(7) (2011) 5.

[81] P. Meixner, S.J. Lim, J. Park, J.S. Kim, S.F. Fischer, J. Seo, Y. Kuk, Growth of niobium on the three-dimensional topological insulator $Bi_2Te_{1.95}Se_{1.05}$, *Applied Surface Science* 361 (2016) 185-189.

[82] S.M. Whittingham, A.J. Jacobson, Intercalation Chemistry, Academic Press, New York, 1982.

[83] L.E. Smart, E.A. Moore, Solid State Chemistry: An Introduction, Third Edition, Taylor & Francis, Boca Raton, 2005.

[84] C.E. Housecroft, A.G. Sharpe, Inorganic Chemistry, Pearson, Essex, 2012.

[85] P. Atkins, J. de Paula, Atkins' Physical Chemistry, OUP Oxford, New York, 2010.

[86] Y.S. Hor, A.J. Williams, J.G. Checkelsky, P. Roushan, J. Seo, Q. Xu, H.W. Zandbergen, A. Yazdani, N.P. Ong, R.J. Cava, Superconductivity in $Cu_xBi_2Se_3$ and its Implications for Pairing in the Undoped Topological Insulator, *Physical Review Letters* 104(5) (2010) 057001.

[87] M. Bianchi, R.C. Hatch, Z.S. Li, P. Hofmann, F. Song, J.L. Mi, B.B. Iversen, Z.M. Abd El-Fattah, P. Loptien, L.H. Zhou, A.A. Khajetoorians, J. Wiebe, R. Wiesendanger, J.W. Wells, Robust Surface Doping of Bi_2Se_3 by Rubidium Intercalation, *ACS Nano* 6(8) (2012) 7009-7015.

[88] K.J. Koski, C.D. Wessells, B.W. Reed, J.J. Cha, D.S. Kong, Y. Cui, Chemical Intercalation of Zerovalent Metals into 2D Layered Bi_2Se_3 Nanoribbons, *Journal of the American Chemical Society* 134(33) (2012) 13773-13779.

[89] M.M. Otrokov, S.D. Borisova, V. Chis, M.G. Vergniory, S.V. Eremeev, V.M. Kuznetsov, E.V. Chulkov, Efficient Step-Mediated Intercalation of Silver Atoms Deposited on the Bi_2Se_3 Surface, *JETP Letters* 96(11) (2013) 714-718.

[90] S.W. Chen, H.J. Wu, C.Y. Wu, C.F. Chang, C.Y. Chen, Reaction evolution and alternating layer formation in $Sn/(Bi_{0.25}Sb_{0.75})_2Te_3$ and Sn/Sb_2Te_3 couples, *Journal of Alloys and Compounds* 553 (2013) 106-112.

[91] C.H. Wang, M.H. Li, C.W. Chiu, T.Y. Chang, Kinetic study of solid-state interfacial reactions of p-type $(Bi, Sb)_2Te_3$ thermoelectric materials with Sn and Sn-Ag-Cu solders, *Journal of Alloys and Compounds* 767 (2018) 1133-1140.

[92] O.D. Iyore, T.H. Lee, R.P. Gupta, J.B. White, H.N. Alshareef, M.J. Kim, B.E. Gnade, Interface characterization of nickel contacts to bulk bismuth tellurium selenide, *Surface and Interface Analysis* 41(5) (2009) 440-444.

[93] Y.C. Lan, D.Z. Wang, G. Chen, Z.F. Ren, Diffusion of nickel and tin in p-type $(Bi,Sb)_2Te_3$ and n-type $Bi_2(Te,Se)_3$ thermoelectric materials, *Applied Physics Letters* 92(10) (2008) 101910.

[94] W.P. Lin, D.E. Wesolowski, C.C. Lee, Barrier/bonding layers on bismuth telluride (Bi_2Te_3) for high temperature thermoelectric modules, *Journal of Materials Science-Materials in Electronics* 22(9) (2011) 1313-1320.

[95] A.G. Ryabishchenkova, M.M. Otrokov, V.M. Kuznetsov, E.V. Chulkov, Ab initio study of the adsorption, diffusion, and intercalation of alkali metal atoms on the (0001) surface of the topological insulator Bi_2Se_3, *Journal of Experimental and Theoretical Physics* 121(3) (2015) 465-476.

[96] M.A. Gosalvez, M.M. Otrokov, N. Ferrando, A.G. Ryabishchenkova, A. Ayuela, P.M. Echenique, E.V. Chulkov, Low-coverage surface diffusion in complex periodic energy landscapes: Analytical solution for systems with symmetric hops and application to intercalation in topological insulators, *Physical Review B* 93(7) (2016) 075429.

[97] A.Y. Kuntsevich, V.P. Martovitskii, G.V. Rybalchenko, Y.G. Selivanov, M.I. Bannikov, O.A. Sobolevskiy, E.G. Chigevskii, Superconductivity in Cu Co-Doped $Sr_xBi_2Se_3$ Single Crystals, *Materials* 12(23) (2019) 3899.

[98] T.V. Bay, T. Naka, Y.K. Huang, H. Luigjes, M.S. Golden, A. de Visser, Superconductivity in the Doped Topological Insulator $Cu_xBi_2Se_3$ under High Pressure, *Physical Review Letters* 108(5) (2012) 057001.

[99] J. Buha, L. Manna, Solid State Intercalation, Deintercalation, and Cation Exchange in Colloidal 2D Bi_2Se_3 and Bi_2Te_3 Nanocrystals, *Chemistry of Materials* 29(3) (2017) 1419-1429.

[100] J.B. Maclachlan, W.H. Kruesi, D.J. Fray, Intercalation of copper into bismuth telluride, *Journal of Materials Science* 27(15) (1992) 4223-4229.

[101] J.S. Zhang, J. Sun, Y.B. Li, F.F. Shi, Y. Cui, Electrochemical Control of Copper Intercalation into Nanoscale Bi_2Se_3, *Nano Letters* 17(3) (2017) 1741-1747.

[102] J. Yao, K.J. Koski, W.D. Luo, J.J. Cha, L.B. Hu, D.S. Kong, V.K. Narasimhan, K.F. Huo, Y. Cui, Optical transmission enhacement through chemically tuned two-dimensional bismuth chalcogenide nanoplates, *Nature Communications* 5 (2014) 5670.

[103] A.A. Kordyuk, T.K. Kim, V.B. Zabolotnyy, D.V. Evtushinsky, M. Bauch, C. Hess, B. Buchner, H. Berger, S.V. Borisenko, Photoemission-induced gating of topological insulators, *Physical Review B* 83(8) (2011) 081303.

[104] K. Sobczak, P. Strak, P. Kempisty, A. Wolos, A. Hruban, A. Materna, J. Borysiuk, Electronic and structural properties of Bi_2Se_3:Cu, *Physical Review Materials* 2(4) (2018) 044203.

[105] T. Kyratsi, E. Hatzikraniotis, K.M. Paraskevopoulos, K. Chrissafis, Changes in the Electronic Properties of Bi_2X_3 (X: Se, Te) Single Crystals due to Intercalation, *Ionics* 3(3-4) (1997) 305-309.

[106] E.Y. Wang, P.Z. Tang, G.L. Wan, A.V. Fedorov, I. Miotkowski, Y.P. Chen, W.H. Duan, S.Y. Zhou, Robust Gap less Surface State and Rashba-Splitting Bands upon Surface Deposition of Magnetic Cr on Bi_2Se_3, *Nano Letters* 15(3) (2015) 2031-2036.

[107] M.R. Scholz, J. Sanchez-Barriga, D. Marchenko, A. Varykhalov, A. Volykhov, L.V. Yashina, O. Rader, Tolerance of Topological Surface States towards Magnetic Moments: Fe on Bi_2Se_3, *Physical Review Letters* 108(25) (2012) 256810.

[108] T. Yilmaz, W. Hines, F.C. Sun, I. Pletikosic, J. Budnick, T. Valla, B. Sinkovic, Distinct effects of Cr bulk doping and surface deposition on the chemical environment and electronic structure of the topological insulator Bi_2Se_3, *Applied Surface Science* 407 (2017) 371-378.

[109] S. Majumder, K. Jarvis, S.K. Banerjee, K.L. Kavanagh, Interfacial reactions at Fe/topological insulator spin contacts, *Journal of Vacuum Science & Technology B* 35(4) (2017) 04f105.

[110] A. Polyakov, H.L. Meyerheim, E.D. Crozier, R.A. Gordon, K. Mohseni, S. Roy, A. Ernst, M.G. Vergniory, X. Zubizarreta, M.M. Otrokov, E.V. Chulkov, J. Kirschner, Surface alloying and iron selenide formation in Fe/Bi_2Se_3(0001) observed by x-ray absorption fine structure experiments, *Physical Review B* 92(4) (2015) 045423.

[111] A. Cavallin, V. Sevriuk, K.N. Fischer, S. Manna, S. Ouazi, M. Ellguth, C. Tusche, H.L. Meyerheim, D. Sander, J. Kirschner, Preparation and characterization of Bi_2Se_3(0001) and of epitaxial FeSe nanocrystals on Bi_2Se_3(0001), *Surface Science* 646 (2016) 72-82.

[112] L.A. Walsh, C.M. Smyth, A.T. Barton, Q.X. Wang, Z.F. Che, R.Y. Yue, J. Kim, M.J. Kim, R.M. Wallace, C.L. Hinkle, Interface Chemistry of Contact Metals and Ferromagnets on the Topological Insulator Bi_2Se_3, *Journal of Physical Chemistry C* 121(42) (2017) 23551-23563.

[113] L.Q. Li, J. Zeng, W. Qin, P. Cui, Z.Y. Zhang, Tuning the hydrogen activation reactivity on topological insulator heterostructures, *Nano Energy* 58 (2019) 40-46.

[114] T. Shoman, A. Takayama, T. Sato, S. Souma, T. Takahashi, T. Oguchi, K. Segawa, Y. Ando, Topological proximity effect in a topological insulator hybrid, *Nature Communications* 6 (2015) 6547.

[115] C.D. Spataru, F. Leonard, Fermi-level pinning, charge transfer, and relaxation of spin-momentum locking at metal contacts to topological insulators, *Physical Review B* 90(8) (2014) 085115.

[116] Z. Zhang, J.T. Yates, Band Bending in Semiconductors: Chemical and Physical Consequences at Surfaces and Interfaces, *Chemical Reviews* 112(10) (2012) 5520-5551.

[117] D. Takane, S. Souma, T. Sato, T. Takahashi, K. Segawa, Y. Ando, Work function of bulk-insulating topological insulator $Bi_{2-x}Sb_xTe_{3-y}Se_y$, *Applied Physics Letters* 109(9) (2016) 091601.

[118] Z.H. Zhu, G. Levy, B. Ludbrook, C.N. Veenstra, J.A. Rosen, R. Comin, D. Wong, P. Dosanjh, A. Ubaldini, P. Syers, N.P. Butch, J. Paglione, I.S. Elfimov, A. Damascelli, Rashba Spin-Splitting Control at the Surface of the Topological Insulator Bi_2Se_3, *Physical Review Letters* 107(18) (2011) 186405.

[119] K. Park, C. De Beule, B. Partoens, The ageing effect in topological insulators: evolution of the surface electronic structure of Bi2Se3 upon K adsorption, New Journal of Physics 15 (2013) 113031.

[120] T. Valla, Z.H. Pan, D. Gardner, Y.S. Lee, S. Chu, Photoemission Spectroscopy of Magnetic and Nonmagnetic Impurities on the Surface of the Bi_2Se_3 Topological Insulator, *Physical Review Letters* 108(11) (2012) 117601.

[121] D.A. Pudikov, E.V. Zhizhin, G.G. Vladimirov, Nickel Adsorption on Bi_2Se_3 Surface, *Physics of the Solid State* 60(5) (2018) 1016-1020.

[122] H.J. Noh, J. Jeong, E.J. Cho, J. Park, J.S. Kim, I. Kim, B.G. Park, H.D. Kim, Controlling the evolution of two-dimensional electron gas states at a metal/Bi_2Se_3 interface, *Physical Review B* 91(12) (2015) 121110.

[123] L.J. Brillson, Interface bonding, chemical reactions, and defect formation at metal-semiconductor interfaces, *Journal of Vacuum Science & Technology A* 25(4) (2007) 943-949.

[124] B. Das, D. Sarkar, S. Maity, K.K. Chattopadhyay, Ag decorated topological surface state protected hierarchical Bi_2Se_3 nanoflakes for enhanced field emission properties, *Journal of Materials Chemistry C* 3(8) (2015) 1766-1775.

[125] X.C. Ren, A.K. Singh, L. Fang, M.G. Kanatzidis, F. Tavazza, A.V. Davydov, L.J. Lauhon, Atom Probe Tomography Analysis of Ag Doping in 2D Layered Material $(PbSe)_5(Bi_2Se_3)_3$, *Nano Letters* 16(10) (2016) 6064-6069.

[126] M.J. Wang, I. Al-Dhahir, J. Appiah, K.J. Koski, Deintercalation of Zero-Valent Metals from Two-Dimensional Layered Chalcogenides, *Chemistry of Materials* 29(4) (2017) 1650-1655.

[127] N. de Jong, E. Frantzeskakis, B. Zwartsenberg, Y.K. Huang, D. Wu, P. Hlawenka, J. Sanchez-Barriga, A. Varykhalov, E. van Heumen, M.S. Golden, Angle-resolved and core-level photoemission study of interfacing the topological insulator $Bi_{1.5}Sb_{0.5}Te_{1.7}Se_{1.3}$ with Ag, Nb, and Fe, *Physical Review B* 92(7) (2015) 075127.

[128] K. Zheng, L.B. Luo, T.F. Zhang, Y.H. Liu, Y.Q. Yu, R. Lu, H.L. Qiu, Z.J. Li, J.C.A. Huang, Optoelectronic characteristics of a near infrared light photodetector based on a topological insulator Sb_2Te_3 film, *Journal of Materials Chemistry C* 3(35) (2015) 9154-9160.

[129] D.S. Kong, J.J. Cha, K.J. Lai, H.L. Peng, J.G. Analytis, S. Meister, Y.L. Chen, H.J. Zhang, I.R. Fisher, Z.X. Shen, Y. Cui, Rapid Surface Oxidation as a Source of Surface Degradation Factor for Bi_2Se_3, *ACS Nano* 5(6) (2011) 4698-4703.

[130] H. Zhu, E.H. Zhao, C.A. Richter, Q.L. Li, Topological Insulator Bi_2Se_3 Nanowire Field Effect Transistors, *ECS Transactions* 64(17) (2014) 51-59.

[131] S.J. Cho, N.P. Butch, J. Paglione, M.S. Fuhrer, Insulating Behavior in Ultrathin Bismuth Selenide Field Effect Transistors, *Nano Letters* 11(5) (2011) 1925-1927.

[132] X.X. Kong, W. Zhu, L.L. Cao, Y.C. Peng, S.F. Shen, Y. Deng, Controllable Electrical Contact Resistance between Cu and Oriented-Bi_2Te_3 Film via Interface Tuning, *ACS Applied Materials & Interfaces* 9(30) (2017) 25606-25614.

[133] X.Y. Zhang, F.S. Wen, J.Y. Xiang, X.C. Wang, L.M. Wang, W.T. Hu, Z.Y. Liu, Wearable non-volatile memory devices based on topological insulator Bi_2Se_3/Pt fibers, *Applied Physics Letters* 107(10) (2015) 103109.

[134] T. Kacsich, E. Kolawa, J.P. Fleurial, T. Caillat, M.A. Nicolet, Films of ni-7 at% V, Pd, Pt and Ta-Si-N as diffusion barriers for copper on Bi_2Te_3, *Journal of Physics D-Applied Physics* 31(19) (1998) 2406-2411.

[135] J.T. Mlack, A. Rahman, G. Danda, N. Drichko, S. Friedensen, M. Drndic, N. Markovic, Patterning Superconductivity in a Topological Insulator, *ACS Nano* 11(6) (2017) 5873-5878.

[136] D.X. Qu, N.E. Teslich, Z.R. Dai, G.F. Chapline, T. Schenkel, S.R. Durham, J. Dubois, Onset of a Two-Dimensional Superconducting Phase in a Topological-Insulator-Normal-Metal $Bi_{1-x}Sb_x$/Pt Junction Fabricated by Ion-Beam Techniques, *Physical Review Letters* 121(3) (2018) 037001.

[137] J.I. Goldstein, D.E. Newbury, D.C. Joy, C.E. Lyman, P. Echlin, E. Lifshin, L. Sawyer, J.R. Michael, Scanning Electron Microscopy and X-ray Microanalysis, 3 ed., Springer, New York, 2003.

[138] D.B. Williams, C.B. Carter, Transmission Electron Microscopy: A Textbook for Materials Science, 2 ed., Springer, New York, 2009.

[139] P. van der Heide, X-ray Photoelectron Spectroscopy: An introduction to Principles and Practices, Wiley, New Jersey, 2011.

[140] V. Pecharsky, P. Zavalij, Fundamentals of powder diffraction and structural characterization of materials, Springer, New York, 2005.

[141] F. Jona, J. Strozier Jr, W. Yang, Low-energy electron diffraction for surface structure analysis, *Reports on Progress in Physics* 45(5) (1982) 527.

[142] C.J. Chen, Introduction to Scanning Tunneling Microscopy, OUP Oxford, New York, 2008.

[143] www.jeol.co.jp

[144] B. Inkson, Materials characterization using nondestructive evaluation (NDE) methods, Woodhead Publishing, Cambridge, 2016.

[145] www.en.wikipedia.org/wiki/Scanning_tunneling_microscope, copy right: CC BY-SA 2.0 at.

[146] C. Castenmiller, R. van Bremen, K. Sotthewes, M.H. Siekman, H.J.W. Zandvliet, Combined I(V) and dI(V)/dz scanning tunneling spectroscopy, *AIP Advances* 8(7) (2018) 075013.

[147] D. Necas, P. Klapetek, Gwyddion: an open-source software for SPM data analysis, *Central European Journal of Physics* 10(1) (2012) 181-188.

[148] M.P. Seah, W.A. Dench, Quantitative electron spectroscopy of surfaces: A standard data base for electron inelastic mean free paths in solids, *Surface and Interface Analysis* 1(1) (1979) 2-11.

[149] X.H. Zhang, Y.M. An, J.C. Han, W.B. Han, G.D. Zhao, X.X. Jin, Graphene nanosheet reinforced ZrB_2-SiC ceramic composite by thermal reduction of graphene oxide, *RSC Advances* 5(58) (2015) 47060-47065.

[150] KolXPD, version 1.8.0 (build 61), software for spectroscopy data measurement and processing; https://www.kolibrik.net/kolxpd/, (accessed May 2020).

[151] B. Schmidt, K. Wetzig, Ion beams in materials processing and analysis, Springer, New York, 2012.

[152] L.V. Yashina, J. Sanchez-Barriga, M.R. Scholz, A.A. Volykhov, A.P. Sirotina, S.N. Vera, M.E. Tamm, A. Varykhalov, D. Marchenko, G. Springholz, G. Bauer, A. Knop-Gericke, O. Rader, Negligible Surface Reactivity of Topological Insulators Bi_2Se_3 and Bi_2Te_3 towards Oxygen and Water, *ACS Nano* 7(6) (2013) 5181-5191.
[153] V.A. Golyashov, K.A. Kokh, S.V. Makarenko, K.N. Romanyuk, I.P. Prosvirin, A.V. Kalinkin, O.E. Tereshchenko, A.S. Kozhukhov, D.V. Sheglov, S.V. Eremeev, S.D. Borisova, E.V. Chulkov, Inertness and degradation of (0001) surface of Bi_2Se_3 topological insulator, *Journal of Applied Physics* 112(11) (2012) 113702.
[154] J. Kim, E.H. Shin, M.K. Sharma, K. Ihm, O. Dugerjav, C. Hwang, H. Lee, K.T. Ko, J.H. Park, M. Kim, H. Kim, M.H. Jung, Observation of Restored Topological Surface States in Magnetically Doped Topological Insulator, *Scientific Reports* 9 (2019) 1331.
[155] C.L. Song, Y.P. Jiang, Y.L. Wang, Z. Li, L.L. Wang, K. He, X. Chen, X.C. Ma, Q.K. Xue, Gating the charge state of single Fe dopants in the topological insulator Bi_2Se_3 with a scanning tunneling microscope, *Physical Review B* 86(4) (2012) 045441.
[156] L.B. Abdalla, L. Seixas, T.M. Schmidt, R.H. Miwa, A. Fazzio, Topological insulator Bi_2Se_3(111) surface doped with transition metals: An ab initio investigation, *Physical Review B* 88(4) (2013) 045312.
[157] G. Abadias, E. Chason, J. Keckes, M. Sebastiani, G.B. Thompson, E. Barthel, G.L. Doll, C.E. Murray, C.H. Stoessel, L. Martinu, Review Article: Stress in thin films and coatings: Current status, challenges, and prospects, J*ournal of Vacuum Science & Technology A* 36(2) (2018) 020801.
[158] Y. Ni, A.K. Soh, On the growth of buckle-delamination pattern in compressed anisotropic thin films, *Acta Materialia* 69 (2014) 37-46.
[159] H.T. Ren, Z.X. Xiong, E.Z. Wang, Z.Q. Yuan, Y.F. Sun, K.L. Zhu, B.L. Wang, X.W. Wang, H.Y. Ding, P. Liu, L. Zhang, J.Q. Wu, S.S. Fan, X.Y. Li, K. Liu, Watching Dynamic Self-Assembly of Web Buckles in Strained MoS_2 Thin Films, *ACS Nano* 13(3) (2019) 3106-3116.
[160] E.A. Flores-Johnson, L. Shen, R.K. Annabattula, P.R. Onck, Y.G. Shen, Z. Chen, The effect of interface adhesion on buckling and cracking of hard thin films, *Applied Physics Letters* 105(16) (2014) 161912.
[161] Y. Wang, Z.W. Li, J.L. Xiao, Stretchable Thin Film Materials: Fabrication, Application, and Mechanics, *Journal of Electronic Packaging* 138(2) (2016) 020801.
[162] N. Bowden, S. Brittain, A.G. Evans, J.W. Hutchinson, G.M. Whitesides, Spontaneous formation of ordered structures in thin films of metals supported on an elastomeric polymer, *Nature* 393(6681) (1998) 146-149.
[163] C. Harrison, C.M. Stafford, W.H. Zhang, A. Karim, Sinusoidal phase grating created by a tunably buckled surface, *Applied Physics Letters* 85(18) (2004) 4016-4018.
[164] M.W. Moon, K.R. Lee, K.H. Oh, J.W. Hutchinson, Buckle delamination on patterned substrates, *Acta Materialia* 52(10) (2004) 3151-3159.
[165] M.W. Moon, S. Chung, K.R. Lee, K.H. Oh, H.A. Stone, J.W. Hutchinson, Directed assembly of fluidic networks by buckle delamination of films on patterned substrates, *International Journal of Materials Research* 98(12) (2007) 1203-1208.
[166] J.C. Fuggle, N. Martensson, Core-level binding-energies in metals, *Journal of Electron Spectroscopy and Related Phenomena* 21(3) (1980) 275-281.
[167] L.F. Sun, C.H. Chen, Q.H. Zhang, C. Sohrt, T.Q. Zhao, G.C. Xu, J.H. Wang, D. Wang, K. Rossnagel, L. Gu, C.G. Tao, L.Y. Jiao, Suppression of the Charge Density Wave State in Two-Dimensional 1T-$TiSe_2$ by Atmospheric Oxidation, *Angewandte Chemie-International Edition* 56(31) (2017) 8981-8985.

[168] S. Negishi, H. Negishi, K. Shimada, X.Y. Cui, M. Higashiguchi, M. Nakatake, M. Arita, H. Namatame, M. Taniguchi, A. Ohnishi, M. Sasaki, Photoemission study on electronic structure of $TiSe_2$, *Physica B-Condensed Matter* 383(1) (2006) 155-157.

[169] W. Jaegermann, C. Pettenkofer, A. Schellenberger, C.A. Papageorgopoulos, M. Kamaratos, D. Vlachos, Y. Tomm, Photoelectron spectroscopy of UHV in situ intercalated Li/$TiSe_2$. Experimental proof of the rigid band model, *Chemical Physics Letters* 221(5-6) (1994) 441-446.

[170] A.S. Shkvarin, Y.M. Yarmoshenko, A.I. Merentsov, I. Pis, F. Bondino, E.G. Shkvarina, A.N. Titov, Guest-Host Chemical Bonding and Possibility of Ordering of Intercalated Metals in Transition-Metal Dichalcogenides, *Inorganic Chemistry* 57(9) (2018) 5544-5553.

[171] A.V. Naumkin, A. Kraut-Vass, C.J. Powell, S.W. Gaarenstroom, *NIST X-ray photoelectron spectroscopy database*, 2012; http://srdata.nist.gov/xps/, (accessed May 2020).

[172] A.S. Shkvarin, Y.M. Yarmoshenko, N.A. Skorikov, M.V. Yablonskikh, A.I. Merentsov, E.G. Shkvarina, A.N. Titov, Electronic Structure of Titanium Dichalcogenides TiX_2 (X = S, Se, Te), *Journal of Experimental and Theoretical Physics* 114(1) (2012) 150-156.

[173] L.N. Zelenina, T.P. Chusova, A.N. Titov, Thermodynamic properties of titanium selenides with variable composition $TiSe_2$-$TiSe_{1.80}$, *Russian Chemical Bulletin* 60(3) (2011) 581-584.

[174] A. Ettema, C. Haas, An X-ray photoemission spectroscopy study of interlayer charge-transfer in some misfit layer compounds, *Journal of Physics-Condensed Matter* 5(23) (1993) 3817-3826.

[175] T. Conard, R. Sporken, J. Ghijsen, L.M. Yu, R. Caudano, R. Seemann, R.L. Johnson, Photoemission study of the Bi/CuO interface, *Surface Science* 369(1-3) (1996) 177-184.

[176] D. Gonbeau, C. Guimon, G. Pfisterguillouzo, A. Levasseur, G. Meunier, R. Dormoy, XPS Study of Thin-Films of Titanium Oxysulfides, *Surface Science* 254(1-3) (1991) 81-89.

[177] M. Binnewies, E. Milke, Thermochemical Data of Elements and Compounds, Wiley, Weinheim, 2002.

[178] Y.-R. Luo, Comprehensive handbook of chemical bond energies, CRC press, Boca Raton, 2007.

[179] J.M. Blakely, Surface Physics of Materials, Academic Press, New York, 1975.

[180] A.J. Francis, P.A. Salvador, Crystal orientation and surface morphology of face-centered-cubic metal thin films deposited upon single-crystal ceramic substrates using pulsed laser deposition, *Journal of Materials Research* 22(1) (2007) 89-102.

[181] J.S. Agustsson, U.B. Arnalds, A.S. Ingason, K.B. Gylfason, K. Johnsen, S. Olafsson, J.T. Gudmundsson, Electrical resistivity and morphology of ultra thin Pt films grown by dc magnetron sputtering on SiO_2, *Journal of Physics: Conference Series* 100(8) (2008) 082006.

[182] A.I. Maaroof, B.L. Evans, Onset of electrical conduction in Pt and Ni films, *Journal of Applied Physics* 76(2) (1994) 1047-1054.

[183] V.K. Karzhavin, Sulfides, selenides, and tellurides of platinum and palladium: Estimation of thermodynamic properties, *Geochemistry International* 45(9) (2007) 931-937.

[184] M. Sreemany, S. Sen, Effect of substrate temperature and annealing temperature on the structural, electrical and microstructural properties of thin Pt films by rf magnetron sputtering, *Applied Surface Science* 253(5) (2006) 2739-2746.

[185] W. Sripumkhai, S. Porntheeraphat, B. Saekow, W. Bunjongpru, S. Rahong, J. Nukeaw, Effect of annealing temperature on platinum thin films prepared by electron beam evaporation, *Journal of the Microscopy Society of Thailand* 24(1) (2010) 51-54.
[186] S. Strobel, C. Kirkendall, J.B. Chang, K.K. Berggren, Sub-10 nm structures on silicon by thermal dewetting of platinum, *Nanotechnology* 21(50) (2010) 505301.
[187] K. Wang, K. Yao, S.J. Chua, Titanium diffusion and residual stress of platinum thin films on Ti/SiO_2/Si substrate, *Journal of Applied Physics* 98(1) (2005) 013538.
[188] M. Sui, M.Y. Li, S. Kunwar, P. Pandey, Q. Zhang, J. Lee, Effects of annealing temperature and duration on the morphological and optical evolution of self-assembled Pt nanostructures on c-plane sapphire, *PLOS One* 12(5) (2017) e0177048.
[189] E. Conforto, P.E. Schmid, Pt-Si reaction through interfacial native silicon oxide layers, *Philosophical Magazine a-Physics of Condensed Matter Structure Defects and Mechanical Properties* 81(1) (2001) 61-82.
[190] E. Conforto, P.E. Schmid, Platinum silicide phase transformations controlled by a nanometric interfacial oxide layer, *Thin Solid Films* 516(21) (2008) 7467-7474.
[191] J.S. Chen, E. Kolawa, M.A. Nicolet, R.P. Ruiz, L. Baud, C. Jaussaud, R. Madar, Solid-state reaction of Pt thin film with single-crystal (001) β–SiC, *Journal of Materials Research* 9(3) (1994) 648-657.
[192] J. Shi, D. Kojima, M. Hashimoto, The interaction between platinum films and silicon substrates: Effects of substrate bias during sputtering deposition, *Journal of Applied Physics* 88(3) (2000) 1679-1683.
[193] U. Schmid, The impact of thermal annealing and adhesion film thickness on the resistivity and the agglomeration behavior of titanium/platinum thin films, *Journal of Applied Physics* 103(5) (2008) 054902.
[194] S.Z. Weng, L. Qiao, P. Wang, Thermal stability of Pt-Ti bilayer films annealing in vacuum and ambient atmosphere, *Applied Surface Science* 444 (2018) 721-728.
[195] S.M. Gasser, E. Kolawa, M.A. Nicolet, Thermal reaction of Pt film with <110> GaN epilayer, *Journal of Vacuum Science & Technology A* 17(5) (1999) 2642-2646.
[196] R.R. Altunin, E.T. Moiseenko, S.M. Zharkov, Structural Phase Transformations in Al/Pt Bilayer Thin Films during the Solid-State Reaction, *Physics of the Solid State* 60(7) (2018) 1413-1418.
[197] E. Okogbue, S.S. Han, T.J. Ko, H.S. Chung, J. Ma, M.S. Shawkat, J.H. Kim, E. Ji, K.H. Oh, L. Zhai, G.H. Lee, Y. Jung, Multifunctional Two-Dimensional $PtSe_2$-Layer Kirigami Conductors with 2000% Stretchability and Metallic-to-Semiconducting Tunability, *Nano Letters* 19(11) (2019) 7598-7607.
[198] C. Xie, L.H. Zeng, Z.X. Zhang, Y.H. Tsang, L.B. Luo, J.H. Lee, High-performance broadband heterojunction photodetectors based on multilayered $PtSe_2$ directly grown on a Si substrate, *Nanoscale* 10(32) (2018) 15285-15293.
[199] Å. Olin, B. Noläng, E.G. Osadchii, L.O. Öhman, E. Rosén, Chemical Thermodynamics of Selenium, 7th ed., Elsevier Science, Amsterdam, 2005.
[200] F. Hulliger, New compounds with cobaltite structure, *Nature* 198(4878) (1963) 382-383.
[201] F. Hulliger, E. Mooser, Semiconductivity in pyrite, marcasite and arsenopyrite phases, *Journal of Physics and Chemistry of Solids* 26(2) (1965) 429-433.
[202] A. Wold, Platinum Metal Chalcogenides, *Advances in Chemistry Series* (98) (1971) 17-27.
[203] Y. Zhang, F. de Juan, A.G. Grushin, C. Felser, Y. Sun, Strong bulk photovoltaic effect in chiral crystals in the visible spectrum, *Physical Review B* 100(24) (2019) 245206.

[204] T. Sakamoto, M. Wakeshima, Y. Hinatsu, Transport properties in normal-metal $Bi_2Pd_3S_2$ and superconducting $Bi_2Pd_3Se_2$, *Physical Review B* 78(2) (2008) 024509.

[205] S. Seidlmayer, F. Bachhuber, I. Anusca, J. Rothballer, M. Brau, P. Peter, R. Weihrich, Half antiperovskites: V. Systematics in ordering and group-subgroup relations for $Pb_2Pd_3Se_2$, $Bi_2Pd_3Se_2$, and $Bi_2Pd_3S_2$, *Zeitschrift Fur Kristallographie-Crystalline Materials* 225(9) (2010) 371-381.

[206] K. Ferfolja, M. Valant, I. Mikulska, S. Gardonio, M. Fanetti, Chemical Instability of an Interface between Silver and Bi_2Se_3 Topological Insulator at Room Temperature, *Journal of Physical Chemistry C* 122(18) (2018) 9980-9984.

[207] P. Vanysek, Electrochemical series, CRC Press, Boca Raton, 2000.

[208] D. Harris, Quantitative chemical analysis, W.H. Freeman and Company, New York, 2010.

[209] D. Feng, P. Taskinen, Thermodynamic stability of AuSe at temperature from (400 to 700) K by a solid state galvanic cell, *Journal of Chemical Thermodynamics* 71 (2014) 98-102.

[210] O.E. Tereshchenko, K.A. Kokh, V.V. Atuchin, K.N. Romanyuk, S.V. Makarenko, V.A. Golyashov, A.S. Kozhukhov, I.P. Prosvirin, A.A. Shklyaev, Stability of the (0001) surface of the Bi_2Se_3 topological insulator, *JETP Letters* 94(6) (2011) 465-468.

[211] L.X. Zhang, E.G. Wang, Q.K. Xue, S.B. Zhang, Z.Y. Zhang, Generalized electron counting in determination of metal-induced reconstruction of compound semiconductor surfaces, *Physical Review Letters* 97(12) (2006) 126103.

[212] L. Pan, D. Berardan, N. Dragoe, High Thermoelectric Properties of n-Type $AgBiSe_2$, *Journal of the American Chemical Society* 135(13) (2013) 4914-4917.

[213] H.J. Wu, P.C. Wei, H.Y. Cheng, J.R. Deng, Y.Y. Chen, Ultralow thermal conductivity in n-type Ge-doped $AgBiSe_2$ thermoelectric materials, *Acta Materialia* 141 (2017) 217-229.

[214] J. Kim, A. Hwang, S.H. Lee, S.H. Jhi, S. Lee, Y.C. Park, S.I. Kim, H.S. Kim, Y.J. Doh, B. Kim, Quantum Electronic Transport of Topological Surface States in beta-Ag_2Se Nanowire, *ACS Nano* 10(4) (2016) 3936-3943.

[215] Z. Zhao, S.B. Wang, A.R. Oganov, P.C. Chen, Z.X. Liu, W.D.L. Mao, Tuning the crystal structure and electronic states of Ag_2Se: Structural transitions and metallization under pressure, *Physical Review B* 89(18) (2014) 180102.

[216] C.L. Zhang, F. Schindler, H.W. Liu, T.R. Chang, S.Y. Xu, G.Q. Chang, W. Hua, H. Jiang, Z.J. Yuan, J.L. Sun, H.T. Jeng, H.Z. Lu, H. Lin, M.Z. Hasan, X.C. Xie, T. Neupert, S. Jia, Ultraquantum magnetoresistance in the Kramers-Weyl semimetal candidate beta-Ag_2Se, *Physical Review B* 96(16) (2017) 165148.

[217] P. Goli, J. Khan, D. Wickramaratne, R.K. Lake, A.A. Balandin, Charge Density Waves in Exfoliated Films of van der Waals Materials: Evolution of Raman Spectrum in $TiSe_2$, *Nano Letters* 12(11) (2012) 5941-5945.

[218] M. Calandra, F. Mauri, Charge-Density Wave and Superconducting Dome in $TiSe_2$ from Electron-Phonon Interaction, *Physical Review Letters* 106(19) (2011) 196406.